

2015

Process planning for robotic wire ARC additive manufacturing

Donghong Ding
University of Wollongong

Follow this and additional works at: <https://ro.uow.edu.au/theses>

University of Wollongong

Copyright Warning

You may print or download ONE copy of this document for the purpose of your own research or study. The University does not authorise you to copy, communicate or otherwise make available electronically to any other person any copyright material contained on this site.

You are reminded of the following: This work is copyright. Apart from any use permitted under the Copyright Act 1968, no part of this work may be reproduced by any process, nor may any other exclusive right be exercised, without the permission of the author. Copyright owners are entitled to take legal action against persons who infringe their copyright. A reproduction of material that is protected by copyright may be a copyright infringement. A court may impose penalties and award damages in relation to offences and infringements relating to copyright material.

Higher penalties may apply, and higher damages may be awarded, for offences and infringements involving the conversion of material into digital or electronic form.

Unless otherwise indicated, the views expressed in this thesis are those of the author and do not necessarily represent the views of the University of Wollongong.

Recommended Citation

Ding, Donghong, Process planning for robotic wire ARC additive manufacturing, Doctor of Philosophy thesis, School of Mechanical, Materials and Mechatronics Engineering, University of Wollongong, 2015.
<https://ro.uow.edu.au/theses/4613>

Research Online is the open access institutional repository for the University of Wollongong. For further information contact the UOW Library: research-pubs@uow.edu.au

UNIVERSITY OF WOLLONGONG

COPYRIGHT WARNING

You may print or download ONE copy of this document for the purpose of your own research or study. The University does not authorise you to copy, communicate or otherwise make available electronically to any other person any copyright material contained on this site. You are reminded of the following:

Copyright owners are entitled to take legal action against persons who infringe their copyright. A reproduction of material that is protected by copyright may be a copyright infringement. A court may impose penalties and award damages in relation to offences and infringements relating to copyright material. Higher penalties may apply, and higher damages may be awarded, for offences and infringements involving the conversion of material into digital or electronic form.

PROCESS PLANNING FOR ROBOTIC WIRE ARC ADDITIVE MANUFACTURING

A dissertation

submitted to the University of Wollongong in partial fulfilment of the
requirements for the degree of

Doctor of Philosophy

September 2015

By

Donghong Ding

School of Mechanical, Materials and Mechatronic Engineering

University of Wollongong, Australia

Abstract

Robotic Wire Arc Additive Manufacturing (WAAM) refers to a class of additive manufacturing processes that builds parts from 3D CAD models by joining materials layer-upon-layer, as opposed to conventional subtractive manufacturing technologies. Over the past half century, a significant amount of work has been done to develop the capability to produce parts from weld deposits through the additive approach. However, a fully automated CAD-to-part additive manufacturing (AM) system that incorporates an arc welding process has yet to be developed. The missing link is an automated process planning methodology that can generate robotic welding paths directly from CAD models based on various process models. The development of such a highly integrated process planning method for WAAM is the focus of this thesis.

The major steps in process planning for robotic WAAM includes generation of 2.5D layers, generation of deposition paths for these layers, the determination of welding parameters (e.g. wire-feed rate, travel speed, and stick-out) associated with the deposition paths, and an optional post-process machining. A more detailed explanation for each of these steps is provided as follows.

In WAAM, the CAD model is sliced into a set of 2.5D layers along the build direction. Unlike existing slicing methods, which divide models into parallel slices of either equally or varying thickness, the newly-developed multi-direction slicing algorithm decomposes CAD models into slices in multiple directions based on geometric evaluations. This allows direct deposition of complex models without the need to introduce additional support structures. In addition, in multi-direction deposition, the accuracy of the deposited part is increased through minimising the “stair-stepping” effect.

Deposition paths are subsequently generated for the 2D cross-section of the obtained 2.5D layers. Path generation for processes that have fine, statistically distributed particles in powder-based AM system are somewhat independent of geometric complexity. However, AM systems based on arc-wire welding produce much larger deposits than powder-based systems, so the deposition paths are significantly influenced by geometric complexity and the material selected. Innovative MAT-based (medial axis transformation) path planning algorithms are proposed to generate void-free deposition paths irrespective of the complexity of the geometry.

Welding parameters associated with the generated deposition paths are selected to produce weld deposits with the desired width and height to produce the necessary layer thickness together with complete material infill between paths. Generally, welding variables such as wire-feed rate and travel speed are manually set by welding experts depending on the deposition process and the material selected. In this study, artificial neural network (ANN) single bead models are established for the gas metal arc welding (GMAW) process of mild steel and aluminium alloy materials, respectively. A multi-bead overlapping model is also developed to determine the appropriate overlapping distances (step-over distances) between the paths in order to obtain a smooth multi-pass surface. Both the ANN model and multi-bead overlapping model are integrated into the process planning methodology allowing the automatic selection of optimum welding parameters corresponding to the generated deposition paths.

As a result, near-net shapes are fabricated using the generated deposition paths and welding parameters. The shapes are then machined to produce the finished parts with the required dimensional tolerances through a series of post-process robotic machining operations. The absence of re-fixturing problems and tool accessibility problems helps in fully automating the generation of robotic machining paths. Several parts were built automatically using this process planning and the results are discussed.

Acknowledgements

I take this opportunity to express my sincere appreciation to my principal supervisor Dr. Zengxi Pan, and associate supervisors Prof. Huijun Li and Dr. Dominic Cuiuri, for their support and guidance in pursuing this research. They kept me free of financial worries and provided the much needed assistance in my program over the last three years. The excellent research atmosphere that provided in our group was very helpful for the successful completion of this work.

Many thanks to Prof. Weihua Li, and A/Prof. Shu-Qing Yang for their guidance during my early PhD life (12.2011~6.2013). Weihua's encouragement allowed me to feel more confident to start my new research topic.

I would like to thank Mr. Nathan Larkin for his support during laboratory experiment. I would also like to thank the other members of our group, Dr. Stephen Van Duin and Prof. John Norrish for their valuable comments and useful suggestions.

A special thanks to my colleague Andrew Short for his supporting in experiments. Also I am grateful to my other colleagues Chen Shen, Alexander Visser, and Yan Ma for exciting and useful discussions.

Finally, I wish to express my special thanks to all my friends, to my parents, to my wife, and to my lovely daughter, for their support and encouragement during this work.

Table of Contents

Abstract.....	I
Acknowledgements	III
List of Figures.....	VII
Chapter 1	1
Introduction.....	1
1.1 Motivation.....	1
1.2 Literature review	2
1.2.1 AM vs. CNC Machining	2
1.2.2 Powder-based vs. wire-feed AM process.....	3
1.2.3 Wire-feed AM processes	6
1.2.4 Wire arc additive manufacturing	8
1.3 Research gaps	14
1.4 Present work	15
1.5 Thesis outline	17
Chapter 2	19
Process Planning Overview	19
2.1 The WAAM process.....	19
2.2 Process planning.....	20
2.3 User interface	22
2.4 Summary.....	23
Chapter 3	25
Bead Modelling.....	25
3.1 Single bead geometry	25
3.1.1 Single bead empirical models.....	26
3.1.2 Experimental set-up	26
3.1.3 Curve fitting results	28
3.2 Multi-bead overlapping model for mild steel	30
3.2.1 Principle of the tangent overlapping model (TOM).....	31
3.2.2 Overlapping of two beads.....	33
3.2.3 Multi-bead overlapping	35
3.2.4 Experimental verification for the overlapping model.....	35
3.3 Artificial neural network bead models.....	41

3.3.1 Forward computing	41
3.3.2 Error backpropagation learning	42
3.3.3 Training of neural network	44
3.3.4 Bead geometry measurement	45
3.3.5 Testing of neural network	46
3.4 Summary	47
Chapter 4	48
3D CAD Slicing	48
4.1 Uni-direction slicing	48
4.1.1 The tolerant uni-direction slicing algorithm	49
4.1.2 Implementation	52
4.2 Multi-direction slicing	54
4.2.1 Related works of multi-direction slicing	55
4.2.2 Strategy overview	57
4.2.3 Multi-direction slicing algorithms	59
4.2.3 Implementation and results	71
4.3 Summary	73
Chapter 5	75
2D Deposition Path Planning	75
5.1 Existing path planning methods	75
5.2 Path planning challenges in WAAM	78
5.3 MAT-based path planning	83
5.3.1 Overview of MAT-based path	83
5.3.2 Definition and computation of the MAT	86
5.3.3 MAT-based path generation	88
5.3.4 Discussions	95
5.4 Adaptive MAT path planning	99
5.4.1 Essential of adaptive MAT path	99
5.4.2 Algorithm for adaptive MAT path generation	101
5.4.3 Validation of the proposed algorithm	106
5.4.4 Discussions	108
5.5 Summary	109
Chapter 6	111
Post-process Machining	111

6.1 Top region machining.....	111
6.2 Side region machining	112
6.3 Base region machining.....	113
6.4 Summary.....	114
Chapter 7	115
Applications	115
7.1 Mild steel components with complex geometries	115
7.2 Aluminium thin-walled structure with finished quality	118
7.3 Adaptive MAT paths with minimum post milling	122
7.3.1 ANN model of mild steel.....	122
7.3.2 Determination of 2D path planning variables	124
7.3.3 Determination of welding process parameters	126
7.3.4 Case studies.....	127
7.3.5 Discussions	131
7.4 Summary.....	132
Chapter 8	134
Summary and Future Work	134
8.1 Contributions.....	134
8.2 Future work.....	136
Appendix.....	139
A. Continuous path generation algorithm	139
B. Smallest enclosing crowns	147
References.....	150
Selected Publications	157

List of Figures

Figure 1.1 Schematic visualization of the AM processes and representative fields [4].....	1
Figure 1.2 Qualitative situation of the AM metal components production relative to usual options (MIM: Metal Injection Moulding; PM-Sintering: Powder Metallurgy Sintering) [8]	2
Figure 1.3 Comparison of surface finish and deposition rate between powder-based and wire-feed technologies. (a) Titanium 3D-micro-framework-structure based on a diamond lattice fabricated using powder-bed electron beam melting [12]; (b) A powder-feed directed light fabrication of 316 stainless steel hemispherical shapes [17]; (c) Three as-consolidated powder-feed laser consolidation IN-625 samples with surface roughness 1-2 μm [23]; (d) A large samples fabricated by WAAM from Cranfield University [30];(e) 2219 Al airfoil produced by wire-feed EFB ³ [31]; (f) As deposited sample made by wire-feed LAM (AeroMet) with “stair stepping” surface, and (g) shows the sample after surface machining.....	5
Figure 1.4 Left: Schematic drawing of the wire-feed process. Right: Top-and side view images of the real process [35].....	6
Figure 1.5 Schematic of electron beam freeform fabrication (EBF ³) system [14].....	7
Figure 1.6 Schematic diagram of the (a) GMAW, (b) GTAW, and (c) PAW process	8
Figure 1.7 Schematic of two deposition techniques [61]	11
Figure 1.8 Deposition patterns for plate substrates [63]	11
Figure 1.9 Ti-6Al-4V wall structure deposited by WAAM process, the deflections along the deposition direction can be observed [68]	12
Figure 1.10 The principle of layer thickness adjustment: (a) original solid model, (b) sliced model with constant layer thickness, and (c) sliced model with adjusted layer thickness [53]	13
Figure 1.11 Approximate surface – “stair stepping” effect [72]	13
Figure 2.1 Steps involved in building parts with WAAM system	20
Figure 2.2 Schematic diagram of the automated process planning algorithm of an arc-welding-based additive manufacturing system	21
Figure 2.3 User friendly interface the arc-welding-based additive manufacturing system. A total of 7 steps from S1 to S7 are described.	22
Figure 3.1 Weld bead geometry.....	26
Figure 3.2 Schematic diagram of the experimental set-up for bead deposition and measurement	27
Figure 3.3 Experimental measurements of weld bead profile.....	28
Figure 3.4 Relative error for predicted and actual area of weld bead cross-section	29

Figure 3.5 Weld bead geometry of a single bead with various welding speeds (V_w) or travel speed (S)	30
Figure 3.6 Sketch of the traditional flat-top overlapping model (FOM).....	31
Figure 3.7 Schematic diagrams of the tangent overlapping model (TOM)	32
Figure 3.8 The overlap area, the area of the critical valley, and $f(d)$ as a function of the step-over distance d	34
Figure 3.9 Schematic overlapped profile of a multi-bead deposit at $d < d^*$	35
Figure 3.10 Comparison of experimental measurements of bead profile with the tangent overlapping model (TOM) and the flat-top overlapping model (FOM)	36
Figure 3.11 The relative errors between the experimental bead profile and the models	37
Figure 3.12 The experimental results of overlapped bead profile at various distance d	38
Figure 3.13 The ratio of the height of the second bead to the first bead (c_2/c_1) at various centre distance d/w	39
Figure 3.14 Experiments of multi-bead and multi-layer deposition.	40
Figure 3.15 Schematic diagram of the feedforward neural network for weld bead geometry	41
Figure 3.16 Architecture of an individual neuron for neural network	42
Figure 3.17 (a) Single beads (60 mm long) deposited onto aluminium substrate with parameter sets No.17-23; welding direction runs from left to right; the red lines represent the locations of cross-sectioning away from arc starting and extinguishing points to eliminate the start and end effects. (b) Schematic diagram of bead geometry measurement using the 3D laser profile scanner.	46
Figure 3.18 Comparison between predicted and measured weld bead geometry (normalised).....	46
Figure 4.1 Example of a STL file format and its model	48
Figure 4.2 (a) STL model with slicing layers in uni-direction; (b) Resulting layer boundary polygons	49
Figure 4.3 Flowchart of the tolerance slicing algorithm [77]	50
Figure 4.4 Possible cases of facet-plane slicing [77]	51
Figure 4.5 Case I. (a) An engineering STL model; (b) Resulting slices	52
Figure 4.6 Case II. (a) A Great Wall STL model; (b) Resulting slices	52
Figure 4.7 Case III. (a) A Triceratops STL model; (b) Resulting slices	53
Figure 4.8 (a) The component and its usual build direction B ; (b) support required (parts coloured in orange); (c) multi-direction slicing and various build directions B_1 , B_2 , and B_3	54
Figure 4.9 Schematic diagram of a robotic multi-direction deposition system	54
Figure 4.10 Illustration of the impact of holes on multi-direction slicing strategy.....	57
Figure 4.11 Architecture of the multi-direction slicing strategy	57

Figure 4.12 An example of a complex model with holes (a) the original model; (b) STL mesh; (c) identified holes; and (d) simplified model without holes.....	58
Figure 4.13 (a) a progressive decomposition of an example into sub-volumes with their own build directions; (b) sub-volume grouping with depth-tree structure; and (c) model slicing along multiple build directions.....	59
Figure 4.14 Illustration of basic concepts: (a) regions (in different colours); (b) boundaries; and (c) loops.....	60
Figure 4.15 (a) The planar edge; (b) The feature edge (convex); (c) The feature edge (concave)	61
Figure 4.16 Rules for constructing boundary loops.....	62
Figure 4.17 An example of a STL model and the generated boundary loops.....	62
Figure 4.18 Rules for identifying the inner loops	64
Figure 4.19 Modified advancing front mesh method for hole-filling	65
Figure 4.20 Illustration of the developed hole-filling algorithm for planar and spatial holes with complex shapes (red regions are holes filled by triangular facets through the proposed hole-filling algorithm).....	65
Figure 4.21 The algorithm for progressive decomposition.....	66
Figure 4.22 Rules for adding triangles and updating the front	67
Figure 4.23 (a) An example for illustration of sub-volumes, feature regions (coloured in red), and base region (b) Grouped sub-volumes (c) Slicing in multiple directions	68
Figure 4.24 Sub-volumes grouping with the depth-tree structure.....	69
Figure 4.25 The optimal build direction for sub-volume.....	70
Figure 4.26 (a) Keel fitting component in aerospace industry; (b) generated boundaries of the model; (c) slicing results; (d) all the detected holes; and (4) holes need to be deposited as supports	72
Figure 4.27 (a) An engineering part; (b) slicing results; (c) all the detected holes; (d) further simplification of slices	73
Figure 5.1 Raster path pattern.....	75
Figure 5.2 Zigzag path pattern.....	76
Figure 5.3 Contour path pattern.....	76
Figure 5.4 Contour path pattern.....	76
Figure 5.5 Hybrid path pattern.....	77
Figure 5.6 Continuous path pattern. (a) Hilbert filling curve; (b) Fractal-like build style; (c) Hybrid continuous path (zigzag & continuous); (d) Hybrid continuous path (zigzag & contour & continuous).	78

Figure 5.7 Illustration of automatic path planning. Green lines represent the generated paths, and black lines represent the boundary of the geometry. (a) CAD model. (b) A slice. (c) Raster paths (green). (d) Contour paths (red).	80
Figure 5.8 (a) A cross-section of a simple thin-walled structure. (b) Contour path patterns generated by offsetting the boundary curves towards its interior. (c) Deposition of materials along the generated path. Narrow gap (middle white area) is left which cannot be filled by the path.	81
Figure 5.9 Weld deposits heights along the welding distance	81
Figure 5.10 Thin walls built by weld deposition showing the changing bead geometry at the start and end of weld paths [57].	82
Figure 5.11 Concerns of crossings in thin-walled structures. (a) Direct crossing induces peaks. (b) Path pattern of opposite angles [103]. (c) One direct and two crossing method [10]. (d) Finished part	83
Figure 5.12 Illustration of path generated from MAT. (a) up: original geometry (green region) and the MAT of the geometry (black line); down: contour path patterns with gaps in middle are clearly seen; (b) up: red region are deposition of excessive materials; down: the MAT path patterns without gaps [104].	84
Figure 5.13 Illustration of MAT-based path planning. (a) The medial axis computing (red lines). (b) Domain decomposition (each domain is described in one different colour. (c) Path generation for domain 3. (d) MAT-based paths at the crossing area.	85
Figure 5.14 (a) Medial axis transformation (MAT) of a geometry. The dash lines represent the medial axis. (b) Red lines represent branches and red dash lines represent sub-branches.	86
Figure 5.15 Computation of the bisector lines for pairs of line segments. Black lines represent the boundary of the geometry. Coloured lines represent the bisector lines. Bold red line in (b) represents the MAT corresponding to the boundary ab. Pink area is the region in which all points are closet to its associated boundary ab.	88
Figure 5.16 Flowchart of the developed approach for generating path from MAT	89
Figure 5.17 Illustration of the general skeleton and branch loop formation for a simple polygon without holes	90
Figure 5.18 Branch loop formation for complex geometries with holes. Black lines represent the boundary of the geometry. Red line loops with arrows represent the formed branch loops.	91
Figure 5.19 Example of the shape with two holes. (a) Computed MAT as represented by dotted lines; (b) Multiple branches as described by red lines; and (c) Formed one branch loop along counter-clockwise direction and other two branch loops inside along clockwise.	92
Figure 5.20 The cell structures of untrimmed paths in the program	92

Figure 5.21 (a) Untrimmed paths for the simple shape. Black lines represent the boundary of the given geometry. Red lines represent the MAT. Green lines stand for the generated untrimmed paths, and blue lines represent the outside of each untrimmed path. (b) Trimmed paths.	93
Figure 5.22 Geometry 1, solid structure with multiple branches. (a) Geometry is represented by black lines, MAT represented by dotted red lines, and red solid lines stand for branches. (b) Generated trimmed path.	94
Figure 5.23 Geometry 2, solid structure with holes. (a) Geometry is represented by black lines, MAT represented by dotted red lines, and red solid lines stand for branches. (b) Generated trimmed path. .	94
Figure 5.24 Geometry 3, thin-walled curved structure. (a) Geometry is represented by black lines, MAT represented by dotted red lines, and red solid lines stand for branches. (b) Generated trimmed path.....	94
Figure 5.25 Geometry 4, thin-walled complex structure. (a) Geometry is represented by black lines, MAT represented by dotted red lines, and red solid lines stand for branches. (b) Generated trimmed path.....	95
Figure 5.26 Geometry 5, thin-walled structure with varied characteristic thicknesses. (a) Geometry is represented by black lines, MAT represented by dotted red lines, and red solid lines stand for branches. (b) Generated trimmed path.	95
Figure 5.27 Material efficiency & non-dimensional build time vs. step-over distance. (a) Geometry 1. (b) Geometry 2. (c) Geometry 3. (d) Geometry 4. (e) Geometry 5.....	97
Figure 5.28 Material efficiency vs. step-over distance for five geometries in WAAM system.....	98
Figure 5.29 Variations for material efficiency in WAAM for Geometry 1, 2, 3, 4, and 5.	99
Figure 5.30 Illustrations of different deposition paths. Black lines represent the boundary of the geometry; green lines represent the deposition paths with the numbers representing the order of the deposition paths; grey regions are deposited area by the relevant paths. (a) Contour path patterns; (b) The predicted high accuracy deposition but with internal gaps; (c) MAT path patterns; (d) The predicted void-free deposition but with extra material deposited along the boundary; (e) Adaptive MAT path patterns with varying step-over distance; (f) The predicted void-free deposition with high accuracy at the boundary through using adaptive MAT path.	100
Figure 5.31 Flowchart of the adaptive MAT path planning algorithm	101
Figure 5.32 Geometry 1, illustrations of adaptive path generation for the given geometry. (a) Three typical simple shapes decomposed from the domain, T1: triangle1; T2: triangle2; and T3: trapezoid. (b) The decomposed shapes are shown in order of processing. (c) Offset rules for three typical shapes. (d) Apply the offset rules for all decomposed shapes. (e) Final generated adaptive paths with varying step-over distances.	102
Figure 5.33 Geometry 2, illustrations of the adaptive path generation for geometry with a single hole. (a) Computed medial axis as represented by red dotted lines. (b) Branch loop formation. (c) Geometry	

sub-division, two domains are divided and displayed in different colours. (d) Domain decomposition, all domains are decomposed into a set of three typical simple shapes. (e) Apply the offset rules for all decomposed shapes. (f) Final generated adaptive paths.	105
Figure 5.34 Example of a geometry with multiple holes. (a) Computed branch loops as represented by red lines; (b) Divided six domains as represented by different colours; (c) Generated numerous radiations from the branch points and the various decomposed simple shapes; (d) Generated adaptive paths for the geometry	106
Figure 5.35 Geometry 3, a thin-walled structure with multiple internal holes recesses.	107
Figure 5.36 Geometry 4, a complex thick-walled structure with multiple internal holes. (a) Adaptive MAT path. (b) Non-adaptive MAT path.....	107
Figure 6.1 Schematic diagram of the near-net shape as deposited. (a) After top region machining; (b) After side region machining; and (c) Base region machining.....	111
Figure 6.2 Top region machining paths generation. (a) Black lines represent the boundary of the geometry; (b) Red dash lines represent the medial axis of the geometry; (c) Red solid lines represent the generated paths through offsetting the medial axis; and (d) Trajectory of machining tool. Blue circles represent the tool cross section.....	112
Figure 6.3 Side region machining paths generation. (a) Red lines represent the path generation through offsetting the boundaries of the geometry; and (b) Trajectory of the machining tool.....	113
Figure 6.4 Base region machining paths generation. (a) Red lines represent the Zigzag path generation; and (b) Trajectory of the machining tool.	114
Figure 7.1 Experimental set-up: (a) ABB 1400 robot with Fronius welder for additive manufacturing, (b) ABB 6660 robot with motor spindle for machining.....	115
Figure 7.2 A turbine blade structure	116
Figure 7.3 A twist turbine blade structure.....	117
Figure 7.4 An impeller structure	117
Figure 7.5 Example of process planning for the impeller structure	118
Figure 7.6 Final MAT-based paths for the thin-walled structure.....	119
Figure 7.7 Tool paths for side region machining	120
Figure 7.8 Experimental results. (a) Near-net shape of the produced aluminium component. (b) Details of crossings and start/strop sections. (c) Details at a corner.	120
Figure 7.9 (a) Process of post machining. (b) Final finished part with the desired dimensional accuracy	121
Figure 7.10 Experimentally measured bead widths and bead heights of all tests	123

Figure 7.11 Measured bead height and width vs. predicted bead height and width using ANN model. Circles represent the bead heights of the independent 8 testing data. Solid red squares represent the bead widths of the independent 8 testing data. Units for both axes are millimetres.	123
Figure 7.12 Surface plots of the bead height and bead width as the function of wire-feed rate and welding travel speed	124
Figure 7.13 Ranges of bead width and bead height through varying wire-feed rate and travel speed.	125
Figure 7.14 Illustration of the deposition process in an expanded domain.....	125
Figure 7.15 The database of weld single bead model. $M = 61$, and $N = 61$ as mentioned in Section 7.3.1.	127
Figure 7.16 Case 1, a thin-walled structure with a single internal hole and varied wall thickness....	128
Figure 7.17 Calculated step-over distance (mm), normalised wire-feed rate, and normalised travel speed along the length of deposition path 1 (in mm)	128
Figure 7.18 Calculated step-over distance (mm), normalised wire-feed rate, and normalised travel speed along the length of the deposition path 2 (in mm)	129
Figure 7.19 (a) Deposited near-net shape after 15 layers. (b) Finished part without voids after surface milling.....	129
Figure 7.20 Examination of the internal cross sections. (a) Cut parts of the case one; the cross section A is parallel to the building direction and the cross section B is perpendicular to the building direction. (b) Close up of the cross section A. (c) Close up of the cross section B.”.....	129
Figure 7.21 Case 2, a solid structure without holes.	130
Figure 7.22 Calculated step-over distance (mm), normalised wire-feed rate, and normalised travel speed along the length of the deposition path 3 (in mm)	131
Figure 7.23 (a) Deposited near-net shape after 15 layers. (b) Finished part without voids after surface milling.....	131

Chapter 1

Introduction

1.1 Motivation

Over the past thirty years, Additive Manufacturing (AM) has gained increasing attention in the manufacturing industry, especially to manufacture component models and prototypes. Various AM processes, such as 3D Printing (3DP) [1], Selective Laser Sintering (SLS) [2], and Fused Deposition Modelling (FDM) [3], have been developed. Figure 1.1 shows the research and development of AM [4]. At the base are the various AM processes, and the branches are representative fields of outcomes and benefits.

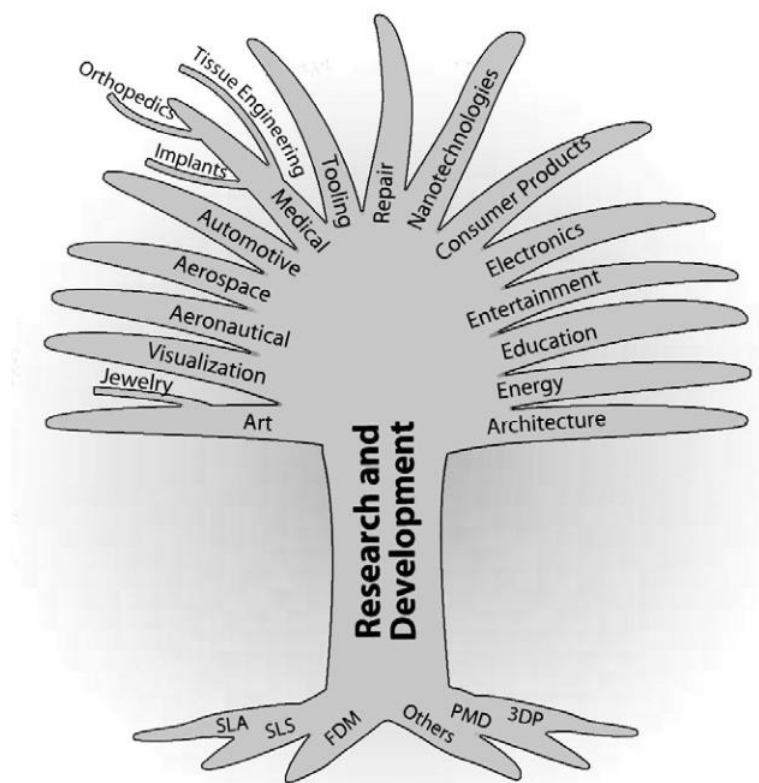


Figure 1.1 Schematic visualization of the AM processes and representative fields [4]

In order to meet the industrial demands of aerospace [5, 6], automotive [7], and rapid tooling [8, 9], the recent focus of AM research has shifted to the fabrication of complex shaped metal components, including titanium and nickel alloys that cannot be economically produced using conventional methods. The arc welding process has been widely explored for additive manufacture of large metal components for the aerospace industry, due to its lower capital cost, an unlimited build envelope, and higher deposition rates [10]. Although significant improvements have been made, an arc welding process has yet to be incorporated in a commercially available AM system. The next step in exploiting “true” arc-welding-based additive manufacturing is to develop the automation system required to produce CAD-to-part capability.

This thesis focuses on developing a fully automated system to additively manufacture metal components using the robotic Gas Metal Arc Welding (GMAW) process, called robotic Wire Arc Additive Manufacturing (WAAM). The developed system reads only the CAD models as inputs and produces the finished parts without human intervention.

1.2 Literature review

1.2.1 AM vs. CNC Machining

The competitive position of AM for metal components relative to alternative manufacturing processes is a function of the geometrical complexity and production volume. Figure 1.2 [8] shows that AM (also referred as Layer Manufacturing) is suitable to fabricate parts with medium to high geometrical complexity at relatively low quantities.

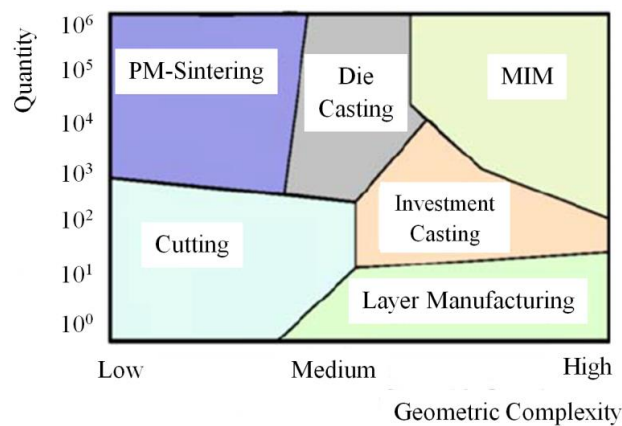


Figure 1.2 Qualitative situation of the AM metal components production relative to usual options (MIM: Metal Injection Moulding; PM-Sintering: Powder Metallurgy Sintering) [8]

When compared with conventional subtractive manufacturing (e.g. CNC machining), AM has several advantages. Firstly, it is possible to automate the AM process from part design to fabrication in a CAD/CAM environment. This reduces both the production time and the amount of human intervention needed for each new part. Although programs for CNC machining can also be automatically generated from CAD models, multiple re-fixturing is necessary for complex geometries, resulting in time-consuming and expensive re-fixturing and calibration procedures. Secondly, AM is a cost-competitive approach for fabricating components made from expensive material such as titanium and nickel alloys in the aerospace industry, where such components often suffer extremely high buy-to-fly ratios. In addition, it is possible to use AM to create single-component structures with complex shapes that would be impractical or impossible to build with traditional subtractive approaches.

1.2.2 Powder-based vs. wire-feed AM process

According to the standard terminology for AM by ASTM (ASTM F2792), AM technologies for metal components are mainly classified into powder bead fusion, directed energy deposition, binder jetting, and sheet lamination as listed in Table 1.1. Typical additive materials are metal powder and metal wire. With regard to how the additive material is supplied, currently popular AM technologies can be classified as powder-feed, powder-bed or a wire-feed process.

Table 1.1 Classification of AM for metal components

Classification	Terminologies	Ref.	Material
Powder bed fusion	Direct metal laser sintering (DMLS)	[11]	Metal powder
	Electron beam melting (EBM)	[12]	
	Selective laser sintering (SLS)	[2]	
	Selective laser melting (SLM)	[13]	
	Electron beam freeform fabrication (EBF ³)	[14]	
Directed energy deposition	Laser engineered net shaping (LENS)	[15]	Metal powder, metal wire
	Laser consolidation (LC)	[16]	
	Directed light fabrication (DLF)	[17]	
	Wire and arc additive manufacturing (WAAM)	[18]	
Binder jetting	Powder bed and inkjet 3d printing (3DP)	[19]	Metal powder
Sheet lamination	Laminated object manufacturing (LOM)	[20]	Metal laminate,
	Ultrasonic consolidation (UC)	[21]	Metal foil

The majority of research in AM has been focused on powder-based AM systems, where the laser or electron beam equipment is usually used as the power source. Powder-based AM techniques generally involve a complex non-equilibrium physical and chemical metallurgical process, which exhibits multiple modes of heat and mass transfer, and in some instances, chemical reactions. A comprehensive review on the materials design, process control,

property characterisation and metallurgical theories for laser sintering, laser melting, and laser metal deposition of a wide variety of metallic powders has been reported recently in the literature [22].

Table 1.2 provides a comparison of the basic features between powder-based and wire-feed processes. The powder-based approach is better developed due to its capability of fabricating parts with high geometrical accuracy. The resolution of typical layer thickness in powder-based technology is 20-100 μm , and the completed components can achieve a dimensional accuracy of ± 0.05 mm and surface roughness of 9-16 μm [23, 24]. In addition, it is possible to produce parts with functionally graded materials (FGM) [25]. However, the deposition rate of powder-based technology is extremely low, typically around 10 g/min, which limits its application in fabricating median to large sized components.

Table 1.2 Comparisons of some representative AM processes

Additive materials	Process	Layer thickness (μm)	Deposition rate (g/min)	Dimensional accuracy (mm)	Surface roughness (μm)	Ref.
Powder	LC	N/A	1 – 30	$\pm 0.025 - \pm 0.069$	1 – 2	[23]
	SLM	20 – 100	N/A	± 0.04	9 – 10	[24]
	SLS	75	~ 0.1	± 0.05	14 – 16	[26]
	DLF	200	10	± 0.13	~ 20	[17]
Wire	WAAM	~ 2000	~ 180	± 0.2	200	[27, 28]
	EBF ³	N/A	50 – 150	Low	High	[10]

In wire-feed AM, a metal wire is used as feed material instead of metal powder. Wire-feed AM has higher material usage efficiency up to 100% of the wire material deposited into the component. Therefore, it is a more environmental friendly process, which does not expose operators to the hazardous powder environment. Compared with the powder-based process, it has a much higher deposition rate of up to 150 g/min and its resolution of typical layer thickness could be higher than 2 mm [10]. Table 1.2 reveals that there is a trade-off between deposition rate and resolution. As also shown in Figure 1.3, by using wire instead of powder materials, the deposition rate increased and large components can be economically produced, while the resolution and complexity of the fabricated parts decreases. Additionally, metal wires are lower in cost and more readily available than metal powders having suitable properties for AM, making wire-feed AM technologies more cost-competitive for large components.

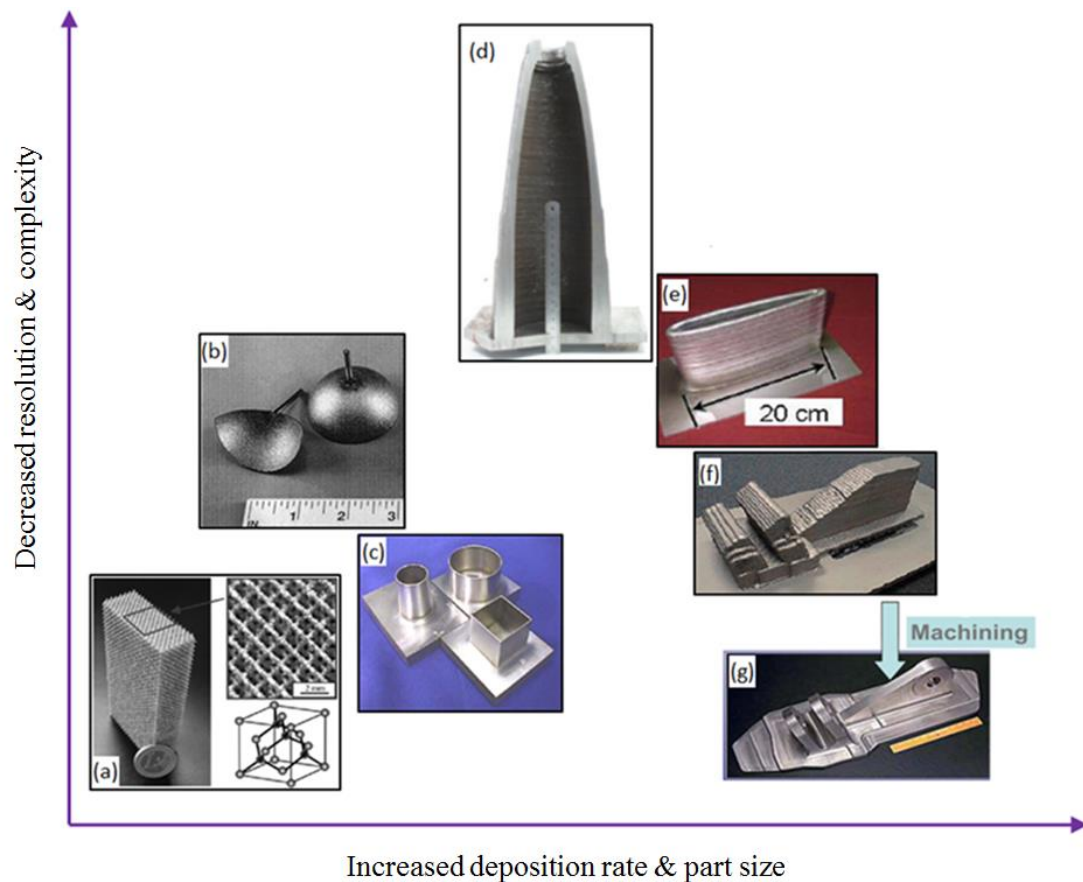


Figure 1.3 Comparison of surface finish and deposition rate between powder-based and wire-feed technologies. (a) Titanium 3D-micro-framework-structure based on a diamond lattice fabricated using powder-bed electron beam melting [12]; (b) A powder-feed directed light fabrication of 316 stainless steel hemispherical shapes [17]; (c) Three as-consolidated powder-feed laser consolidation IN-625 samples with surface roughness 1-2 μm [23]; (d) A large samples fabricated by WAAM from Cranfield University [29]; (e) 2219 Al airfoil produced by wire-feed EFB³ [30]; (f) As deposited sample made by wire-feed LAM (AeroMet) with “stair stepping” surface, and (g) shows the sample after surface machining.

The material properties of parts deposited using either metal wire or metal powder as the additive materials have been investigated [31]. The comparisons indicate that the microstructure of samples from both methods is similar, although some porosity is found in the powder-fed deposited parts. Other studies have investigated the combination of both wire-feed and powder-fed deposition strategies [32, 33]. One study [32] found that the deposition efficiency can be increased if these two feeding technologies are combined. Also, the level of porosity was approximately 20% to 30 % lower than of samples made with powder feeding only. In [33], a combination of Ti-6Al-4V wire feeding and TiC powder feeding was investigated. It was found that a uniform distribution of the TiC particles in the new Ti-6Al-4V/TiC composites could be achieved as long as the rates of TiC addition remained above a certain value.

1.2.3 Wire-feed AM processes

Depending on the energy source used for metal deposition, wire-feed AM can be further classified into three groups: laser based, arc welding based, and electron beam based [34]. These wire-feed AM technologies are described below.

Wire and Laser Additive Manufacturing (WLAM) is an AM process to produce metal components with full density using metal wires as the additive material and laser as the energy source. The WLAM system normally consists of a laser, an automatic wire-feed system, a computer numerically controlled work table or a robot system, and some accessories (e.g. shielding gas, preheating or cooling system). As schematically shown in Figure 1.4, the laser generates a melt pool on the substrate material, into which the metal wire is fed and melted, forming a metallurgical bond with the substrate [35]. By moving the laser processing head and wire feeder or moving the substrate, a bead is formed during solidification. The relative motion of the welding tool and the substrate can be achieved by using either a robot arm or a computer numerically controlled worktable.

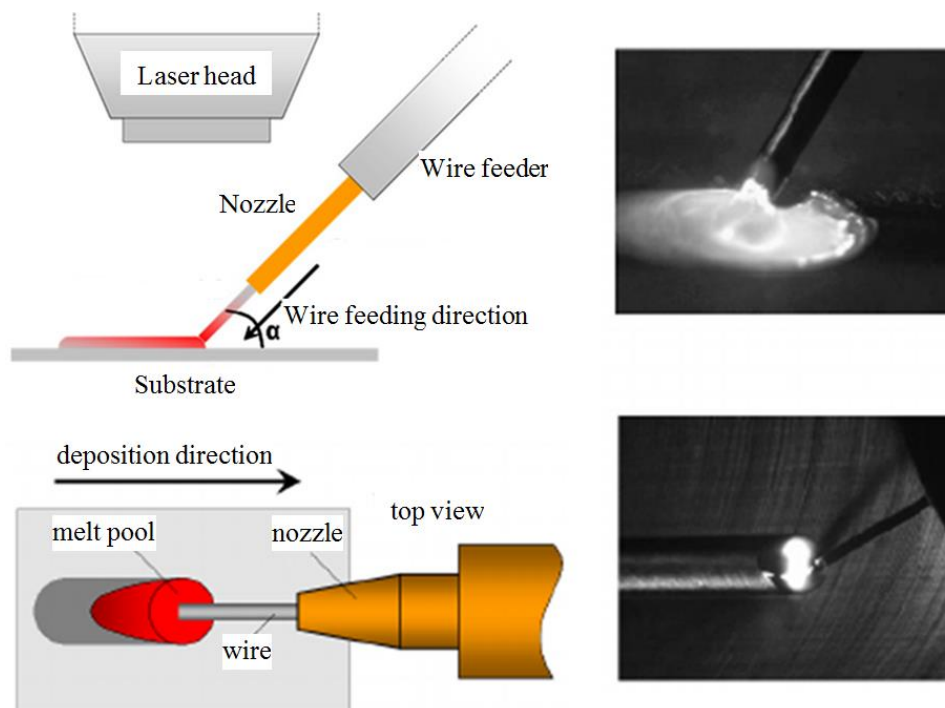


Figure 1.4 Left: Schematic drawing of the wire-feed process. Right: Top-and side view images of the real process [35].

Electron Beam Freeform Fabrication (EBF³) is a NASA-patented additive manufacturing process designed to build complex, near-net-shape parts requiring substantially less raw material and finish machining than traditional manufacturing methods. Figure 1.5 shows a schematic of the primary components in an EBF³ system. The process

introduces metal wire feedstock into a molten pool that is created and sustained using a focused electron beam in a high vacuum environment. The electron beam couples effectively with any electrically conductive material, including highly reflective alloys such as aluminium and copper. The EBF³ process is capable of bulk metal deposition at high deposition rates as well as finer deposition at lower deposition rates with the same piece of equipment, limited only by the positioning accuracy and wire feed capability. The diameter of the wire feedstock is the controlling factor determining the smallest feature attainable using this process: fine diameter wires may be used for adding fine details, and larger diameter wires can be used to increase deposition rate for bulk deposition. The electron beam power and focus can be adjusted to suit the required resolution.

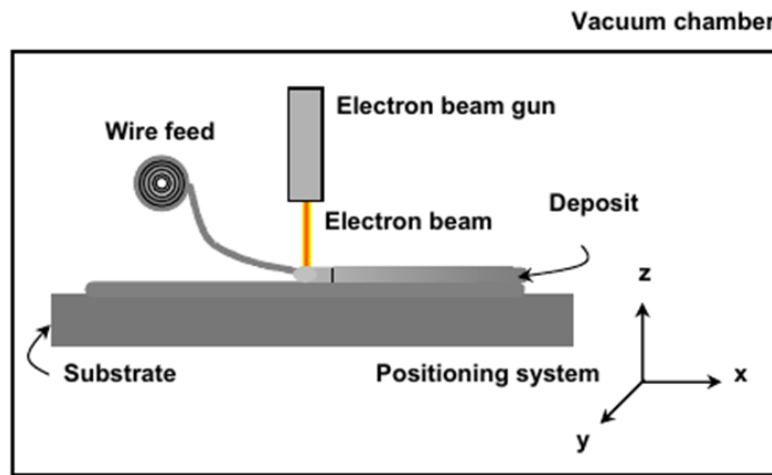


Figure 1.5 Schematic of electron beam freeform fabrication (EBF³) system [14]

Wire Arc Additive Manufacturing (WAAM) is another popular Wire-feed AM technology. Several research groups have investigated the WAAM processes using Gas Metal Arc Welding (GMAW), Gas Tungsten Arc Welding (GTAW), or Plasma Arc Welding (PAW) as a heat source.

A schematic diagram of the GMAW, GTAW, and PAW process is shown in Figure 1.6. GMAW is a welding process in which an electric arc forms between a consumable wire electrode and the workpiece metal. The wire is typically perpendicular to the substrate. There are four primary metal transfer modes in GMAW, globular, short-circuiting, spray, and pulsed-spray, each having its distinct features. In addition, Cold Metal Transfer (CMT), a modified GMAW variant based on controlled dip transfer mode mechanism has also been widely implemented for AM processes [5], due to its high deposition rate and low heat input.

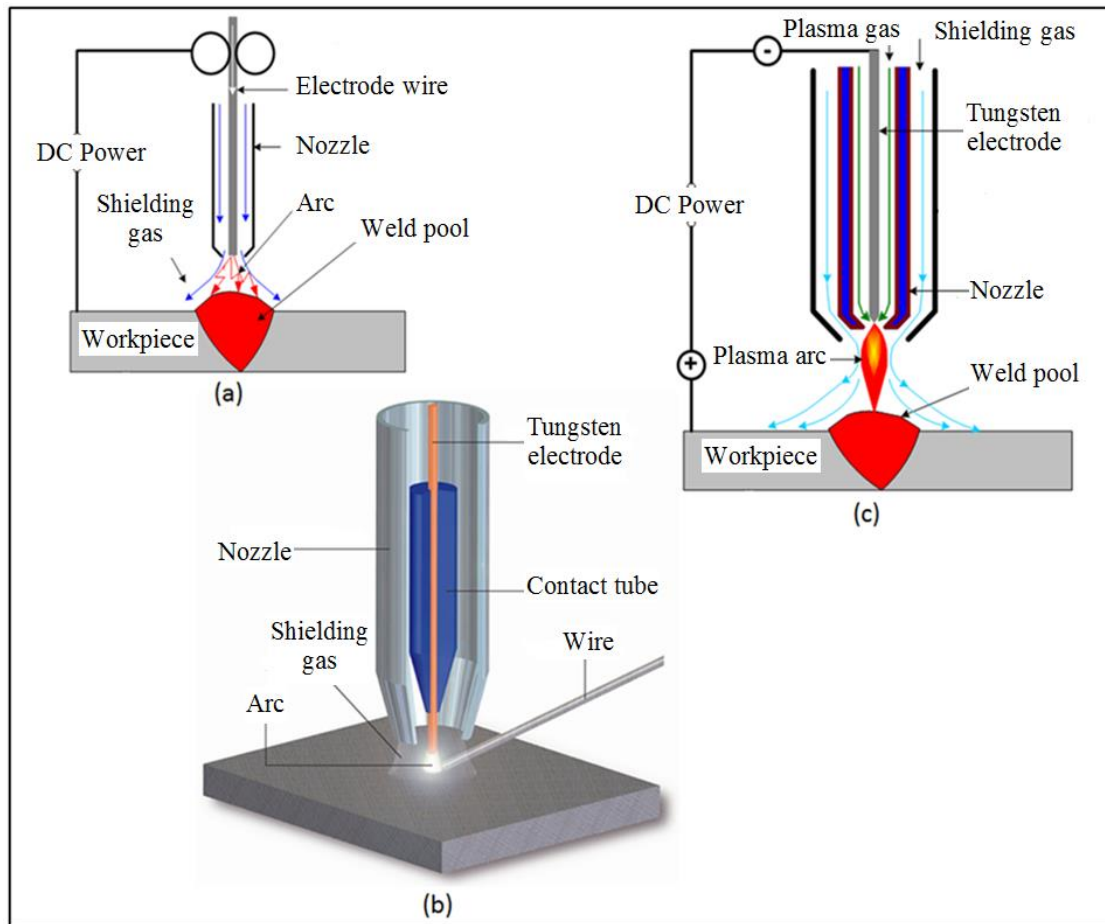


Figure 1.6 Schematic diagram of the (a) GMAW, (b) GTAW, and (c) PAW process

GTAW and PAW use a non-consumable tungsten electrode to produce the welding arc, while the consumable wire is fed into the molten weld pool. Unlike GMAW, the wire feed orientation in GTAW and PAW is an additional variable which affects the quality of the deposit. The best results are typically obtained by feeding the wire at the “front” of the weld pool with respect to the direction of travel, although this condition may not always be achievable during deposition of a practical component.

1.2.4 Wire arc additive manufacturing

Robotic wire arc additive manufacturing (WAAM) is one of additive manufacturing technologies for producing large metal components using robotic arc welding. The advantages of such a system over the laser or electron beam additive manufacturing system include higher energy efficiency, lower capital investment, and a strong supply chain capability in industry. Laser has been the most popular due to its “precision”, or ability to narrowly and accurately focus the coherent light beam. However, it has very poor energy efficiency (2-5%) [36]. Electron beam has a slightly higher energy efficiency (15-20%) and

similar focusing ability to laser, but it requires a high vacuum working environment that limits its applications [37]. In comparison, the energy efficiency of arc welding processes such as GMAW or GTAW processes can be as high as 90% in some circumstances [38, 39], although the welding arc diameter is typically 3 to mm, depending on the chosen welding parameters. Additionally, the cost of the traditional arc welding equipment is much lower compared to the laser or electron beam equipment.

A large amount of work has been done over the previous three decades to develop the capability to fabricate parts from weld deposits using a layer-by-layer approach. Early studies exploring arc welding for AM have been reported by European researchers [40-42]. The ability of arc welding to produce high quality full density near-net shapes has been confirmed. A preliminary automated system for welding-based AM was developed by Zhang et al. [43]. The deposition parameters, including the travel speed, welding current, and arc voltage were discussed in detail. Hybrid approaches to “3D welding and milling” have been established to fabricate parts with a high quality surface finish [34, 44]. The effects of bead modelling and process optimization in arc-welding-based AM were also investigated [27, 45, 46]. Recently, vision-sensing systems have been designed to on-line monitor and control the robotic arc welding process in real time to deposit the desired bead geometry [47-49]. Several other organizations throughout the world continue to work in this exciting field of arc-welding-based AM, as summarized in Table 1.3.

Table 1.3 Different phrases of WAAM from various research groups

Synonyms	Institutions/Universities	Energy Source	Ref.
3D welding	University of Nottingham	GMAW	[40, 42]
Welding-based deposition	Southern Methodist University	GMAW, GTAW	[50-52]
3D welding	Korea Institute of Science and Technology	GMAW	[44]
Welding-based rapid prototyping	University of Kentucky	GMAW	[53]
Near-net shape manufacturing	Tufts University	GMAW, PAW	[54]
Shape deposition manufacturing	Carnegie Mellon and Stanford University	GMAW, GTAW	[55]
GMAW-based rapid prototyping	Harbin Institute of Technology	GMAW	[46]
MPAW-based rapid prototyping	Xi'an Jiaotong University	Micro-PAW	[56]
Hybrid layered manufacturing	Indian Institute of Technology	GMAW	[45]
WAAM	Cranfield University	GMAW, GTAW, PAW	[5, 57]
WAAM	University of Wollongong	GMAW, GTAW	[27, 28, 58-60]

While WAAM is a promising technology for producing large aerospace components with moderate complexity, such as flanges or stiffened panels, there are a few technical challenges yet to be resolved, including the residual stress and distortion from excessive heat input, relatively poor part accuracy caused by the “stair stepping” effect, and poor surface finish.

Residual stresses and distortion: The control of residual stresses and distortion, especially for large-scale WAAM process is one of the major concerns because they not only cause poor dimensional tolerances but also induce premature failure. In welding, thermally induced stresses are the result of thermally induced strains during the non-uniform expansion and contraction of the material. The induced strain causes a material or structure to respond by distorting. If it is unable to cause a structure to respond by distorting macroscopically, it will either cause the structure to deform microscopically (e.g. yield or crack) or result in stresses that are “locked in” as residual stresses. When the fabricated component is unclamped from its production fixture, residual stresses will release, resulting in distortion of the component. Although the residual stresses could be minimized by post-processing technologies, residual stress induced distortions are a major cause of loss in tolerances. Therefore, the best way to limit distortions is to control the build-up of residual stresses during the deposition cycle.

Researchers have analysed the stresses produced within deposits of multi-pass single-layered structures by altering deposition patterns, deposition sequences, and preheating or interpass cooling. The selective deposition approach, which deposits a series of small patches (“towers”) first and later joins them together to form a large patch, has been used to minimize the deformation due to thermal stresses for shape deposition manufacturing [61]. As shown in Figure 1.7, these “towers” are only constrained at the bottom and their large surface area to volume ratio allows them to relax significantly as they cool down. Selective deposition can reduce deformation of the final part by allowing much of the deformation produced during cooling to occur before the deposit is fully constrained. The influence of deposition patterns, such as long raster and spiral, on the deflection of the metal part has been studied by Nickel et al. [62, 63] using a combination of finite element analysis and experiments as shown in Figure 1.8. It was found that the short raster pattern produced the lower deflection for a beam substrate, but for a plate substrate a spiral pattern scanned from the outside to the inside produces lower and more symmetrical deflections. The same result was also obtained in laser powder deposition process as reported by Foroozmehr [64]. This indicates that the deposition pattern significantly affects the temperature history of the process, and consequently, the stress distribution.

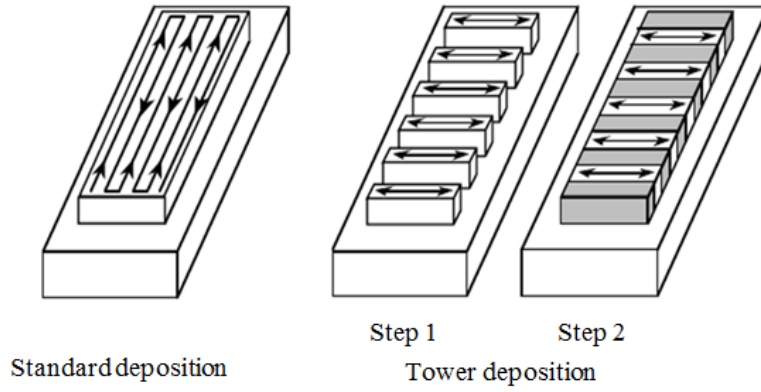


Figure 1.7 Schematic of two deposition techniques [61]

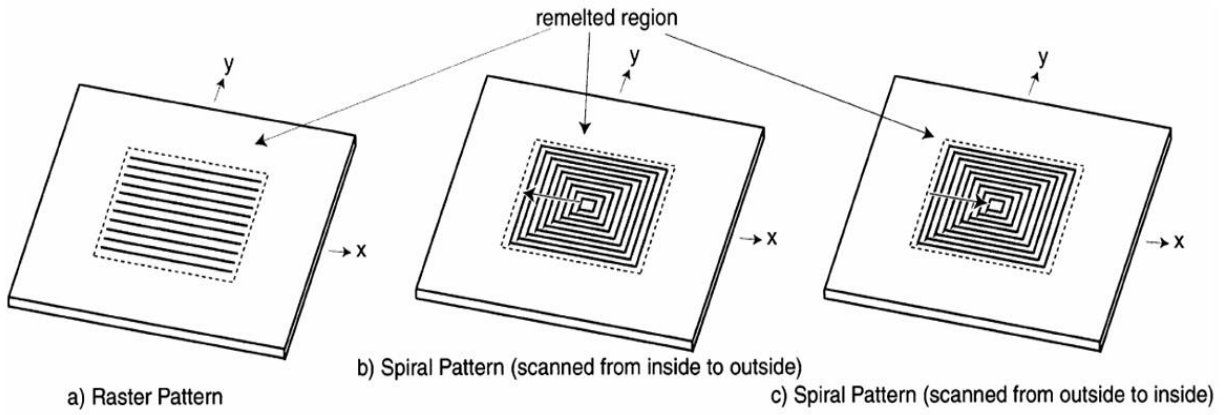


Figure 1.8 Deposition patterns for plate substrates [63]

Mughal et al. [65, 66] have developed a thermo-mechanical model to predict the residual stress induced deformations. It has been found that continuous deposition without interpass cooling results in less deformation as it equivalently provides a preheating for the substrate. Chin [67] also reported that uniform substrate preheating reduces residual stresses and deformation. However, continuous deposition may cause excessive heat input in a local area resulting in high temperature gradients and large remelting of the substrate, which will cause poor dimensional tolerances and surface finish [42]. Consequently, a compromise needs to be made between employing sufficient interpass cooling to avoid excessive heating and maintaining enough preheating to minimise deformation.

The effects of deposition sequences on residual stresses have also been investigated [66]. It was found that residual stresses are dependent on deposition sequences in continuous deposition. While the maximum stress value does not vary, the highest stresses are always found at the last deposition rows, since latter deposition is a reheating process which relaxes the stresses in the former deposits. However, with enough (or excessive) interpass cooling, the residual stress distribution becomes insensitive to the deposition sequence as each deposition sequence does not provide any preheating effects to the next sequence.

Thermo-mechanical analysis of material deposition on a single-pass multi-layer wall structure (see Figure 1.9) has also been widely investigated [68]. The study from [65] shows that the process using monotonic (single) deposition direction compared with alternating deposition directions provides better heat diffusion conditions and a more favourable temperature gradient trend. Recently, research works on wall structures [5] have shown that the heat from the welding process causes a tensile residual stress along the weld bead due to material contraction during solidification, which causes a balancing compressive residual stress in the base plate. A significant distortion of the component and relaxation of the stresses was observed after the base plate clamping mechanism was removed. It was also found that the stresses across the deposited wall are uniform with very little influence from the preceding layers. Rolling can reduce residual stresses and distortions on WAAM parts, particularly in the areas adjacent to the baseplate [69]. In addition, rolling also induced grain refinement when the rolled material was reheated during the subsequent deposition pass.

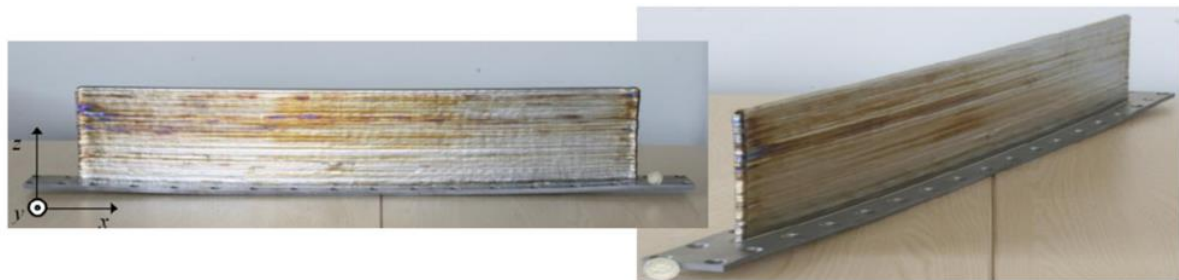


Figure 1.9 Ti-6Al-4V wall structure deposited by WAAM process, the deflections along the deposition direction can be observed [68]

Reported experimental research of the effects of deposition pattern, deposition sequences, and preheating on the residual stress mainly involves 2D layers or thin wall structures. For real engineering applications, finite element models are commonly used to predict residual stresses and distortions [70]. Currently an optimum deposition strategy for reducing the residual stresses induced by AM of any given 3D components remains unavailable.

Accuracy and surface finish: Besides the distortions induced from residual stresses, another significant factor that affects the accuracy of the part is the slicing method, which produces the un-match effect and also the staircase effect. Normally, a solid model is sliced with a constant layer thickness, as shown in Figure 1.10a. The partially fractional-height layers cannot be faithfully reproduced by the deposition process, effectively resulting in the inaccurate deposition model shown in Figure 1.10b. The adaptive slicing strategy which involves non-constant layer thickness is an effective way to address this issue. In the adaptive

slicing strategy [53, 71], the layer thickness can be adjusted automatically within a certain range to suit the shape of the model, as shown in Figure 1.10c.

The “stair-stepping” effect comes from the approximate construction of surfaces using deposition layers with a certain layer thickness. It exhibits dimensional errors normal to the build (deposition) direction as shown in Figure 1.11. For a given part surface, increased layer thickness produces a larger staircase error [72]. Therefore, the accuracy of a part manufactured by wire-feed AM technology is typically 10 times lower than that made by powder-bead/feed technology, due to the thicker layer thickness of the wire-feed AM technology (about 1.5 mm compared to 100 microns for powder). With a high deposition rate, the WAAM process is effective for simpler geometries. However, when high accuracy parts are desired, it is necessary to integrate post-process machining in WAAM process.

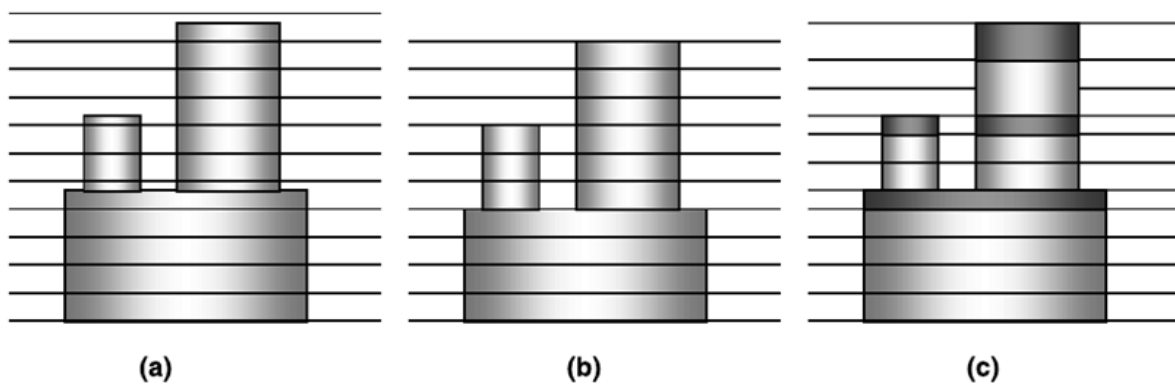


Figure 1.10 The principle of layer thickness adjustment: (a) original solid model, (b) sliced model with constant layer thickness, and (c) sliced model with adjusted layer thickness [53]

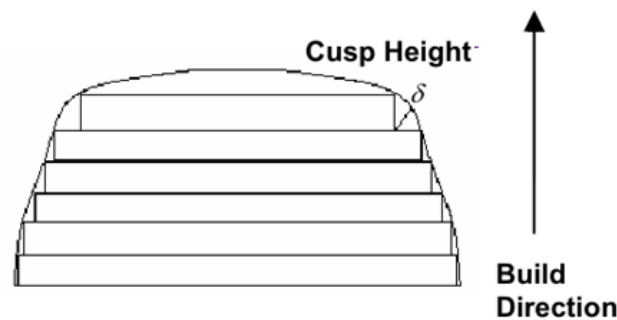


Figure 1.11 Approximate surface – “stair stepping” effect [72]

In AM, since a surface is usually fabricated through deposition of a large number of adjacent weld beads with or without overlapping and each weld bead is a parabola-like curve rather than a regular rectangle, the surface finish (also referred to as “surface roughness”) needs to be controlled. Therefore, accurate models for single bead geometry as well as the multi-bead overlapping play an important role in determining the surface finish of the fabricated components.

For GMAW-based WAAM process, due to the inherent characteristics of the process, the weld bead geometry within a single weld pass is not uniform, particularly at the start and end portions. This will lead to the uneven bead geometry, poor surface finish and part accuracy.

To overcome this issue, Zhang et al. [53] adjusted the welding parameters at the start and end portions of weld paths to control the bead geometry. At the start portion of the weld pass, the current and travel speed are decreased from initially higher values to the nominal or steady-state values. This avoids the typical “fattening” that occurs at the start of weld beads that are deposited with constant wire-feed rate and travel speed, due to initially cold conditions. At the end portion of the pass, the current and the travel speed are reduced gradually to fill the weld crater that is typically produced if the GMAW process is abruptly terminated. Although the shape of the weld pass can be flexibly controlled using this method, the adjustment procedures are empirical and time-consuming. Instead of changing the process parameters, an alternative method has been developed to optimise the deposition tool path pattern. A continuous path has been proposed to minimize the number of weld passes for each layer to eliminate the unwanted side effects of the arc starting/stopping [28]. It has been shown that the surfaces deposited using the continuous tool-path planning method (only one starting/stopping) are better than those produced by welding paths that use multiple starting/stopping. However, the proposed continuous deposition path method has been developed without considering the undesirable side effects of residual stress and distortion. Further research efforts will need to be applied towards optimising the deposition patterns in order to reduce residual stresses as well as improve surface finish.

1.3 Research gaps

Although significant progresses have been made, a commercially available additive manufacturing system based on arc welding process is yet to be developed. This is due to the lack of an automated process planner to optimally set all of the process parameters based on the information of the input CAD models. Process parameters such as deposition path, wire-feed rate, and travel speed are, insofar as described in the literature set by an experienced AM technician depending upon part geometry, energy source, and the material selected. However, for the case of components with complex geometries, the selection of process parameters will need to be fully automatic as human intervention in this complicated process is impractical.

Accordingly, the next step towards a “true” WAAM system is to develop the automation software required to produce seamless CAD-to-part capability. Existing commercial AM software has been developed for either powder-based processes or polymer materials, and cannot be directly used for WAAM. The main challenges in process planning are listed as follows.

Bead modelling: The effects of welding parameters on bead geometry should be systematically investigated. The single bead modelling with respect to different materials and feeding wire diameter is required to be established. The selection of the appropriate welding parameters should be automated based on a reliable weld bead model.

In WAAM, the step-over distance, i.e. the distance between adjacent weld beads, needs to be carefully selected to obtain a smooth overlapped surface. In order to improve the surface quality and dimensional accuracy of the fabricated products, therefore, accurate models for single weld bead geometry as well as multi-bead overlapping are required.

Slicing: CAD models are generally sliced into a set of parallel layers in the building direction, and the part is built layer-upon-layer. Some complex models may have overhangs which require the deposition of sacrificial supports resulting in an increased build time, wastage of material and costly post-processing. Robotic WAAM has the capability to deposit materials along multiple directions and therefore, eliminate or reduce the need for supports. However, the majority of the existing multi-direction slicing strategies apply to only a subset of potential part geometries. More emphasis should be placed on multi-direction AM to develop robust algorithms capable of automatically slicing any CAD model which satisfies support-less and collision-free layered deposition.

Path planning: Path generation for WAAM is more complicated since special attention should be paid to residual stress evolution and the dimensional relationship between the weld bead and the part geometry. In addition, the quality of material produced by WAAM is closely related to the appropriate selection of deposition paths. A poorly planned path often results in voids or gaps between adjacent passes. The number of path passes should be reduced to avoid the start/stop effects, particularly for the GMAW process. However, there are currently no solutions for producing appropriate paths that satisfy all requirements. The automatic generation of deposition paths for any given arbitrary geometry is still a challenge.

1.4 Present work

This work has the objective of developing a robotic Wire Arc Additive Manufacturing (WAAM) system with an incorporated robotic machining process. Robotic GMAW is used to additively manufacture near-net metal shapes through melting metal wire. Then robotic machining process is conducted to obtain the finished components with the desired dimensional tolerances. WAAM is a hybrid process, thereby exploiting the advantages of both additive manufacturing and conventional subtractive manufacturing.

Being a new manufacturing process, WAAM poses new challenges in process planning. This study addresses the process planning issues in WAAM. The major steps involve the development of bead models, generation of 2.5D layers, generation of deposition paths for these layers, and an optional step of post-process robotic machining.

Artificial neural network (ANN) single bead models for mild steel and aluminium alloys are established as essential process databases for the robotic WAAM system. The ANN models are integrated into the process planning methodology allowing the automatic selection of welding parameters (e.g. wire-feed rate, travel speed, and stick-out). A tangent multi-bead overlapping model is then developed to determine the appropriate step-over distance between deposition paths in terms of producing smooth overlapping surfaces.

An algorithm for multi-direction slicing of 3D CAD models into a variety of 2.5D layers along multiple directions is developed. Multi-direction slicing allows the robotic arc welding system to deposit complex components in multiple directions, which can eliminate or significantly reduce the usage of supports for fabricating overhangs. In addition, the deposition direction changes as required to accommodate the geometry of the model, which minimises the “stair-stepping” effect and increases the accuracy of the fabricated component. Compared to existing multi-direction slicing algorithms, the proposed algorithm is more efficient for components with sharp edges and hole-features.

Algorithms for generating deposition paths are also developed. Some of the factors that influence the derivation of deposition paths are identified. Algorithms for deriving the innovative Medial Axis Transformation (MAT)-based paths are developed. MAT paths are generated through offsetting the medial axis of the geometry from the centre towards the boundaries, allowing complete coverage of the cross-section area without overlapping or revisiting. In addition, MAT paths are contour-like curves which are suitable for WAAM to control the build-up of thermal stresses by avoiding locally high heat input. As a final advantage for WAAM, adaptive MAT paths are a set of closed curves that require a

minimum number of start/stop sequences within a given layer. For many geometries, the step-over distance can be adaptively changed along the deposition path so that all path loops in a given layer are continuous and closed, while conforming accurately to the modelled external boundaries of each layer and producing complete filling within the build area. These features enable the production of void-free components with minimum post machining at the external boundaries or surfaces.

Post-process robotic machining operations are conducted for producing finished parts with the desired dimensional tolerances. As an optional step, generation of robotic machining paths for side milling, top milling, and base milling are simply described.

The proposed process planning methodology and the developed algorithms have been verified through building several complex sample parts. The process planning problems that are typically encountered in building some of those parts are detailed, and future developments that are needed to overcome these issues are outlined.

1.5 Thesis outline

The objective of this thesis is to develop a highly integrated and automated process planning methodology that can generate robotic deposition and machining paths directly from CAD models. The proposed WAAM process is optimised for using the wire-feed gas metal arc welding process for deposition process, chosen due to its advantages of lower capital cost, a much larger build envelope, higher production rates, and a strong supply chain capability in industry.

Chapter 2 gives an overview of the proposed WAAM process outlining the variety of processing steps needed to produce a finished part from a CAD model.

Chapter 3 establishes an artificial neural network single bead model as well as a multi-bead overlapping model. Bead modelling provides the essential information for process parameters selection in the following Chapters.

Chapter 4 provides the multi-direction slicing algorithm. CAD models are decomposed into various sub-volumes, where each can be built along a single direction. These sub-volumes are then sliced according to their appropriate building directions. Sliced layers are finally organized in a certain sequences based on the layer-upon-layer manner.

Chapter 5 details the deposition path generation algorithms. Existing path planning methods are reviewed and their suitability for WAAM are discussed. Innovative MAT-based paths are proposed for the arc welding process. Generation algorithms of these paths are developed.

Chapter 6 introduces post-process machining. The machining process is divided into three classes, namely top region machining, side region machining, and base region machining. Algorithms for generation of machining paths are provided.

In Chapter 7 a variety of sample parts are built for verification of the developed algorithms and process planning methodology. The problems that were encountered in building some of these parts are described.

Chapter 8 concludes the thesis by outlining the accomplishments of this work. Some of the process planning issues that are not addressed in this work are discussed, and some suggestions for the improvement of the methods given in this work are also outlined.

Chapter 2

Process Planning Overview

Robotic wire arc additive manufacturing (WAAM) has been widely investigated as an option for fabricating metallic full density near-net shapes. But little progress has been made towards the ability to directly build metal shapes from CAD models without human intervention. In addition, industrial applications often require fully dense metal parts that have accurate dimensions and good surface appearance. This study attempts to address the issue of directly fabricating full density metal components with the desired dimensional tolerances. The major steps of process planning in WAAM will be identified in this chapter.

2.1 The WAAM process

Wire Arc Additive Manufacturing (WAAM) is a manufacturing process that creates functional metal parts by incremental material deposition and material removal. It combines the benefits of AM (handling complex geometries), traditional machining (accurate and precise with good surface quality), and arc-welding-based deposition (superior material properties).

Although progress has been made in process planning for CNC machines (such as identification of machining features, process sequencing, selection of fixtures, and generation of cutting tool paths), significant human intervention is still required resulting in long lead time and high cost.

In contrast, one of the advantages of AM processes is to produce physical objects from CAD models in a completely automated fashion. Complex geometries are sliced into a set of 2.5D layers, resulting in highly automated fabrication of simplified sub-geometries. Although it is argue that there are many potential issues, such as thermal build up, process optimization, and possible fusion defects, to automatically fabricate finished function metal components using AM methods, the layer-by-layer manner in AM makes fully automation of fabricating

complex structures easier, especially for some components that traditional CNC process could not build due to the tool accessibility or collision.

The steps involved in building parts with robotic WAAM are shown in Figure 2.1. The system starts from the CAD model, and ends with the finished component. The input CAD model is sliced into a set of layers using the 3D slicing module. Then deposition paths are generated for each layer through the 2D path planning module. Welding parameters associated with each generated paths are automatically selected based on the ANN bead geometry model. Deposition paths together with the determined welding parameters are translated to robot code proceeding to the fabrication process. Finally, the near-net shape is fabricated and post-process robotic machining is conducted if necessary.

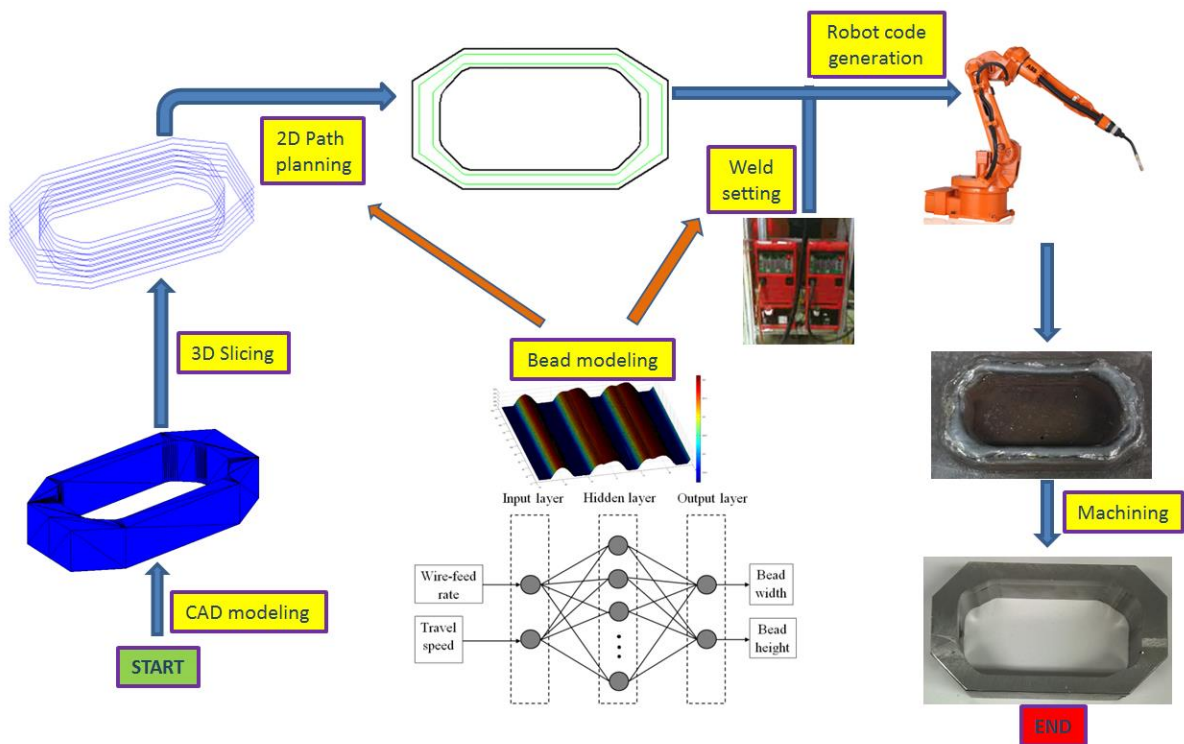


Figure 2.1 Steps involved in building parts with WAAM system

By using these step-by-step modules in a robust and autonomous fashion, producing parts using the WAAM processes requires very little human intervention. Of course, issues such as distortions and residual stresses would make process planning a far more challenging process. However, addressing these additional issues is beyond the scope of this study.

2.2 Process planning

An automated process planning methodology for implementing WAAM from CAD model inputs to finished parts is shown in Figure 2.2. Several modules are essential including

slicing, path planning, welding parameter setting, post-process machining, and the robot code generation module.

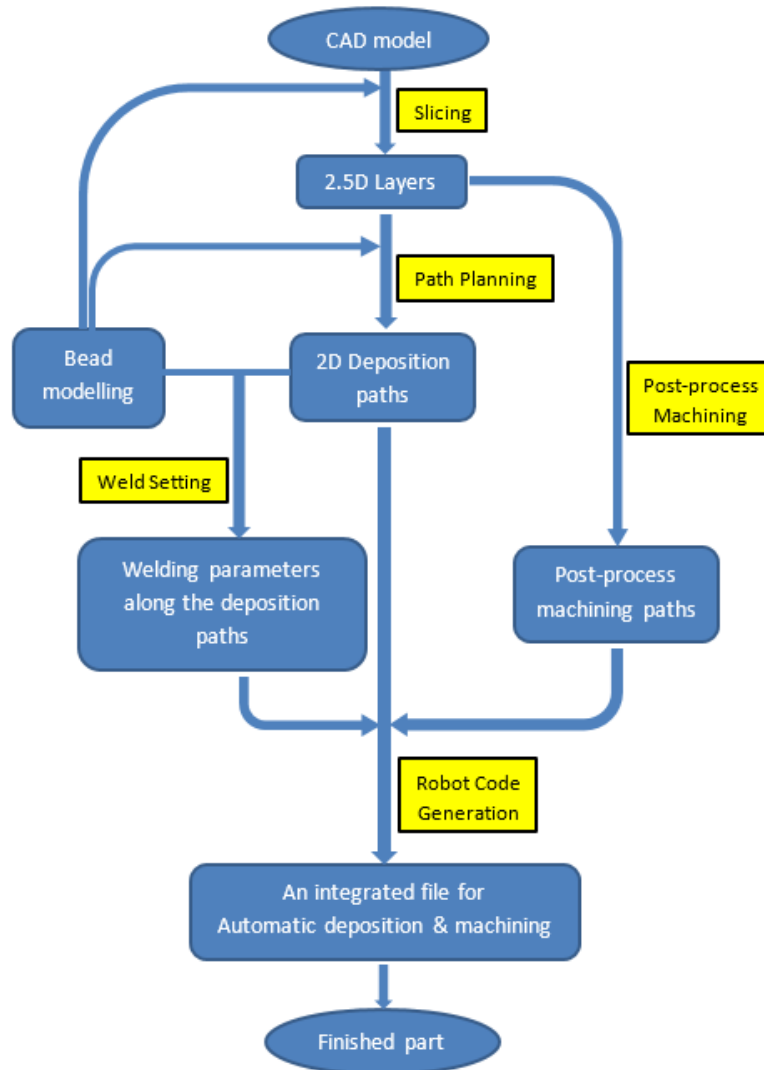


Figure 2.2 Schematic diagram of the automated process planning methodology of WAAM

The 3D CAD model in STL format is firstly sliced into a set of 2.5D layers through the slicing module. Then the path planning module generates deposition paths for each of the sliced layers. After the paths are generated, the desired bead geometries along the path are determined accordingly.

Bead geometry model controls two of the key slicing and path planning variables, namely layer thickness and step-over distance, respectively. In addition, it determines the optimum welding parameters corresponding to the desired bead geometry. Welding parameters include wire-feed rate, travel speed, and stick-out length for the GMAW process used in this study.

The post-process machining module generates machining tool paths for the post-weld machining process. With the geometries of the sliced layers, the machining paths can be generated by offsetting the boundaries of each layer by half of the machining tool diameter.

Subsequently, the welding deposition paths together with the automatically-selected welding parameters and the machining tool paths are transformed into an integrated robot code file through the robot code generation module.

Finally, a near-net shape deposit is produced automatically by the robotic arc welding system and the finished component with the desired dimensional tolerances is obtained through robotic machining.

2.3 User interface

Based on the developed automated process planning described in Section 2.2, the following user interface has been designed for a non-expert operator as shown in Figure 2.3. A total of seven steps are included, from loading the STL model to generating the robot code.

The screenshot displays a software interface titled 'Interface' with the 'University of Wollongong' logo. It contains seven main steps, each in a colored box:

- S1. Load STL Model** (Green box)
- S2. Bead Modelling** (Yellow box): Includes input fields for Wire-feed Rate (mm/min), Travel Speed (m/min), and Stick-Out (mm). It also has output fields for Bead Height (mm) and Bead Width (mm), an 'Add to List' button, and a table of bead data.

No.	1	5.0	0.35	9	3.43	6.74
No.2	5.0	0.46	11	2.96	5.97	
No.3	5.0	0.58	13	2.59	5.48	
No.4	5.0	0.70	15	2.33	5.32	
No.5	5.7	0.35	11	3.36	7.70	
No.6	5.7	0.46	9	2.82	6.81	

 Buttons: Delete, Select All, (Artificial Neural Network) Train, Save.
- S3. Slicing** (Pink box): Includes a 'Direction' section with 'Uni-direction (Z+)' (selected) and 'Multi-direction'. It also has a 'Layer Thickness (mm)' section with 'Auto' (selected) and 'Manual' (with a text input field). A 'Slice' button is at the bottom.
- S4. Path Planning** (Orange box): Includes 'Path Patterns' with options: Raster, Hybrid, Zig-zag, MAT-based (selected), Contour, and Adaptive MAT. It also has a 'Step-over Distance (mm)' section with 'Auto' (selected) and 'Manual' (with a text input field). A 'Generate' button is at the bottom.
- S5. Weld Setting** (Purple box)
- S6. Post-process Machining** (Light Blue box): Includes a 'Machine Region' section with checkboxes for 'Top Region', 'Side Region', and 'Base Region' (all checked). It also has a 'Tool Information' section with 'Diameter (mm)' set to 10 and 'Depth (mm)' set to 30. A 'Generate Machining Code' button is at the bottom.
- S7. Robot Code Generation** (Red box)

Figure 2.3 User interface for the WAAM. A total of 7 steps from S1 to S7 are described.

Step 1, load STL model: The input is a digital 3D STL file.

Step 2, bead modelling: By adding experimental results from weld bead profile tests into the list, the bead geometry model is trained using the artificial neural network (ANN). The inputs in this study are wire-feed rate, travel speed, and stick-out length; while the outputs are bead height and bead width. The bead database is saved for the later steps. This step is only performed once for a welding wire of any given composition, diameter and corresponding shielding gas.

Step 3, slicing: After slicing the 3D STL model, a set of 2D slices (layers) are obtained. In this study, both uni-direction and multi-direction slicing algorithms are developed. Layer thickness can be user defined or automatically selected with the aid of the bead database.

Step 4, path planning: Deposition paths are automatically generated with appropriate step-over distances according to the information contained in the bead database. The optimal step-over distance of weld beads is determined to obtain a smooth upper surface for each deposited layer. Step-over distance can also be set manually at this step. Although various path patterns are provided, MAT-based path is preferred for many practical parts since it is more suitable for the arc-welding-based system.

Step 5, weld setting: Weld settings (wire-feed rate, travel speed, and stick-out length) along each of the generated deposition paths are selected automatically based on the established ANN bead model.

Step 6, post-process machining: Machining paths are also generated automatically by offsetting the boundary of the geometry by half of the diameter of the machining tool.

Step 7, robot code generation: An integrated robot code file is generated, where the information of deposition paths, the welding parameters along the paths, and the machining tool paths are included.

2.4 Summary

This chapter has described the WAAM process and the process planning methodology. WAAM is a layered manufacturing process that employs material deposition and material removal processes for fabricating parts. As a new manufacturing method, process planning poses several challenges.

Three major tasks in WAAM are identified, including bead modelling, slicing, and path planning. Robotic post-process machining is considered as an optional step in this study. The relationships between each task are introduced, and a user interface is developed. Challenges and solutions for each task are discussed individually in the following chapters.

Chapter 3

Bead Modelling

In WAAM, the layer-by-layer building strategy incorporates the deposition of a large number of single weld beads side by side. Therefore, accurate model for single bead geometry as well as the multi-bead overlapping play important roles in determining the surface quality and dimensional accuracy of the fabricated products.

This chapter firstly builds models for a single bead profile through curve fitting methods. A multi-bead overlapping model is then developed to determine the appropriate step-over distance in the path planning module. Consequently, the artificial neural network (ANN) bead models are established for mild steel and aluminium alloys. ANN models provide the essential information that not only guide the layer thickness in slicing module but also control the appropriate welding parameters in weld settings step.

3.1 Single bead geometry

Figure 3.1 shows the typical weld bead geometry with bead height (h) and bead width (w). Much research has been directed towards developing mathematic functions to describe the single bead geometry. A symmetric parabola profile of the weld bead has been described by Suryakumar et al. [45]. Cao et al. [73] fitted the weld bead boundary with Gaussian, logistic, parabola and sine functions, and found that the sine function can fit the measured data with highest accuracy. Xiong et al. [46] compared the measured weld beads under different welding parameters to three frequently-used profile models, namely circular arc, parabola, and cosine function. It was shown that the optimal model for the bead profile is largely dependent on the ratio of wire-feed rate to travel speed (welding speed).

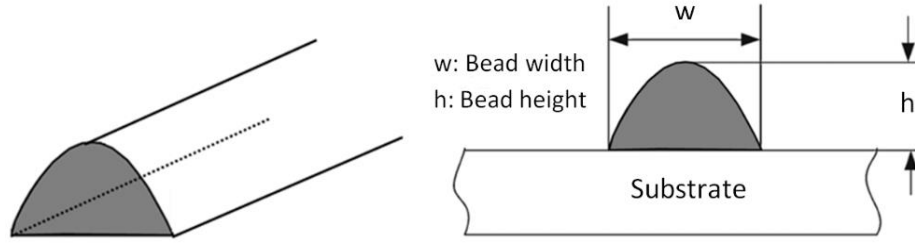


Figure 3.1 Weld bead geometry

Previous research used measured bead height and width instead of complete cross-sectional profile for the model parameters identification. Nevertheless, the relative errors of bead cross-sectional area predicted by their models were as high as 15 – 20% in certain circumstance [45, 46]. Therefore, a further detailed measurement of the bead cross-sectional profile and the curve fitting based method are developed for accurate modelling of bead geometry.

3.1.1 Single bead empirical models

Three popular mathematic functions, parabola, cosine and arc, are used here to model the cross-sectional profile of a single weld bead, as shown in Table 3.1. The bead height, h , bead width, w , and the bead area A for each model are summarised using various model parameters. In these functions, a , b , and c are model parameters which must be identified through experimental measurements. Note that the single bead models developed in this section is only suitable for placing such a bead on a larger substrate or previously deposited large area, but not for building components using a single bead only.

Table 3.1 Three bead models and the related bead height, bead width, and bead area.

Models	Model function	Bead height, h	Bead width, w	Bead Area
Parabola model	$y = ax^2 + c$	c	$2\sqrt{-\frac{c}{a}}$	$A_p = \frac{4c}{3} \sqrt{-\frac{c}{a}}$
Cosine model	$y = a \cos(bx)$	a	$\frac{\pi}{b}$	$A_c = \frac{2a}{b}$
Arc model	$y = \sqrt{a^2 - x^2} + b$	$a-b$	$2\sqrt{a^2 - b^2}$	$A_a = \arccos\left(-\frac{b}{a}\right) - b\sqrt{a^2 - b^2}$

3.1.2 Experimental set-up

Experimental tests were conducted using a robotic welding system at the University of Wollongong. The WAAM system and 3D laser scanning system have been integrated into a welding cell to conduct the experiments, as described in Figure 3.2. A computer interface (1) is used to program the experimental processes and collect the experimental results. The robot controller (2) is used to coordinate both the robot motions and welding processes. (3) A programmable GMAW power source is used to control the welding process. A large industrial robot (4) implements the movement of the welding torch (5) for metal deposition, and subsequently a laser profiler (6) to measure the bead profile. An example of weld bead deposits on a work piece is shown (7).

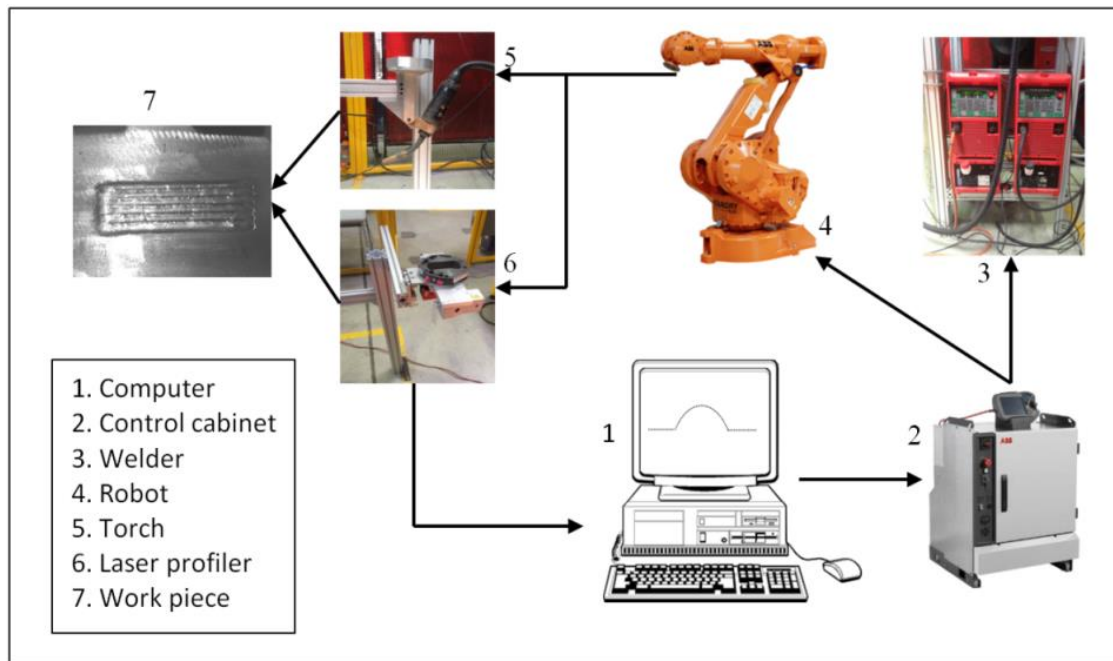


Figure 3.2 Schematic diagram of the experimental set-up for bead deposition and measurement

The pulsed-spray GMAW transfer mode was used to minimize the heat input. The wire electrode was copper coated steel wire with the diameter of 1.2 mm. The stick-out length was set to 18mm to minimise weld spatter for this particular process. A shielding gas mixture of 82% argon and 18% CO₂ was used with a flow rate of 22 L/min. The wire-feed rate was set at 5 m/min and the welding speed was varied from 0.2 to 0.55 m/min. A 3D laser profile scanner with a resolution of 0.02 mm was used to accurately measure the cross-sectional profile of the weld beads at different locations along the welding direction. In order to improve the accuracy of measurements that are subject to random errors, each bead profile was scanned 200 times. The experimental data obtained from the laser profiler was processed using MATLAB. A 3D plot of some measured weld bead profiles is shown in Figure 3.3. The

left profile is a single bead with 200 cross-sections, while the centre and right are the profiles of welds having two overlapping beads.

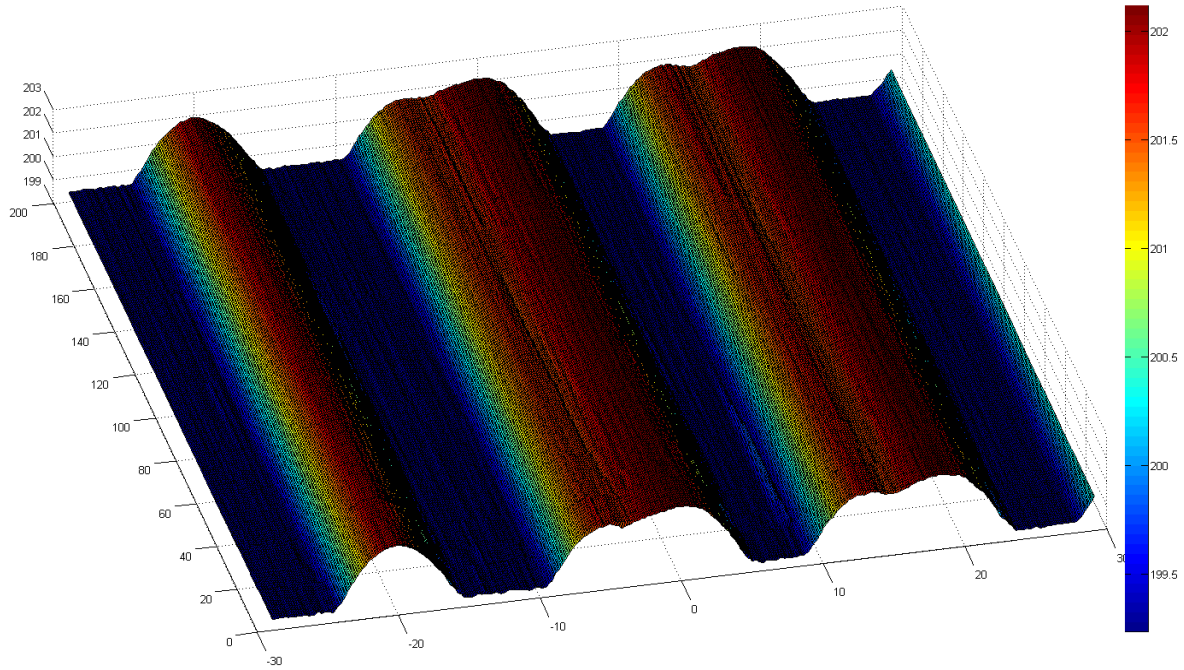


Figure 3.3 Experimental measurements of weld bead profile

3.1.3 Curve fitting results

Experiments were carried out for a combination of one wire-feed rate (F , m/min) and eight different travel speeds (S , m/min). Each of the eight weld bead profiles is fitted using the three previously mentioned models with parameters that produce the highest value of R^2 , which is the square of the correlation between the response values and the predicted response values. The parameters obtained from each model are summarised in Table 3.2. The ratio (λ) of wire-feed rate to welding speed is also calculated. With λ ranges from 9.1 to 25, the R^2 of all models are higher than 0.975, indicating that all of the models can represent the weld bead geometry accurately.

Table 3.2 Curve fitting with three mathematic models

S. No	Process parameters		Parabola model			Cosine model			Arc model		
	S	Ratio λ	a	c	R^2	a	b	R^2	a	b	R^2
1	0.2	25	-0.0840	3.3418	0.9989	3.395	0.2411	0.9937	7.010	-3.720	0.9990
2	0.25	20	-0.0955	3.0176	0.9996	3.071	0.2716	0.9969	6.216	-3.251	0.9841
3	0.3	16.7	-0.1040	2.7210	0.9994	2.765	0.2971	0.9951	5.715	-3.042	0.9859
4	0.35	14.3	-0.1144	2.5420	0.9976	2.592	0.3248	0.9991	5.220	-2.727	0.9786
5	0.4	12.5	-0.1262	2.4615	0.9934	2.483	0.3461	0.9968	4.941	-2.571	0.9915
6	0.45	11.1	-0.1221	2.1919	0.9943	2.239	0.3625	0.9988	4.866	-2.717	0.9923
7	0.5	10	-0.1405	2.1513	0.9934	2.198	0.3925	0.9982	4.299	-2.194	0.9967
8	0.55	9.1	-0.1511	2.0704	0.9873	2.123	0.4173	0.9961	4.052	-2.034	0.9943

The relative error of area prediction, e_{Area} , is defined as the percentage of the area difference between the predicted and the actual bead area over the actual bead area,

$$e_{Area} = \frac{A_p - A_a}{A_a} \times 100\% \quad (3.1)$$

where, A_p is the prediction of the bead area by the mathematical models listed in Table 3.2. The actual area, A_a of a weld bead cross-section, namely metal deposition rate per unit length, can be calculated as

$$A_a = \frac{\pi F D_w^2}{4S} = \frac{\pi \lambda D_w^2}{4} \quad (3.2)$$

where, D_w is the diameter of the wire electrode.

As shown in Figure 3.4, the relative errors of all three models are within $\pm 4\%$. Compared with relative errors up to 15% in previous literature, the model parameters identified in this study are much more accurate without considering the material loss during the welding process. This is mainly due to the use of curve fitting with detailed bead cross-sectional measurements instead of only employing the bead height and width in the model fitting. As shown in Figure 3.4, between the three empirical models, the parabola model and the cosine model provide a better approximation than the arc model. Good agreement between experimental results and the parabola model is obtained under all welding speeds, as shown in Figure 3.5. In the following sections, the parabola model will be used for developing the overlapping model.

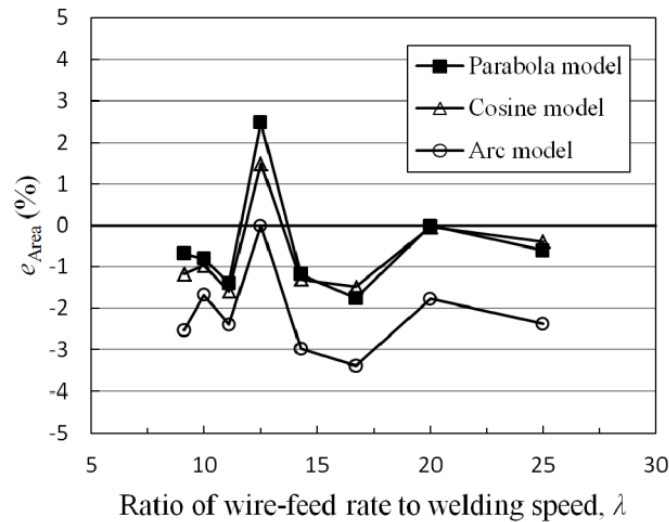


Figure 3.4 Relative error for predicted and actual area of weld bead cross-section

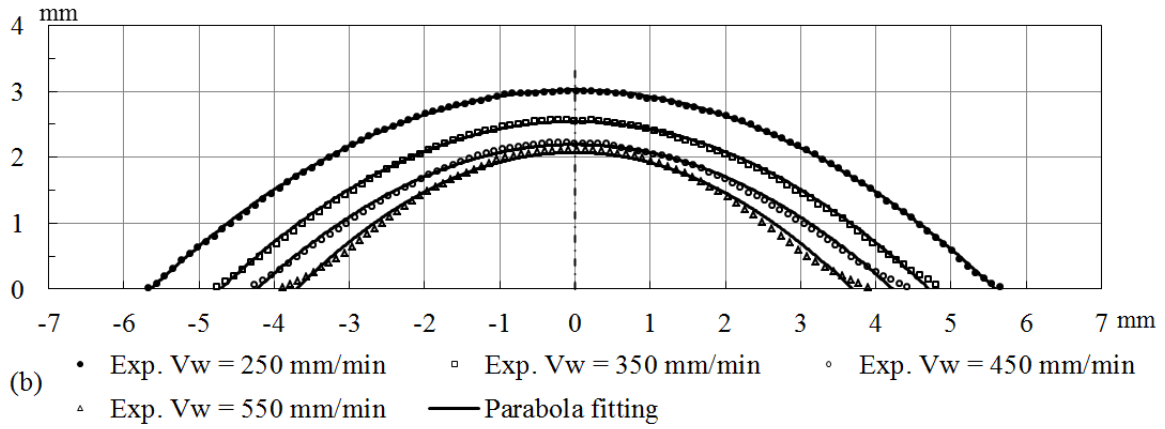
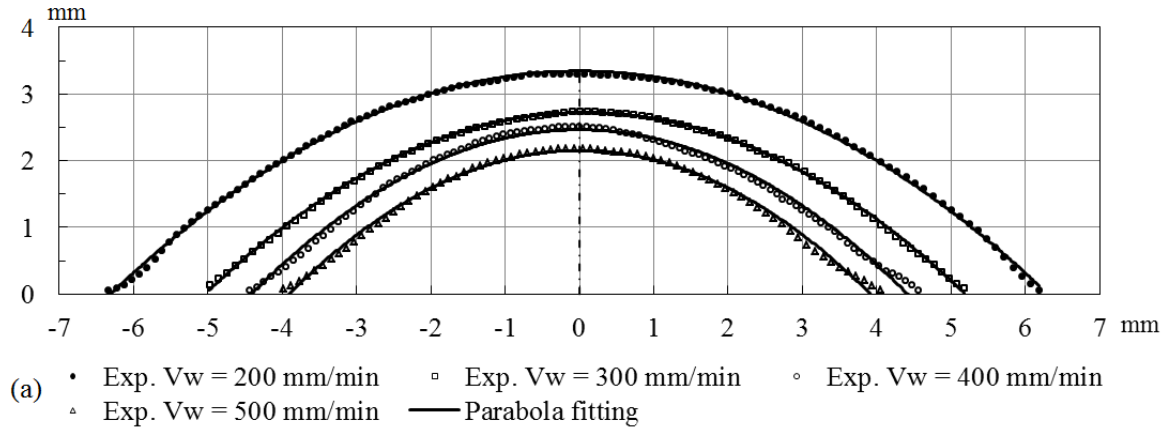


Figure 3.5 Weld bead geometry of a single bead with various welding speeds (V_w) or travel speed (S) through pulsed spray GMAW synergic model. Note that the parabola fitting parameters may not suitable if the arc welding deposition system or the deposition model was changed.

3.2 Multi-bead overlapping model for mild steel

Some preliminary investigations on multi-bead overlapping models have been made in recent years [46, 56]. A simple Flat-top Overlapping Model (FOM) has been developed in the literature, and is described as follows. Let a single bead have a height h and width w ; and the adjacent beads have a centre distance or step-over distance d . The area of valley and overlapping area in adjacent beads are depicted in Figure 3.6.

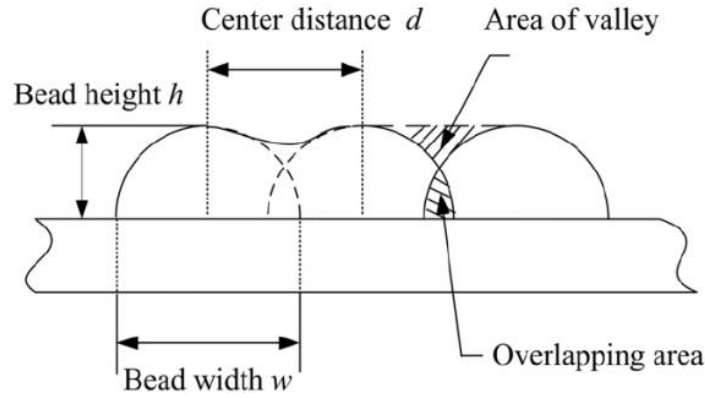


Figure 3.6 Sketch of the traditional flat-top overlapping model (FOM)

The step-over distance d between adjacent beads plays an important role in determining surface quality and smoothness. When d is greater than the single bead width w , there is no overlap within the two adjacent beads. As the step-over distance is decreased, the overlapping area in Figure 3.6 increases, and the area of the valley decreases. As the distance d decreases to a certain value, the overlapping area becomes equal to the area of the valley and the overlapped surface will become an optimal plane. With a further decrease of d , excessive overlapping area leads to an increased thickness of the deposited layer and decreasing surface smoothness.

Consequently, the optimal step-over distance d is determined by the criterion that a flat plane will be obtained when the overlapping area is equal to the area of valley. However, it has been observed through experimentation that it is impossible to achieve the ideally flat overlapped surface [45, 56]. Therefore the overlap criterion proposed in these studies is not optimal and produces an undesired wavy surface. As a work piece requires deposition of several layers, uneven layer surface may lead to accumulating errors along the vertical direction, resulting in unstable deposition after several layers. Therefore, it is very important to build a more accurate bead overlapping model based on the determination of the optimal centre distance, so that a stable overlapping process can be achieved.

3.2.1 Principle of the tangent overlapping model (TOM)

In the traditional flat-top overlapping model (FOM) of Figure 3.6, the area of valley consists of the boundaries of two beads and one straight line which connect the summits of both weld beads. However, during welding tests described in the previous section, it was observed that there is a “critical valley” geometry that better approximates the cross-section of multiple welding beads in Gas Metal Arc Welding (GMAW). Note that the phenomenon

of “critical valley” is the experimental observation while its principle is not further investigated in this work.

As shown in Figure 3.7(a), for two weld beads with a width w and a height h , Bead 1 is first deposited on the substrate, and Bead 2 is deposited next to Bead 1 with a step-over distance of d . A is the left-most point of Bead 2, at the toe of the weld. Point B is the point on Bead 1 which shares the same abscissa with point A. Line BC is tangential to Bead 2. In contrast to previous studies, this newly proposed model defines the critical valley as the zone BEC. The overlapping area is AED; the same as the previous FOM model. As the distance d is decreased from w to $w/2$, the size of the overlapping area (SAED) increases from zero, while the size of the critical valley (SBEC) increases initially from zero but then decreases.

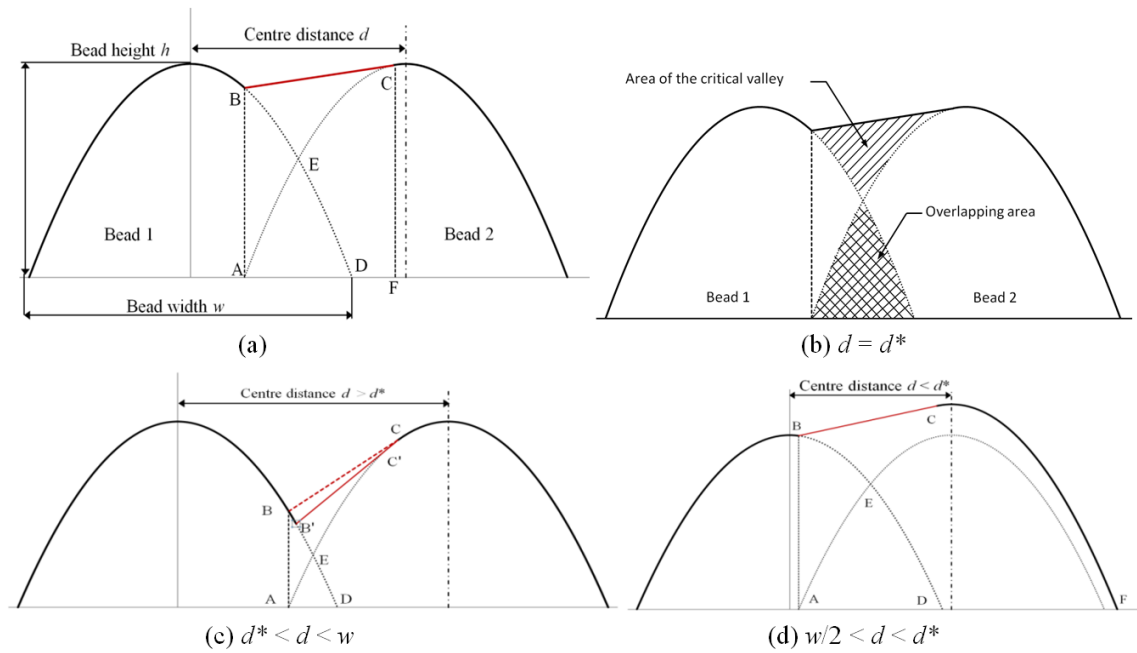


Figure 3.7 Schematic diagrams of the tangent overlapping model (TOM)

The detailed calculations of the area variations are provided in the following sections. As an introduction, the principle of TOM can be summarised as follows:

- (1) When $S_{AED} = S_{BEC}$, the overlapped profile is described by Figure 3.7(b). The corresponding centre distance is called the critical distance d^* .
- (2) When the centre distance d varies from d^* to w , $S_{AED} < S_{BEC}$. In this case, the overlapped profile is shown in Figure 3.7(c). Since the area of the critical valley BEC is larger than the overlapping area AED, the actual area of valley will be B'EC' with the area of B'EC' is equal to the area of AED, where B' is a point on Bead 1, and line B'C' is tangential to Bead 2.
- (3) When the centre distance d varies from $w/2$ to d^* , $S_{AED} > S_{BEC}$, as shown in Figure 3.7(d). The excessive overlapping area results in the altered profile of Bead 2.

Through experimental tests, the parabolic curve of Bead 2 has been measured. As for previous geometric cases, B is also a point on bead one that shares the same abscissa with point A, but point A is defined on the non-altered profile of Bead 2 rather than the actual altered profile. Line BC is tangential to the altered profile of Bead 2. The profile of Bead 2 has been changed, indicating that the overlapping process is not stable for the first few beads. When multiple beads are deposited, the layer thickness will increase in comparison with the case $d^* \leq d < w$. This results in the height of the first bead being much lower than the rest.

3.2.2 Overlapping of two beads

With the proposed overlapping principles of TOM, the key step of the overlapping model is to calculate the critical centre distance for any given weld bead.

Case (1) The step-over distance $d = d^*$

In Figure 3.7(a), two weld beads are considered as two parabolic functions expressed as:

$$y = ax^2 + c \quad (3.3)$$

$$y = a(x - d)^2 + c \quad (3.4)$$

where c is equal to the weld height h and $a = -4h/w^2$. For a given weld bead, a and c are derived from the model of a single bead.

If the coordinates of points A, B, F, C are defined as $A(x_1, 0)$, $B(x_1, y_1)$, $F(x_2, 0)$, $C(x_2, y_2)$, the gradient of the line BC is k , then S_{AED} and S_{BEC} can be represented using the following functions:

$$S_{AED} = 2 \int_{x_1}^{d/2} (ax^2 + c) dx \quad (3.5)$$

$$\begin{aligned} S_{BEC} &= S_{ABCF} + S_{AED} - S_{ABD} - S_{ACF} \\ &= \frac{y_1 + y_2}{2} (x_2 - x_1) + 2 \int_{x_1}^{d/2} (ax^2 + c) dx - \int_{x_1}^{\sqrt{-c/a}} (ax^2 + c) dx - \int_{x_1}^{x_2} [a(x - d)^2 + c] dx \end{aligned} \quad (3.6)$$

We define $f(d)$ as the function of the difference between S_{AED} and S_{BEC} :

$$f(d) = S_{BEC} - S_{AED} = \frac{1}{3}ad^3 + \frac{1}{6}aw^3 - \frac{1}{2}awd^2 - \frac{ad(w-d)}{3} \sqrt{wd - d^2} \quad (3.7)$$

When $S_{AED} = S_{BEC}$, $f(d) = 0$. Among the four roots obtained from this equation, only two of them have positive real values:

$$d_1 = w$$

$$d_2 = w \left[\left(\sqrt{\frac{1}{512}} + \frac{1}{16} \right)^{\frac{1}{3}} + \frac{1}{8} \left(\sqrt{\frac{1}{512}} + \frac{1}{16} \right)^{\frac{1}{3}} \right] \approx 0.738w$$

This indicates that within the range of $(w/2, w)$, there exist a unique critical distance, $d^* = 0.738w$. Figure 3.8 plots the trends of S_{AED} , S_{BEC} , and $f(d)$ as the centre distance d varies from $w/2$ to w . With increasing centre distance, the S_{AED} decreases, while S_{BEC} increases at the beginning but decreases to zero in the end. S_{AED} is equal to S_{BEC} when the step-over distance d is equal to the critical centre distance $0.738w$.

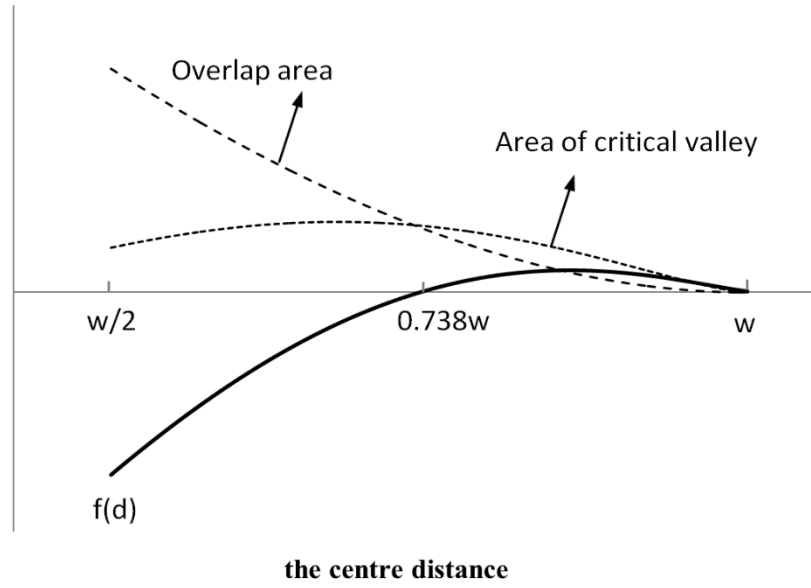


Figure 3.8 The overlap area, the area of the critical valley, and $f(d)$ as a function of the step-over distance d

Case (2) The step-over distance d in the range $d^* < d < w$

As described in Figure 3.7(c), B' is a point on Bead 1, C' is a point on Bead 2. Line $B'C'$ is tangential to Bead 2. By applying the relationship that S_{AED} is equal to $S_{B'EC'}$, the coordinates of point B' and C' can be solved, and the overlapped profile can be obtained similarly to case (1).

Case (3) The step-over distance $w/2 < d < d^*$

When the step-over distance d is less than the critical centre distance, the second bead profile is changed. In this case, the overlapping process is more complicated. Through experimental measurements, it was found that the boundary of the second weld bead can also be represented by a parabola function with the same parameter a as the parabolic curve of the first weld bead. Therefore, the second bead can be represented as:

$$y = a(x - d)^2 + c_2 \quad (3.8)$$

where, the parameter c_2 , the height of the second weld bead, can be solved at the certain step-over distance d . For simplicity, the detailed calculations are omitted here.

3.2.3 Multi-bead overlapping

In WAAM, each layer is usually fabricated by depositing a large number of single weld beads side by side. The overlapping processes of weld beads determine the surface quality and dimensional accuracy of the fabricated products. Therefore, it is important to investigate the overlapping process of multi-bead deposits.

In the case of $d \geq d^*$, the all weld beads have the same height, so the parabolic function of all weld beads have the same value of parameter c ($c_1 = c_2 = \dots = c_n$). This means that the overlapping process of the third weld bead on the second weld bead is the same as that the process of overlapping the second weld bead on the first weld bead. Therefore, the process of multi-bead overlapping can be considered as the repeated two-bead overlapping processes.

However, in the case of $d < d^*$, the parabolic function of the second weld bead boundary will be changed during the overlapping process. For any given weld bead in the multi-bead deposit, the overlapped profile can be simulated numerically. The schematic overlapped profile of a multi-bead deposit at $d < d^*$ is represented in Figure 3.9. It can be found that such overlapping processes are not stable, with the thickness of the layer increasing as more beads are deposited.

It should be note that this multi-bead overlapping is not suitable for single bead walls and the minimum resolution of this approach might be $d + w$ in width and h in height corresponding to two beads overlapped geometry.

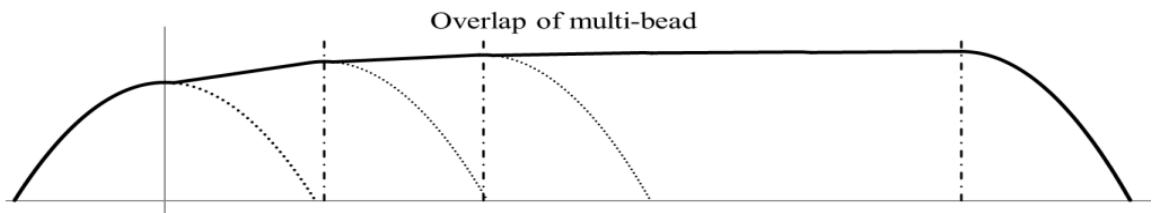


Figure 3.9 Schematic overlapped profile of a multi-bead deposit at $d < d^*$

3.2.4 Experimental verification for the overlapping model

Based on the traditional FOM, to achieve a flat deposition surface the optimal step-over distance is $d = 0.667w$ using the parabola model for single bead. According to the proposed TOM, a centre distance of $0.667w$ would induce an unstable overlapping processes as it is less than the critical step-over distance $d^* = 0.738w$. Figure 3.10 compares the experimental

measurements of overlapping bead profile with the predictions from the proposed TOM and the traditional FOM. The welding speed was set at 400 mm/min for this test. The single bead model parameters can be obtained from row 5 in Table 3.2. The bead width is calculated using the formula in Table 3.1.

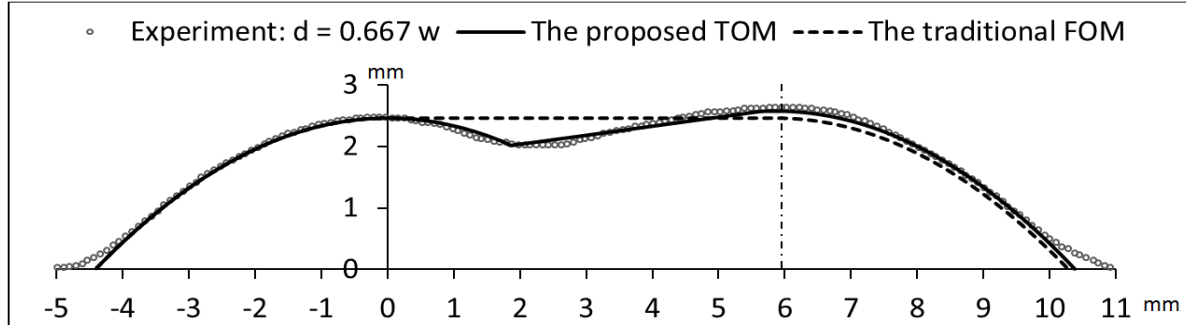


Figure 3.10 Comparison of experimental measurements of bead profile with the tangent overlapping model (TOM) and the flat-top overlapping model (FOM)

Prediction of the overlapped profile at $d = 0.667w$ through the traditional FOM yields:

$$y = \begin{cases} ax^2 + c & -w/2 < x < 0 \\ c & 0 < x < d \\ a(x-d)^2 + c & d < x < d + w/2 \end{cases} \quad (3.9)$$

Prediction of the overlapped profile at $d=0.667w$ through the proposed TOM yields:

$$y = \begin{cases} ax^2 + c_1 & -w/2 < x < x_1 \\ k(x-x_1) + y_1 & x_1 < x < x_2 \\ a(x-d)^2 + c_2 & x_2 < x < d + w_2/2 \end{cases} \quad (3.10)$$

where, $c_1 = c$ is the height of the first bead; c_2 is the height of the second bead, which could be solved numerically; x_1 , x_2 and k are parameters as mentioned in Section 3.2.2, all of these can be solved for any given weld bead; w_2 is the width of the second bead which could be solved when c_2 is obtained.

In Figure 3.10, the experimental data, FOM and proposed TOM are represented by the dotted line, dashed line and solid line respectively. It can be seen that the proposed TOM approximates the experimental results much better than the traditional FOM, particularly in the zone of the valley.

Using the traditional FOM, a flat plane would be obtained at the optimal step-over distance, which does not match with the experimental data. The proposed TOM model is more suitable in describing the zone of the valley. Additionally, the proposed model predicts a higher peak for the second bead as the centre distance is less than d^* , which has been confirmed in the experimental measurements.

To compare the accuracy of both models quantitatively, relative errors between the measured profile and the predicted profile along the bead width direction are plotted in Figure 3.11, with e_y defined as,

$$e_y(\%) = \frac{y_{model} - y_{measurement}}{y_{measurement}} \times 100\% \quad (3.11)$$

It can be found that FOM results in a high relative error in the zone of the valley (0 ~ 6mm in Figure 3.11). This is because the valley is assumed to be a flat plane in the literature, but it is waved in the experiments. The proposed TOM is more accurate than the traditional FOM. Although both models are not accurate at the zone near the substrate, it is inconsequential and may be disregarded when compared to the zone of the valley, because the volume of deposited material is much lower near the weld toe in comparison to the valley.

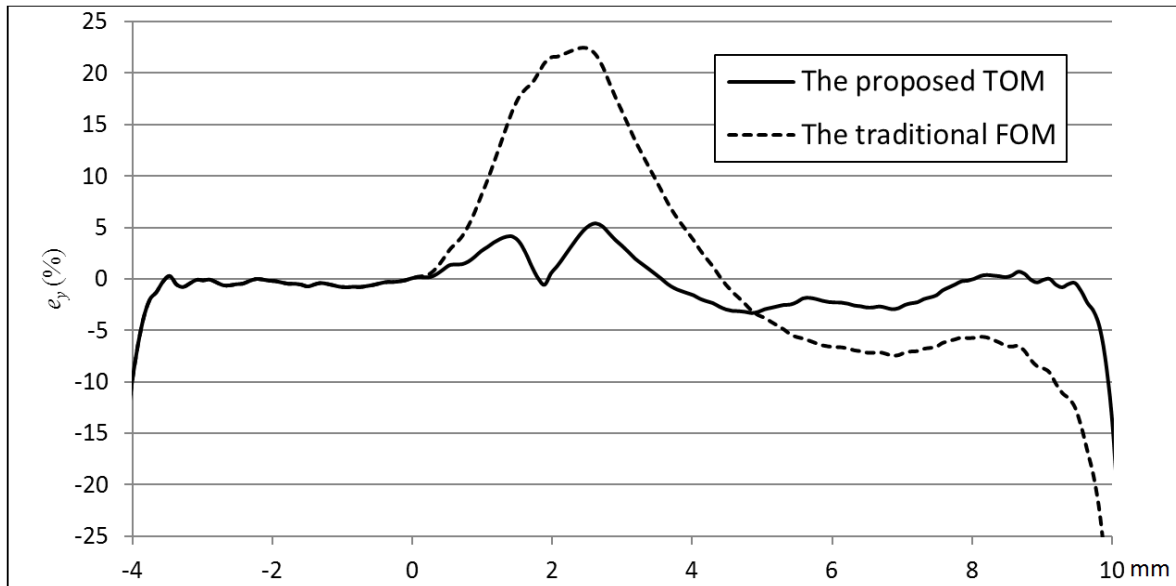


Figure 3.11 The relative errors between the experimental bead profile and the models

Further experimental measurements of overlapped bead profile for various step-over distance d are provided. Figure 3.12 presents the model predictions and measurement data in all three circumstances, namely: (a) $d = d^*$, (b) $d > d^*$, (c) $d < d^*$. It can be seen that, the proposed TOM agree with experiments very well in all three situations.

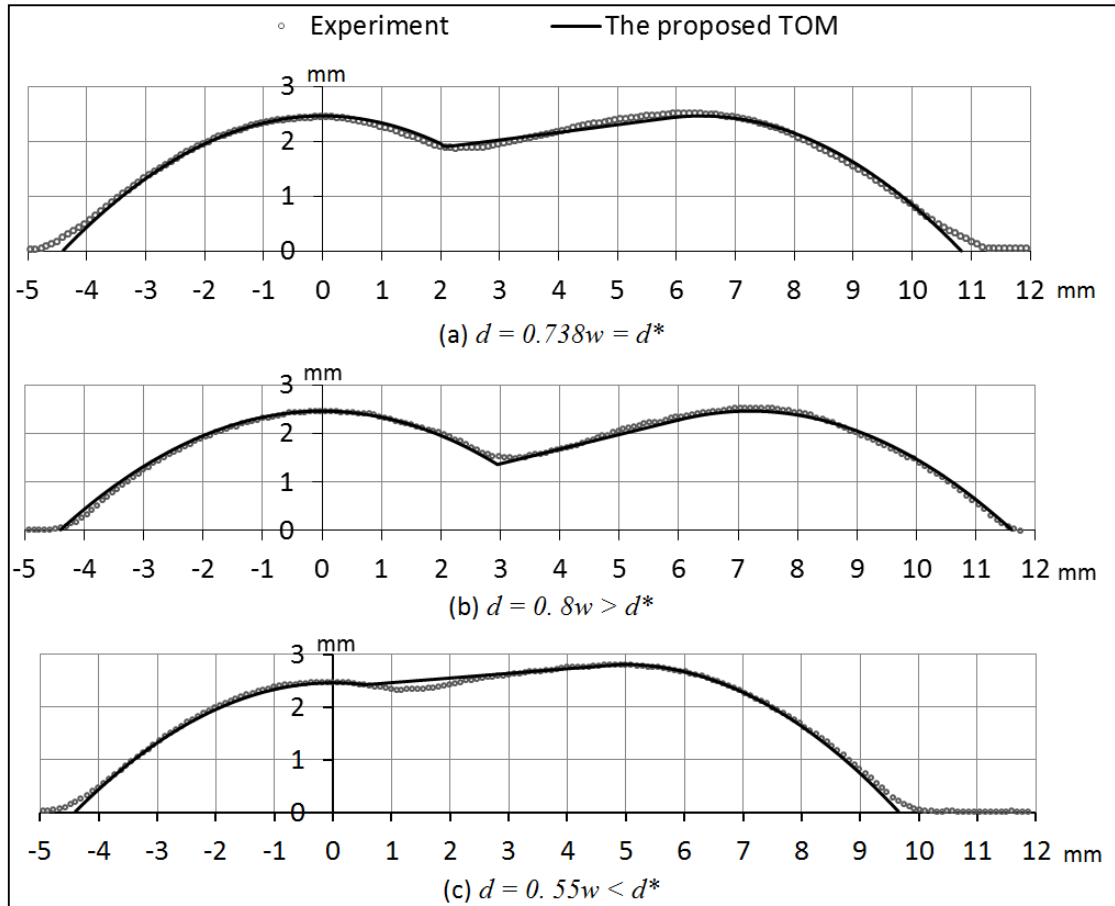


Figure 3.12 The experimental results of overlapped bead profile at various distance d

Unlike the traditional FOM, the proposed TOM model predicts an asymmetrical overlapping geometry between the peaks of the two beads. In addition, the experimental measurements show that the height of second bead is higher than the first one when the step-over distance is smaller than the critical step-over distance, which agrees with the proposed model. The ratio of the height for the second bead over the first bead at various step-over distances are calculated and compared to experimental measurements, as shown in Figure 3.13. It can be seen that when the step-over distance d is larger than the critical step-over distance d^* , the ratio is approximately 1.0, i.e. the second bead has the same height as the first one. When the centre distance is less than the critical step-over distance, the ratio increases, indicating an increase in the height of the second bead. The proposed TOM model has been quantitatively verified through these experimental measurements. According to the step-over distance, there are stable and unstable overlap zones, which is has significant implications for process planning in WAAM.

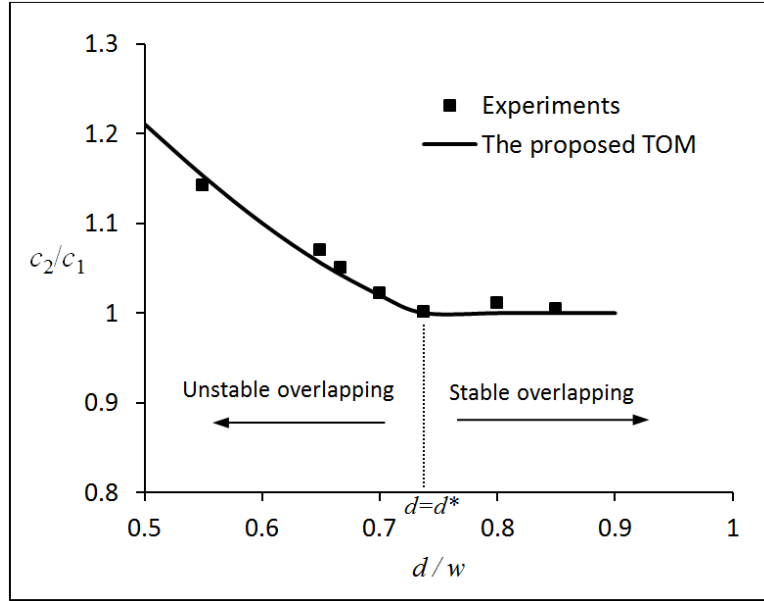


Figure 3.13 The ratio of the height of the second bead to the first bead (c_2/c_1) at various centre distance d/w

The best use of the bead overlapping model is to provide an estimate of optimal step-over distance for AM. The traditional model proposes $d_{opt} = 0.667w$ while the proposed model claims $d_{opt} = 0.738w$. Further experiments were conducted at both of these step-over distances for multi-bead and multi-layer deposition to compare the performance of the models. As shown in Figure 3.14, AM deposits were made at these step-over distances with five layers of deposition and six beads in each layer. The welding speed was 0.5 m/min for these tests. The cross section was scanned after the first, third and fifth layers were deposited. It should be noted that, during the deposition processes, a few minutes of waiting time was used between each pass as well as subsequent layers to eliminate the temperature's effects on weld bead geometries as much as possible.

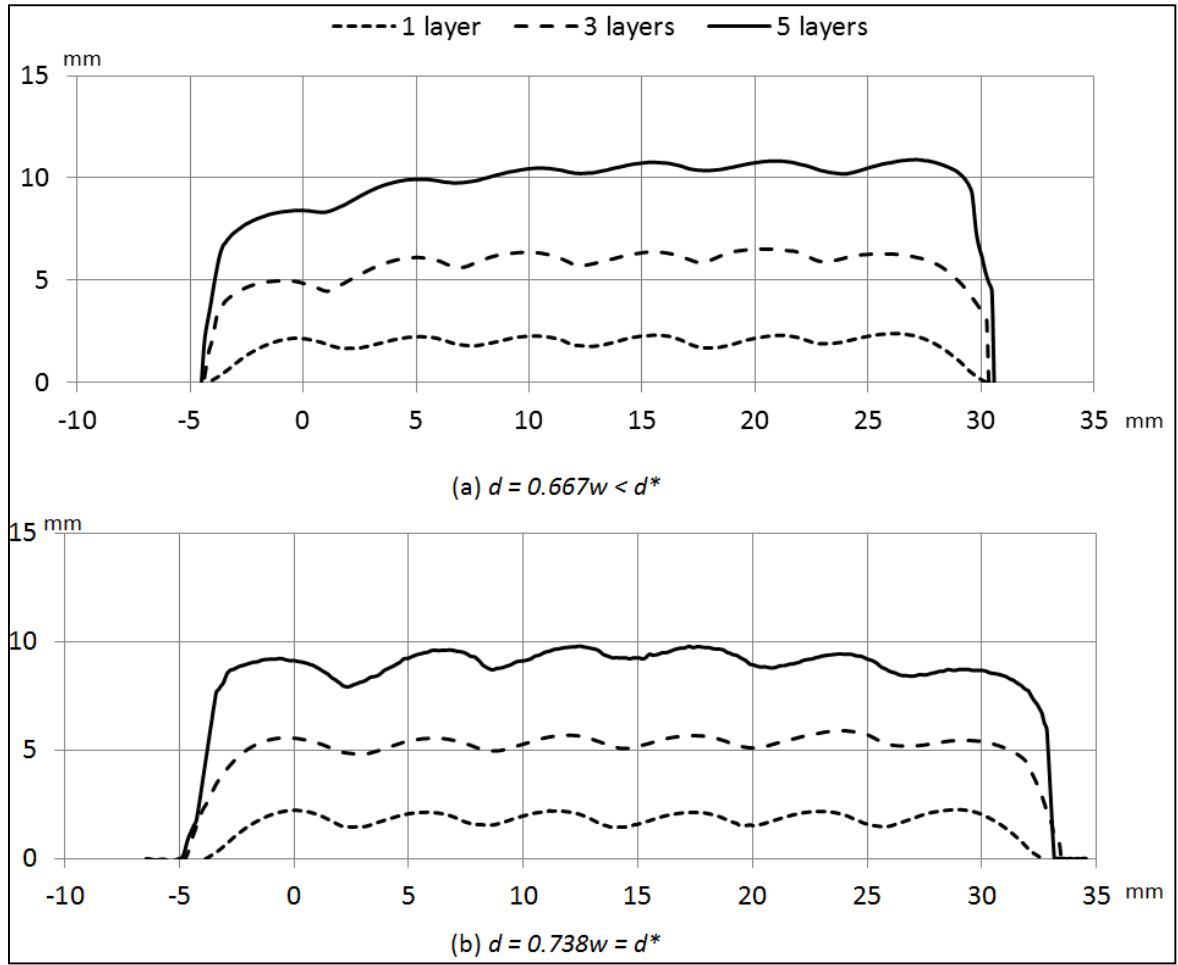


Figure 3.14 Experiments of multi-bead and multi-layer deposition.

In Figure 3.14(a), a step-over distance of $d = 0.667w$ was used. After deposition of five layers, it can be seen that the layer thickness at the first bead becomes much lower than the rests. This result is predicted by the proposed TOM. Since the centre step-over distance is less than d^* , the height of the following bead will be higher than the previous one. In Figure 3.14(b), the critical step-over distance ($d = 0.738w$) proposed by the TOM is used. After deposition of five layers, the variations in the height of the bead peaks from left to right hand are relatively smaller. As more layers are deposited, the variation in bead peak height becomes progressively worse when the centre distance $d = 0.667w$, while it is significantly more stable when the step-over distance $d = 0.738w$. These results demonstrate that the critical step-over distance proposed by the TOM results in a stable overlapping process, which is a necessary condition for the additive manufacture of large components.

Generally, any component that is built by depositing a series of overlapping beads is subjected to a machining process to remove the scallops. Yield η is the ratio of the volume of the part remaining after machining to the volume of the total metal deposited. Yield reflects the material utilization for a process, very similar to casting. In Figure 3.14(a) and (b), the

maximum yield at two centre distance are 75.7% and 84.1% respectively, indicating that the proposed TOM is more material efficient than the traditional FOM.

3.3 Artificial neural network bead models

Through adjusting process parameters such as wire-feed rate and travel speed, different bead profiles can be obtained. In the present work, an attempt has been made to develop a neural network model in order to correlate the welding parameters and bead geometry. The artificial neural network has been demonstrated to be a powerful tool for representing complex relations between multiple inputs and responses, especially for the welding process which exhibits strong nonlinearity [74, 75].

Based on the effect on weld bead geometry, the chosen input factors for this study are wire-feed rate (F), travel speed (S), and stick-out length (L); the responses are bead height (h) and bead width (w). Figure 3.15 shows the diagram of the feedforward neural network for weld bead geometry. The network is composed of an input layer (has three input neurons), a single hidden layer, and an output layer (has two output layers). Neurons in the hidden layer are computational elements accomplishing nonlinear mapping between process variables and responses.

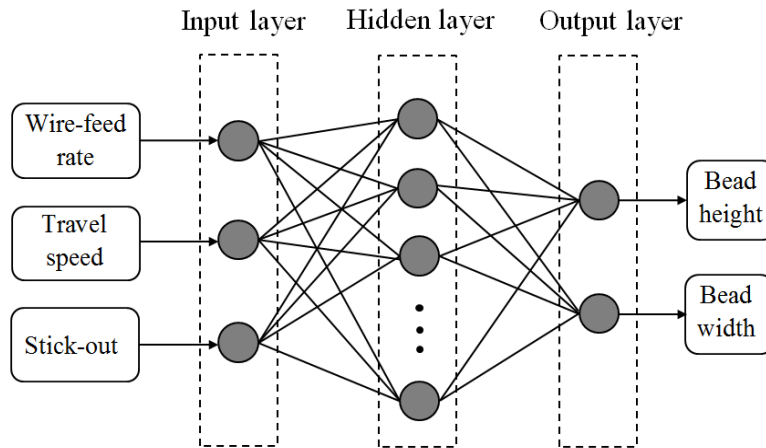


Figure 3.15 Schematic diagram of the feedforward neural network for weld bead geometry

3.3.1 Forward computing

Consider a general single hidden-layer feedforward network which has L input neurons, M hidden neurons, and N output neurons. Let $\mathbf{x} = (x_1, x_2, \dots, x_L)$ be the input vector, $\mathbf{h} = (h_1, h_2, \dots, h_M)$ and $\mathbf{o} = (o_1, o_2, \dots, o_N)$ be the output vectors of the hidden layer and output layer respectively. Figure 3.16 shows the connections of each hidden neuron between inputs and

outputs (responses). Let w_{ij} denotes the weight between the i^{th} input neuron and the j^{th} hidden neuron. The weight matrix between the input and hidden layers is then an $L \times M$ matrix denoted by $\mathbf{W} = (\omega_{ij})$. Similarly, the weight matrix between the hidden and output layers is an $M \times N$ matrix denoted by $\mathbf{V} = (v_{jk})$. Training patterns are indicated by the superscript as \mathbf{x}^s , $s = 1, \dots, p$.

As shown in Figure 3.16, the weighted sum net_j to the j^{th} hidden neuron is expressed as

$$net_j = \sum_{i=1}^L \omega_{ij} x_i, j = 1, 2, \dots, M. \quad (3.12)$$

The value of j^{th} hidden neuron is calculated by

$$h_j = f_{act}(net_j). \quad (3.13)$$

where, f_{act} is the activation function which is continuously differentiable. Similar expressions could be derived between the hidden and output layers,

$$net_k = \sum_{j=1}^M v_{jk} h_j, k = 1, 2, \dots, N. \quad (3.14)$$

$$o_k = f_{act}(net_k). \quad (3.15)$$

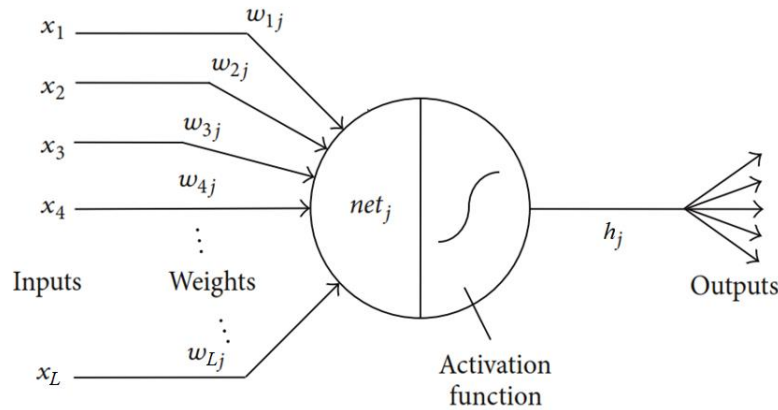


Figure 3.16 Architecture of an individual neuron for neural network

3.3.2 Error backpropagation learning

The main task in neural network is to obtain the weight matrix \mathbf{W} and \mathbf{V} through backpropagation learning. In backward learning, the generated output of the network is compared to the desired output. The error signal at the k^{th} output neuron at the training pattern s is defined by

$$e_k^s = d_k^s - o_k^s, \quad (3.16)$$

where d_k^s and o_k^s denotes the desired and output values of the k^{th} output neuron at the training pattern s . In this study, the mean squared error is used and written as

$$E = \frac{1}{N} \sum_{k=1}^N \frac{1}{2} (e_k^s)^2. \quad (3.17)$$

After all the training patterns are fed into the inputs, the weights are updated and thus the error becomes

$$E = \frac{1}{pN} \sum_{s=1}^p \sum_{k=1}^N \frac{1}{2} (d_k^s - o_k^s)^2. \quad (3.18)$$

For the output layer, the derivative of E with respect to the weights v_{jk} is:

$$\begin{aligned} \frac{\partial E}{\partial v_{jk}} &= \frac{\partial E}{\partial e_k} \cdot \frac{\partial e_k}{\partial o_k} \cdot \frac{\partial o_k}{\partial net_k} \cdot \frac{\partial net_k}{\partial v_{jk}} \\ &= \frac{1}{N} e_k \cdot (-1) \cdot f'_{act}(net_k) \cdot h_j. \end{aligned} \quad (3.19)$$

Similarly, the derivative of E with respect to the weights ω_{ij} is:

$$\begin{aligned} \frac{\partial E}{\partial \omega_{ij}} &= \sum_{k=1}^N \frac{\partial E}{\partial e_k} \cdot \frac{\partial e_k}{\partial o_k} \cdot \frac{\partial o_k}{\partial net_k} \cdot \frac{\partial net_k}{\partial h_j} \cdot \frac{\partial h_j}{\partial net_j} \cdot \frac{\partial net_j}{\partial \omega_{ij}} \\ &= \sum_{k=1}^N \frac{1}{N} e_k \cdot (-1) \cdot f'_{act}(net_k) \cdot v_{jk} \cdot f'_{act}(net_j) \cdot x_i. \end{aligned} \quad (3.20)$$

In this study, the normally log-sigmoid activation function is used for the hidden layer:

$$h_j = f_{act}(net_j) = \frac{1}{1 + e^{(-net_j)}}. \quad (3.20)$$

The output value lies in the range $0 \leq h_j \leq 1$. Its derivative is computed as

$$f'_{act}(net_j) = f_{act}(net_j) [1 - f_{act}(net_j)]. \quad (3.21)$$

The simple linear activation function

$$f_{act}(net_k) = net_k. \quad (3.22)$$

is used for the output layer, and its derivative is

$$f'_{act}(net_k) = 1. \quad (3.23)$$

The optimization of the error function over the weights ω_{ij} and v_{jk} is typically taking the steepest descent algorithm,

$$\Delta \omega_{ij} = -\eta \frac{\partial E}{\partial \omega_{ij}} = \eta x_i \cdot f_{act}(net_j) \cdot [1 - f_{act}(net_j)] \cdot \frac{1}{N} \cdot \sum_{k=1}^N e_k \cdot v_{jk}, \quad (3.24)$$

$$\Delta v_{jk} = -\eta \frac{\partial E}{\partial v_{jk}} = \eta \cdot \frac{1}{N} \cdot e_k \cdot h_j. \quad (3.25)$$

where η is a positive constant and called the learning rate. In the steepest descent method, a momentum term is often added into the above equation [76],

$$\Delta\omega_{ij}(t) = -\eta \frac{\partial E(t)}{\partial \omega_{ij}} + \beta \cdot \Delta\omega_{ij}(t-1), \quad (3.26)$$

$$\Delta v_{jk}(t) = -\eta \frac{\partial E(t)}{\partial v_{jk}} + \beta \cdot \Delta v_{jk}(t-1). \quad (3.27)$$

where t denotes the iteration number, and β is a positive constant between 0 and 1 called the momentum constant.

Weight matrix \mathbf{W} and \mathbf{V} are independent and initially distributed randomly. Through iterative learning, the appropriate weight matrix could be obtained after the mean square error is less than the minimum acceptable value. The number of neurons in the hidden layer is also optimized according to the final mean square error.

3.3.3 Training of neural network

The artificial neural network can find multi-dimensional dependencies between process parameters by learning. The development and the training of the network were carried out using MATLAB Neural Network Toolbox. In this study, the values of the chosen process variables at various levels are presented in Table 3.3. However, the data for teaching or training the artificial neural network need to be carefully selected.

Table 3.3 Input process parameters

Parameters	Factor levels			
	Level 1	Level 2	Level 3	Level 4
Wire-feed rate, F (m/min)	5.0	5.7	6.4	7.0
Travel speed, S (m/min)	0.35	0.46	0.58	0.7
Stick-out, L (mm)	9	11	13	15

The Taguchi method, which is one of the fractional factorial designs, has a good reappearance of experiment concerned only with the main effects of design parameters. Therefore, if the training data for the artificial neural network are selected using an orthogonal array table in the statistical design of experiments, and the process characteristics as output data of the artificial neural network are transformed by the Taguchi method, then this method has been shown to produce more accurate data using a smaller training set than other methods. Using the four levels of inputs selected in Table 3.3, the optimum parameter design for artificial neural network training is obtained as 16 test runs provided in Table 3.4

denoted in blue. A further 7 parameter test runs (No.17 to No.23 denoted in green in Table 3.4) are randomly chosen to test the performance of the trained network.

Table 3.4 Welding process input parameters (blue, green) and responses (orange)

No.	Parameter design			Bead height h , (mm)	Bead width w , (mm)
	Wire-feed rate F , (m/min)	Travel speed S , (m/min)	Stick-out L , (mm)		
1	5.0	0.35	9	3.43	6.74
2	5.0	0.46	11	2.96	5.97
3	5.0	0.58	13	2.59	5.48
4	5.0	0.70	15	2.33	5.32
5	5.7	0.35	11	3.36	7.70
6	5.7	0.46	9	2.82	6.81
7	5.7	0.58	15	2.57	6.19
8	5.7	0.70	13	2.21	5.70
9	6.4	0.35	13	3.42	8.53
10	6.4	0.46	15	2.91	7.53
11	6.4	0.58	9	2.38	7.07
12	6.4	0.70	11	2.11	6.39
13	7.0	0.35	15	3.21	9.22
14	7.0	0.46	13	2.86	8.17
15	7.0	0.58	11	2.56	7.79
16	7.0	0.70	9	2.29	7.28
17	6.0	0.50	12	2.75	7.04
18	6.5	0.60	10	2.50	7.27
19	5.5	0.40	11	2.94	7.34
20	5.8	0.48	11	2.56	7.12
21	6.2	0.52	10	2.49	7.45
22	6.2	0.35	13	3.26	8.86
23	6.2	0.70	11	2.17	6.65

3.3.4 Bead geometry measurement

One single bead was produced for each parameter set in Table 3.3. Weld beads deposited for No.16-23 are shown in Figure 3.17 as examples. A 3D laser profile scanner with a resolution of 0.02 mm, projecting a laser line on the weld bead cross-section, was used to measure the bead height and width, as shown in Figure 3.17b. The scanner was carried by a robot moving along the deposited weld beads. Each bead having a total length of 60 mm was cross-sectioned three times, i.e. at a length of 15 mm, 30 mm, and 45 mm as shown in Fig.4a. The measured bead height and bead width are listed in Table 2 as columns coloured in orange.

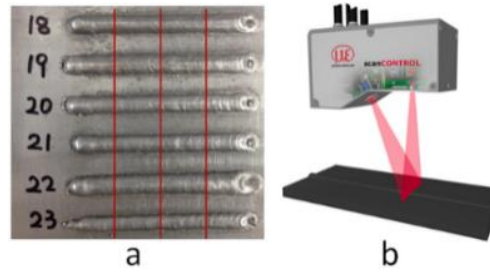


Figure 3.17 (a) Single beads (60 mm long) deposited onto aluminium substrate with parameter sets No.17-23; welding direction runs from left to right; the red lines represent the locations of cross-sectioning away from arc starting and extinguishing points to eliminate the start and end effects. (b) Schematic diagram of bead geometry measurement using the 3D laser profile scanner.

3.3.5 Testing of neural network

The performance of the trained ANN bead model (using data No.1-16 from Table 3.4) was evaluated using 7 independent testing data sets (No.17-23 from Table 3.4). A comparison of the predicted bead geometry using the trained ANN and measured bead geometry is shown in Figure 3.18.

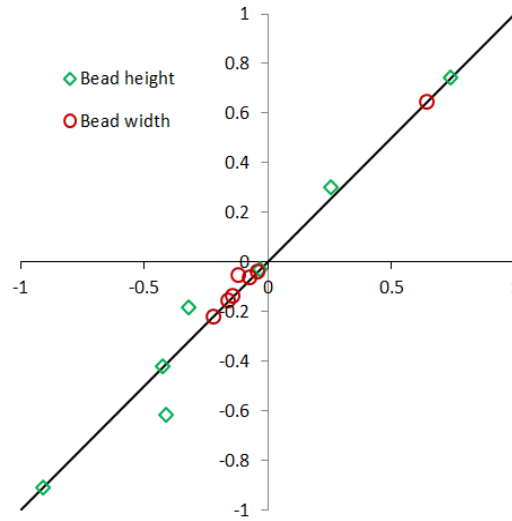


Figure 3.18 Comparison between predicted and measured weld bead geometry (normalised)

In Fig 3.18, the horizontal axis represents the measured bead height and bead width, and the vertical axis represents the predicted bead height and bead width. For comparison, the linear solid line representing the measured values are equal to the predicted values is provided. It can be seen that most of the data points lie on or near to the provided linear line indicating the ANN model is able to predict bead height and bead width within the range of reliable accuracy. Note that to train and test the network accurately, all inputs and outputs are normalised within the range of -1 and +1. The normalised value (X_i) for each raw input or output (R_i) was calculated as

$$X_i = \frac{2}{R_{\max} - R_{\min}} (R_i - R_{\min}) - 1 \quad (3.24)$$

where, R_{\max} and R_{\min} are the maximum and minimum values of the raw data, respectively. The trained neural network bead model is used as the essential database to determine the optimum welding parameters corresponding to the desired bead geometry (bead height and bead width).

3.4 Summary

This chapter provides the detailed development of bead modelling. First, single weld bead was modelled as parabola curve with high accuracy through using the whole bead cross-sectional profile instead of using only the bead width and bead height to fit the bead geometry with mathematic models. Then, an innovative multi-bead overlapping model, tangent overlapping model, was developed to describe the multi-bead overlapping process. The optimal step-over distance is confirmed to be function of bead width. Finally, artificial neural network model aluminium bead model was established. With this neural network, the optimal welding parameters in terms of the desired bead geometry could be determined automatically. Note that ANN mild steel bead model is also developed and introduced in chapter 7.

Chapter 4

3D CAD Slicing

The process planning requires an input CAD model of the part which may be designed in a CAD system, or obtained from reverse engineering such as 3D scanners. Once the CAD model is completed, it is converted to the standard STL format, which is most commonly used to represent 3D CAD models in additive manufacturing. A section of a STL file and its 3D model are shown in Figure 4.1. In an ASCII STL file, the CAD model is represented using triangular facets, which is described by the X-, Y-, and Z-coordinates of the three vertices and a unit vector to indicate the normal direction that point outside of the facet. Redundant information for indicating model name, facet normal, and vertex are also included.

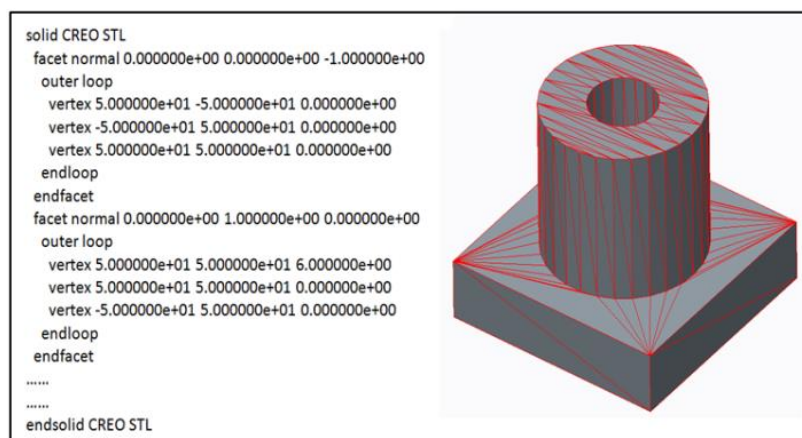


Figure 4.1 Example of a STL file format and its model

In this chapter, algorithms for uni-direction slicing and multi-direction slicing of STL models are provided.

4.1 Uni-direction slicing

Uni-direction slicing algorithm slices the STL model into a variety of 2.5D layers parallel to the build direction. Figure 4.2a shows a STL model and various cutting planes for uni-direction slicing; and Figure 4.2b shows the resulting slicing layers which are polygons.

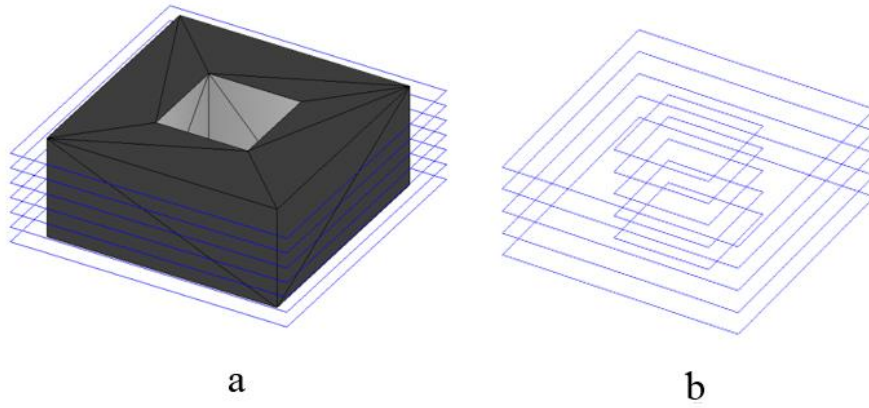


Figure 4.2 (a) STL model with slicing layers in uni-direction; (b) Resulting layer boundary polygons

Uniform slicing method slices CAD model with a constant thickness. The accuracy of the additive manufactured parts could be controlled by altering the layer thickness. The smaller layer thickness, the higher accuracy will be obtained. Adaptive slicing approach slices a model with a variable thickness. Based on the surface geometry of the model, this approach adjust automatically the layer thickness to improve the accuracy or to improve the build-time.

With the increasing size of the STL file, a major challenge of slicing algorithms is the computing efficiency. An efficient and fault-tolerant slicing algorithm was proposed by Choi et al. [77]. This study applies this tolerant algorithm for slicing purposes. The detailed slicing algorithm is presented as follows.

4.1.1 The tolerant uni-direction slicing algorithm

Figure 4.3 shows the flowchart of the tolerant slicing algorithm [77]. Two stages are included, namely, pre-processing stage concerning orientation, and slicing stage. The orientation of the STL model is usually user defined or obtained with respect to the optimal build time or the surface quality, and support structures required. Algorithms regarding the orientation of CAD models is beyond the scope of this thesis.

In the slicing stage, the algorithm mainly involves manipulation of the facet data and comparison of the z -coordinates, and then calculates the line segments that are subsequently joined to construct layer contours.

For each layer construction, the algorithm scans the STL file to extract one facet at a time sequentially and compares the z -coordinates of its three vertices to the z -height of the cutting plane. Setting a small value bound tolerance, ϵ , the possibilities of intersection of a facet with a cutting plane can be divided into the following four classes, as shown in Figure 4.4 [77].

Class 1 is shown in case 1 in Figure 4.4, where a facet intersects with the cutting plane without one vertex lies on the plane. Two intersecting points are calculated by the

intersection of the plane and the triangular facet in this case. A line segment is generated by connecting the intersection points and stored for constructing the slice layer contour.

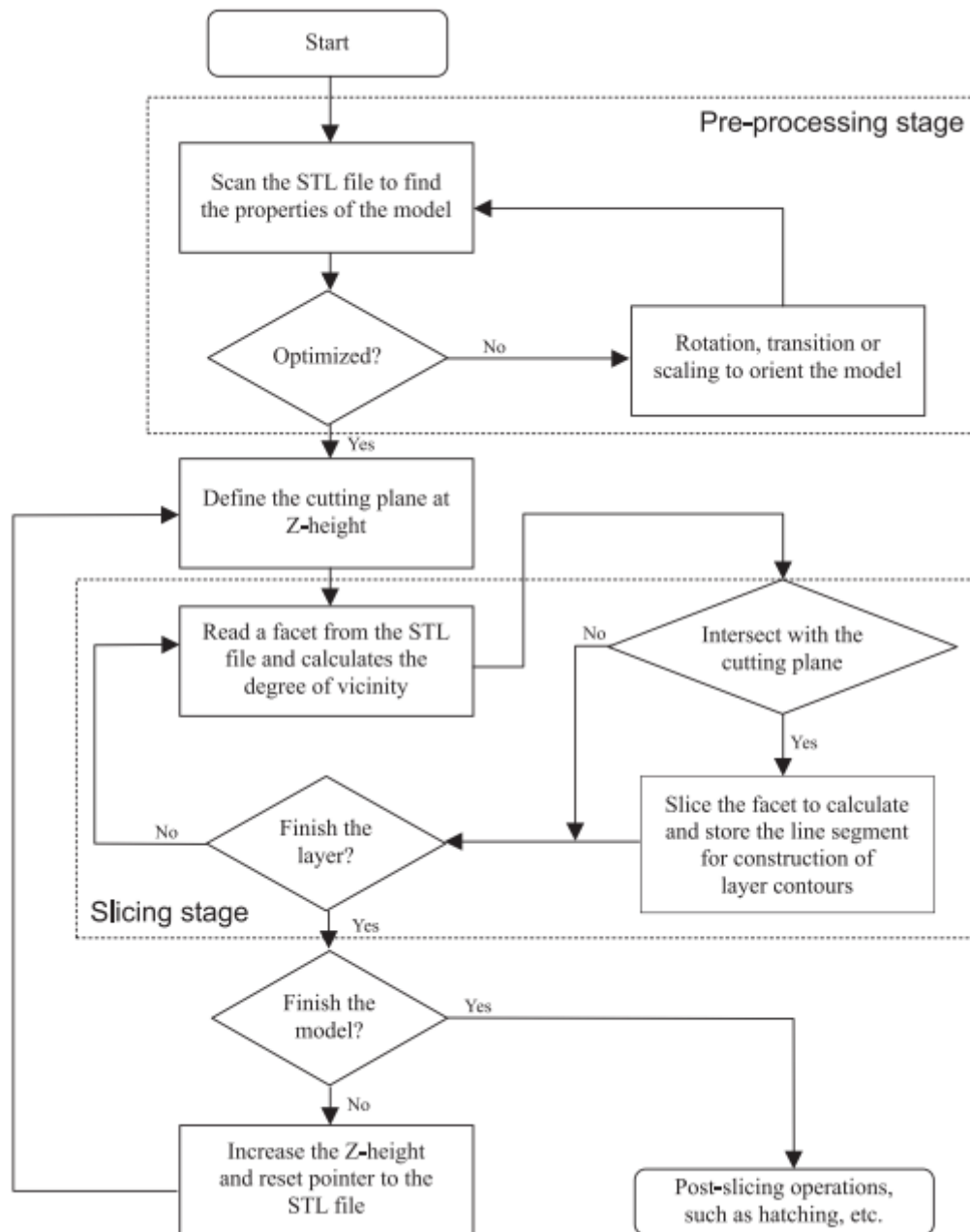


Figure 4.3 Flowchart of the tolerance slicing algorithm [77]

Class 2 is shown in case 2 in Figure 4.4, where one vertex lies in the cutting plane while the two remaining vertices lie in different sides of the cutting plane. Case 3 and case 4 show also one vertex lies in the cutting plane while other vertices lie in the same side of the cutting plane. In this case, there will be no intersection line segment calculated.

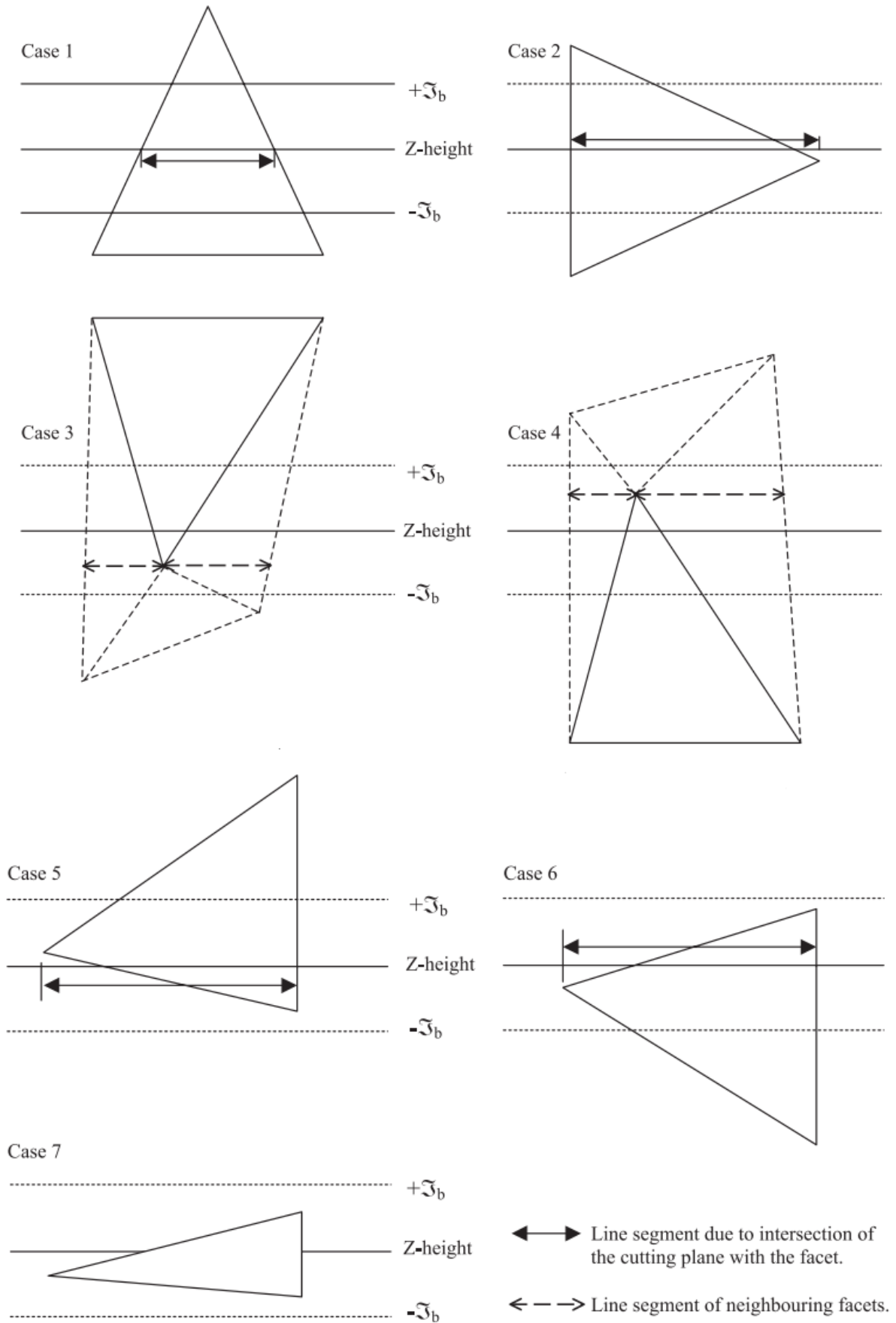


Figure 4.4 Possible cases of facet-plane slicing [77]

Class 3 is shown in case 5 and case 6 in Figure 4.4, where two vertices of the facet lie in the cutting plane. The remaining vertex can be either above or below the cutting plane. This is a concurrent case in a valid STL model that results in one duplicated line segment and either one should be ignored.

Class 4 is shown in case 7 in Figure 4.4, where all three vertices lie in the cutting plane. In this case, the whole triangular facet lie in the cutting plane and will not contribute any line segments to the contour of the slice layer. Therefore this case can be directly ignored without any ambiguity.

After all the possible intersection line segments have been calculated and stored, the contour of the slice layer is constructed through head-to-tail connecting of the line segments.

4.1.2 Implementation

The algorithm has been implemented in MATLAB program. The slicing algorithm was able to slice complex STL models with good performance. Three case studies are provided as shown in Figure 4.5 – 4.7. The number of facets of three models are provided in Table 4.1. The algorithm is verified to be efficient with the computing times less than half second for all cases.

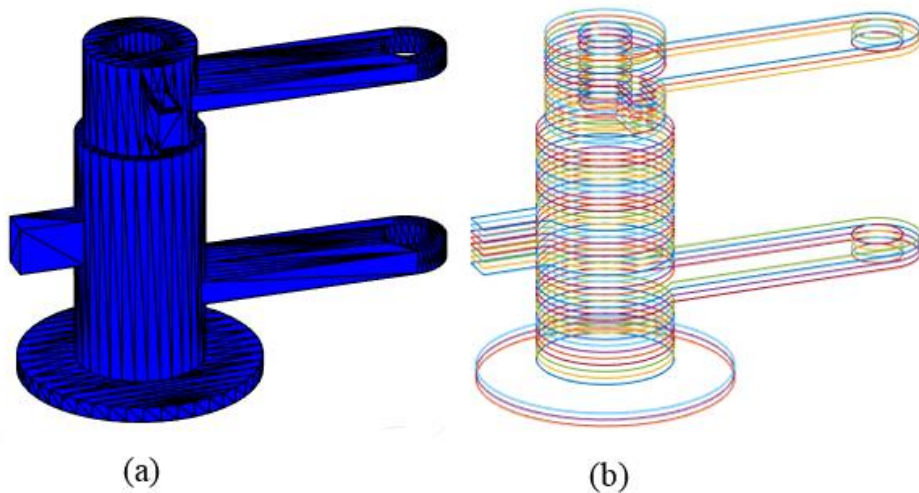


Figure 4.5 Case I. (a) An engineering STL model; (b) Resulting slices

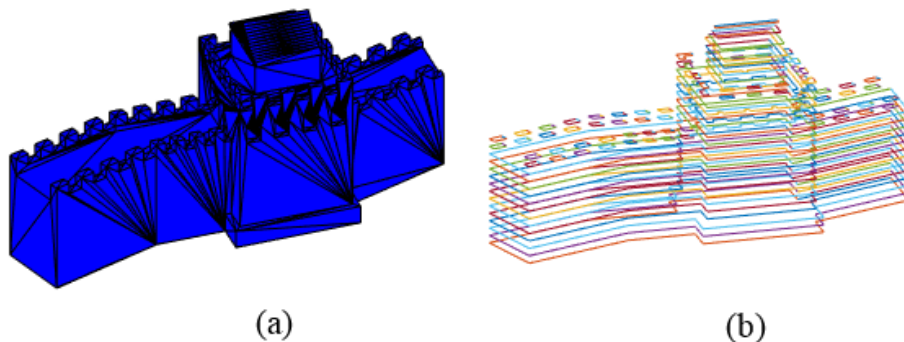
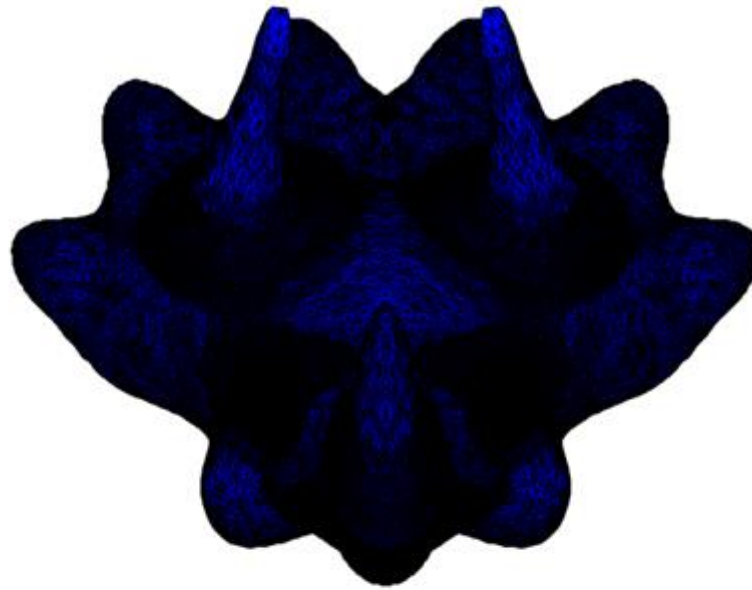
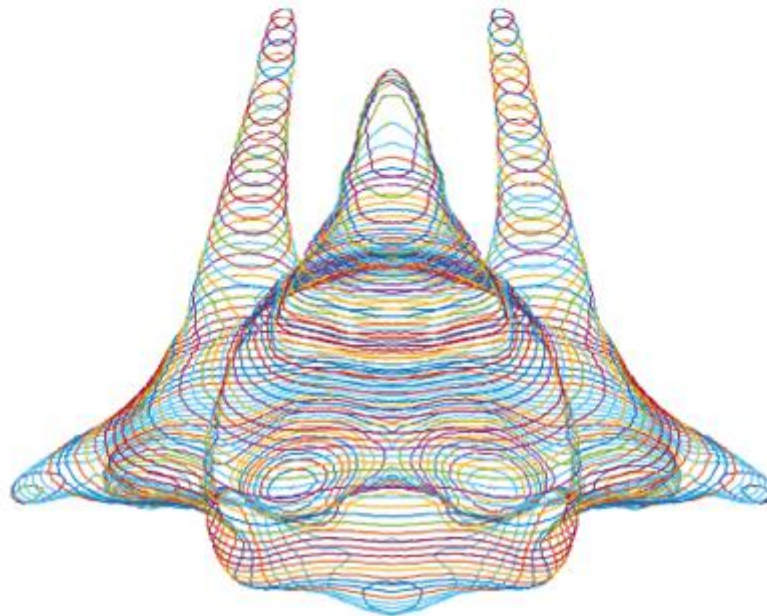


Figure 4.6 Case II. (a) A Great Wall STL model; (b) Resulting slices



(a)



(b)

Figure 4.7 Case III. (a) A Triceratops STL model; (b) Resulting slices

Table 4.1 The computing time of the program

No.	Facets	Computing time
Case I	1,076	12 ms
Case II	1,584	34 ms
Case III	172,122	352 ms

4.2 Multi-direction slicing

Most of the current AM processes involve slicing a 3D CAD model into a set of 2.5D layers with a constant or adaptive thickness perpendicular to the build-up direction as mentioned in uni-direction slicing. However, to fabricate parts with complex shapes in WAAM technologies, processes based on a uni-directional slicing strategy are generally limited by the need for support structures to deposit overhangs. Figure 4.8a shows a component and its usual build direction B . It is clear that to fabricate the component in direction B , support structures (refer Figure 4.8b) are required due to overhangs. For metal components, the supports are normally deposited using the same material. The deposition of supports results in the wastage of materials and the removal of these supports requires costly post-processing.

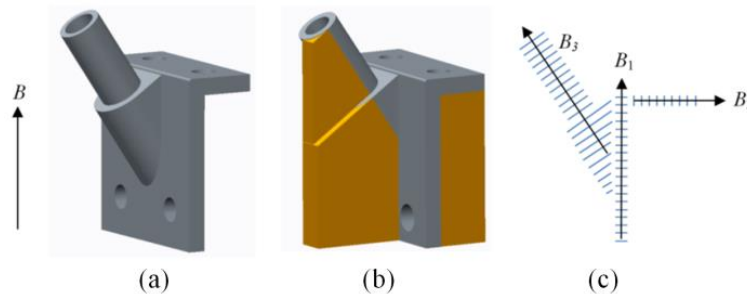


Figure 4.8 (a) The component and its usual build direction B ; (b) support required (parts coloured in orange); (c) multi-direction slicing and various build directions B_1 , B_2 , and B_3

WAAM, which mounts a deposition nozzle on a multi-axis robot arm, is able to deposit materials along multiple directions as shown in Figure 4.9. The application of multi-direction deposition could eliminate or significantly decrease the usage of supports for complex components. As shown in Figure 4.8c, the component can be fabricated in multiple directions, e.g., B_1 , B_2 , B_3 , without support structures. Such a multi-direction deposition system furthers the capability of layered manufacturing by reducing the need for supports.

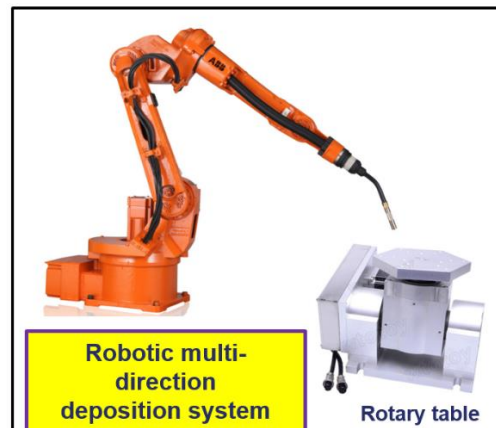


Figure 4.9 Schematic diagram of a robotic multi-direction deposition system

A key challenge in multi-direction AM is to develop robust algorithms capable of automatically slicing any 3D model into a set of layers which satisfy support-less and collision-free layered deposition. This study proposes an innovative strategy to slice CAD models in multiple directions for WAAM system.

4.2.1 Related works of multi-direction slicing

In AM, slicing is an important process that yields a set of layers for subsequent tool-path generation. These 2.5D layers are generally parallel to each other and perpendicular to the build-up direction. Slicing algorithms producing 2.5D layers with both a constant and adaptive thickness have been widely studied. Recently, research focus has shifted to multi-direction slicing which varies not only in layer thickness but also in slicing direction. This technique significantly improves the ability of AM for producing complex components. Some existing multi-direction slicing strategies are reviewed here.

Silhouette edges projection [78]: This strategy firstly identifies the unbuildable surface features of a model by projecting silhouette edges along the user defined original build direction. Then the part is decomposed into buildable and unbuildable sub-volumes using the silhouette-edge based method. For the unbuildable sub-volume, a new suitable build direction is determined using the Gauss and Visibility maps. With the new build direction, the unbuildable sub-volume is further decomposed through repeating the same projection procedures. This projection method is recursively used to decompose the sub-volume until the generated sub-volume is buildable along one direction. The framework for the multi-direction slicing and some essential problems have been addressed and discussed by the authors. However, the implementation of the strategy could be complicated and computationally expensive for complex components with inner cavities.

Transition wall [79]: The key idea of this strategy is to identify the overhang layers by computing the difference between the current layer and the previous layer. Then, to build an overhang structure, the machine is turned 90° to start depositing a transition, namely thin wall. After the deposition of the first few layers, the wall is finished and the subsequent overhang structures can be deposited in the vertical direction again. Although this strategy is simple, it is only suitable for a subset of part geometries. In some cases, the deposition of the transition wall is difficult or impossible to implement due to deposition nozzle collision, such as the part shown in Figure 4.8a.

Centroid axis extraction [80]: The first step in this strategy is to extract the centroid axis of the model which provides a global perspective on the geometry, allowing the slicing procedure to be conducted on an optimal sequence. Through analysing the topological information from the centroid axis, the splitting surface is identified and the subsequent decomposition operation is conducted. For each sub-component obtained from decomposition, multi-axis slicing is performed and the collision free slicing sequence is finally generated. The centroid axis extraction method decomposes the component by detecting the change of centroid of pre-sliced layers, making the geometry analysis process easier. However, in some cases it will be difficult to decompose components efficiently as required since the centroid axis does not always indicate the change of the geometry.

Other multi-direction slicing methods have been proposed that are either adaptations or combinations of a few techniques from the above strategies, such as adaptive slicing algorithm [81], offset slicing [82], skeleton method [83], and modular boundary decomposition [84]. However, each method is only suitable for a subset of part geometries. In addition, these methods are not efficient for processing parts with holes and depression features. As shown in Figure 4.10, the part is decomposed into buildable volume and unbuildable volume due to the direction of hole, H , is vertical to the build direction, B , of its associated volume. Figure 4.10b shows the part with holes as well. The part is firstly decomposed into buildable and unbuildable sub-volume [78]. The unbuildable sub-volume could be further build by offset slicing strategy [82] with the direction as shown in Figure 4.10b. Even though, unbuildable volume also exists due to the holes. It is clear that holes would be obstacle for implementing multi-direction slicing algorithm.

Differing from these existing slicing approaches, which are mainly focused on finding an optimal volume decomposition strategy, this study presents simplification of holes and a decomposition-regrouping method. A model simplification step is introduced before CAD decomposition to significantly enhance the capability of the proposed multi-direction strategy. The CAD model is then decomposed into sub-volumes using a simple curvature-based volume decomposition method and consequently a depth-tree structure based on topology information is introduced to merge them into ordered groups for slicing. The proposed strategy is proven to be simple and efficient on various tests parts. Since there is no robust multi-direction slicing algorithm validated for any complex geometry, the proposed multi-direction slicing algorithm is not versatile also, while it is particularly useful for components with large number of holes.

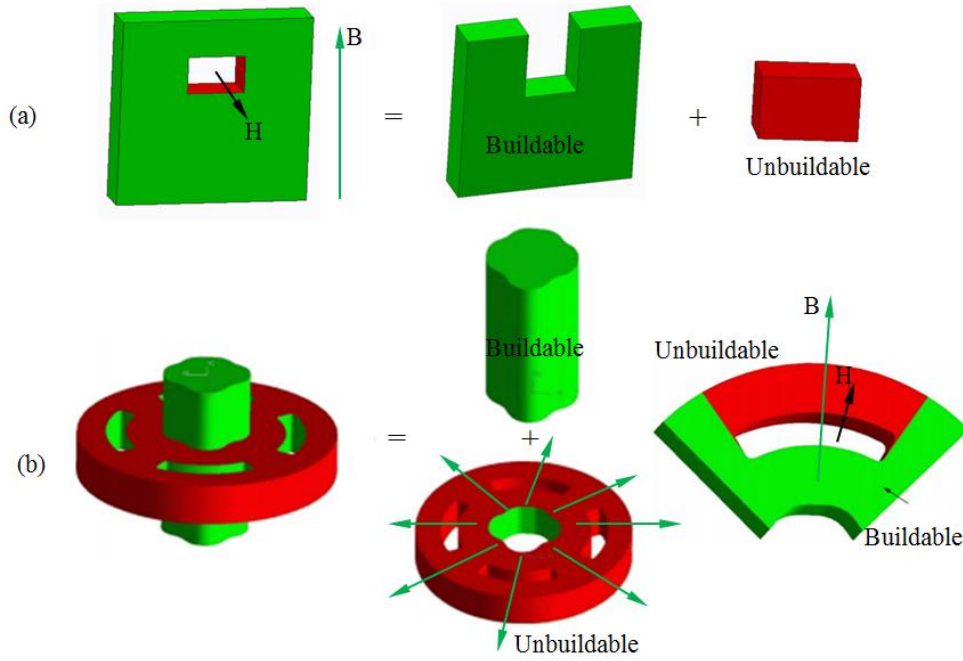


Figure 4.10 Illustration of the impact of holes on multi-direction slicing strategy

4.2.2 Strategy overview

The algorithm proposed in this study for generating multi-direction slices consists of five modules, including STL input, Model simplification, Volume decomposition-regrouping, Build direction identification, and Model slicing as shown in Figure 4.11.

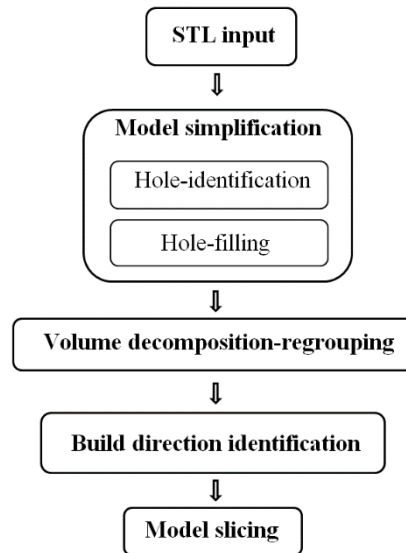


Figure 4.11 Architecture of the multi-direction slicing strategy

Model simplification of 3D geometry is a strategy commonly used in applications such as dynamic simulation and finite element analysis (FEA) in order to improve the mesh quality and reduce the computational time. It is adopted here to greatly simplify the volume decomposition and to generate optimised sub-volumes and building directions. The complex

models are categorised into meaningful parts, i.e., major object features, and subtle parts, such as small holes, appendixes, etc. As shown in Figure 4.12, performing volume decomposition directly on the original CAD model with many small holes is difficult and often generates excessive sub-volumes and problematic building directions. To simplify CAD models with respect to holes, there are two tasks: hole-identification (Figure 4.12c) and hole-filling (Figure 4.12d). It should be noted that holes may have various shapes and are not limited to a single feature plane.

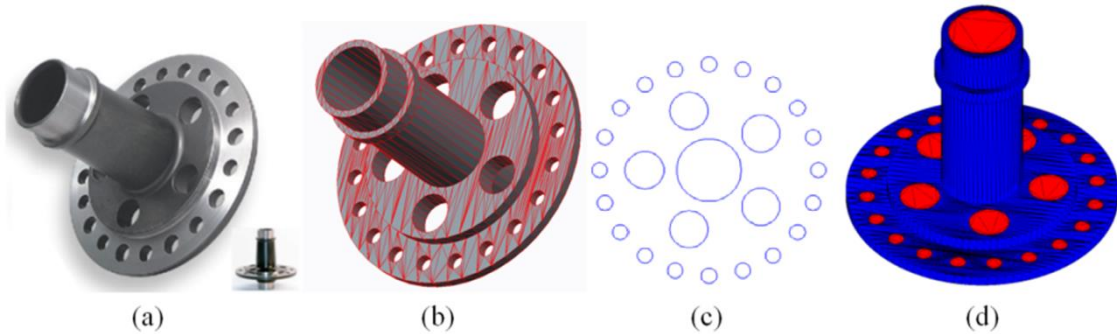


Figure 4.12 An example of a complex model with holes (a) the original model; (b) STL mesh; (c) identified holes; and (d) simplified model without holes

Volume decomposition-regrouping module firstly decomposes a complex part into a variety of convex sub-volumes through progressively using a curvature-based decomposition method. A variety of sub-volumes are obtained from the volume decomposition, and the region from which the sub-volume has been split is stored as the topology information. Then a depth-tree structure based on the topology information is constructed to regroup the sub-volumes and provide the order of sequences for the latter slicing module.

Build direction identification module is developed to identify the build direction for each sub-volume to guide the subsequent slicing procedure. For convenience, Gauss Map is used to calculate the optimal build directions for sub-volumes.

Model Slicing module slices each sub-volume along its own build direction (Z^+) using a tolerant slicing algorithm that has been mentioned [77]. Differing from the existing slicing algorithm, an important step in this module is to process the subtle parts from model simplification. The decision for hole-filling is determined under a set of rules. If the axis of a hole is not parallel to the build direction of its sub-volume, the hole is required to be filled as a support. In this situation, post process milling is needed to reconstruct the hole afterwards. If the axis of a hole is parallel to the build direction of its sub-volume, the hole can be either filled or not based on its dimension. If the size of the hole is very small and close to the deposition accuracy of the machine, the hole will be filled and drilled out in post-processing,

which would significantly reduce the complexity of the sliced layer and facilitate the subsequent path-planning.

The volume decomposition process, the depth-tree structures, build-directions, and model slicing for a sample part are shown in Figure 4.13. With the multi-direction deposition method proposed in this study, the part can be fabricated without additional supports. The original orientation of the part with respect to its base is considered as a user defined input and not to be changed in the proposed algorithm.

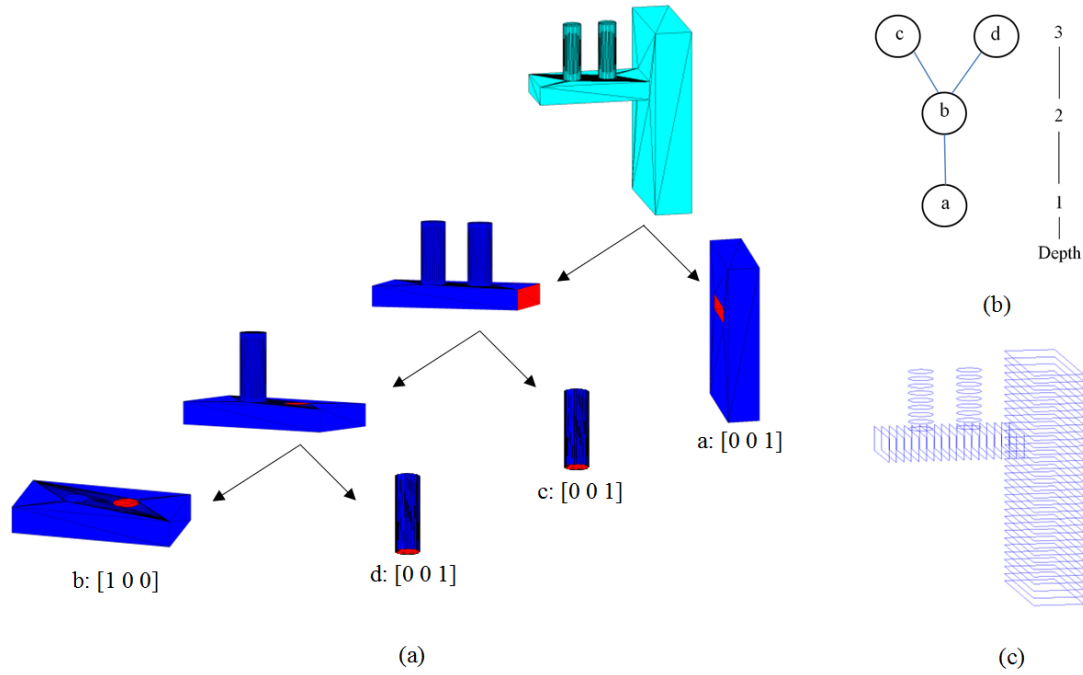


Figure 4.13 (a) a progressive decomposition of an example into sub-volumes with their own build directions; (b) sub-volume grouping with depth-tree structure; and (c) model slicing along multiple build directions

4.2.3 Multi-direction slicing algorithms

A. Terminologies

To simplify the presentation in the paper, the basic terminologies and concepts related to STL model (triangle mesh) are given as follows:

- (1) Feature edge: An edge shared by two triangular facets whose normal vectors make an angle greater than a certain threshold;
- (2) Region: A set of connected triangular facets with the same normal vectors within a given tolerance, usually corresponding to a face of the model (as shown in Figure 4.14a in different colours);
- (3) Boundary: A set of connected feature edges (refer Figure 4.14b);

- (4) Loop: An ordered and connected feature edge set which forms the closed boundary of a region. There are two types of loops: outer loop and inner loop. The outer boundary of a region forms the outer loop (Figure 4.14c red loops), while the boundary of an inner hole or protrusion forms the inner loop (Figure 4.14c blue loops);
- (5) Concave/convex edge: An feature edge is concave/convex if the angle between its two adjacent triangles is smaller/larger than π ;
- (6) Concave loop: A loop is concave if all the edges of the loop are concave edges;
- (7) Sub-volume: Any volume that is decomposed from the CAD model;
- (8) Base region: The region from which the input volume is grown perpendicularly.

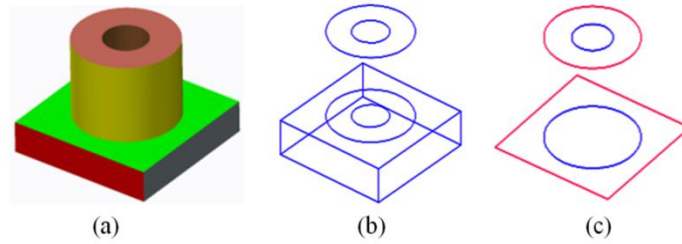


Figure 4.14 Illustration of basic concepts: (a) regions (in different colours); (b) boundaries; and (c) loops

B. Model simplification

To simplify the model, all holes are initially identified and filled. As STL files use triangle meshes to represent the surface of CAD models, the main issues are how to recognize the hole and how to fill the hole using triangular facets.

a) Identification of the holes

As has been described, holes are represented by one type of inner boundary loops. There are three steps to identify the holes: find the feature edges, construct the boundary loops, and extract the inner boundary loops.

1) Find the feature edges

An efficient curvature-based method is used to find the feature edges. The dihedral angle of the adjacent facets is the main curvature parameter, which has been used to estimate surface curvature [85]. The edges with a dihedral angle greater than a certain threshold can be extracted and grouped as the boundaries. As shown in Figure 4.15, two adjacent facets i and j with the normal vectors of n_i and n_j respectively are presented. $e(i, j)$ is the shared edge which contains the shared vertices a and b of the two adjacent facets. The dihedral angle of $e(i, j)$ is

$$\theta(i, j) = \arccos(n_i \cdot n_j), \quad (4.1)$$

Considering the various resolutions of STL files triangulation, different thresholds would be used. Normally, the threshold of 10° is chosen, and the edges whose dihedral angles are greater than this threshold are marked as the feature edges. The feature edges are further divided into convex edges and concave edges, by calculating the following expression

$$\phi_{ab} = (n_i \times n_j) \cdot \vec{ab}. \quad (4.2)$$

If $\phi_{ab} > 0$, the edge $e(i, j)$ is a convex edge; If $\phi_{ab} < 0$, the edge $e(i, j)$ is a concave edge. By applying the above equations to all edges, the feature edges of the model can be extracted.

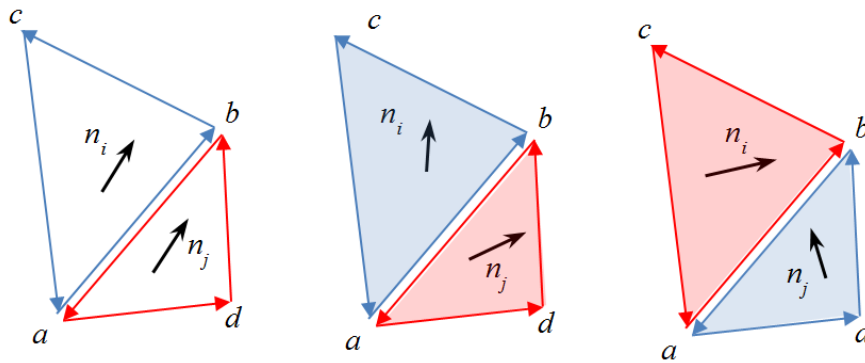


Figure 4.15 (a) The planar edge; (b) The feature edge (convex); (c) The feature edge (concave)

2) Constructing boundary loops

The above procedure extracts all the feature edges which will form a variety of boundary loops by tail-to-head search and region filtering. The start and end vertex of a feature edge are called the head and the tail of the feature edge, respectively. The tail-to-head search repeatedly connects a feature edge (e.g. edge ab as shown in Figure 4.16) to a neighbouring one by checking the vicinity of its tail and the head of the neighbouring edges. Generally, two neighbouring edges are detected (edge bc and bd are the neighbouring edges of ab as shown in Figure 4.16) due to the characteristics of triangle meshes.

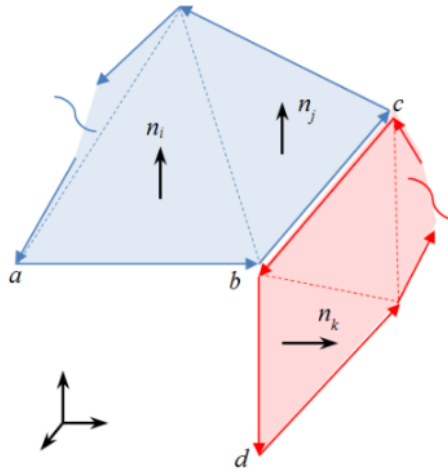


Figure 4.16 Rules for constructing boundary loops

Region filtering is used to choose the right edge. The reference feature edge (e.g. edge ab) and the neighbouring edge will have their normal vectors parallel to each other within a certain tolerance. As shown in Figure 4.16, the blue feature edges belong to one region while the red feature edges belong to another. The vector n_i is the normal vector of the facet where edge ab belongs to, and n_j and n_k are the normal vector of the neighbouring edges, respectively. By calculating the respective angles between neighbouring normal vectors n_j , n_k and reference n_i , it is easy to find the lesser angle and thereby identify the appropriate neighbouring edge to ab . When no further neighbouring edges have been detected, the construction of the boundary loop is finished and a new boundary loop starts if there are any feature edges that have not been engaged. The iterative tail-to-head search and region filtering are used to construct all the boundary loops, and the procedure ends when all the feature edges have been chosen. An example of the boundary loops constructed from the mesh is shown in Figure 4.17.

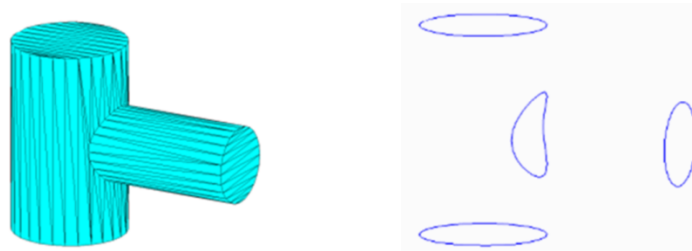


Figure 4.17 An example of a STL model and the generated boundary loops

3) Find the inner boundary loops

As shown in Figure 4.18, holes are represented by inner loops. The outer loops (blue) are ordered in an anti-clockwise direction, while the inner loops (red) are ordered in clockwise

direction. Two methods for identifying the orientation of a set of 2D closed contours, or polygons, based on ray-tracing and the point-in-polygon tests have previously been reported [86]. In this study, a simpler but more effective algorithm is developed to identify the direction of each loop by calculating the sum of the inner angles. As described in Figure 4.18, one can obtain the following expressions:

$$\sin(\theta_i^j) = \frac{\vec{n}_{avg} \cdot (\vec{e}_i^j \times \vec{e}_{i+1}^j)}{|\vec{e}_i^j| \cdot |\vec{e}_{i+1}^j|}, \quad (4.3)$$

$$\cos(\theta_i^j) = \frac{\vec{e}_i^j \cdot \vec{e}_{i+1}^j}{|\vec{e}_i^j| \cdot |\vec{e}_{i+1}^j|}. \quad (4.4)$$

where, θ_i represents one of the angle of the vertex i from the loop j ; \vec{e}_i^j represents the unit vector of the edge i from the loop j ; n_{avg} is the average normal of the facets where the edges of the loop j belong to. We define $\varphi_i^j = \pi - \theta_i^j$, which represents the supplementary angle of θ_i . If $\varphi_i^j < 0$, then set $\varphi_i^j = \varphi_i^j + 2\pi$. It is found that, for outer loops, φ_i^j represents the inner angle, while for inner loops, it represents the outer angle. The sum of the inner angles of the loop having N edges is $(N-2)\pi$, and that of the outer angle is $(N+2)\pi$. The sum of φ_i^j for the loop j can be expressed as $\sum_{i=1}^N \varphi_i^j$. Then one can identify the inner or outer boundary loop by the following expressions:

if $\sum_{i=1}^N \varphi_i^j = (N-2)\pi$, the loop is an inner loop

if $\sum_{i=1}^N \varphi_i^j = (N+2)\pi$, the loop is an outer loop.

This simple method is developed for identify the direction of loops in one plane. It is found that this strategy is also suitable for spatial loops by determining which value of either $(N-2)\pi$ or $(N+2)\pi$ is closer to the value of $\sum_{i=1}^N \varphi_i^j$.

After the inner loops have been extracted, the checking of the convexity is required to determine whether an inner loop belongs to a hole or protrusion. If all the feature edges of the inner loop are convex edges, the inner loop represents a hole; otherwise it belongs to a protrusion.

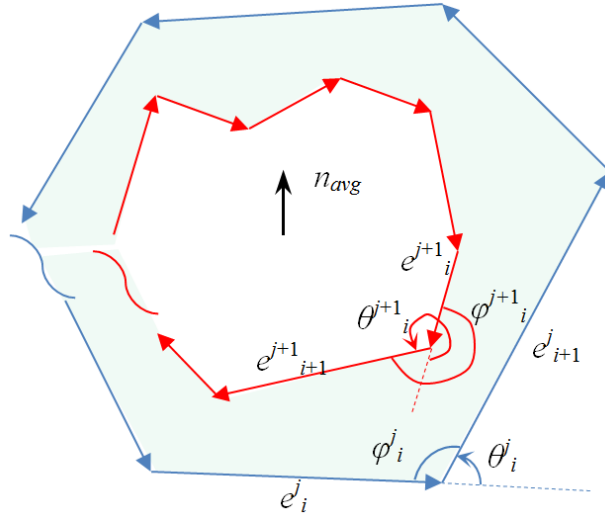


Figure 4.18 Rules for identifying the inner loops

b) Hole-filling

Many researchers have focused on developing automatic hole-filling algorithms, which should be able to efficiently process any arbitrary holes [87, 88]. In this study, a modified advancing front mesh method is developed to fill the holes. The method consists of the following steps:

Step1. Initialize the front using the vertices of the hole (see in Figure 4.19a, vertices $V_1, \dots, V_i, \dots, V_N$ in the order as shown).

Step 2. Calculate the angle of θ_i between two adjacent edges (e_i and e_{i+1}) at each vertex V_i on the front; The normal of the facet where V_i and V_{i-1} belongs to is used for calculating the angle of θ_i .

Step 3. Identify notches. A notch is defined as a vertex whose interior angle is larger than π .

Step 4. Starting from the notch (V_{i+1} in Figure 4.19a) for which the next vertex (V_{i+2}) is not a notch, create a new triangle by connecting the notch V_{i+1} and the vertex (V_{i+3}). This step will either eliminate the notch or reduce the interior angle of the notch.

Step 5. Update the front as shown in Figure 4.19b.

Step 6. Repeat Steps 2 through 5 until all the vertices of the front are not notches. As long as this step is done, no matter what shape the hole is, it will become to a convex polygon. A polygon that has at least one notch is called a non-convex polygon; otherwise, it is a convex polygon.

Step 7. Reorder all the vertices. Starting from any vertex V_i , create a new triangle by connecting V_i and V_{i+2} .

Step 8. Update the front.

Step 9. Repeat Steps 7 through 8 until the entire hole region has been patched by all newly created triangles.

This method fills the hole by repeatedly creating a new triangle and advancing the front of the hole at each time. For simple holes whose geometries are convex polygons, the procedure from Step 2 to 6 is not engaged and the computing time will be greatly reduced. As shown in Figure 4.20, the experiments indicate that this proposed approach is simple, efficient, and robust for any hole geometry.

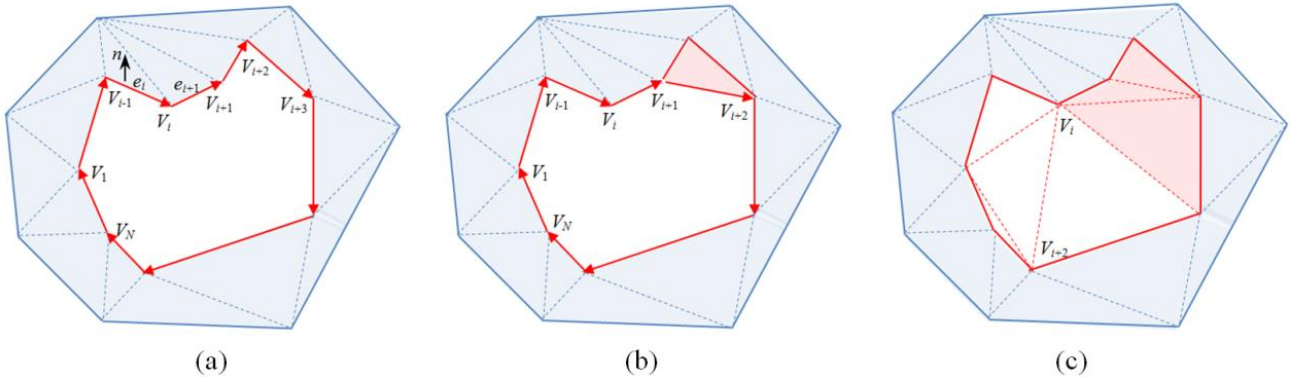


Figure 4.19 Modified advancing front mesh method for hole-filling

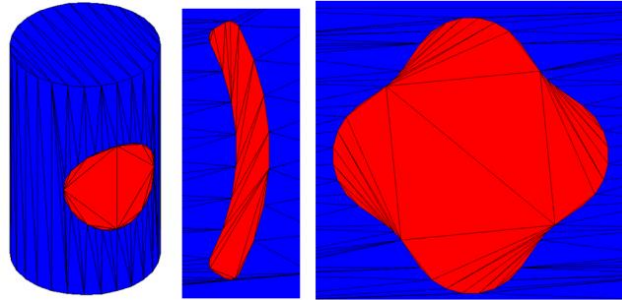


Figure 4.20 Illustration of the developed hole-filling algorithm for planar and spatial holes with complex shapes (red regions are holes filled by triangular facets through the proposed hole-filling algorithm)

C. Volume decomposition-grouping

1) Volume decomposition

In this section, the algorithm for progressive decomposition of the volume is summarized with the aid of the flowchart shown in Figure 4.21. The input for this task is the simplified STL model (triangle mesh) in which all the holes been filled. The volume is decomposed into several sub-volumes by splitting the triangular facets along the concave loops. Consequently, a set of sub-volumes free of any concave loops is obtained.

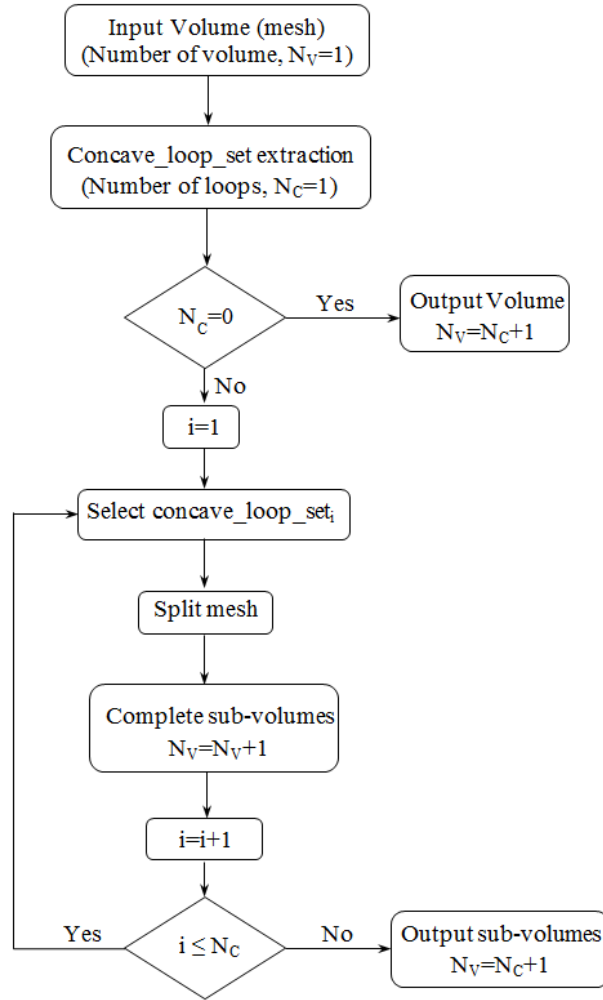


Figure 4.21 The algorithm for progressive decomposition

Concave_loop_set extraction module: Generate the boundary loops of the input mesh again and check the convexity of the edges for each boundary loops. Then concave loop sets are extracted. The process of decomposing an input mesh can be considered to be the process of progressively eliminating concave loops. For a complex model with N_C concave loops, the algorithm outputs N_{C+1} sub-volumes.

Split mesh module: When the $\text{concave_loop_set}_i$ is selected as the split loop, an effective algorithm is required to divide the facet set into two facet sets. An advancing front search technique is developed to split the mesh into two new facet sets. This method consists of the following steps:

Step 1. Initialize the front using the selected $\text{concave_loop_set}_i$. As shown in Figure 4.22, e_i and e_{i+1} are the front edges.

Step 2. Search the related triangle facet for each front edge. In Figure 4.22a and 4.22b, j and k are the related triangle facets of e_i and e_{i+1} respectively; while in Figure 4.22c, e_i and e_{i+1} share the same facet j .

Step 3. Add triangles to a new facet set and update the front with the following three rules, as shown by the three cases in Figure 4.22. Rule (a): If the related triangle facets are independent (such as facet j and k in Figure 4.22a), add the related triangle facets into the new facet set, and update the front edge using the other edges of the related triangle facets (dashed red lines with arrow). Rule (b): If the related triangle facets share one edge (such as facet j and k in Figure 4.22b), add the related triangle facets into the new facet set, but update the front using the other edges except the shared edge of the related triangle facets. Rule (c): If the related triangle facets are overlapped (such as facet j in Figure 4.22c), add the triangle facet into the new facet set, and update the front using the rest edge of the related triangle facet.

Step 4. Repeat Steps 2 through 3 until the front is empty.

Step 5. The triangle facets, which haven't been detected from Step 2 through 4, are collected to another new facet set.

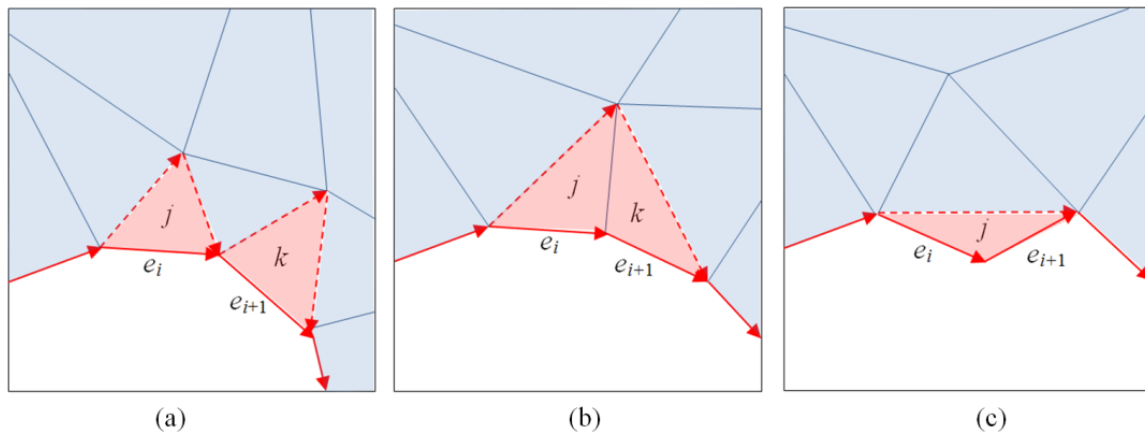


Figure 4.22 Rules for adding triangles and updating the front

This method can always split the input mesh into two facet sets, whatever its shape, and guarantee the robustness of the proposed algorithm. Note that the generated two facet sets are two open half volumes.

Complete sub-volume module is developed to complete the two sub-volumes from the two open facet sets generated by applying the above procedure. The selected concave_loop_seti is considered as the hole loop, and the hole-filling algorithm is used again to close the two open sub-volumes. The filled hole regions are recorded as the feature regions of the sub-volume, which is useful for the subsequent grouping process. With the progressive decomposition, the component is decomposed into a variety of sub-volumes.

2) Sub-volume regrouping

Since the obtained sub-volumes are disordered, topology information between each sub-volume and its feature regions is constructed for the grouping process. The feature region represents the connection between two sub-volumes and is important information for ordering sub-volumes. As the example shown in Figure 4.23, seven disordered sub-volumes are obtained from the decomposition. The regions coloured in red are feature regions. As the orientation is the user defined input, the base region is the bottom of the input component. Only one of the sub-volumes has the base region. Starting from the base region on basis of the characteristics of AM, all sub-volumes are connected by searching the shared feature regions as shown in Figure 4.23b.

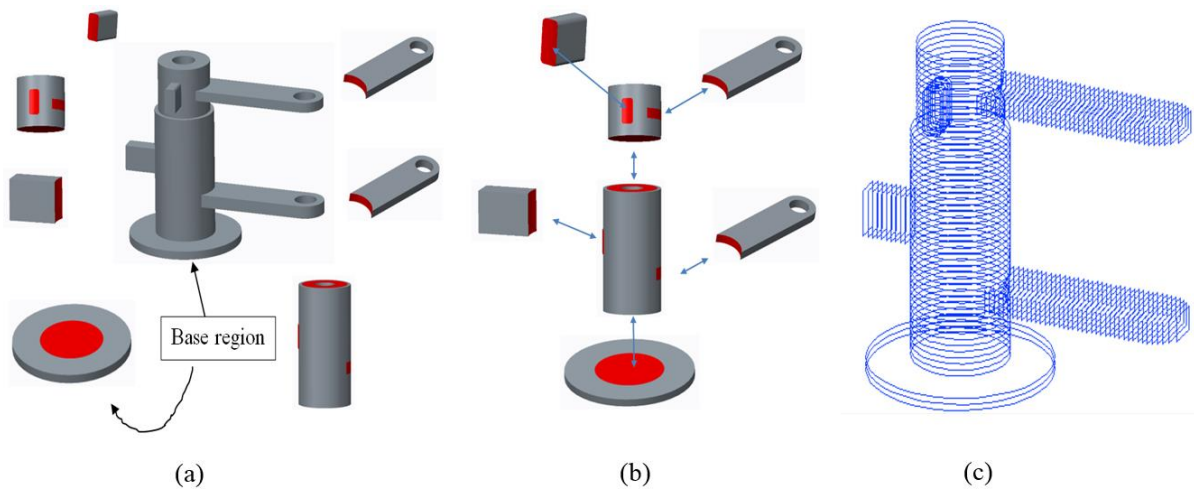


Figure 4.23 (a) An example for illustration of sub-volumes, feature regions (coloured in red), and base region (b) Grouped sub-volumes (c) Slicing in multiple directions

The sub-volumes then are ordered and grouped with the depth-tree structure starting from the sub-volume that has the base region. As schematically shown in Figure 4.24, sub-volumes are stored as (i, j) , where i represents the depth of the sub-volume. As the orientation is the user defined input, the base region is the bottom of the input component, therefore sub-volume $(1, 1)$ is easily identified from the sub-volumes. Usually, there is only one sub-volume that has the depth of 1. Then, sub-volumes whose base regions are connected with the sub-volume $(1, 1)$, have the depth of 2. Finally, all the sub-volumes are stored within the depth-tree structure.

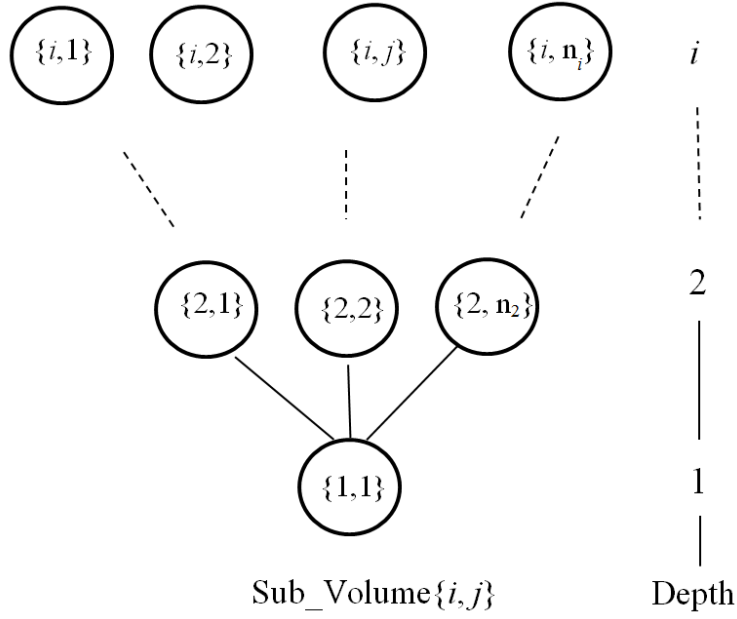


Figure 4.24 Sub-volumes grouping with the depth-tree structure

D. Build directions determination

The optimal build direction of each sub-volume must be determined to guide the subsequent slicing procedure. Figure 4.25 shows two sub-volumes V_1 and V_2 . Assume the build direction of V_1 has already been determined, but the optimal build direction of V_2 is not yet determined. The base region of V_2 was obtained in section 4.3.2.C. All the regions except the base region of V_2 are used to find the optimal build direction B_{opt} . The normal vectors of the facets in these regions are recorded in a set n . The problem is stated as follows:

Given a set of normal vectors $n = (n_1, \dots, n_i, \dots, n_n)$. Find the optimal vector B_{opt} that produces the smallest maximum angle between this vector and any vector n_i within the set.

Gauss Map [89] is used, which collects all the normal on a unit sphere. A set of normal vectors n can be represented in a set of points on the surface of a unit sphere. For this set of points, a spherical crown C with a minimum-radius bottom surface that contains all the points can be found on the sphere surface [90]. The unit vector from the centre of the sphere to the centre of the bottom circle of the spherical crown C is the desired optimal build direction. The optimisation problem is thereby simplified to searching for the minimum spherical crown which contains all the points of the normal vectors n . Algorithms to find the minimum spherical crown basing on the algorithm for the smallest enclosing discs problem were developed [90], [91]. The detailed algorithm for the smallest enclosing discs problem is provided in Appendix B.

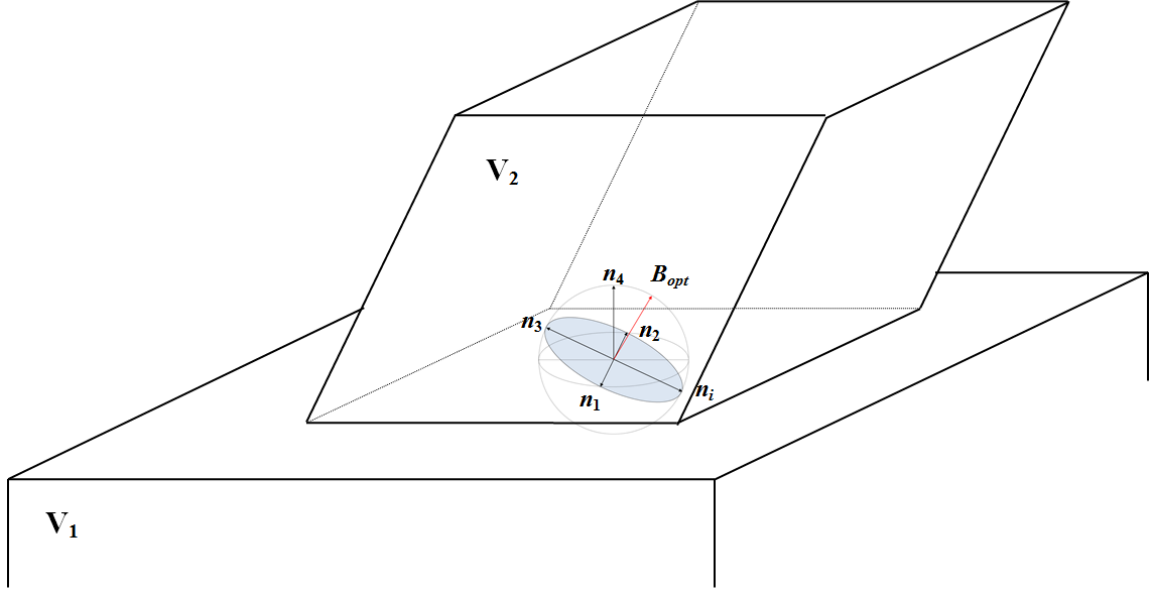


Figure 4.25 The optimal build direction for sub-volume

E. Slicing

According to the depth of each sub-volume, the slices of each sub-volume along its optimal build direction can be generated one by one. Slicing algorithms for STL models along the Z+ [0 0 1] direction has been widely reported [77]. In this study, matrix transformations are used to apply these basic tolerant slicing algorithms to each sub-volume in the model along the optimal build direction.

Assume the build direction of a sub-volume is $B_i = [B_{ix} \ B_{iy} \ B_{iz}]$. Through the rotation θ and φ about x and y respectively, the z axis is made parallel to the build direction. One can obtain the following equation:

$$\begin{pmatrix} B_{ix} \\ B_{iy} \\ B_{iz} \end{pmatrix} = M^{-1} \begin{pmatrix} 0 \\ 0 \\ 1 \end{pmatrix} = \begin{pmatrix} \cos \varphi & \sin \varphi & 0 \\ -\cos \theta \sin \varphi & \cos \theta \cos \varphi & \sin \theta \\ \sin \theta \sin \varphi & -\sin \theta \cos \varphi & \cos \theta \end{pmatrix}^{-1} \begin{pmatrix} 0 \\ 0 \\ 1 \end{pmatrix}. \quad (4.5)$$

One can obtain the value of rotation θ and φ , and consequently the transfer matrix M and the inverse matrix M^{-1} . Transfer all the facets vertices and facet normal of the sub-volume i , then slice along Z+ direction using the existing algorithms [77]. Finally, transfer the slice layers back to the original orientation of the sub-volume. With this process, each sub-volume is sliced along its build direction individually. Note that this proposed process can also be extended to utilise the adaptive direction and thickness slicing algorithm [90] which could generate non-uniform thickness layers matching the surface curvature of the sub-volume appropriately.

At this point, filled holes need to be reconsidered. If the sub-volume contains a hole-loop, this hole belongs to the sub-volume. Each hole is uniquely associated to its related sub-volume. If the hole is parallel to the build direction of its sub-volume, it is not require filling. Therefore, the slice of the hole is conducted, otherwise, deposition of the hole is needed for support purposes and the volume of the hole is extracted from the final part by post-process milling.

4.2.3 Implementation and results

The strategies presented in this study were implemented by programs written in MATLAB. Besides the slicing results shown in Figure 4.13c and Figure 4.23c, two more examples and slicing results are presented here. As shown in Figure 4.26 and Figure 4.27, both components have many holes which are difficult to handle when using previously-developed multi-direction slicing algorithms from the literature.

In Figure 4.26, the boundaries of the component are generated as shown in Figure 4.26(b). Seven holes are detected (refer Figure 4.26d) and four of them are required to be deposited as supports, since the hole directions are not parallel to the build directions of their sub-volumes. Three large holes do not need to be deposited as supports and therefore the slicing procedure is applied. Figure 4.26c shows the slicing results, in which four build directions are used. Figure 4.26e shows the deposited holes (four small holes) which will need to be produced by post-process of milling.

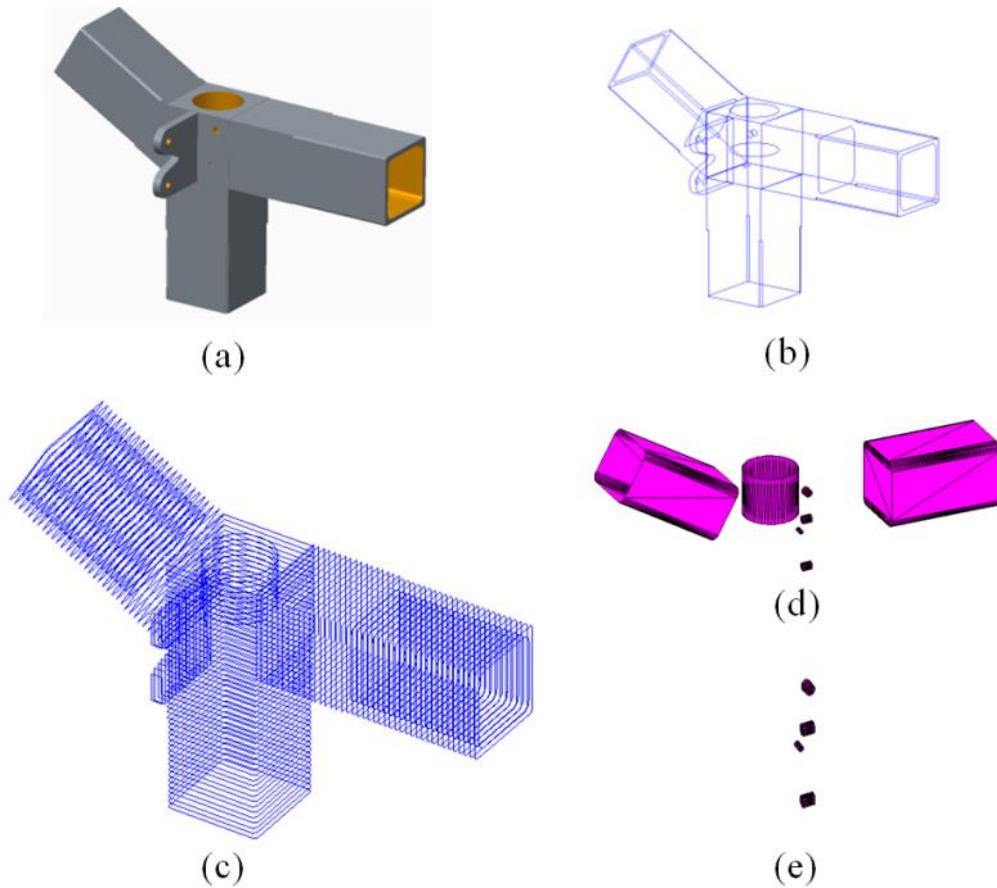


Figure 4.26 (a) Keel fitting component in aerospace industry; (b) generated boundaries of the model; (c) slicing results; (d) all the detected holes; and (4) holes need to be deposited as supports

Another example is shown in Figure 4.27. The slicing results are given in Figure 4.27b and all the holes are presented in Figure 4.27c. As discussed earlier, a sufficiently large hole with the direction parallel to the build direction of its sub-volume does not need to be deposited. The 12 small holes on the top of the surface in Figure 4.27a satisfy this requirement. However, if the hole is much smaller than the geometry of its sub-volume, depositing the hole would significantly reduce the complexity of the geometry of the layer. This simplification is desirable for subsequent path-planning. Further simplification of the slices could be obtained as shown in Figure 4.27d, in which it is more convenient to mill these small holes in post process rather than form them during the AM deposition process.

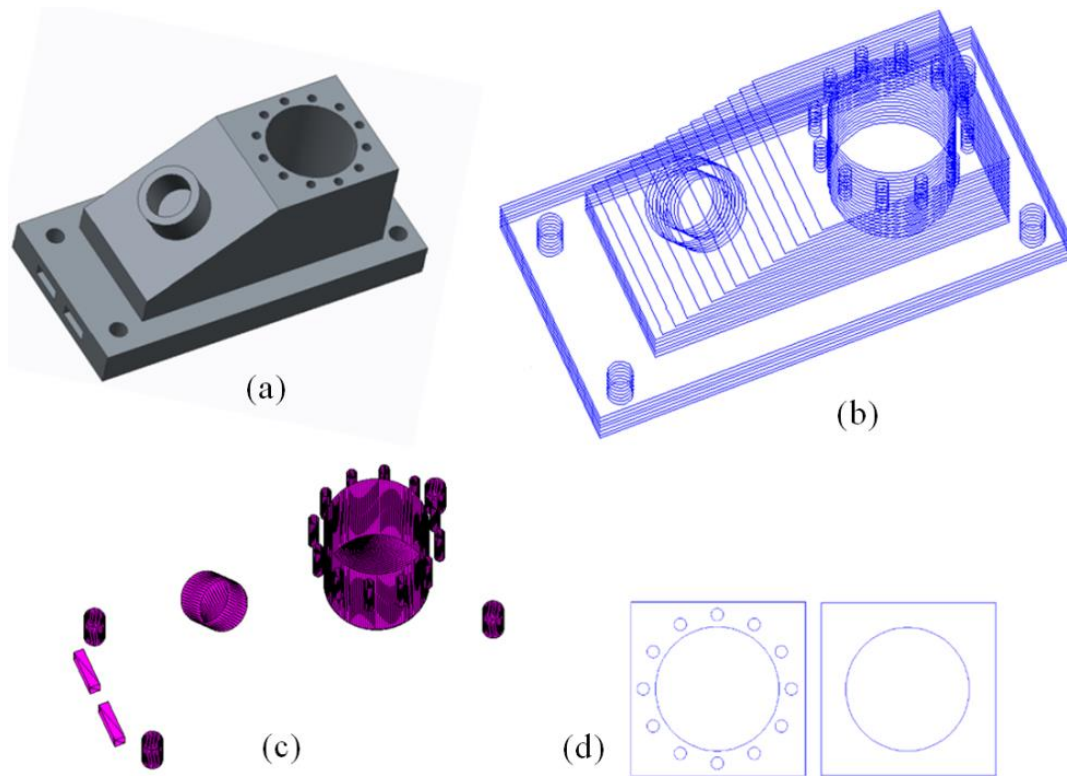


Figure 4.27 (a) An engineering part; (b) slicing results; (c) all the detected holes; (d) further simplification of slices

These implementations indicate that the proposed multi-direction slicing strategy is simple and efficient for AM. Special concerns on hole-features could significantly simplify the algorithms for volume decomposition. In addition, flexible choice on small holes would increase the efficiency of the multi-deposition system. These examples illustrate the enhanced capability of AM using multi-direction slicing. As the reader will note, both parts can indeed be fabricated by conventional (unidirectional) deposition. However, support structures will be required.

4.3 Summary

This chapter presented the widely reported tolerant slicing algorithm for uni-direction slicing and developed a new strategy for multi-direction slicing of CAD models represented in STL format for WAAM. The layer thickness could be variable while should within the ranges of the bead height established in chapter 3.

Differing from the previously devised methodologies in the literature, model simplification and the concept of decomposition-regrouping are introduced in the workflow. The algorithm is verified to be an efficient and flexible method for various types of CAD models in AM application. Since each step of the process maintains the integrity of STL

format (triangle mesh), then intermediate results from each of the modules (such as model simplification, volume decomposition, and holes-extraction) can produce standard STL files to be used at other downstream CAD/CAM applications that are not limited to AM.

It should be noted that in this study, only the closed concave loops are adopted to decompose the components. A complete decomposition module, which could process components with any complex geometry, collision problems, as well as issues related to the orientation of the components for multi-direction AM, will be our future research interest.

Chapter 5

2D Deposition Path Planning

One of the crucial requirements for an automated AM system is the development of an elaborate path planning strategy. Path planning for powder-based AM processes that have fine, statistically distributed particles are somewhat independent of geometric complexity. However, path planning for wire-feed AM processes that have coarse and large sized deposits is influenced by geometric complexity. Also, the property of the deposited shape will be influenced by the deposition path trajectory. In the following section, methods are described to generate different types of deposition paths.

5.1 Existing path planning methods

Many types of tool-path patterns have been developed for AM processes in general. Examples are raster, zigzag, contours, hybrid, and continuous path patterns. The raster scanning path technique, as shown in Figure 5.1, is based on planar ray casting along one direction. In this strategy, 2D regions are filled by a set of scan lines with finite width [92]. It is commonly employed in commercial AM systems due to its simple implementation and suitability for almost any arbitrary boundary.



Figure 5.1 Raster path pattern

Derived from the raster strategy, zigzag tool-path generation is the most popular method used in commercial AM systems. While it fills geometries line-by-line along one direction like the raster approach, the zigzag approach combines the separate parallel lines into a single continuous pass (see Figure 5.2) which significantly reduces the number of tool-path passes [93, 94]. This method significantly improves the productivity of the AM process by reducing the required transition motions of the machine. However, the outline accuracy of the part for

both raster and zigzag approaches is poor due to the discretization errors on any edge that is not parallel to the tool motion direction.



Figure 5.2 Zigzag path pattern

Contour path generation as shown in Figure 5.3, which is another typical method, can address the above geometrical quality issue effectively by following the geometrical trend of the boundary contours [95, 96]. Various contour-map patterns were investigated by Li et al. [97] to develop optimal tool-path patterns for sculptured parts with a single island and no seriously non-convex shape.

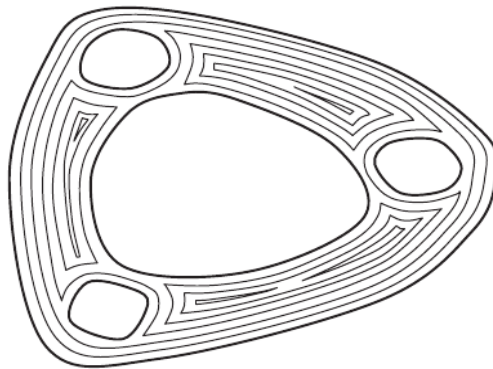


Figure 5.3 Contour path pattern

The spiral tool-path generation, as shown in Figure 5.4, has been widely applied in numerically controlled (NC) machining, especially for 2D pocket milling and uniform pocket cutting [98, 99]. This method can also be used to solve the problems of zigzag tool-paths in AM process, but is only suitable for certain special geometrical models.

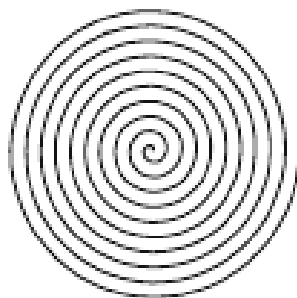


Figure 5.4 Contour path pattern

The hybrid path planning strategy is promising as it shares some merits of various approaches. A combination of contour and zigzag pattern is commonly developed to meet both the geometrical accuracy and build efficiency requirements. Zhang et al. [53] applied a new image algorithm for welding-based AM. The planned approach includes one inner zigzag path which is faster and more universal, and one outline vector path which is very helpful for maintaining the surface accuracy and quality. Jin et al. [100] proposed a mixed tool-path algorithm to generate contour and zigzag tool-path for AM of biomedical models, as shown in Figure 5.5. The zigzag tool-path is employed to fill the interior area of the part to improve the efficiency, while the contour tool-path is used to fabricate the area along the boundary of the contours to improve the geometrical quality of the model.



Figure 5.5 Hybrid path pattern

Continuous path planning can be considered as another tool-path generation method. Hilbert filling curve applied by Bertoldi et al. [101] is a continuous path, which can cover a region of space without intersecting itself as shown in Figure 5.6a. It has been found to be particularly useful in reducing shrinkage during AM fabrication processes. However, the large number of path direction turning motions that are produced by using this strategy are not suitable for WAAM. Wasser et al. [102] introduced a fractal-like build style using a simulated annealing algorithm. This method is able to generate filling patterns that allow the continuous deposition of a single path to fill arbitrarily shaped area, as shown in Figure 5.6b. In this method, the area to be deposited is firstly decomposed into nodes, with the number of the nodes determined by the accuracy requirement of the AM process. However, when the area to be filled is large and the accuracy requirement is high, the processing time required would be unacceptably long. Moreover, highly convoluted paths may result in accumulation of heat in certain regions, therefore inducing excessive distortion of the part. Frequent alternations of tool-path travel directions are also not preferred in WAAM. Dwivedi et al. [51] developed a continuous path planning approach which combines the merits of zigzag and continuous path patterns, as shown in Figure 5.6c. In this method, the 2D geometry is firstly decomposed into a set of monotone polygons. For each monotone polygon, a closed

zigzag curve is then generated. Finally, a set of closed zigzag curves are combined together into an integrated continuous torch path. The continuous path planning approach significantly reduces the number of welding passes. However, purely employing zigzag based curves would have a surface accuracy issue, as Zhang et al. [53] point out the importance of filling the outline of the image with vector motions in WAAM. Recently, we proposed another continuous path pattern which leverages the advantages of zigzag, contour, and continuous path patterns, as shown in Figure 5.6d [28]. It is indicated that this continuous path pattern is suitable for WAAM of solid structures. The algorithm for the continuous path generation is provided in Appendix A.

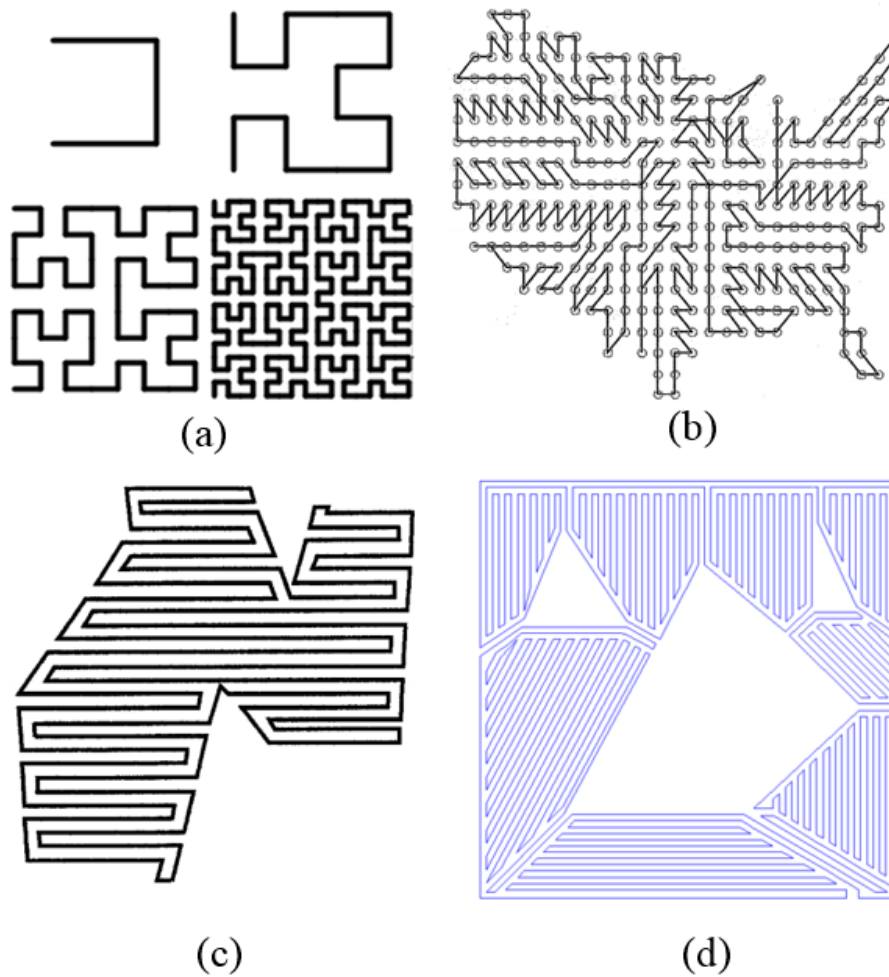


Figure 5.6 Continuous path pattern. (a) Hilbert filling curve; (b) Fractal-like build style; (c) Hybrid continuous path (zigzag & continuous); (d) Hybrid continuous path (zigzag & contour & continuous).

5.2 Path planning challenges in WAAM

For arc-welding-based additive manufacturing process, some of the requirements of path planning are:

Robustness: The deposition paths should be automatically generated irrespective of the complexity of the geometry.

Existing path planning methods were mainly developed for powder-based additive manufacturing process, in which the size of deposits is far less than the dimensions of the geometry. Path planning is independent of geometry in such powder-based additive manufacturing systems and the existing path patterns could be generated successfully for any complex geometries.

However, path planning in WAAM is dependent of part geometries due to the large size of the deposits. Therefore, existing path planning methods cannot be directly used for WAAM. An automatic path generation should take the following requirements into account.

Void-free deposition: All portions of the given geometry should be covered by the deposited material. Since gaps or voids would result in serious problems, void-free deposition is required for path planning.

Gaps or voids could occur due to the unappropriated path planning, especially for thin-walled structures, where the parts thickness is close to one deposit width. The example of a thin-walled structure is shown in Figure 5.7. Figure 5.7a illustrates the 3D CAD model and Figure 5.7b shows the sliced geometry. Applying a contour path planning algorithm to this example is likely to fail since the thin-walled areas would not allow sufficient width for a contour path to be applied. As shown in Figure 5.7d, after applying contour path planning with a step-over distance of 3 mm (a typical minimum value for the arc welding process), paths for the thin-walled areas are lost. Step-over distance is defined as the distance between a deposition track and the previous one. Typical step-over distance for powder-based AM ranges from 0.01 mm to 1mm, while for arc-welding-based AM ranges, from 3 mm to 8 mm depending on the chosen material and wire diameter.

Another example is shown in Figure 5.8, a cross-section of a simple thin-walled geometry is described by the boundary (Figure 5.8a). The contour paths (green lines shown in Figure 5.8b) are generated by offsetting the boundary towards its interior with the i^{th} contour path offset at distance $(i-(1/2)d)$ from the boundary, where d is the step-over distance. The deposition process can be considered as a constant-radius disk with the diameter of d being swept along the computed path. It is found that contour path patterns leave narrow gaps since

there is not enough space for offsetting the next path as the middle white area shown in Figure 5.8c. The area of the produced gaps is highly dependent on the step-over distance d , which varies for different AM system. For powder-based system, d could be generally small. The negative effects of gaps with small area on the quality of the produced components could be neglected for many applications. However, for WAAM, gaps resulting from poorly planned paths could be as large as 2 mm width, therefore poses a severe problem, especially for thin-walled structures. The unavoidable gaps may potentially lead to structural failure of highly loaded components.

Note that, the unsuccessful path planning for thin-walled structures in WAAM could also occur using other existing path planning method, such as zigzag, hybrid, and continuous path generation.

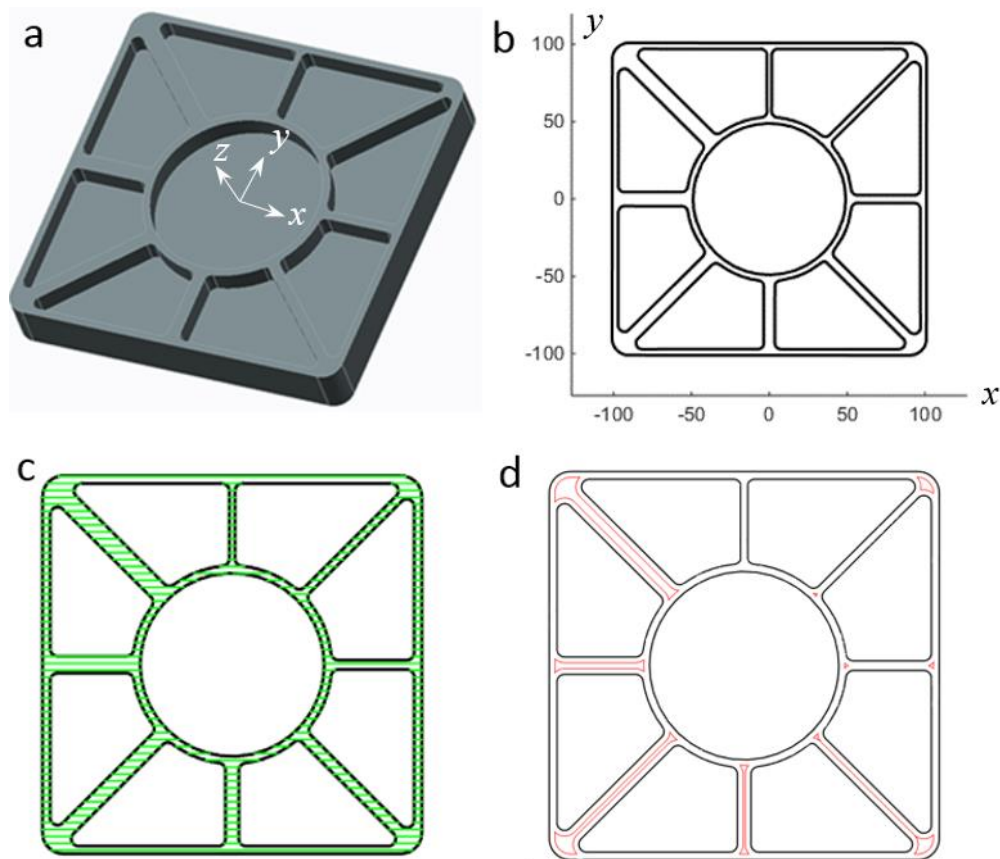


Figure 5.7 Illustration of automatic path planning. Green lines represent the generated paths, and black lines represent the boundary of the geometry. (a) CAD model. (b) A slice. (c) Raster paths (green). (d) Contour paths (red).

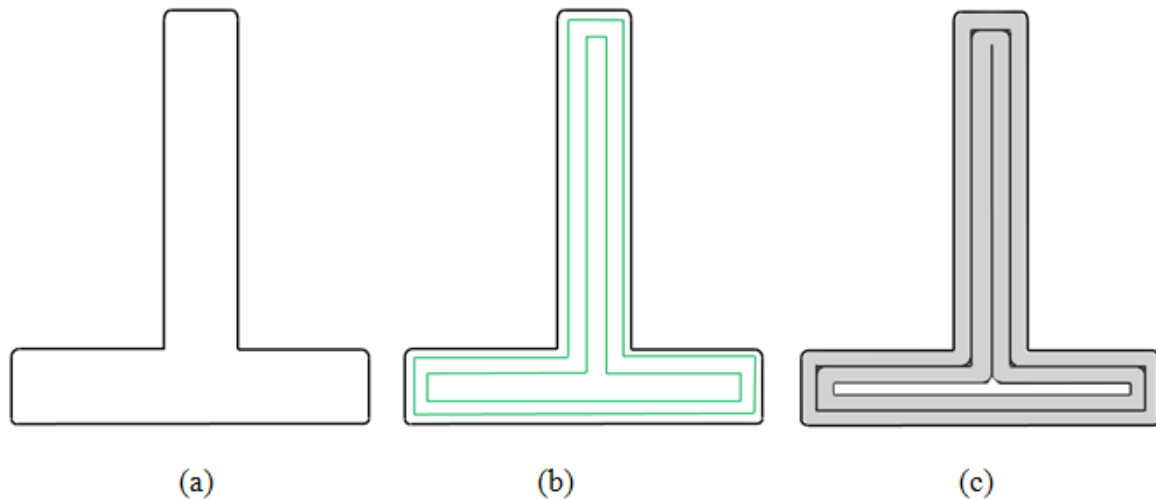


Figure 5.8 (a) A cross-section of a simple thin-walled structure. (b) Contour path patterns generated by offsetting the boundary curves towards its interior. (c) Deposition of materials along the generated path. Narrow gap (middle white area) is left which cannot be filled by the path.

Uneven bead profile: Weld bead profile distribution within weld paths is uneven, particularly in arc start and arc end portions. Weld bead profiles at various travel speeds are measured using the 3D laser scanner described in chapter 3. Figure 5.9 shows weld deposits heights along the welding distance at various welding speed. Since the wall height is mainly determined by the wire-feed rate, the wall heights for all conditions are relatively homogenous along the welding distance. However, in the arc start portion, the welding process requires a certain time to stabilise and during this time the deposited material does not correspond well to the steady-state bead behaviour. Excessive materials are deposited in arc start portion since part of the arc energy is used for heating up the substrate. While in arc end portion, the slope shape are created gradually due to the flowing of the molten metal.

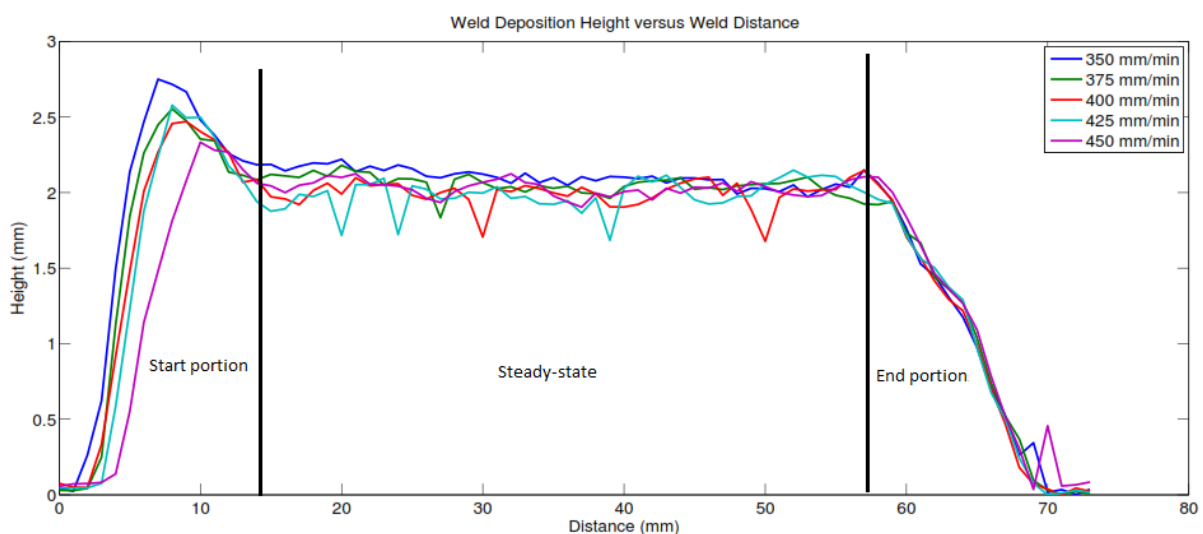


Figure 5.9 Weld deposits heights along the welding distance

Uneven weld bead profile may lead to the accumulation of errors in the vertical direction after the deposition of several layers. Figure 5.10 shows an example of thin walls built by weld deposition where there are significant differences in bead geometry at the start and end of the weld paths [57]. As can be seen, the errors introduced in lower layers are compounded as further layers are added. To overcome this issue of uneven surface induced by arc start and arc end procedures, the number of deposition passes should be minimized to reduce or eliminate the arc start/end effects. Raster path patterns are not suitable for some geometries, and continuous or contour path patterns are desired.



Figure 5.10 Thin walls built by weld deposition showing the changing bead geometry at the start and end of weld paths [57]

Crossings: Crossings in thin-walled structures make path planning more complex. Thin-walled structures are most commonly seen in aerospace components, which are attractive applications for AM due to their high buy-to-fly ratios. Crossings always exist in the case of these structures, as shown in Figure 5.11. Experiments reveal that directly crossing paths produce peaks where the weld beads overlap at the crossing points, as shown in Figure 5.11a. In addition, sharp angles in the intersections can concentrate stresses. The path pattern of opposite angle, as shown in Figure 5.11b, has been demonstrated to produce the best crossings with smooth radii in corners [103].

An alternative approach is shown in Figure 5.11c in the red circle [10]. The crossing is fabricated through one central deposition and two crossing branches. The two branches are always deposited tangentially to existing material, so no crossing occurs. Both strategies solve the issue of crossings, however, it is quite complex to design the program for the path planning algorithm so that it functions automatically and correctly for all situations.

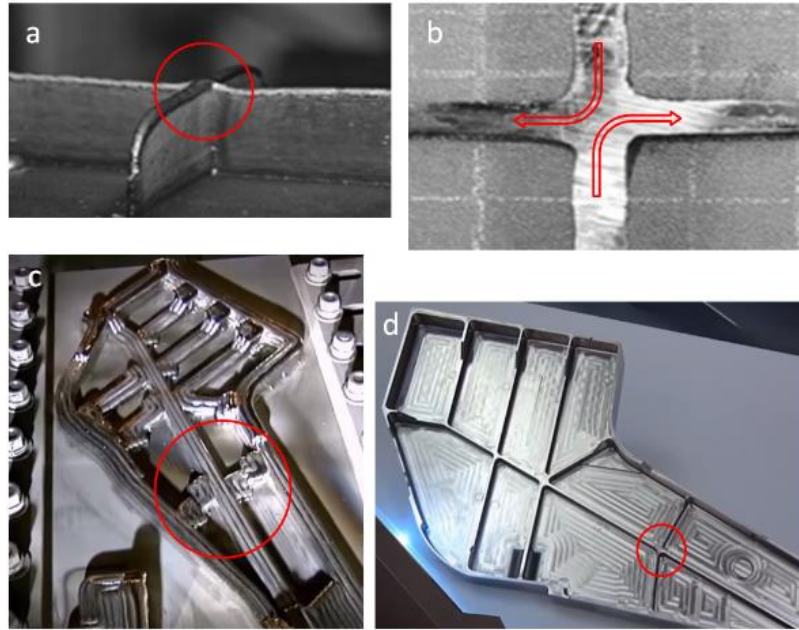


Figure 5.11 Concerns of crossings in thin-walled structures. (a) Direct crossing induces peaks. (b) Path pattern of opposite angles [103]. (c) One direct and two crossing method [10]. (d) Finished part

As the limitations of the arc welding deposition process mentioned above, the performance of the existing popular path planning is discussed and summarized in Table 5.1.

Table 5.1 The performance of the existing popular path planning for WAAM

Requirements	Raster path	Zigzag path	Contour path	Continuous path
Robustness	+	+	+	+
Void-free deposition	+	-	-	-
Uneven bead profile	-	-	+	+
Crossings	-	-	+	-

“+” represents good performance; “-” represents bad performance.

It is found that none of the existing paths are suitable for WAAM especially for thin-walled structures. Among these paths, contour path is most preferable while it cannot guarantee fully cover of the region. Therefore, a special path planning strategy which fulfils all the requirements in WAAM is required. To automatically generate appropriate paths, the challenge is to develop an adaptable strategy that can cater for variable geometry and use the information to produce paths that are appropriate to the limitations of the arc welding deposition process.

5.3 MAT-based path planning

5.3.1 Overview of MAT-based path

Kao [104] has proposed an alternative methodology of using the Medial Axis Transformation (MAT) of the geometry to generate the offset curves by starting at the inside and working towards the outside, instead of starting from the boundary and filling towards the inside. This approach is able to compute paths which can entirely fill the interior region of geometry as the paths are generated from interior to the boundary. This strategy avoids producing gaps by depositing excess material outside the boundary, as illustrated in Figure 5.12. The extra material can subsequently be removed by post-processing. Therefore, the traditional contour path patterns from outside to inside is natural for machining whereas MAT-based path starting from inside and working towards the outside is suitable for WAAM of void-free components.

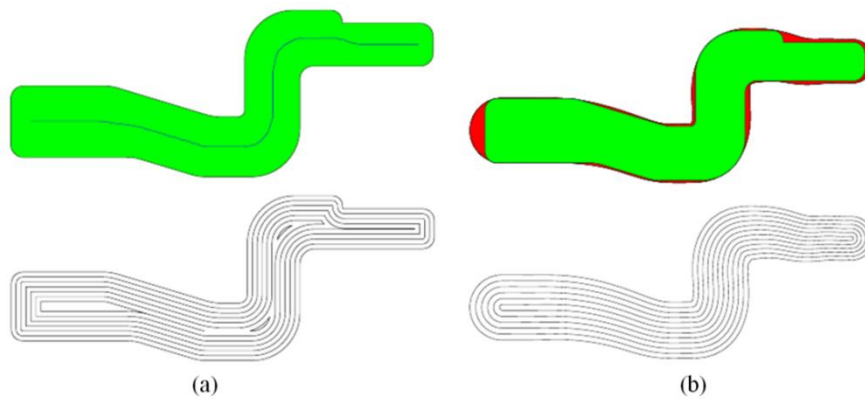


Figure 5.12 Illustration of path generated from MAT. (a) up: original geometry (green region) and the MAT of the geometry (black line); down: contour path patterns with gaps in middle are clearly seen; (b) up: red region are deposition of excessive materials; down: the MAT path patterns without gaps [104].

However, the previous authors limit their discussion to geometries with simple MAT paths, and the MAT-based path for general geometries or arbitrary shapes, to our knowledge, is still unavailable.

This study developed a methodology of generating MAT-based paths for an arbitrary geometry, either thin-walled or solid structures. Medial axis transformation (MAT) –based path planning is able to generate a set of closed loop paths which cover entirely the sliced layers. The detailed path planning methodology will be reported in the following section. Here, the path planning strategy is described through an example and its capability of fulfilling the requirements for an arc-welding-based system is explained.

There are the main steps for generating MAT-based paths:

Compute the medial axis: The cross-section of a sliced layer with a thin-walled structure is shown in Figure 5.13a. The medial axis or skeleton of the geometry is computed and

represented using red lines. The computed skeleton is the crucial information, which describes the shape of the geometry.

Decompose the geometry: Using the computed medial axis, the geometry is decomposed into several domains. As the geometry with N holes will be decomposed into $N+1$ domains, this geometry is decomposed into 10 domains as shown in Figure 5.13b. As displayed in different colours, each domain is bounded by a portion of medial axis (red lines in Figure 5.13a) and a boundary loop (black line loop in Figure 5.13a).

Generate path for the domain: Deposition paths for each domain are generated by offsetting the medial axis loop (red line loop in Figure 5.13c for domain 3) towards the corresponding boundary loop (black line loop in Figure 5.13c) with an appropriate step-over distance. The offsetting is repeated and terminates when the domain is fully covered. Green line loops in Figure 5.13c, represent the generated deposition paths.

Complete the deposition paths: A complete set of MAT-based deposition paths is obtained by repeating step 3) for all the decomposed domains. The generated paths are a set of closed loop lines without start/stop sequences, which is preferred for the arc welding system.

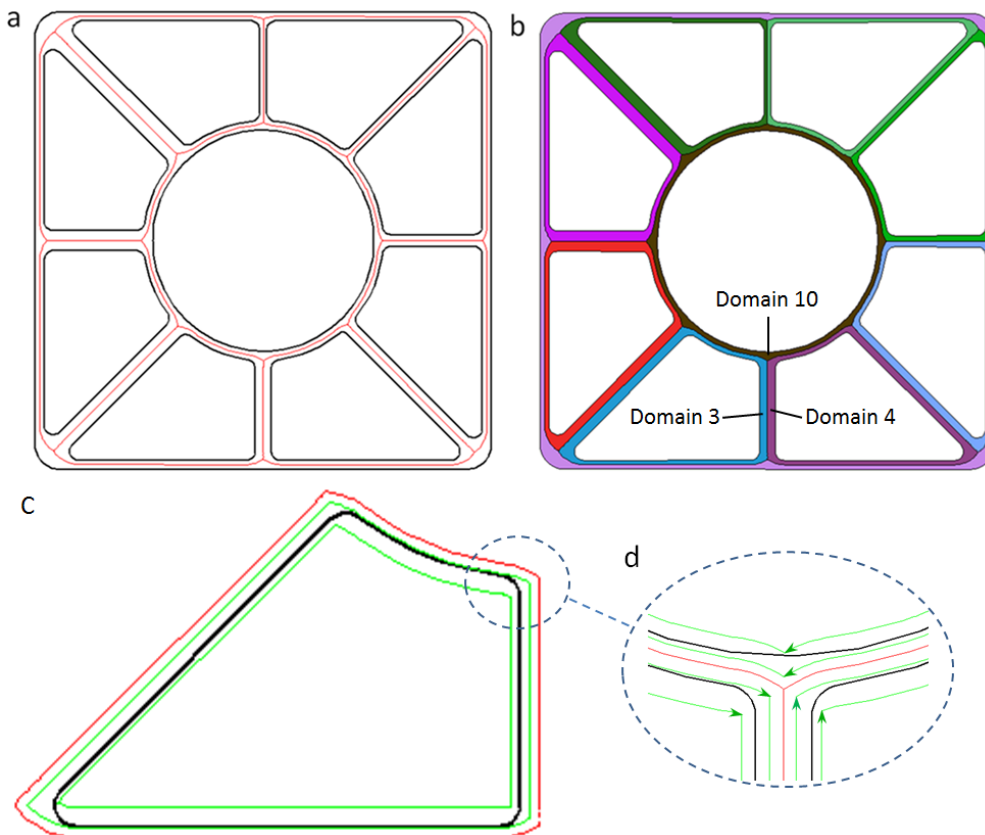


Figure 5.13 Illustration of MAT-based path planning. (a) The medial axis computing (red lines). (b) Domain decomposition (each domain is described in one different colour). (c) Path generation for domain 3. (d) MAT-based paths at the crossing area.

From the above description, the MAT-based path planning algorithm for an arc welding process is able to be automated for any complex geometry; just as the existing commercially available raster and contour path planning strategies have been automatically applied to powder-based AM. In addition, the process to form crossings is shown in Figure 5.13d, where no direct crossings occur. The issue of crossings is inherently solved using MAT-based path planning since it produces crossings in a manner similar to opposite angle deposition [103].

5.3.2 Definition and computation of the MAT

A. Definition

The Medial Axis Transformation (MAT) is a technique first proposed by Blum [105] to better describe geometrical features. The medial axis is defined as loci of centres of locally maximal spheres inside a 3D geometry. For a 2D polygon, the medial axis is the loci of centres of locally largest circles inside the polygon, as the dash lines shown in Figure 5.14a [104]. The points on the medial axis are called medial axis points. Depending on how many points of the largest circle that touches the boundary of the polygon, the medial axis points are further classified into end points, branch points, and normal points.

Definition 1:

- *End points are points on the medial axis that touch the boundary at only one point. End points must be the convex vertices of the polygon.*
- *Branch points are points on the medial axis that are centres of circles that touch the boundary at more than two points.*
- *Normal points are points on the medial axis that that are centres of circles that touch the boundary at only two points.*

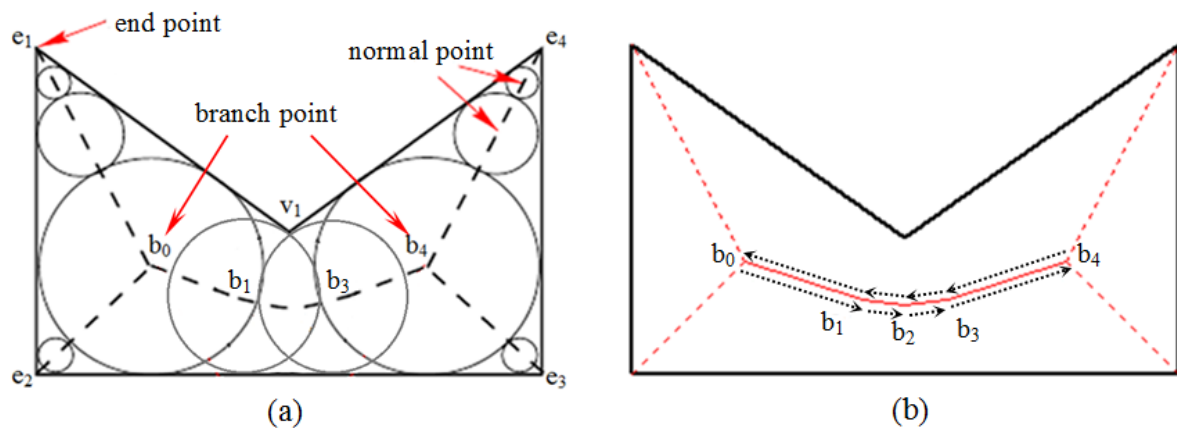


Figure 5.14 (a) Medial axis transformation (MAT) of a geometry. The dash lines represent the medial axis. (b) Red lines represent branches and red dash lines represent sub-branches.

As shown in Figure 5.14a, four end points (e_1 , e_2 , e_3 , and e_4) and four branch points (b_0 , b_1 , b_3 , and b_4) are marked, and a large number of normal points are located on the medial axis either between a branch point and an end point or between two branch points.

The medial axis or skeleton of a polygon consists of either line segments or parabolas, as the medial axis points must have the same distance to two points or one point and one line. The skeleton of the polygon in Figure 5.14a is represented by six line segments (b_0e_1 , b_0e_2 , b_0b_1 , b_4e_3 , b_4e_4 , and b_4b_3) and one parabola (b_1b_3). Associated with the medial axis is a radius function, which defines for each point on the axis its distance to the boundary of the polygon. The medial axis and the radius function together are important topological information for a given geometry. Refer to [106] for a more detailed description of MAT.

B. Computation

Medial Axis Transformation, or skeletonization, has been widely studied over the past few decades in the computer vision field. Lee [106] proposed a divide-and-conquer approach that constructs the generalized Voronoi diagram for simple polygons. The medial axis transformation can be easily extracted by removing the Voronoi edges connecting to concave vertices of the polygon. Srinivasan et al. [107] extends Lee's algorithm to computing a generalized Voronoi diagram for polygons with holes. Choi [108] presents an MAT approximation algorithm in the planar domain via domain decomposition. Kao [109] proposes a method that directly associates boundary points to the corresponding proximity metrics based on Lee's and Srinivisan's methodology.

Based on Lee's and Kao's approach, a simple MAT method is developed through computing the bisector of each pair of segments. As shown in Figure 5.15, the geometry is represented by line segments ab , bc , cd , de , and ea . For line segment ab , there are four pairs, and the bisectors of each pairs, $B(ab, bc)$, $B(ab, cd)$, $B(ab, de)$, $B(ab, ea)$, are computed. Each bisector of two closed line segments (a pair) is formed by straight lines and parabolic curves as shown in Figure 5.15a. By definition, the MAT produces a set of lines which divide the geometry into several sub-regions. In each sub-region, all the points are closet to its associated boundary. Therefore, the medial axis is constructed by using the bisectors which are closest to the relevant boundary, as the bold red line shown in Figure 5.15b. The detailed computing algorithms refer to [106-109].

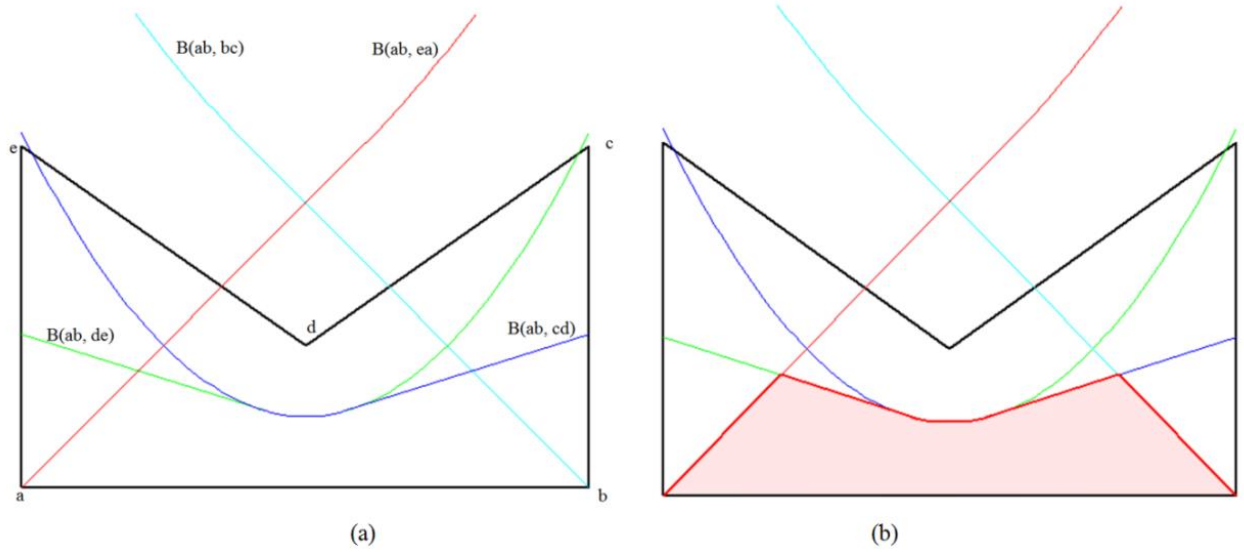


Figure 5.15 Computation of the bisector lines for pairs of line segments. Black lines represent the boundary of the geometry. Coloured lines represent the bisector lines. Bold red line in (b) represents the MAT corresponding to the boundary ab. Pink area is the region in which all points are closest to its associated boundary ab.

5.3.3 MAT-based path generation

The overview of the developed algorithms is described as shown in Figure 5.16. The flowchart of the algorithms consists of two phases: *Phase 1*, preparing the MAT of the geometry; and *Phase 2*, generating the path from the medial axis. Algorithms for phase 1 (from CAD model to MAT) are not detailed in this section, since slicing algorithm has already introduced in chapter 4 and algorithms for medial axis transformation can be found in the literature [106-109]. The detailed algorithms for Phase 2 are presented in this section.

A. Generation of branch vectors

The skeleton of the geometry identified in the previous step can be classified into branches and sub-branches. Branch vectors can be generated from the obtained branches. These branch vectors are extracted to form branch loops, which are used for offsetting welding paths at a later stage in the algorithm.

Definition 2:

- *Branches are line segments of the skeleton between two branch points.*
- *Sub-branches are line segments of the skeleton between one branch point and one end point.*
- *Branch vectors are two vectors with opposite directions that are generated from each branch.*

- A branch loop is a closed loop formed by a set of branch vectors, with the set having a head-to-end connection.

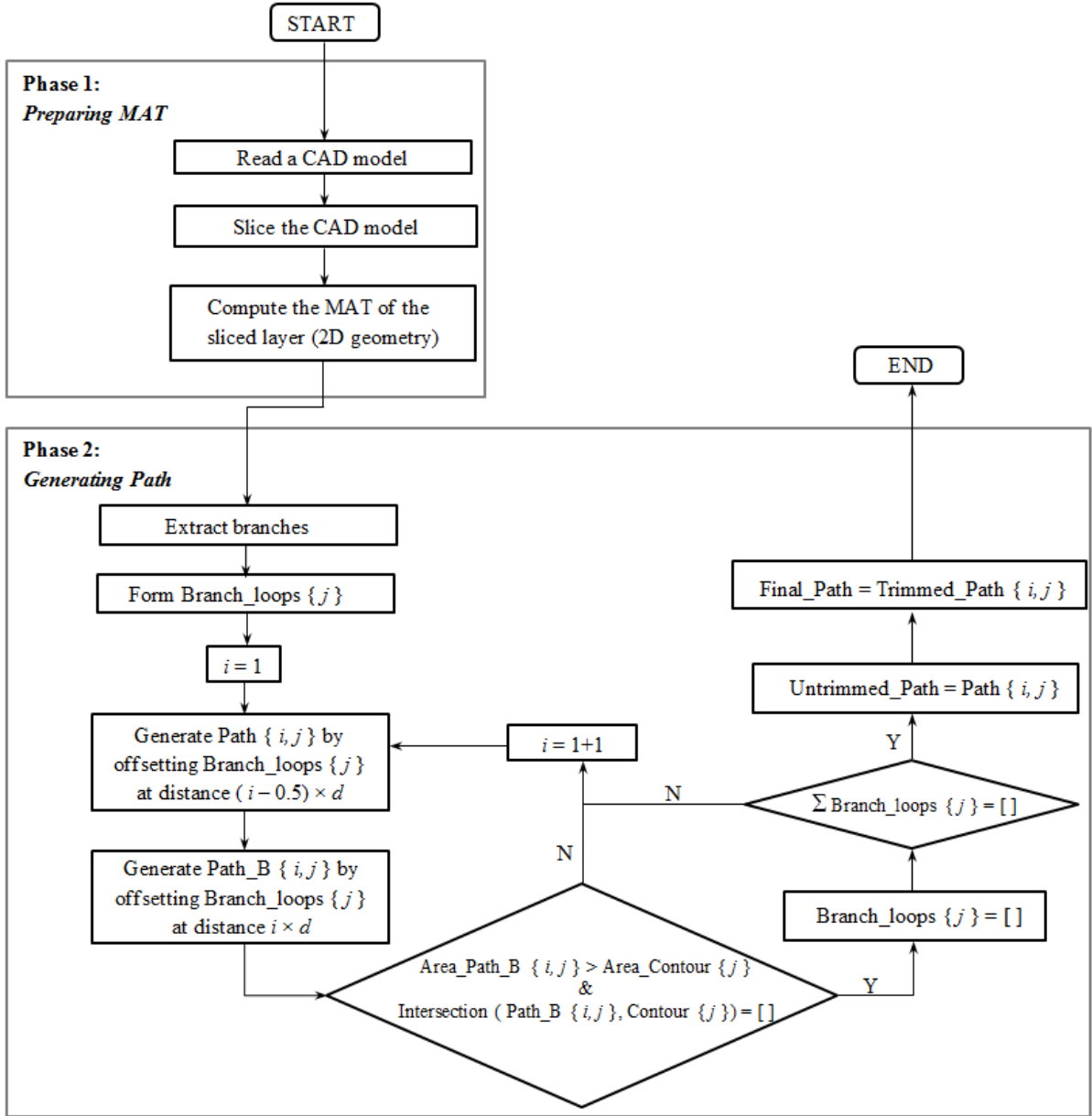


Figure 5.16 Flowchart of the developed approach for generating path from MAT

In this study, any existing parabolic section within the skeleton is simplified into two line segments. This simplifies subsequent steps in the algorithm without producing excessive positional errors for the skeleton. For example, in Figure 5.14b, the parabola (b_1b_3) is simplified as two line segments (b_1b_2) and (b_2b_3), where b_2 is the middle point of parabola b_1b_3 . Therefore, four branches (as solid red lines b_0b_1 , b_1b_2 , b_2b_3 , and b_3b_4 shown in Figure 5.14b) and four sub-branches (as dashed red lines shown in Figure 5.14b) can be obtained. Accordingly, eight branch vectors ($\overrightarrow{b_0b_1}$, $\overrightarrow{b_1b_0}$, $\overrightarrow{b_1b_2}$, $\overrightarrow{b_2b_1}$, $\overrightarrow{b_2b_3}$, $\overrightarrow{b_3b_2}$, $\overrightarrow{b_3b_4}$, and $\overrightarrow{b_4b_3}$) are generated (shown as black vectors in Figure 5.14b).

B. Branch loop formation

For a simple polygon (without holes or other internal features), a single branch loop will be formed. Starting from any branch vector, the connected branch vector is added into the branch loop one by one with a counter-clockwise order. The branch loop is completed when all the branch vectors have been included.

Figure 5.17 shows the skeleton of a simple polygon, the computed branch points (a, b, c, d, e, and f), branches, and branch vectors. If the branch loop starts from the branch vector, \vec{ab} , four branch vectors (\vec{bd} , \vec{bc} , \vec{be} , and \vec{ba}) are found as the connected branch vector. Among them, \vec{bd} is the vector that forms a branch loop in the counter-clockwise direction. The completed branch loop is (abdbegfebcba) following the branch vectors. For the geometry in Figure 5.14b, the resulted branch loop is (b₀b₁b₂b₃b₄b₃b₂b₁b₀).

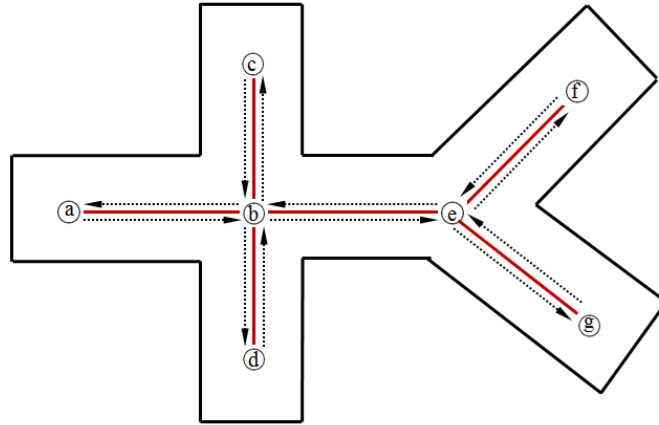


Figure 5.17 Illustration of the general skeleton and branch loop formation for a simple polygon without holes

For complex geometries with N holes, there will be $N+1$ boundary loops, with one external contour and N internal contours, one for each hole. During the branch loop formation step, a closed branch loop is firstly formed as well, but not all the branch vectors are included as would be the case for a simple geometry. Accordingly, more new branch loops will be formed by the remaining branch vectors and branch loop formation will be completed when all branch vectors are included. Consequently there will be $N+1$ branch loops formed, with one loop formed in the contour-clockwise direction corresponding to the single external contour of the geometry and N loops formed in the clockwise direction corresponding to the N internal contours.

Figure 5.18 shows the geometry with two holes. Black lines represent the three boundary loops, and red lines represent the calculated skeleton of the geometry. Through the steps of branch vectors generation and branch loop formation for complex geometries, $N+1$ branch loops are formed with one closed loop in the counter-clockwise direction (for the external boundary loop) and N closed loop (for the holes) in clockwise direction as the red loops with arrows shown in Figure 5.18.

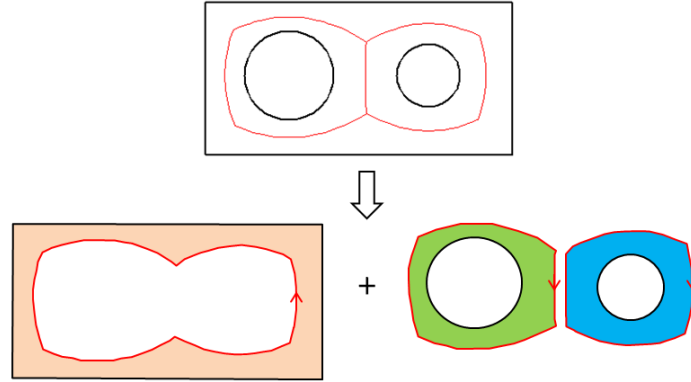


Figure 5.18 Branch loop formation for complex geometries with holes. Black lines represent the boundary of the geometry. Red line loops with arrows represent the formed branch loops.

C. Domain

For a simple polygon without holes, there is only one boundary loop and one branch loop. The whole region can be considered as a single domain enveloped by the boundary loop and the branch loop.

For a complex geometry with N holes, there will be $N+1$ domains that compose the whole area of the geometry. The first domain is enveloped by the branch loop in the counter-clockwise direction and its associated external boundary loop. The other N domains are enveloped by the remaining branch loops in a clockwise direction and their associated internal boundary loops. As shown in Figure 5.18, three domains are formed and displayed in different colours.

D. Path generation

Paths are generated by recursively offsetting contour-clockwise branch outward and clockwise branches inward at distance $(i - \frac{1}{2})d$. i represents i^{th} offset, and d represents the step-over distance. It should be noted that during the offsetting self-intersection may happen regardless of whether it is inward or outward offset. Algorithm for solving self-intersection is not detailed in this paper since they have been reported elsewhere in the literature [96]. As

shown in Figure 5.16, $Path_{ij}$ represents the i^{th} offset of the Branch_loops j . $Path_B_{ij}$ represents the path outside boundary of the i^{th} path. When the area of the i^{th} path boundary j is larger than its relevant contour j , and there is no intersection between the boundary and the contour, the Branch_loops j will be updated to empty. Meanwhile the offsetting of this branch loop will be ceased since the region relevant to this branch loop is fully filled by deposition material. The iterative procedure ends when all the branch loops are updated to be empty and there is no more offset needed.

The output is a set of untrimmed paths, and the structures of the untrimmed paths for the geometry in Figure 5.19 are shown in Figure 5.20 using Matlab cell structures. There are three branch loops corresponding to three columns in Fig. 10, and the iterative procedure ceases at the 6th offset. The generated untrimmed paths for the geometry in Figure 5.14 are shown in Figure 5.21 (a). The whole procedure ceases after the 5th offset as the area of the 5th path boundary (the outside blue lines) is larger than the area of the geometry and there is no intersection between them. It can be seen from Figure 5.21 (a) that the geometry is fully filled but there is an obvious excess of deposited material. To improve the material efficiency, the last step is to trim the paths. The parts of blue lines outside of the geometry represent extra materials and the associated paths are trimmed as shown in Figure 5.21 (b).

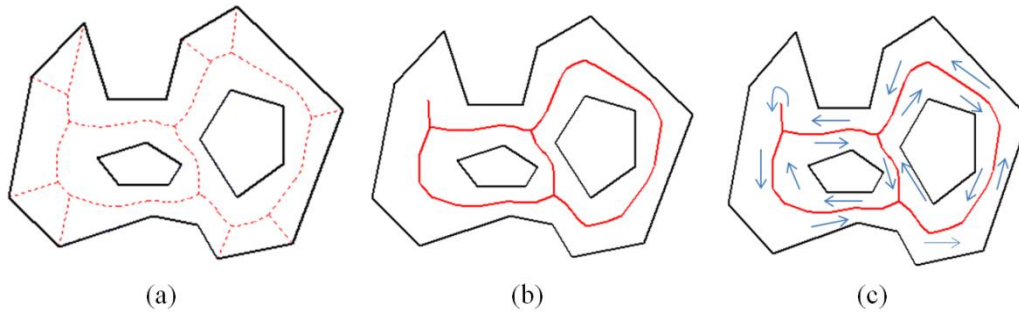


Figure 5.19 Example of the shape with two holes. (a) Computed MAT as represented by dotted lines; (b) Multiple branches as described by red lines; and (c) Formed one branch loop along counter-clockwise direction and other two branch loops inside along clockwise.

UntrimmedPath: 5x3 cell =		
[50x9 double]	[26x9 double]	[32x9 double]
[44x9 double]	[25x9 double]	[26x9 double]
[36x9 double]	[13x9 double]	[16x9 double]
[33x9 double]		[]
[30x9 double]	[]	[]

Figure 5.20 The cell structures of untrimmed paths in the program

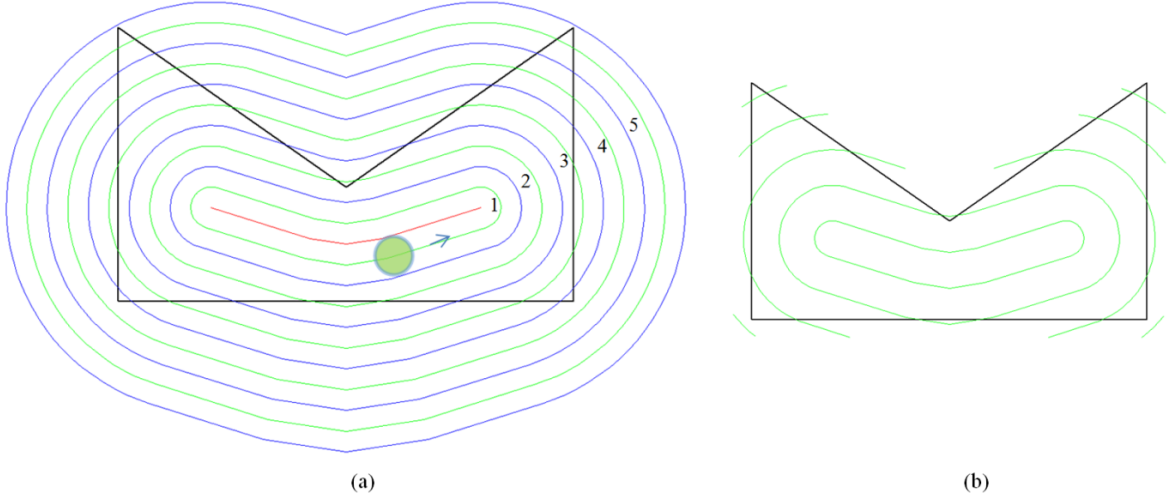


Figure 5.21 (a) Untrimmed paths for the simple shape. Black lines represent the boundary of the given geometry. Red lines represent the MAT. Green lines stand for the generated untrimmed paths, and blue lines represent the outside of each untrimmed path. (b) Trimmed paths.

The generated adaptive paths are a set of closed loop line segments. The generated adaptive MAT paths and the associated step-over distances are stored in the format of

$$Path_i^j(P_k^s, P_k^e, L_k, d_k^s, d_k^e),$$

where $Path_i^j$ represents the i^{th} closed curve from the j^{th} domain. j has value from 1 to $N+1$ for a geometry with N holes. P_k^s, P_k^e , and L_k represent the coordinate of the start point, the coordinate of the end point, and the length of the k^{th} path line segment of $Path_i^j$, respectively. d_k^s and d_k^e represent the step-over distance at the start and the end point of the k^{th} line segments of $Path_i^j$, respectively.

E. Implementation

Five geometries sliced from CAD models are tested to validate the effectiveness and robustness of the developed algorithms. As shown in Figure 5.22-5.26, various types of geometries are tested including solid structures with or without holes, and thin-walled structures. Table 5.2 provides basic information of the geometries. The MATs and the trimmed paths for all geometries are successfully generated using the developed algorithms.

Table 5.2 Basic information for five case study geometries.

No. Geometry	1	2	3	4	5
Area of enveloped box ($\times 10^4 \text{ mm}^2$)	28.64	31.06	12.74	17.52	4.84
Area of geometry ($\times 10^4 \text{ mm}^2$)	9.25	17.06	1.29	2.78	1.44
Volume ratio (%)	32.3	54.9	10.1	15.9	29.8

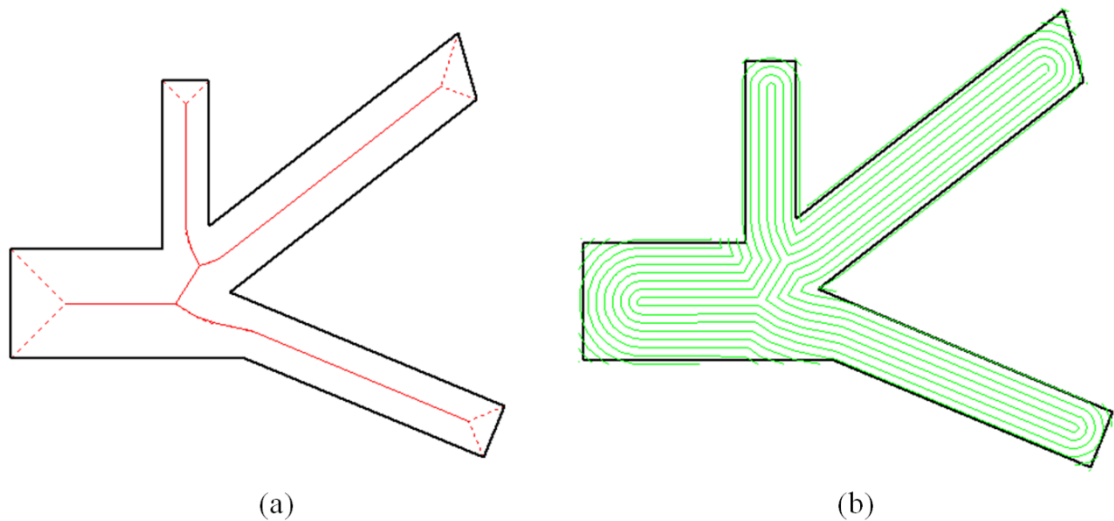


Figure 5.22 Geometry 1, solid structure with multiple branches. (a) Geometry is represented by black lines, MAT represented by dotted red lines, and red solid lines stand for branches. (b) Generated trimmed path.

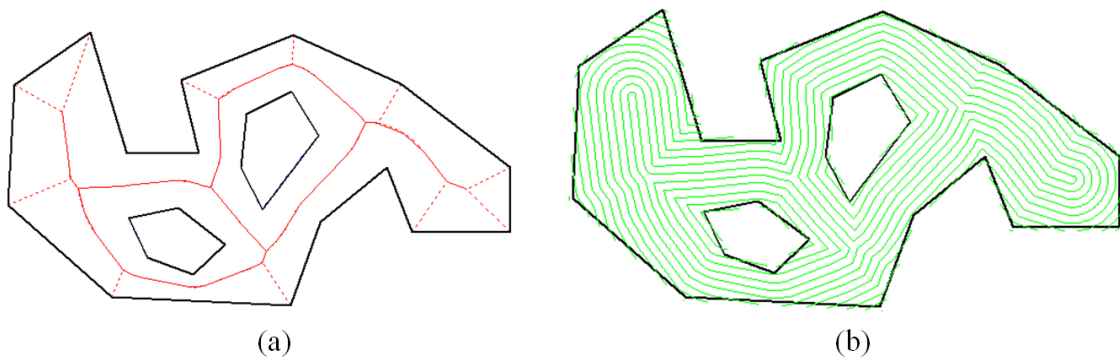


Figure 5.23 Geometry 2, solid structure with holes. (a) Geometry is represented by black lines, MAT represented by dotted red lines, and red solid lines stand for branches. (b) Generated trimmed path.

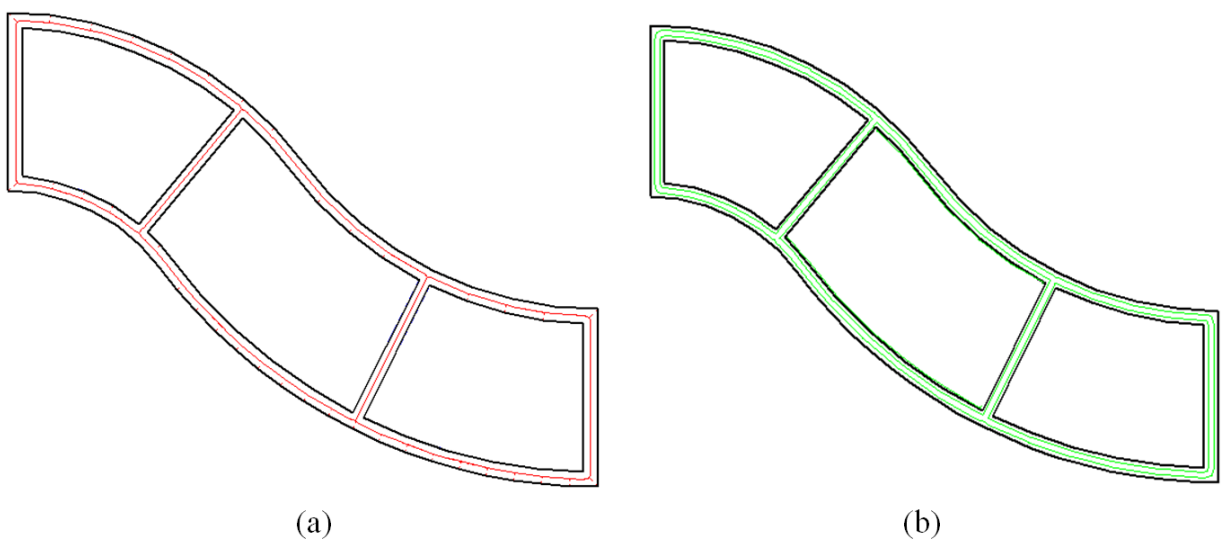


Figure 5.24 Geometry 3, thin-walled curved structure. (a) Geometry is represented by black lines, MAT represented by dotted red lines, and red solid lines stand for branches. (b) Generated trimmed path.

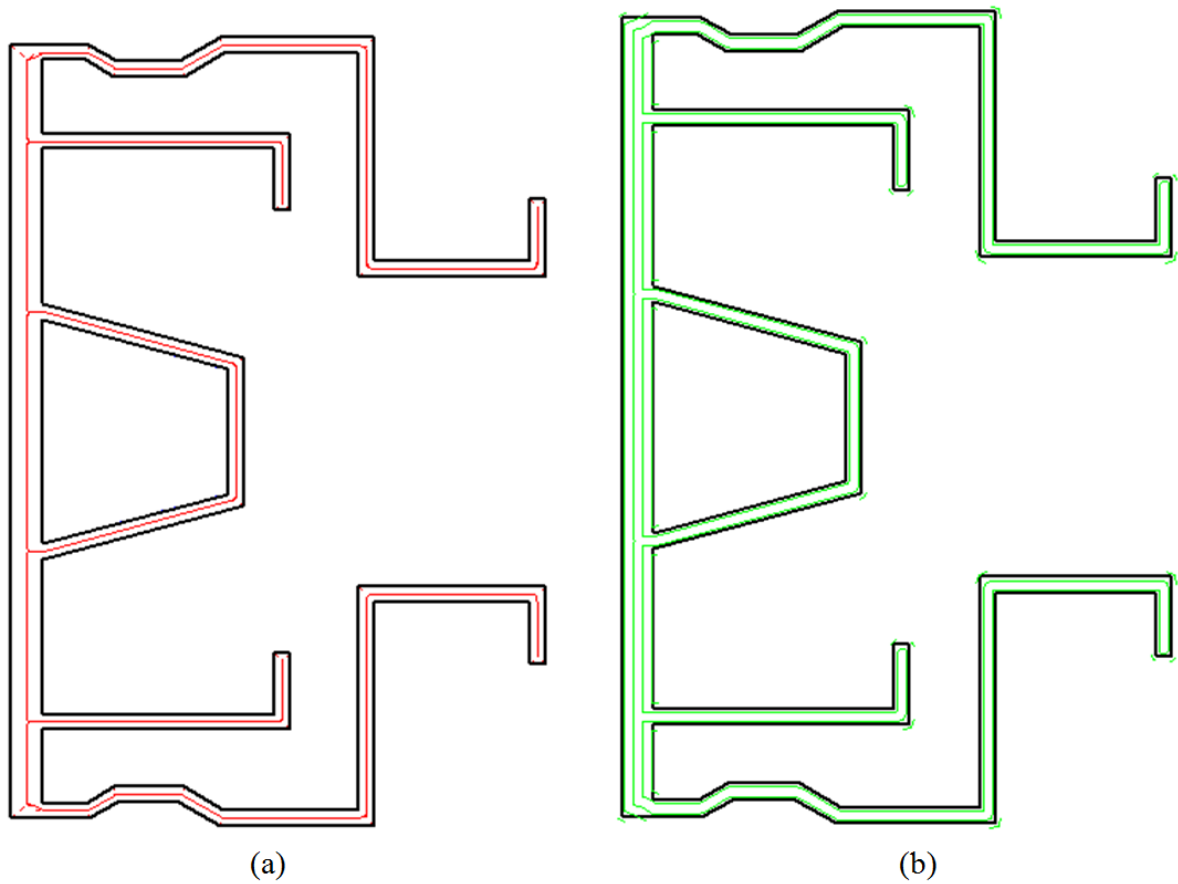


Figure 5.25 Geometry 4, thin-walled complex structure. (a) Geometry is represented by black lines, MAT represented by dotted red lines, and red solid lines stand for branches. (b) Generated trimmed path.

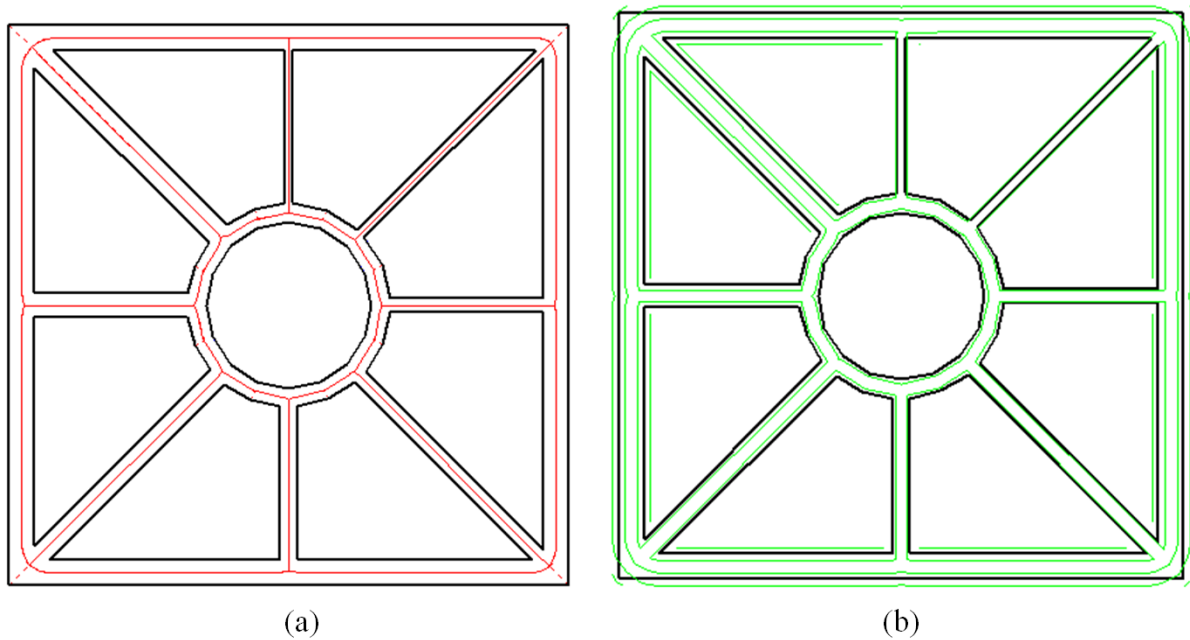


Figure 5.26 Geometry 5, thin-walled structure with varied characteristic thicknesses. (a) Geometry is represented by black lines, MAT represented by dotted red lines, and red solid lines stand for branches. (b) Generated trimmed path.

5.3.4 Discussions

Using the MAT-based path generated in this study, the gaps that would be generated by using traditional contour path patterns are removed. And other requirements for WAAM are also fulfilled. However, this has been achieved at the cost of creating some discontinuity of the path and extra deposition at the boundary. Post-processing, such as milling or grinding, is required to remove excess materials and improve the accuracy of the fabricated components. Material efficiency, which defined as the ratio of the real area of the geometry to the deposited area, is an important factor for the AM process. Material efficiency, E , is expressed as: $E = A_r/A_d = A/(Ld)$. A_r represents the real area of the geometry; A_d represents the deposited material which is calculated by times of the total path length L and the step-over distance d .

The material efficiency of AM, based on the proposed MAT-based path at various step-over distances, is simulated for the different geometries as shown in Figure 5.27. Material efficiency of the traditional CNC machining is also provided as a comparison. It is found that, in general, material efficiency decreases with the increasing of step-over distance. This is intuitive as step-over distance represents the resolution of the deposition system. To fill geometry with deposition material, the greater the step-over distance, the more excess material will need to be deposited. The results also show that AM technology has a much higher material efficiency compared to traditional subtractive manufacturing.

The effects of the step-over distance on part building time are also discussed. The building time t is determined by the sum of the total path length L and the travel speed, V , of the deposition head. If the build time at the step-over distance of 1 mm, t_1 , is set to be the characteristic time, the non-dimensional building time T at the step-over distance of d is expressed as $T = \frac{t_d}{t_1} = \frac{L_d/V}{L_1/V} = \frac{L_d}{L_1}$. Where, L_d represents the total path length at the step-over distance of d ; and the travel speed V is assumed to be the same at various step-over distances. The non-dimensional building time as the function of step-over distances are calculated as shown in Figure 5.27. With the increasing of the step-over distance, the build time T declines exponentially. It reveals that it is always better to have a small step-over distance for high material efficiency whereas that would be at the expense of productivity.

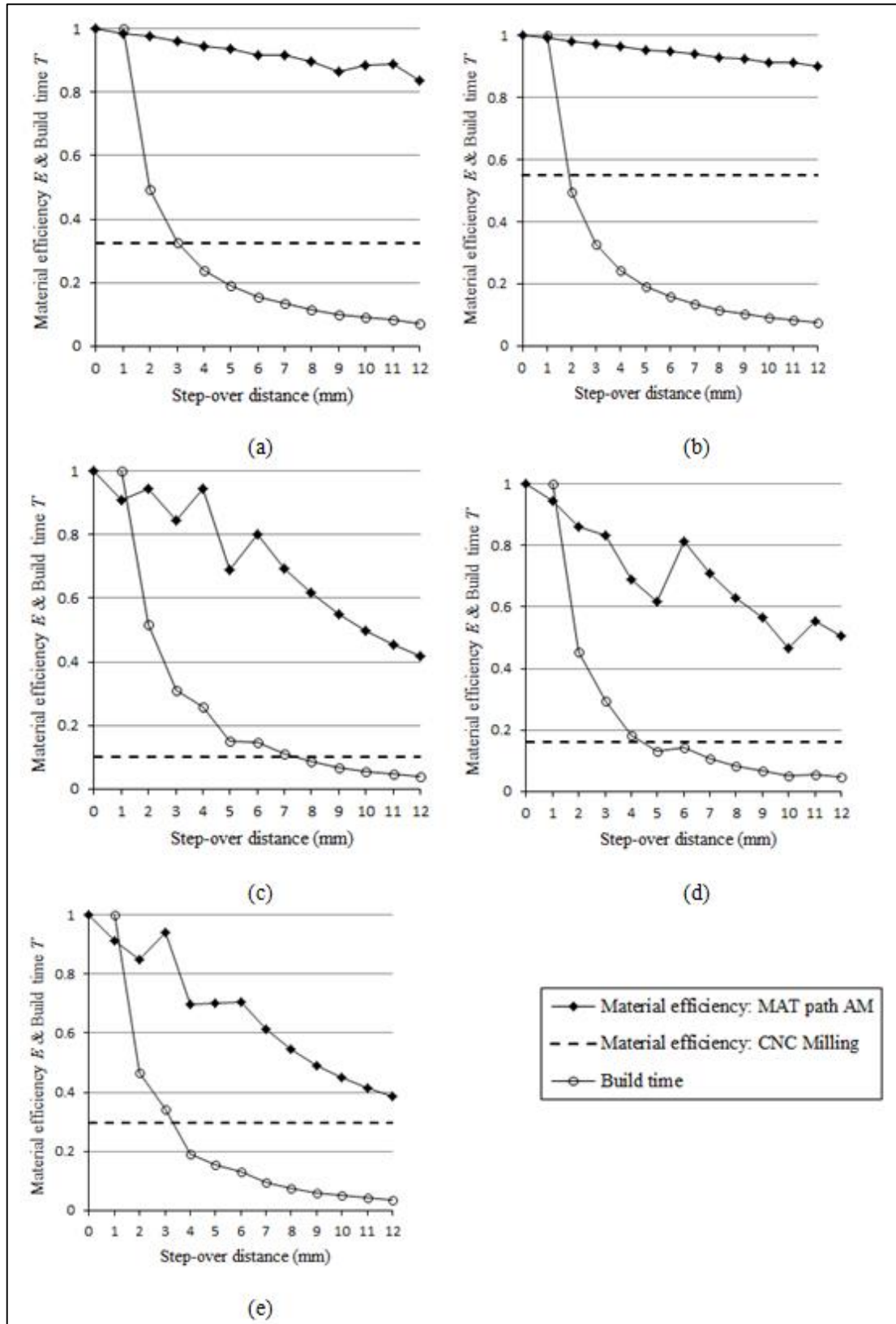


Figure 5.27 Material efficiency & non-dimensional build time vs. step-over distance. (a) Geometry 1. (b) Geometry 2. (c) Geometry 3. (d) Geometry 4. (e) Geometry 5.

For powder-based AM system, the step-over distance generally ranges from 0.01mm to 2 mm. Material efficiency in this range decreases only slightly, indicating that the step-over

distance does not have a significant effect on the material efficiency of powder-based AM. As inferred above, material efficiency is determined by the resolution of the deposition system in relation to the size of the geometry. Building time changes significantly in this range, therefore, build rate will be an important factor for powder-based AM system.

On the other hand, for WAAM technology, the typical step-over distance varies from 2 mm to 12 mm for mild steel materials. Building time in this range as shown in Figure 5.27 doesn't change significantly and therefore build rate for WAAM is not the major concern. Material efficiency in WAAM using the proposed MAT-based paths is shown in Figure 5.28. It is found that for solid structures (Geometry 1 and Geometry 2) material efficiency is relatively constant, with a slight decrease as step-over distance increases. However for thin-walled structures, such as Geometry 3, 4, and 5, the variation of material efficiency corresponding to the step-over distance are significant. Although the generally-descending trend of material efficiency can still be found, the variation cannot be predicted since the shapes of various geometries are very different. The optimal step-over distances for Geometry 1 and 2 are 4 mm, while for Geometry 3 is around 4 mm, for Geometry 4 is near 6 mm and for Geometry 5 is approximately 3 mm.

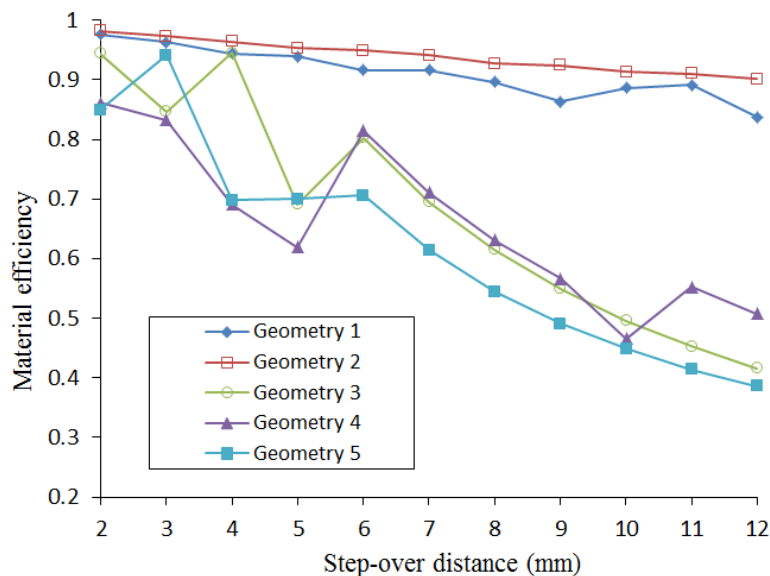


Figure 5.28 Material efficiency vs. step-over distance for five geometries in WAAM system

Variations of material efficiency in WAAM for the five tested geometries are shown in Figure 5.29. It is clear that while the variation of material efficiency for different step-over distances is minimal for solid structures, it is quite significant for thin-walled structures. For geometry 5, by choosing the optimal step-over distance, material efficiency could be increased by 2.4 times from 38.63% to 94.15%. This indicates that step-over distance plays

an important role on material efficiency when fabricating thin-walled structures using WAAM technology.

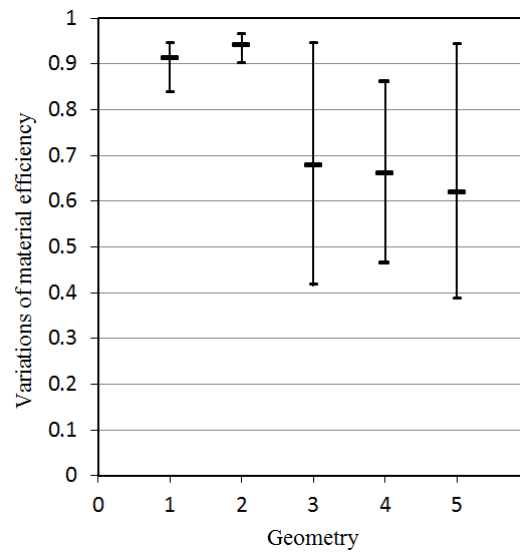


Figure 5.29 Variations for material efficiency in WAAM for Geometry 1, 2, 3, 4, and 5.

5.4 Adaptive MAT path planning

5.4.1 Essential of adaptive MAT path

Traditional contour path always generates gaps or voids as shown in Figure 5.30a and b. To avoid internal voids, the MAT (Medial Axis Transformation) path was introduced and its extension for complex geometries was developed in section 5.3. MAT paths are generated by offsetting the medial axis of the geometry from the centre towards the boundary. Figure 5.30c shows an example of MAT path with the deposition sequence indicated by numbers. Although void-free deposition is obtained using MAT paths, this is achieved at the cost of creating discontinuity of the path (such as path 3, 4, and 5 in Figure 5.30c) and extra deposition at the boundary as described in Figure 5.30d. Post-process machining must be used to remove the extra materials and improve the accuracy at the cost of material and energy wastage.

Step-over distance, which is defined as the distance between the next deposition path and the previous one, is always constant for both contour path patterns (refer to Figure 5.30a) and MAT path patterns (refer to Figure 5.30c). For certain geometries, it is not possible to achieve both high accuracy (refer to Figure 5.30b) and void-free (refer to Figure 5.30d) components using paths with constant step-over distance. However, the wire-feed AM process is capable of producing different widths of deposits within a layer through varying travel speed and

wire-feed rate, while maintaining a constant deposit height. Therefore, we propose an adaptive path planning strategy that uses continuously varying step-over distances by adjusting the process parameters to deposit beads with variable width within any given path. The developed adaptive MAT path planning algorithm is able to automatically generate path patterns with varying step-over distances (refer to Figure 5.30e) through analysing geometry information to achieve better part quality (void-free deposition), accuracy at the boundary, and material efficiency, as shown in Figure 5.30f.

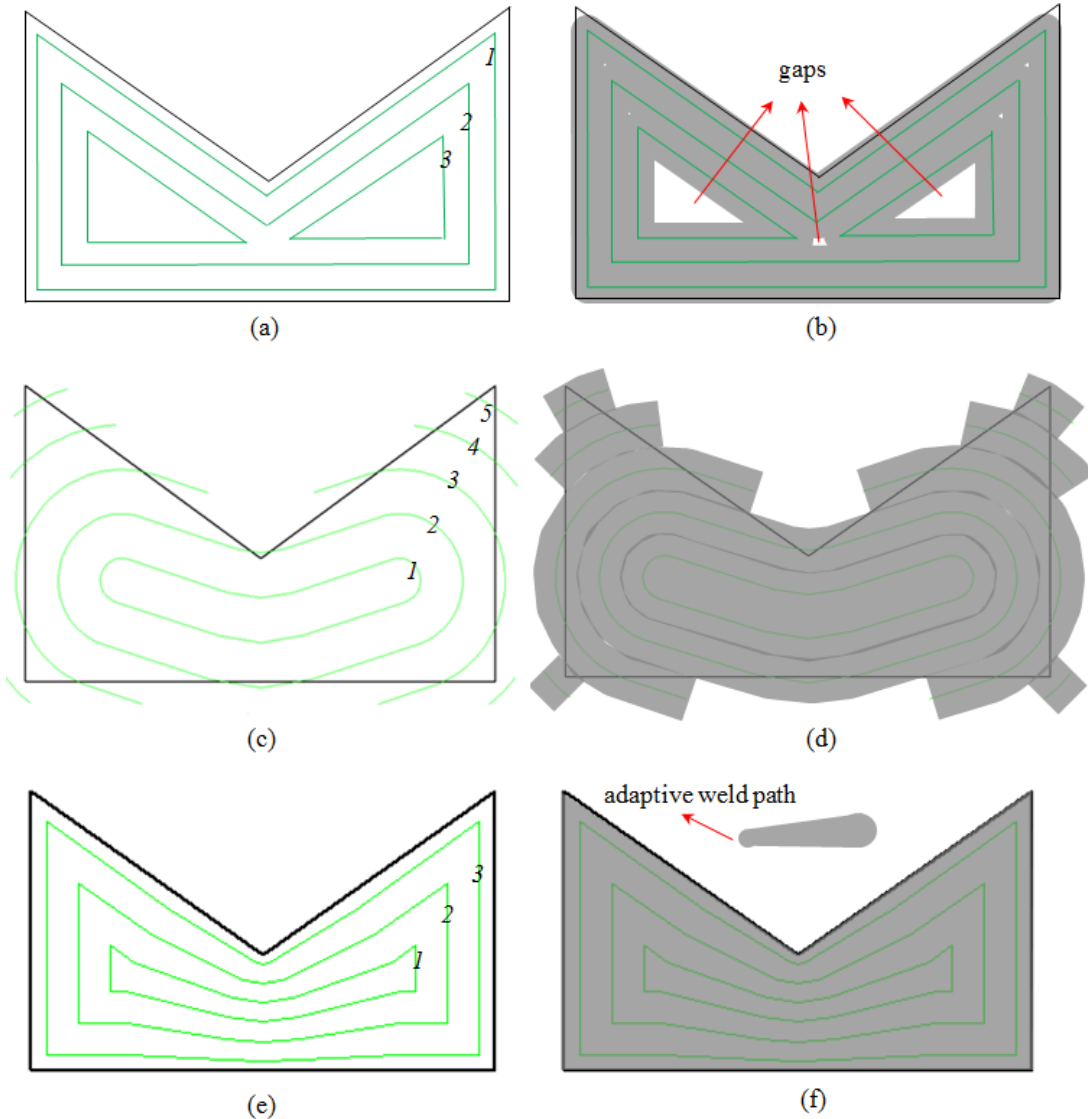


Figure 5.30 Illustrations of different deposition paths. Black lines represent the boundary of the geometry; green lines represent the deposition paths with the numbers representing the order of the deposition paths; grey regions are deposited area by the relevant paths. (a) Contour path patterns; (b) The predicted high accuracy deposition but with internal gaps; (c) MAT path patterns; (d) The predicted void-free deposition but with extra material deposited along the boundary; (e) Adaptive MAT path patterns with varying step-over distance; (f) The predicted void-free deposition with high accuracy at the boundary through using adaptive MAT path.

This section presents an innovative adaptive MAT path planning algorithm for wire-feed AM to generate void-free parts with better continuity and geometrical accuracy, improved buy-to-fly ratio and less energy consumption.

5.4.2 Algorithm for adaptive MAT path generation

The flowchart of the adaptive MAT path planning algorithm is shown in Figure 5.31. Different from MAT-based path (non-adaptive) generation, domain decomposition module is required before path generating for each domain.

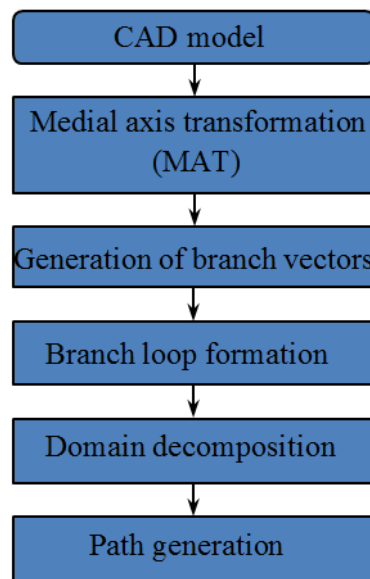


Figure 5.31 Flowchart of the adaptive MAT path planning algorithm

A. Domain decomposition

For a simple polygon without holes, there is only one boundary loop and one branch loop. The whole region can be considered as a single domain enveloped by the boundary loop and the branch loop. In this step, the domain is decomposed into a set of simple shapes for the following subsequent path generation.

As has been defined before, the circle corresponding to a branch point touches the boundary at more than two points. Radial line segments of the branch point are formed by connecting the branch point and its touch points, as shown by the blue line segments in Figure 5.32a. These radial line segments as well as sub-branches (red dashed lines shown in Figure 5.32a) decompose the domain into a variety of simple shapes. Three types of shapes can be found, namely T_1 , T_2 , and T_3 .

Definition 3:

- *Radial line segment is a line segment connects the branch point and one of its touch points.*
- *T_1 shape is a triangle that consists of one sub-branch segment, one boundary line segment, and one radial line segment.*
- *T_2 shape is a triangle that has one branch segment and no boundary line segments.*
- *T_3 shape is a trapezoid that consists of two parallel radial line segments, one branch, and one boundary line segment.*

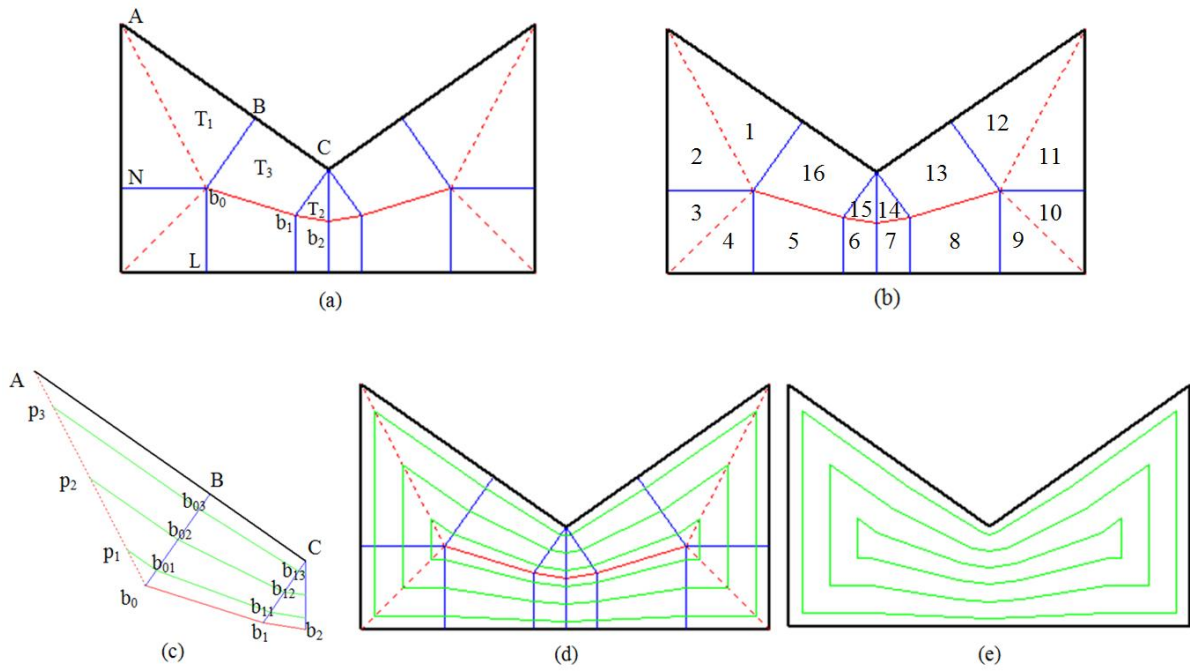


Figure 5.32 Geometry 1, illustrations of adaptive path generation for the given geometry. (a) Three typical simple shapes decomposed from the domain, T_1 : triangle1; T_2 : triangle2; and T_3 : trapezoid. (b) The decomposed shapes are shown in order of processing. (c) Offset rules for three typical shapes. (d) Apply the offset rules for all decomposed shapes. (e) Final generated adaptive paths with varying step-over distances.

As shown in Figure 5.32a, triangle ABb_0 is a T_1 shape, triangle Cb_1b_2 is a T_2 shape, and trapezoid BCb_1b_0 is a T_3 shape. Any complex domain can be decomposed into these three fundamental shapes. These shapes are sequenced according to the previously-formed branch loop. The processing order of the shapes is shown in Figure 5.32b for example.

B. Path generation

Adaptive paths are generated separately for each shape. If the number of n closed paths is required for the domain, the rules for generating paths on different shapes are provided as follows.

(a) Path generation for T₁ shape

The i^{th} path is generated by parallel offsetting the boundary line segment at the distance $(i-(1/2))d_1$ from the branch point to the touch point. d_1 is the step-over distance for the given shape T₁. d_1 is a constant and expressed as

$$d_1 = \frac{R_1}{n}, \quad (5.1)$$

where, R_1 represents the radius of the T₁ shape, which is equal to the length of the radial line segment; n represents the total number of offset paths.

For the T₁ shape ABb₀ shown in Figure 5.32c, AB is the boundary line segment, b₀B is the radial line segment. Three paths b₀₁p₁, b₀₂p₂, and b₀₃p₃ parallel to the boundary line segment AB are generated if n is chosen to be 3 for the domain.

(b) Path generation for T₂ shape

The i^{th} path is generated by parallel offsetting the branch at the distance $(i-(1/2))d_2$ from any one of the two branch points to the touch point. d_2 is the step-over distance for the given shape T₂. d_2 is also a constant and expressed as

$$d_2 = \frac{R_2}{n}, \quad (5.2)$$

where, R_2 represents the radius of the T₂ shape, which is the distance from the touch point to the branch.

For the T₂ shape Cb₁b₂ shown in Figure 5.32c, C is the touch point, b₁ and b₂ are two branch points and b₁b₂ is the branch. Three paths parallel to the branch are shown in Fig.6c.

(c) Path generation for T₃ shape

Since T₃ has two branch points and each branch point has its own touch point, there are two radii and therefore the paths will be generated by non-constant offsetting. The i^{th} path is generated by offsetting one of the branch points at the distance $(i-(1/2))d_{31}$ towards its touch point, and offsetting the other branch point at the distance $(i-(1/2))d_{32}$ towards its touch point, respectively. d_{31} and d_{32} are step-over distances at two branch points and are expressed as

$$\begin{cases} d_{31} = \frac{R_{31}}{n} \\ d_{32} = \frac{R_{32}}{n} \end{cases}, \quad (5.3)$$

where, R_{31} and R_{32} represents the two radii of the T_3 shape. Consequently, the paths in a T_3 shape are non-parallel curves with varying step-over distances from d_{31} to d_{32} .

For the T_3 shape BCb_1b_0 shown in Figure 5.32c, BC is the boundary line segment, b_0b_1 is the branch, b_0B and b_1C are two radial line segments and their lengths are two radiuses, respectively. Three paths $b_{01}b_{11}$, $b_{02}b_{12}$, and $b_{03}b_{13}$ with varying step-over distances are generated.

By applying this offset rules for all decomposed simple shapes of the domain (refer to Figure 5.32d), the final adaptive paths which consists of n continuous closed loops are generated as shown in Figure 5.32e. Figure 5.32 shows the adaptive MAT-based path generation of simple geometry without holes.

Figure 5.33 and Figure 5.34 show the step-by-step process of adaptive MAT path generation for complex geometries. Figure 5.33(a) shows the medial axis as red dotted lines for an example geometry with a single hole. Branches are extracted as red solid lines shown in Figure 5.33b. Two branch loops are formed. $(b_0b_1b_2b_3b_4b_5b_4b_1b_0)$ in the counter-clockwise direction and $(b_1b_4b_3b_2b_1)$ in the clockwise direction. Accordingly, two domains (displayed in different colours in Figure 5.33c) are formed with each enveloped by its branch loop and boundary loop. Then, each domain is decomposed into a set of three fundamental shapes as shown in Figure 5.33d. By applying path generation algorithm on each domain separately, both domains are covered by the generated paths as shown in Figure 5.33e. Final paths with varying step-over distances are shown in Fig.8f.

Figure 5.34 shows a geometry with multiple holes. Branches are extracted and six branch loops are formed, namely, loop $(b_0b_1b_2b_3b_4b_5b_6b_7b_8b_9b_{10}b_{11}b_0)$ in the counter-clock direction, and other loops $(b_0b_{11}b_{10}b_{15}b_0)$, $(b_1b_{12}b_3b_2b_1)$, $(b_4b_{13}b_6b_5b_4)$, $(b_7b_{14}b_9b_8b_7)$, and $(b_0b_{15}b_{10}b_9b_{14}b_7b_6b_{13}b_4b_3b_{12}b_1b_0)$ all in the clockwise direction. Accordingly, six domains are generated and displayed in different colours in Figure 5.34b. Domain decomposition and the final adaptive MAT paths are shown in Figure 5.34c and Figure 5.34d, respectively. Note that not all branch points are displayed in Figure 5.33 and Figure 5.34 for the explanation of branch loop formation.

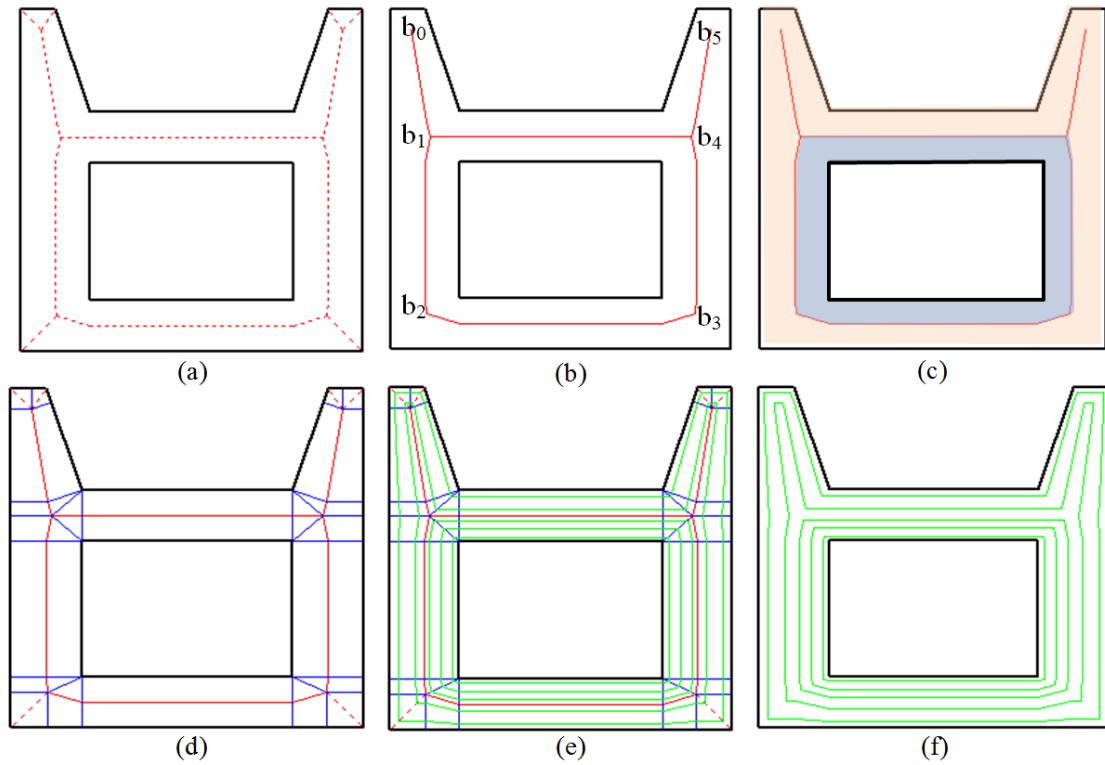


Figure 5.33 Geometry 2, illustrations of the adaptive path generation for geometry with a single hole. (a) Computed medial axis as represented by red dotted lines. (b) Branch loop formation. (c) Geometry sub-division, two domains are divided and displayed in different colours. (d) Domain decomposition, all domains are decomposed into a set of three typical simple shapes. (e) Apply the offset rules for all decomposed shapes. (f) Final generated adaptive paths.

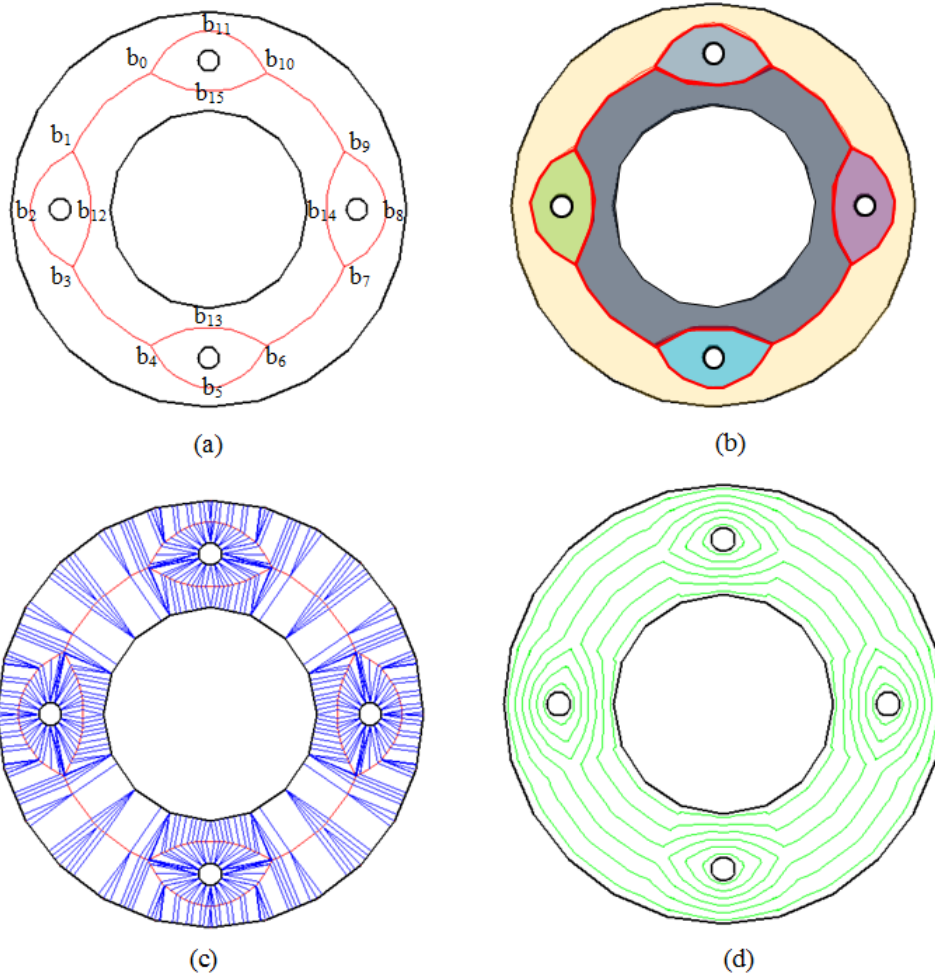


Figure 5.34 Example of a geometry with multiple holes. (a) Computed branch loops as represented by red lines; (b) Divided six domains as represented by different colours; (c) Generated numerous radiations from the branch points and the various decomposed simple shapes; (d) Generated adaptive paths for the geometry

5.4.3 Validation of the proposed algorithm

The newly developed path planning algorithms are validated by application to different geometries as shown in Figure 5.35 and Figure 5.36. Figure 5.35 shows a thin-walled structure with multiple holes and varied wall thickness, which will result in severe problems using existing path generation strategies, due to the geometrical complexity and the large deposition width of wire-feed AM. In this case, 16 branch loops are formed and consequently 16 domains are generated. Adaptive paths are generated through non-constant offsetting from the branch loops towards the boundary loops. Adaptive paths with varying step-over distances accommodate the changing wall thickness of the geometry. Figure 5.36a shows a more complex geometry and the generated paths clearly demonstrate the variance of step-over distances in each domain. Figure 5.36b shows the previously non-adaptive MAT paths for the geometry. It can be seen that, non-adaptive MAT generates a set of discontinues paths

at the boundary of the component and would result in excessive material deposition at the boundary. The proposed adaptive MAT generates closed-loop paths and improves the accuracy at the boundary.

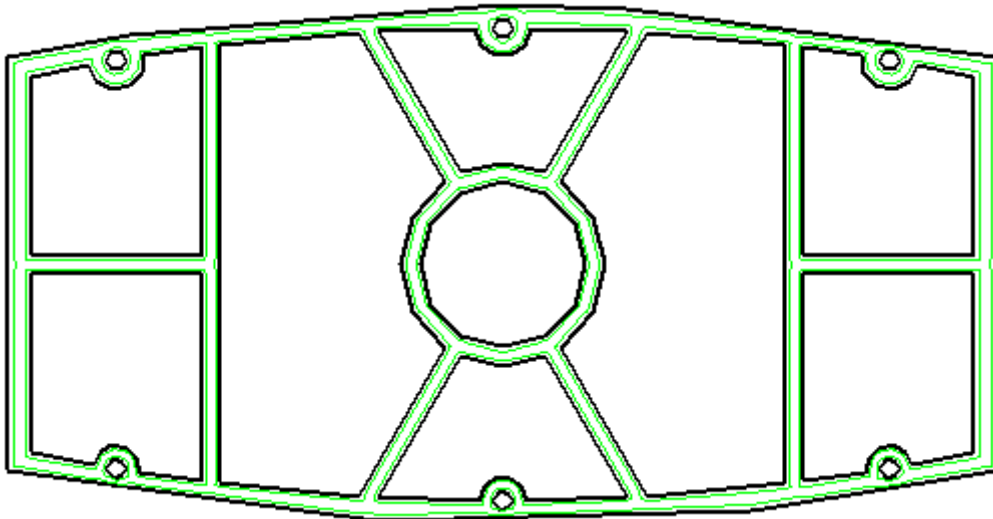


Figure 5.35 Geometry 3, a thin-walled structure with multiple internal holes recesses.

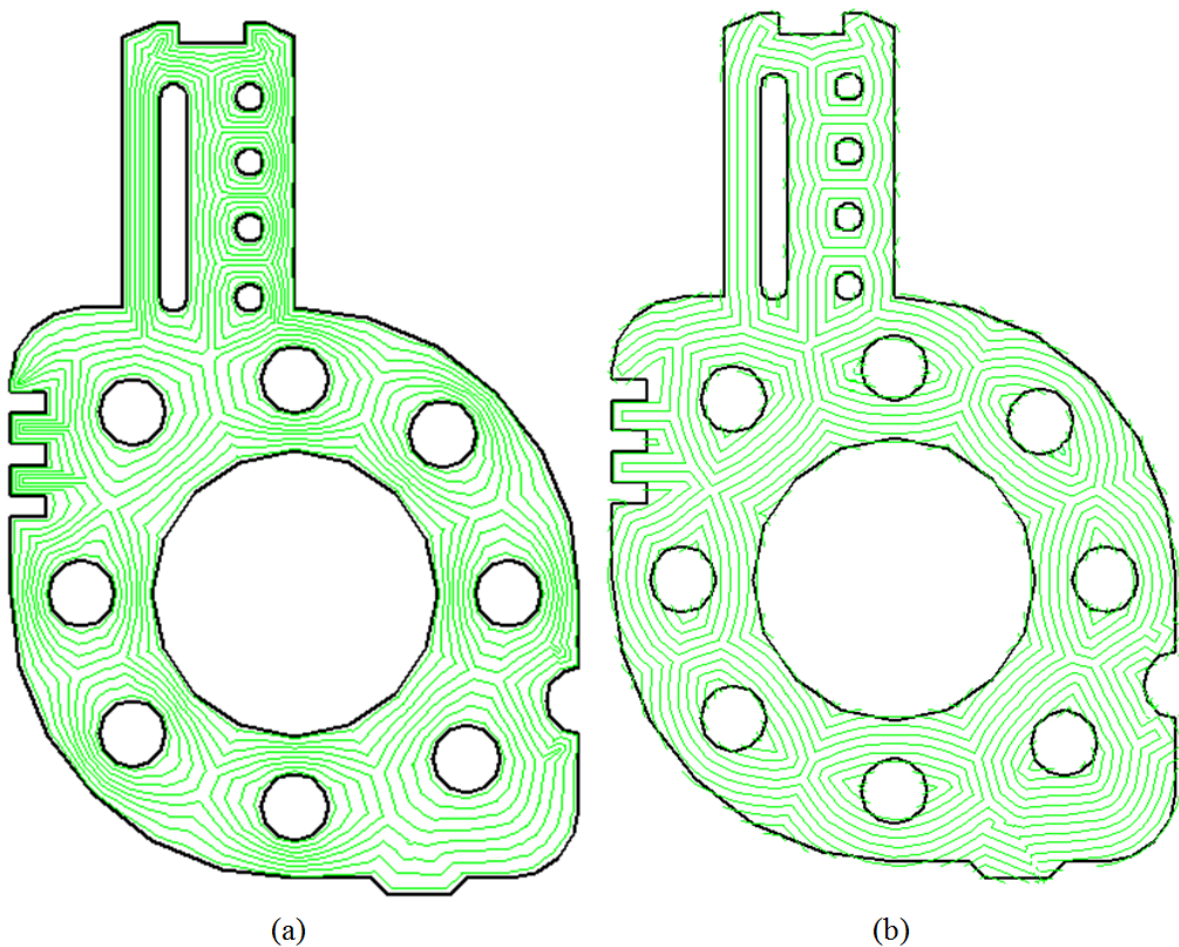


Figure 5.36 Geometry 4, a complex thick-walled structure with multiple internal holes. (a) Adaptive MAT path. (b) Non-adaptive MAT path

Unlike other offsetting-based path generation methods such as non-adaptive MAT path and contour path, the proposed adaptive MAT path algorithm will not produce self-intersection. This is because the adaptive MAT systematically decomposes the complex geometry into simpler domains and these are further decomposed into a set of fundamental shapes, which can be linked together with a single path loop without self-intersection. The proposed algorithm is proven to be efficient and robust.

5.4.4 Discussions

Buy-to-fly ratio, which is defined as the mass ratio of the raw material used to fabricate a component and the final component itself, is an important factor for the AM process. Buy-to-fly, BTF , for a sliced layer can be defined as:

$$BTF = \frac{A_{deposited}}{A_{desired}}. \quad (5.4)$$

$A_{desired}$ is the desired area of the geometry which is determined from the sliced CAD model. $A_{deposited}$ represents the deposited area, which depends on the path planning strategy. The deposition process can be represented as a circle with a diameter d_k (the step-over distance) being swept along the computed path. Since d_k varies for each line segment of the path, $A_{deposited}$ could be obtained by the sum of the area deposited by every line segment of the computed path. The deposition area of a line segment is generally a trapezoidal shape and therefore one can obtain

$$A_{deposited} = \sum_{j=1}^{N+1} \sum_{i=1}^{n_j} \sum_{k=1}^{n_i^j} \left[Path_i^j(L_k) \cdot \frac{Path_i^j(d_k^s) + Path_i^j(d_k^e)}{2} \right]. \quad (5.5)$$

where, n_j represents the maximum offset closed paths in domain j . n_i^j represents the maximum path line segments of the $Path_i^j$.

For the different geometries described in Section 5.4.3, the BTF using the proposed adaptive MAT path is computed and summarized in Table 5.3. The BTF of the previously reported non-adaptive MAT path and the traditional CNC machining (equal to the volume ratio of the geometry, assuming no over-dimensioning of the raw material billet) are also provided for comparison. It can be seen that AM technology (both adaptive MAT path and non-adaptive MAT) has a much better BTF compared to traditional subtractive manufacturing. The results also show that BTF can be further improved to almost 1.0 by using the proposed adaptive MAT path. For the thin-walled geometry No.3, BTF for the

adaptive MAT path is improved by 27% from the value of 1.39 achieved by using non-adaptive MAT, and improved by 79% from 4.76 for subtractive manufacturing. Using the adaptive MAT paths achieves higher deposition accuracy at the component boundary, which result in less material waste in deposition and less energy consumption for post-process milling.

Table1 5.3 Basic information for four geometries presented in this paper and their BTF associated with different manufacturing methods.

No. Geometry	Figure	Area (10^4 mm^2)			Buy-to-fly ratio, BTF		
		Real geometry	Enveloped box	Volume Ratio (%)	Adaptive MAT path	Non-adaptive MAT path	CNC
1	6	0.45	0.6	75.0	1.01	1.08	1.33
2	8	0.55	1.0	55.0	1.01	1.24	1.82
3	10	1.93	9.18	21.0	1.01	1.39	4.76
4	11	11.5	24.5	46.9	1.01	1.11	2.13

Table 5.4 compares the performance of different path planning algorithm in terms of, quality, accuracy, and buy-to-fly ratio. Contour path is not suitable for certain geometries in wire-feed AM due to the large deposition width of the arc welding process, and the geometrical complexity of the paths would result in gaps during deposition. Non-adaptive MAT path is able to produce void-free part; however it deposits excessive materials due to its low accuracy at the component boundary. Adaptive path generates void-free paths with improved accuracy and therefore better BTF is obtained compared to existing algorithms. The adaptive MAT path has significant advantages for wire-feed AM, particularly where the wall thickness is similar to the range of deposition width of the wire-feed AM process.

Table 5.4 Comparison of three paths for wire-feed AM: “+” represents good, and “−” represents poor.

	Quality (void-free)	Accuracy	Buy-to-fly ratio (BTF)
Contour path	−	+	+
Non-adaptive MAT path	+	−	−
Adaptive MAT path	+	+	+

5.5 Summary

This chapter reviews the existing path planning methods and the challenges of path planning in WAAM. Since none of existing path patterns are suitable for WAAM of any complex geometries, newly MAT-based non-adaptive and adaptive paths are proposed. Algorithms for generating the proposed paths are developed and tested.

The research has revealed that MAT-based paths are able to generate void-free deposition paths which are beneficial for arc-welding-based process. And the further developed adaptive MAT path improves geometrical accuracy as well as buy-to-fly ratio. Application of MAT-based path and adaptive MAT path will be provided in Chapter 7.

Chapter 6

Post-process Machining

Post-process machining is required to obtain the finished parts from the produced near-net shapes. In traditional CNC machining process, full automation has been difficult due to the possible problems related to tool accessibility and fixture. However, in WAAM, automation of post-process machining could be possible since the CAD model will be decomposed into layers, and post-process could also be divided into layer-by-layer machining.

This Chapter briefly introduce the robot machining steps. The machining process could be classified into three types, top region machining, side region machining, and base region machining as shown in Figure 6.1. Details of the machining path generation are given as follows.

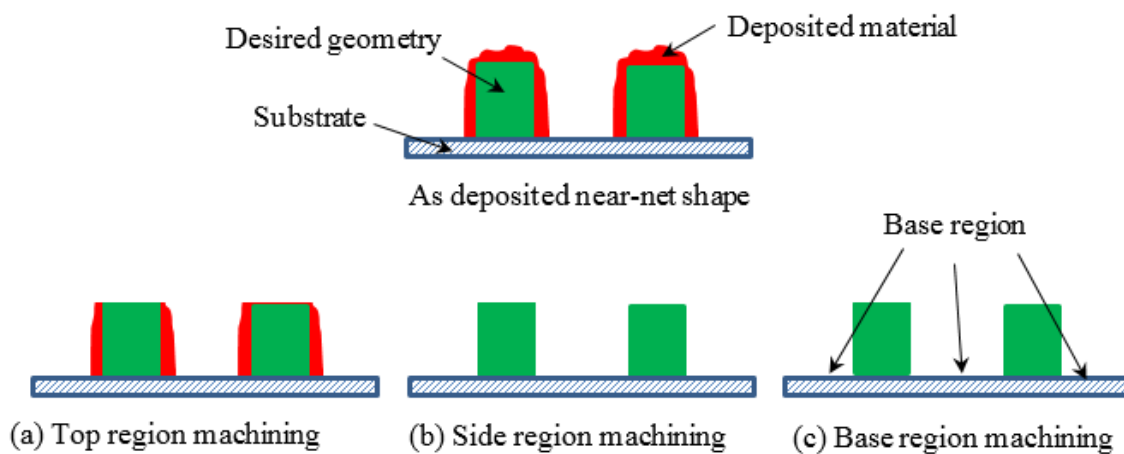


Figure 6.1 Schematic diagram of the near-net shape as deposited. (a) After top region machining; (b) After side region machining; and (c) Base region machining.

6.1 Top region machining

Top region machining is used to maintain the top surface of the deposited layers, as shown in Figure 6.1. The machining paths for top region is relatively simple since there is no self-intersection or revisiting issues.

In this study, MAT-based paths are implemented to the generation of top region machining paths. The path generation algorithm is similar to the algorithm for deposition paths. The machining tool radius is used as the step-over distance between each top region machining paths. For example, the boundary of the desired layer is represented by black lines in Figure 6.2a. The medial axis of the geometry is calculated as the red dash lines shown in Figure 6.2b. Through offsetting the medial axis, the machining paths for the top region is generated as the red solid lines shown in Figure 6.2c. Figure 6.2d shows part of the trajectory of machining tool. Blue circles represent the tool cross section.

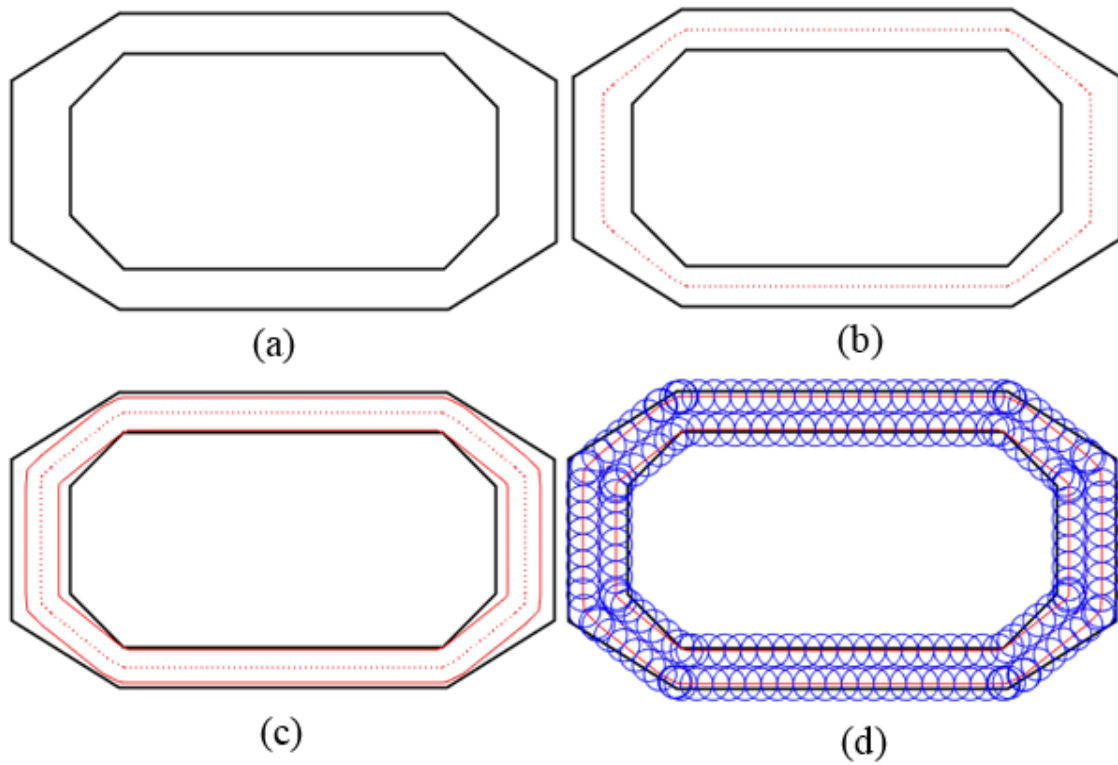


Figure 6.2 Top region machining paths generation. (a) Black lines represent the boundary of the geometry; (b) Red dash lines represent the medial axis of the geometry; (c) Red solid lines represent the generated paths through offsetting the medial axis; and (d) Trajectory of machining tool. Blue circles represent the tool cross section.

6.2 Side region machining

Side region machining could be conducted after the deposition of each layer or several layers depending on the complexity of the geometry and the depth of the machining tool. The machining paths for side region is generated through offsetting the boundaries of the geometry. As shown in Figure 6.3a, two red lines are calculated machining paths, and the trajectory of the machining tool is shown in Figure 6.3b. The algorithms for offsetting the boundaries could be found in [96].

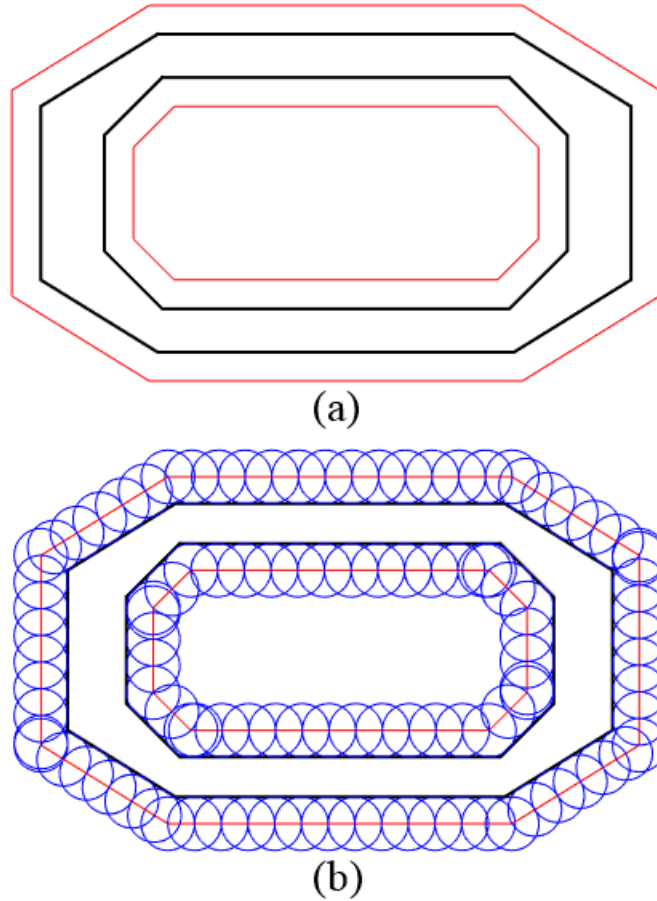


Figure 6.3 Side region machining paths generation. (a) Red lines represent the path generation through offsetting the boundaries of the geometry; and (b) Trajectory of the machining tool.

6.3 Base region machining

Due to the high heat input of arc welding process, the substrate would have distortions resulting the dimensional errors in base region. Therefore, base region is also required to be machined. Zigzag path pattern is implemented for base region machining for its simplicity. Figure 6.4 shows the zigzag paths generation for the base region. And the trajectory of the machining tool is described in Figure 6.4b.

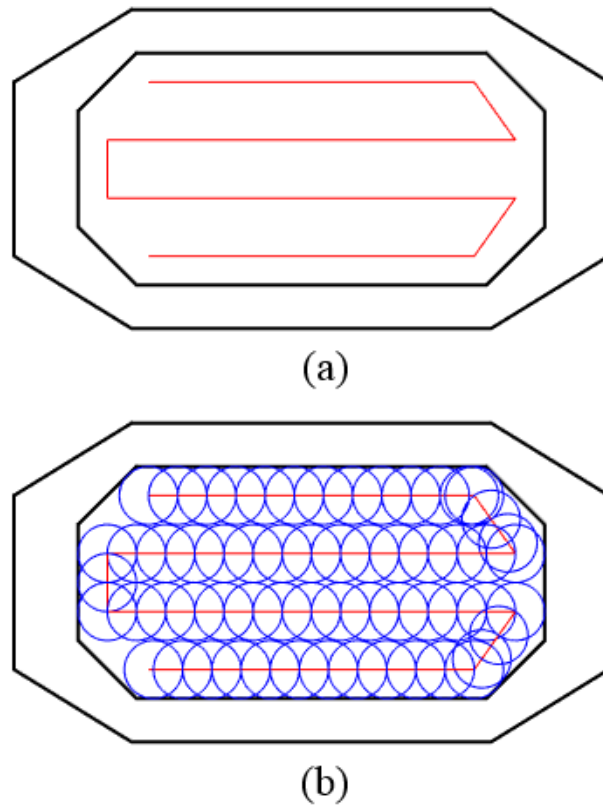


Figure 6.4 Base region machining paths generation. (a) Red lines represent the Zigzag path generation; and (b) Trajectory of the machining tool.

6.4 Summary

For some complex workpiece, 3D machining after the deposition of the whole component would be impossible due to the occurrence of collision. Periodic milling after each layer deposition is possible to produce high accuracy components, however, it is time-consuming and wastage materials.

This Chapter provides a preliminary investigation of path generation methods for post-process machining. The effective machining tool path is generated from the geometry information of the original 3D components and machining tool. In future, the sequence of machining operations need to be coordinated properly to avoid accessibility issues as well as maintain the efficiency of the system.

Chapter 7

Applications

A few sample parts are fabricated using the developed WAAM system to test its performance. Building these parts also helped to better understand some of the finer aspects of the process planning.

Most of the experiments were conducted using a robotic gas metal arc welding (Fronius) system and a robotic machining system at the University of Wollongong, as shown in Figure 7.1. An ABB 1400 industrial robot arm with six degrees of freedom was used to generate the movement of the welding torch relative to the substrate, as shown in Figure 7.1a. A larger ABB 6660 robot was used for post-process machining, since it is able to withstand high process forces and enables high-performance applications of finishing and milling. Note that the 3D profiler scanner mentioned in Chapter 3 was carried by another ABB 4400 industrial robot, separately, for process measurements.

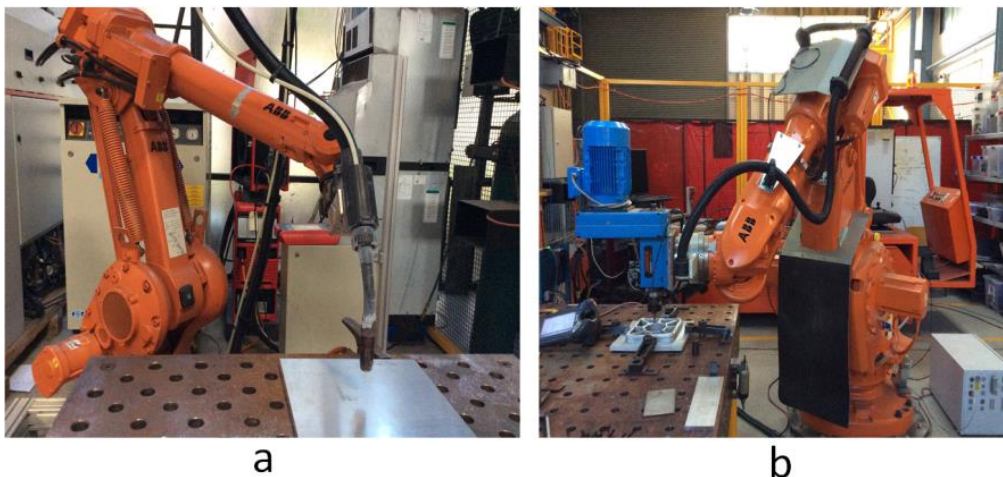


Figure 7.1 Experimental set-up: (a) ABB 1400 robot with Fronius welder for additive manufacturing, (b) ABB 6660 robot with motor spindle for machining.

7.1 Mild steel components with complex geometries

Figure 7.2 to Figure 7.4 show three parts with complex geometries that would require significant materials, time, and effort to be fabricated using the conventional subtractive manufacturing methods. These parts would require quite a lot of manual programming and adjustments to be manufactured using a CNC machine. However, using the developed automated WAAM system, these parts could be produced in a fairly automated fashion.



Figure 7.2 A turbine blade structure

Figure 7.2 shows a turbine blade structure produced in WAAM. The contour path pattern with the single path and therefore single bead is implemented since the geometry of the sliced layer is relatively simple. The wire-feed rate is 2.5 m/min, and the travel speed is 0.4 m/min. Each layer is deposited in around 30 seconds and has an average thickness of 1.3 mm. With the deposition of 150 layers without any interlayer machining, the blade has a height of 195 mm. During the deposition, a 60 seconds-wait time is used between each layer to avoid distortion and poor surface finish due to overheating of the previously deposited layers. The whole deposition process takes around 4 hours. Minimum distortion is found with the use of 8 mm thickness mild steel plate as the substrate.

Figure 7.3 shows a twist blade structure. Similar welding parameters, contour path planning method, and cooling time were used for this part. No interlayer or post machining process was conducted. It is nearly impossible to fabricate this highly curved structure

automatically using the traditional machining method. This case demonstrates the kind of complex parts that robotic WAAM system can build.



Figure 7.3 A twist turbine blade structure

Figure 7.4 shows an impeller structure. Figure 7.5 shows briefly the architecture of process planning from CAD model to robot code generation. A special continuous path planning and multi-bead overlapping method were used for this structure as shown in Figure 7.5. 5 m/min wire-feed rate and 0.8 m/min travel speed were chosen. Each layer has an average thickness of 1.8 mm. During the deposition, a certain amount of waiting time was used. With the deposition of 40 layers without any interlayer surface machining, the impeller has a total height of 70 mm. After cleaning and milling the top surface and part of the side walls, the partially machined components is illustrated in Figure 7.4b.

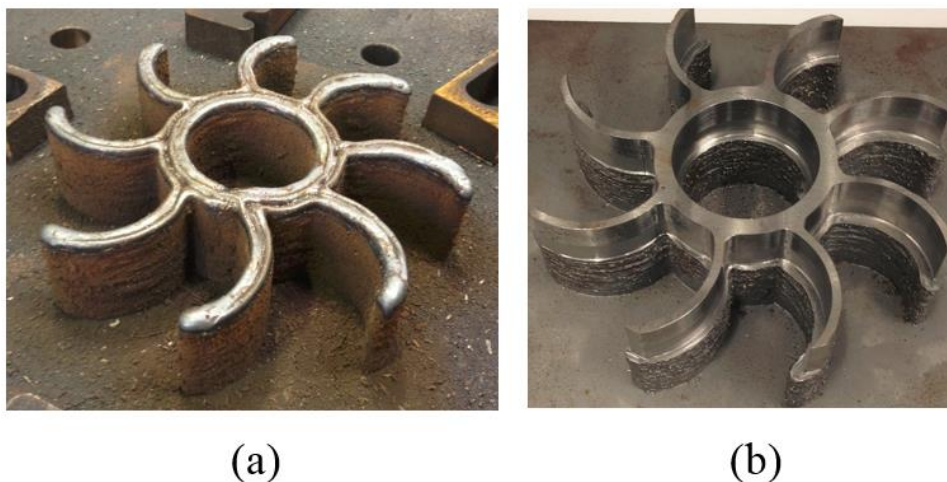


Figure 7.4 An impeller structure

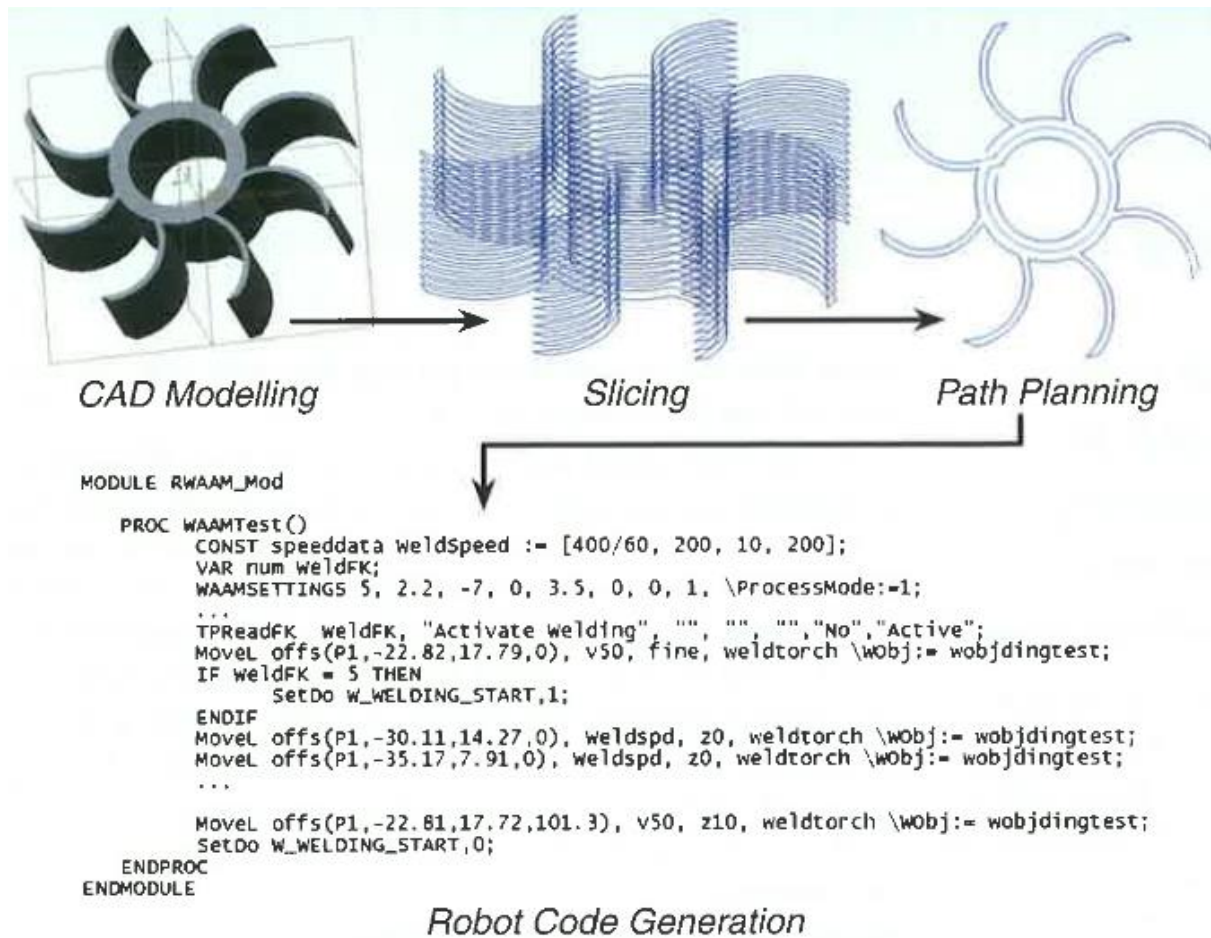


Figure 7.5 Example of process planning for the impeller structure

For mild steel structures, the pulsed-spray GMAW transfer mode was used to minimize the heat input. The wire electrode was copper coated steel wire with the diameter of 1.2 mm. The stick-out length was set to 18mm to minimise weld spatter for this particular process. A shielding gas mixture of 82% argon and 18% CO₂ was used with a flow rate of 22 L/min.

Above three cases verified the capability of WAAM to fabricate near-net shapes. Different path planning strategies were used depending on the geometry of the sliced layers.

7.2 Aluminium thin-walled structure with finished quality

An aluminium thin-walled structure was built to test MAT-based path planning, bead modelling and post-process machining.

The geometry of the structure is shown as black lines in Figure 7.6. It should be noted that the wall thicknesses are varied making the previous path planning impossible for this particular part. MAT-based paths were proposed for this particularly thin-walled structure. Using algorithms developed in Chapter 5, MAT-based paths are automatically generated with appropriate step-over distances according to the information to obtain a smooth upper surface

for each deposited layer. The final deposition paths are 15 closed loops, as green lines shown in Figure 7.6. Note that it seems the generated paths haven't envelope the geometry in some edge areas (such as top left corner), while materials with certain bead width are deposited along the path enables fully covering of the geometry. The optimum step-over distance for each path are listed in Table 7.1.

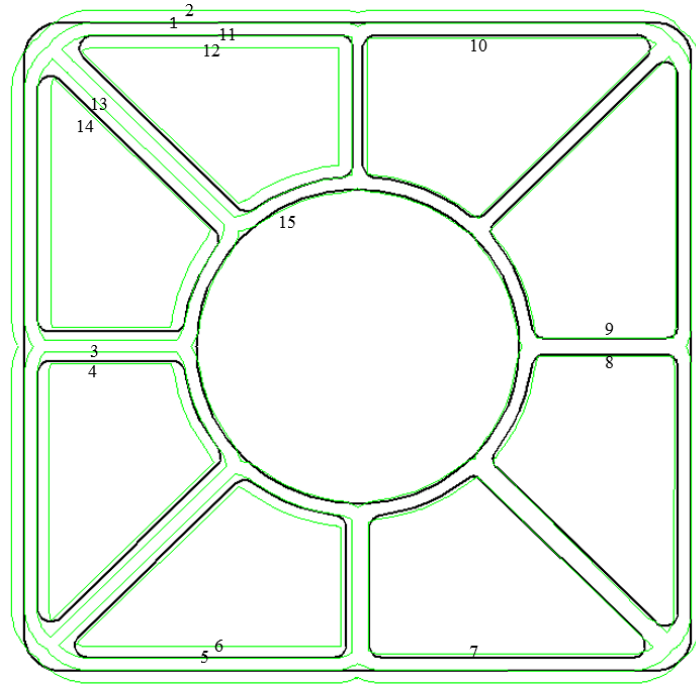


Figure 7.6 Final MAT-based paths for the thin-walled structure

Table 7.1 Process variables

Process variables	Deposition path														
	1	2	3	4	5	6	7	8	9	10	11	12	13	14	15
Step-over distance (mm)	4.0	4.0	3.5	3.5	3.5	3.5	6.3	6.3	5.4	5.4	4.0	4.0	4.0	4.0	5.3
Wire-feed rate, F (m/min)	5.7	5.7	5.3	5.3	5.3	5.3	6.0	6.0	5.1	5.1	5.7	5.7	5.7	5.7	6.3
Travel speed, S (m/min)	0.55	0.55	0.47	0.47	0.47	0.47	0.50	0.50	0.39	0.39	0.55	0.55	0.55	0.55	0.59
Stick-out Length, L (mm)	14	14	14	14	14	14	13	13	11	11	14	14	14	14	14

Weld settings (wire-feed rate, travel speed, and stick-out length) along each of the generated deposition paths are selected automatically based on the ANN bead model. The welding parameters for each path are listed in Table 7.1.

Machining paths are also generated automatically for this case. Figure 7.7 shows the tool path for side region milling. This single path indicates that the excess material will be removed in a single cut, and that the machining robot has the capacity to perform this action.

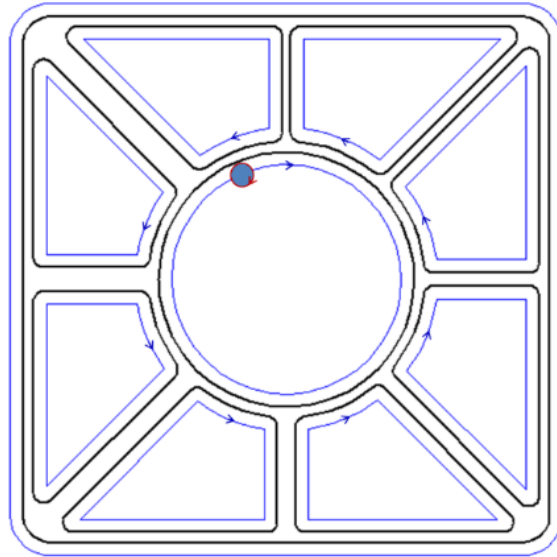


Figure 7.7 Tool paths for side region machining

During the experiments, the pulsed-spray GMAW transfer mode was used and the wire electrode was aluminium alloy (5% Mg) wire with a diameter of 1.2 mm. Argon shielding gas with a flow rate of 15 L/min was used.

After the deposition of 8 layers, the part was built up to 20 mm height. Figure 7.8a shows the near-net shape of the produced aluminium component. Details of crossings, start/stop sections and corners are shown in Figure 7.8b and Figure 7.8c. Figure 7.9a shows the process of post machining, and the final finished part with the desired dimensional tolerances is shown in Figure 7.9b.

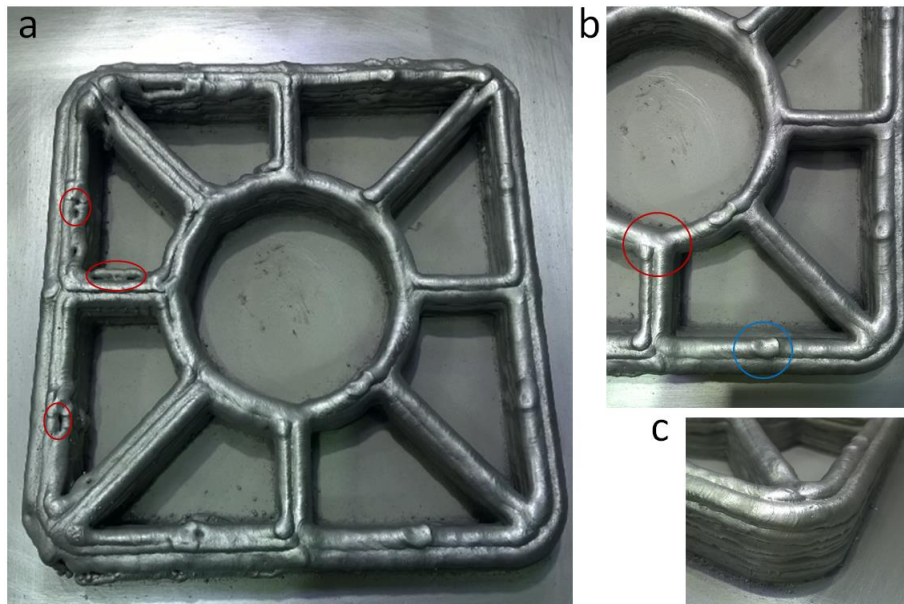


Figure 7.8 Experimental results. (a) Near-net shape of the produced aluminium component. (b) Details of crossings and start/stop sections. (c) Details at a corner.

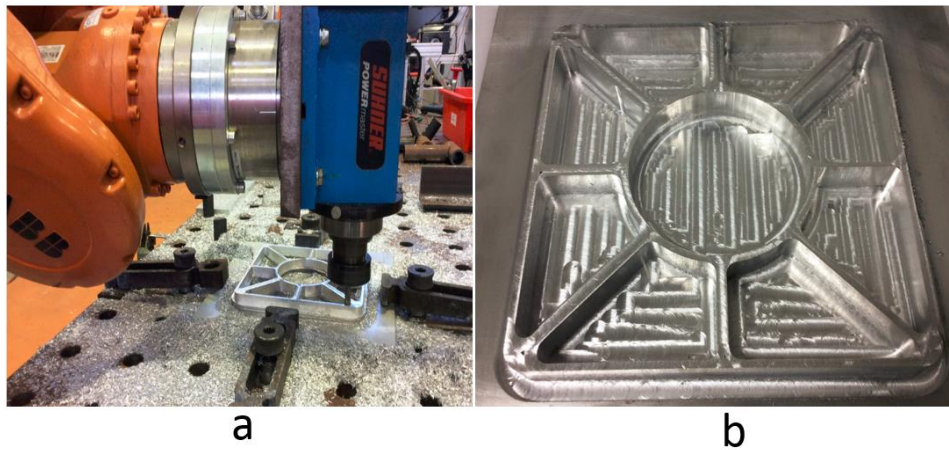


Figure 7.9 (a) Process of post machining. (b) Final finished part with the desired dimensional accuracy

This experiment verifies that the proposed WAAM system can be used to fabricate near-net shape part automatically from the CAD model. The excellent appearance of the produced shape at crossings (shown in Figure 7.8b in the red circle) indicates that the MAT-based path planning algorithm has effectively solved the issues at crossings of thin-walled structures. Height errors at start/stops (shown in Figure 7.8b in the blue circle) are minimised due to the closed loop of the paths. Good quality deposition is also evident at corners, as shown in Figure 7.8c.

In conducting this experiment, a few observations are worth mentioning. For example, the condition of the substrate, including temperature and geometrical shape, has a remarkable influence on the deposition accuracy and surface quality of the following layers. Furthermore, disturbances to the welding process may occasionally occur, depending on the materials, equipment, and deposition process selected, and also the previously deposited layers. The deposition process is sensitive to disturbances from the surface condition of the previously deposited layer. Consequently, defects may be produced as shown in Figure 7.8a in the red circles. Further online monitoring and control are required to be integrated to the proposed system for automatic in-process control of the deposition. In the event that a disturbance is detected during the deposition of a layer, an intermediate milling operation is required to maintain the surface quality.

In this study, different robots are used for deposition and machining. This results in additional calibration and re-fixturing steps, which imposes difficulties for post-process machining. Therefore, to produce components with high accuracy it is preferable to have an integrated system with the ability to generate a final part using a single machine.

In this particular case study, the machining process was performed after the near-net shape was completely deposited. For other component designs, it may not be possible to

delay all machining until the part is entirely deposited due to the limitations of the machining tool or spindle collision issues. Machining from time to time during the deposition process may be required. This will need to be determined through analysing the geometry of the input CAD parts. So, future work concerning optimization of the machining process is necessary to further develop CAD-to-part arc-welding-based additive manufacturing systems.

7.3 Adaptive MAT paths with minimum post milling

This section provides the implementation of adaptive MAT path in WAAM through case studies. Firstly, the relationship between single bead geometry and welding process parameters is established through an artificial neural network (ANN) model. Then, the adaptive MAT path is implemented by using the single bead ANN model together with a previously developed multi-bead overlapping model. Finally, the adaptive MAT path planning strategy and the established bead models are tested through experimental deposition of two metal components (mild steel).

7.3.1 ANN model of mild steel

Similar to the former established ANN model for aluminium alloys, single bead profile measurements were carried out first. For mild steel material, two inputs of wire-feed rate (F) and travel speed (S) were chosen. Bead width and bead height were responses as well. Table 7.2 shows a total 81 combinations of 9 different F and 9 different S .

Table 7.2 Welding parameters for weld bead model

Parameters	Value
Wire-feed rate, F , m/min	2.0, 2.8, 3.6, 4.4, 5.0, 5.6, 6.4, 7.2, 8.0
Travel speed, S , m/min	0.4, 0.47, 0.54, 0.61, 0.68, 0.75, 0.82, 0.91, 1.0

The weld bead height and width of all the tests are shown in Figure 7.10. It can be seen that the obtained bead widths range from 2 to 12 mm and bead heights range from 1 to 3 mm. With the changing of bead height, the range of bead width at the same height also varies.

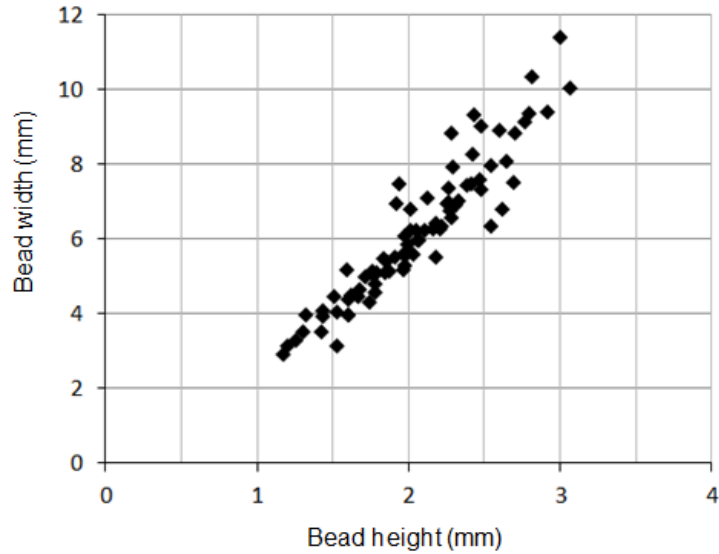


Figure 7.10 Experimentally measured bead widths and bead heights of all tests

The relationships of 81 combinations between process parameters and the weld bead geometry were randomly divided into two datasets, of which 65 were used for training and 8 for validation. The remaining 8 combinations were reserved for independent testing. The experimental data were linearly normalized for ANN training, validation and testing. The best architecture of 2-13-2 network with the mean square error of 0.0019 was trained. The predicted bead geometry in the training of the network was confirmed by correlation with the independent 8 testing experimental data as shown in Figure 7.11. It can be seen that there is high correlation between the predicted and experimental values of the bead geometry, indicating the ANN has the ability to accurately predict the bead geometry from welding parameters input.

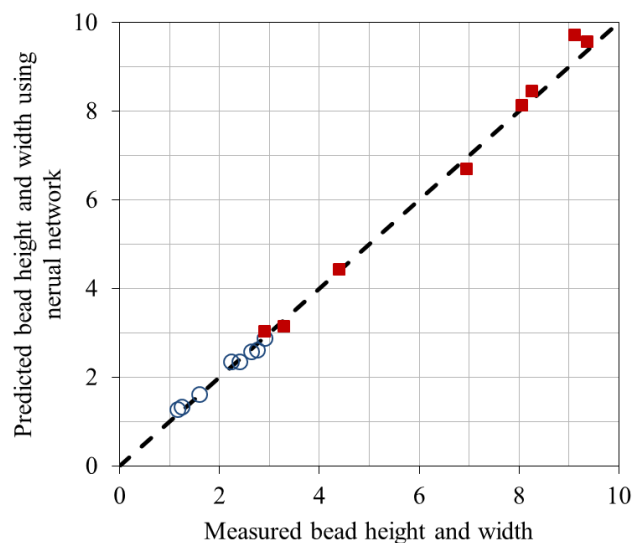


Figure 7.11 Measured bead height and width vs. predicted bead height and width using ANN model. Circles represent the bead heights of the independent 8 testing data. Solid red squares represent the bead widths of the independent 8 testing data. Units for both axes are millimetres.

In order to optimise the welding parameters based on the desired bead geometry simply, a database of 3721 combinations (61 by 61 input matrix) of welding parameters has been built, with the wire-feed rate ranging from 2 to 8 m/min in the steps of 0.1 m/min and the travel speed ranging from 0.4 to 1 m/min in the steps of 0.01 m/min. An output matrix (61 by 61) of the predicted bead height and width is then generated through the trained neural network as shown in Figure 7.12. This database is used to select the optimal welding parameters that will produce a given bead geometry.

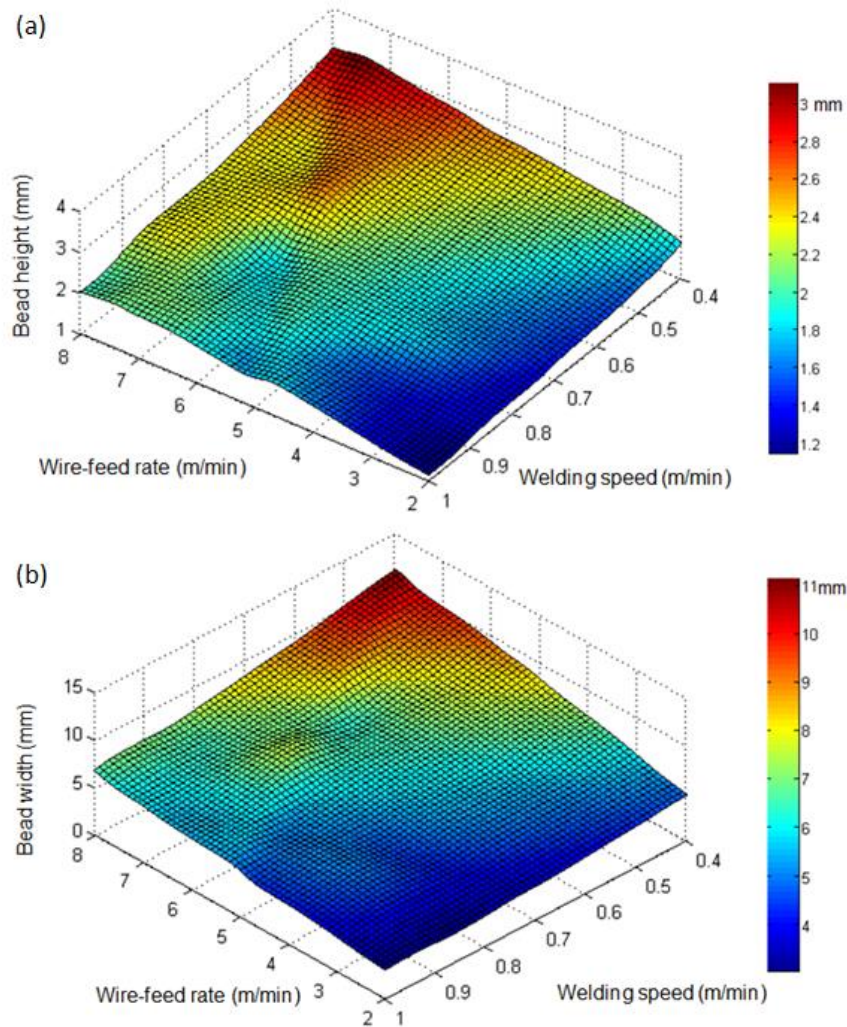


Figure 7.12 Surface plots of the bead height and bead width as the function of wire-feed rate and welding travel speed

7.3.2 Determination of 2D path planning variables

To implement the adaptive MAT path algorithm, one important task is to determine appropriate values of n_j for domain j . The values of n_j has significant effects on the desired bead size, with small n corresponding to larger weld deposits. If the desired weld bead height is chosen to be h , then a number of beads with the same height could be chosen by

combinations of different wire-feed rate and travel speed. Using the weld bead database matrix developed in Section 7.3.1, the range of weld bead width as a function of weld bead height are shown in Figure 7.13 as the shaded area within the black curve. For certain a height of h , the width of these weld beads are within a range $[w(h)_{\min}, w(h)_{\max}]$.

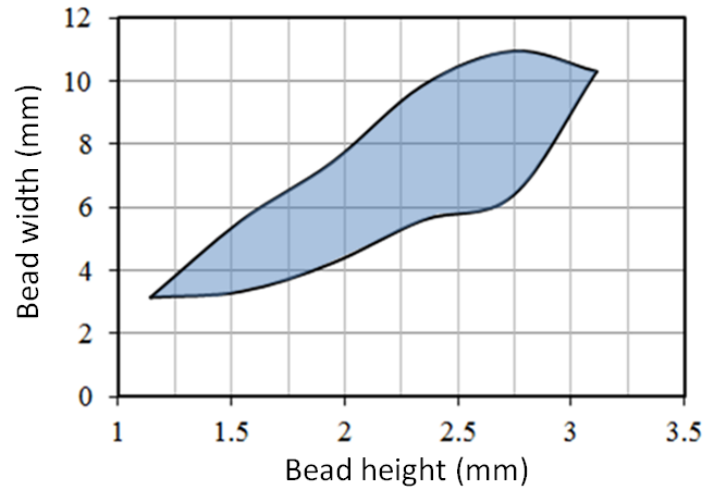


Figure 7.13 Ranges of bead width and bead height through varying wire-feed rate and travel speed.

In adaptive MAT path planning, the deposition process can be considered as a disk with varying diameter being swept along the computed path. As shown in Figure 7.14, the domain is expanded along the branch loop, with the internal or external boundary represented by the black solid line. The maximum step-over distance d_{\max} is obtained at the maximum radius $(R_j)_{\max}$ and the minimum step-over distance d_{\min} is obtained at the minimum radius $(R_j)_{\min}$.

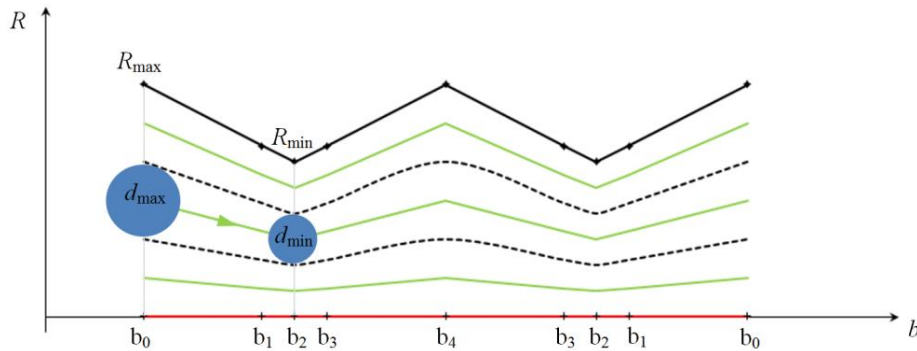


Figure 7.14 Illustration of the deposition process in an expanded domain.

The following relationships can be obtained if n_j paths are generated

$$\left\{ \begin{array}{l} d_{\min}^* \leq \left(d_{\min} = \frac{R_{\min}}{n} \right) \leq d_{\max}^* \\ d_{\min}^* \leq \left(d_{\max} = \frac{R_{\max}}{n} \right) \leq d_{\max}^* \end{array} \right. , \quad (7.1)$$

where, $d_{\min}^* = 0.738w(h)_{\min}$ and $d_{\max}^* = 0.738w(h)_{\max}$ by means of the multi-bead overlapping model. Eq.7.1 reveals the path planning for WAAM is highly geometry-related which is

affected by both the complexity of the geometry (variations of R) and the shape of deposit (w or d^*). By solving n , one can obtain

$$\begin{cases} \frac{R_{\min}}{d_{\max}^*} \leq n \leq \frac{R_{\min}}{d_{\min}^*} \\ \frac{R_{\max}}{d_{\max}^*} \leq n \leq \frac{R_{\max}}{d_{\min}^*} \end{cases}, \quad (7.2)$$

Eq.7.2 can be further simplified as

$$\frac{R_{\max}}{d_{\max}^*} \leq n \leq \frac{R_{\min}}{d_{\min}^*}, \quad (7.3)$$

Since n must be an integer, the final solution for n is given as

$$\text{ceil}\left(\frac{R_{\max}}{d_{\max}^*}\right) \leq n \leq \text{floor}\left(\frac{R_{\min}}{d_{\min}^*}\right), \quad (7.4)$$

where, function *ceil* rounds the elements within it to the nearest integers towards infinity and function *floor* rounds the elements within it to the nearest integers towards minus infinity.

In Eq.7.4, R_{\max} and R_{\min} are sliced layer geometry parameters which are obtained from medial axis transformation. For a given bead height (layer thickness) and the established bead model as shown in Figure 7.12, the range of achievable bead width can be determined, as well as d_{\min}^* and d_{\max}^* by means of the multi-bead overlapping model. Therefore, the optimum n for a domain can be easily solved. If there is no integer solution then the adaptive MAT path algorithm is not suitable for the domain. This means that the capability of the deposition system to vary the bead width while maintaining a constant bead height is not sufficient to accommodate the width variation of the given domain. In this case another path planning method such as non-adaptive MAT is applied to the domain, at the cost of increased deposition outside of the component boundary.

7.3.3 Determination of welding process parameters

When the desired weld bead geometries have been determined according to the generated adaptive paths, the next step is to determine appropriate welding parameters to produce the desired weld beads. To determine the optimal process parameters with the desired bead geometry, the following database with wire-feed rate and travel speed as the inputs and bead width and bead height as the outputs is established as shown in Figure 7.15.

$$\begin{bmatrix} F_1, S_1 & \dots & F_1, S_N \\ \vdots & F_i, S_j & \vdots \\ F_M, S_1 & \dots & F_M, S_N \end{bmatrix} \Rightarrow \begin{bmatrix} w_1, h_1 & \dots & w_1, h_N \\ \vdots & w_i, h_j & \vdots \\ w_M, h_1 & \dots & w_M, h_N \end{bmatrix}$$

Figure 7.15 The database of weld single bead model. $M = 61$, and $N = 61$ as mentioned in Section 7.3.1.

Given the outputs, the $error(i,j)$ corresponding to all input combinations are computed as the relevant error between the predicted bead geometry and the desired bead geometry. One can obtain the following formula

$$error(i, j) = \sqrt{\left(\frac{w_i - w_d}{w_d}\right)^2 + \left(\frac{h_j - h_d}{h_d}\right)^2}, (i = 1, 2, \dots, M; j = 1, 2, \dots, N), \quad (7.5)$$

where, w_d and h_d are the desired bead width and bead height, respectively. Through solving for the minimum value of $error(i,j)$, the optimal wire-feed rate and travel speed F_i and S_j are found.

7.3.4 Case studies

A. Case study 1

Figure 7.16 shows a thin-walled structure with a single internal hole and wall thickness ranging from 7 mm to 11 mm. Table 7.3 provides the main parameters of the geometry and path planning variables. The geometry is decomposed into two domains since it has one hole. The maximum and minimum radii for the two domains are listed in Table 7.3. For the given bead height h of 2 mm, the bead width ranges from 4.42 mm to 7.76 mm through altering wire-feed rate and travel speed. Accordingly, the critical step-over distances, d_{min}^* and d_{max}^* are 3.26 mm and 5.73 mm, respectively. By applying Eq.7.4, the path planning variables n_1 and n_2 are both solved as 1. Consequently, the adaptive MAT path for the geometry is generated as path 1 and path 2 shown in Figure 7.16. Red arrows show the start point (randomly set) and the deposition direction.

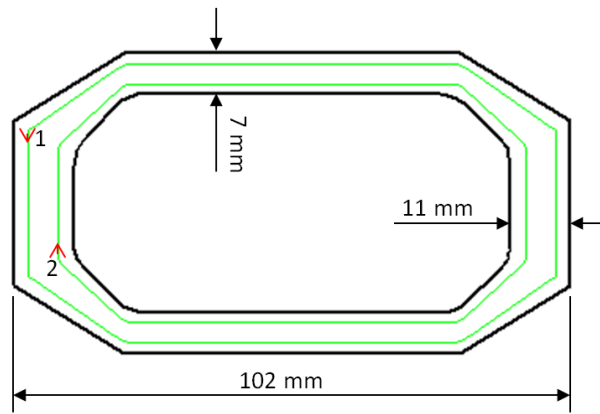


Figure 7.16 Case 1, a thin-walled structure with a single internal hole and varied wall thickness

Table 7.3 Information for Case 1 geometry and the resulting range of bead width. All units are millimetres except for n_1 and n_2 which are dimensionless variables

h	$(R_1)_{min}$	$(R_1)_{max}$	$(R_2)_{min}$	$(R_2)_{max}$	w_{min}	w_{max}	d^*_{min}	d^*_{max}	n_1	n_2
2	3.45	5.66	3.45	5.66	4.42	7.76	3.26	5.73	1	1

As the adaptive MAT path is generated, the step-over distances along the paths are progressively determined as shown in Figure 7.17 and Figure 7.18. Step-over distances vary along the length of the deposition path to accommodate the variation in thickness of the geometry. The wire-feed rates and travel speeds for the two paths are also shown in Figure 7.17 and Figure 7.18. For clarity, the minimum wire feed rate of 2.0 m/min and minimum travel speed of 0.4 m/min have been normalised to 1.0. It can be seen that with the changing of step-over distance, both wire-feed rate and travel speed are changed to produce the desired bead geometry suitable for the given range of step-over distance.

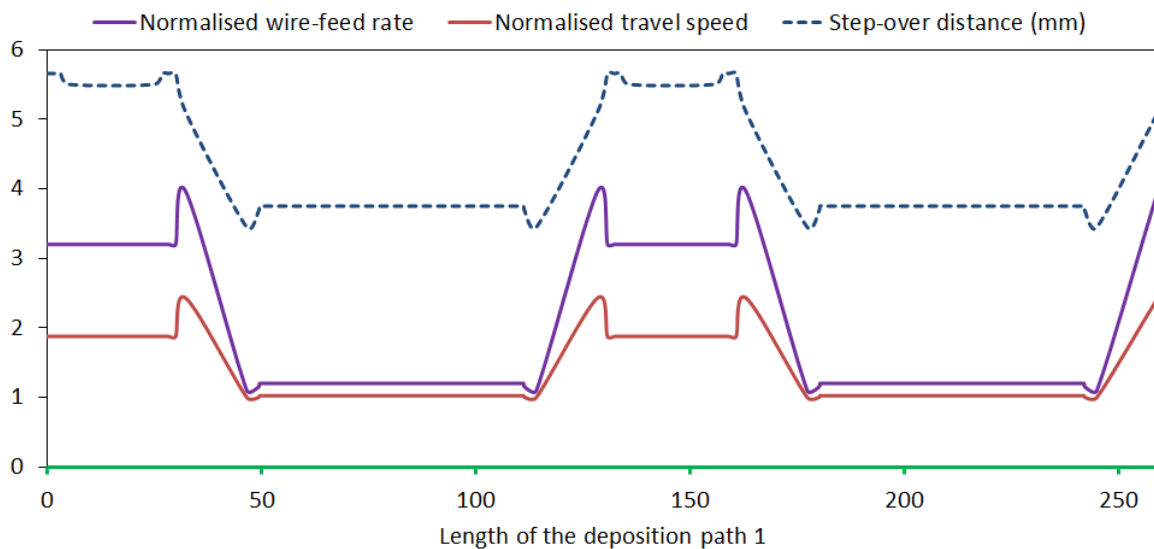


Figure 7.17 Calculated step-over distance (mm), normalised wire-feed rate, and normalised travel speed along the length of deposition path 1 (in mm)

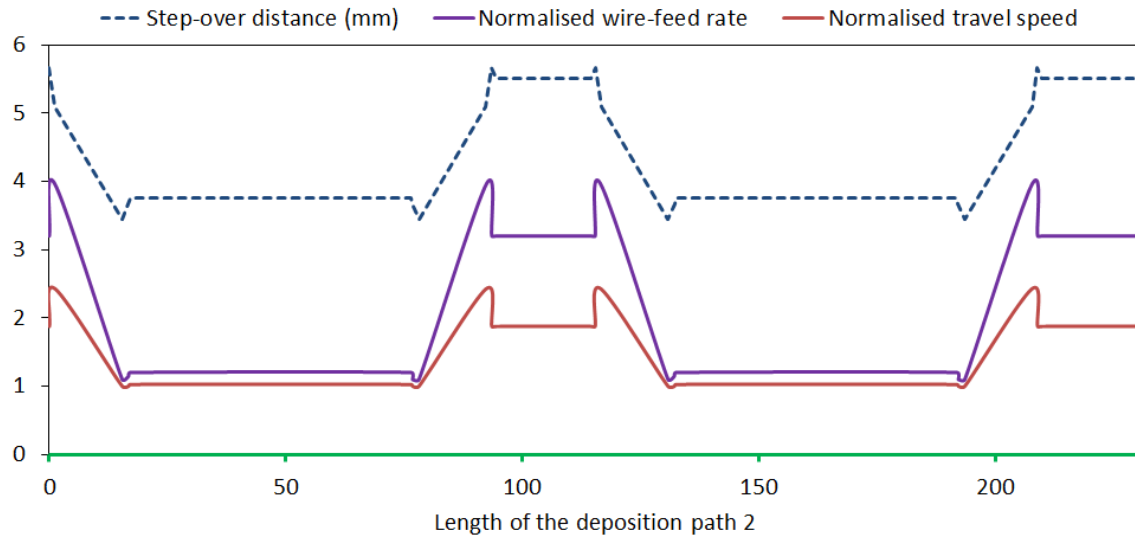


Figure 7.18 Calculated step-over distance (mm), normalised wire-feed rate, and normalised travel speed along the length of the deposition path 2 (in mm)

Using the generated paths and the welding process parameters, program code for the robotic manipulator and the welding power source is automatically generated. The near-net shape component was deposited with 15 layers, as shown in Figure 7.19a. Figure 7.19b shows the finished component after surface milling.

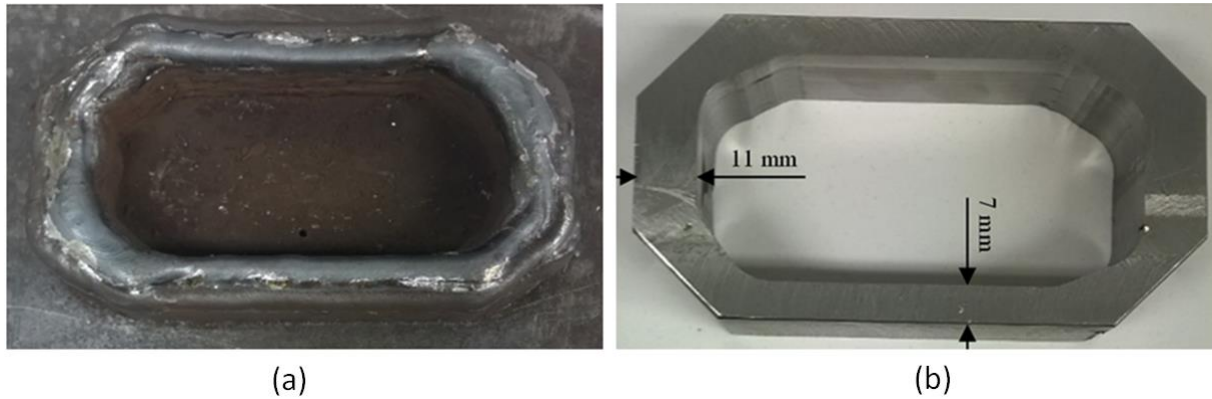


Figure 7.19 (a) Deposited near-net shape after 15 layers. (b) Finished part without voids after surface milling.

In order to check the potential internal defects, the finished component was cut into two pieces as shown in Figure 7.20a. The cross section A is parallel to the building direction and the cross section B is perpendicular to the building direction. Close up of the cross sections are shown in Figure 7.20b and Figure 7.20c. It can be seen that the deposited part is 100% solid and free of porosity.

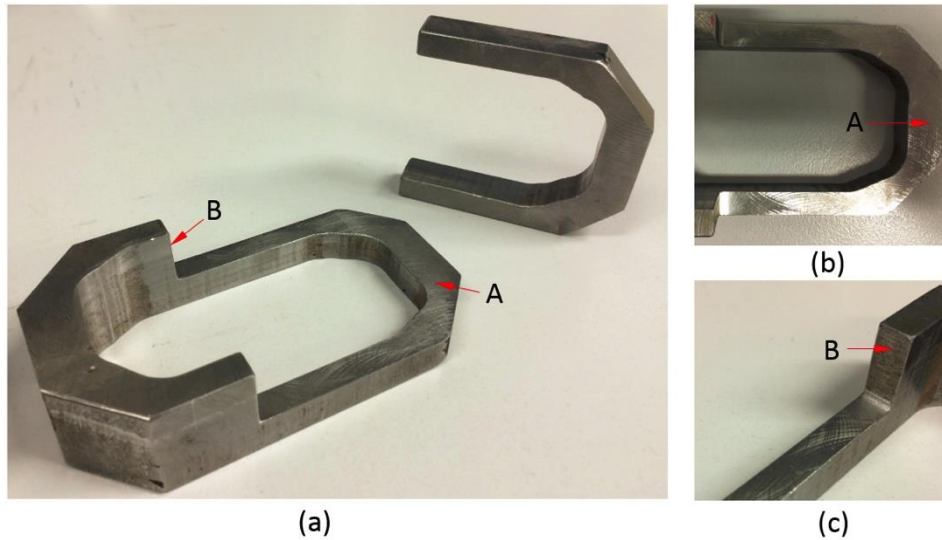


Figure 7.20 Examination of the internal cross sections. (a) Cut parts of the case one; the cross section A is parallel to the building direction and the cross section B is perpendicular to the building direction. (b) Close up of the cross section A. (c) Close up of the cross section B.”

B. Case study 2

Figure 7.21 shows an example of a solid structure without holes. The geometry has a length of 100 mm while the width ranges from 25 mm to 50 mm as described in Figure 7.21. Table 7.4 provides the geometrical parameters that were determined by the adaptive MAT path planning algorithm. The deposition path comprised of three closed loops with varied step-over distances. The red arrows in Figure 7.21 indicate the start points and the travel directions. For each layer, deposition was performed from the centre towards the boundary of the geometry. Figure 7.22 shows the step-over distance and the non-dimensional wire-feed rate and travel speed for the outermost path.

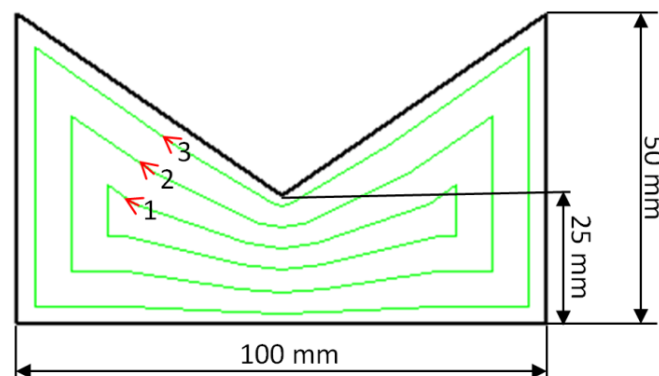


Figure 7.21 Case 2, a solid structure without holes.

Table 7.4 Information of Case 2 geometry and the resulting range of bead width. All units are millimetres except for n which is a dimensionless variable

h	R_{min}	R_{max}	w_{min}	w_{max}	d^*_{min}	d^*_{max}	n
2.5	16.15	21.69	5.90	10.28	4.35	7.59	3

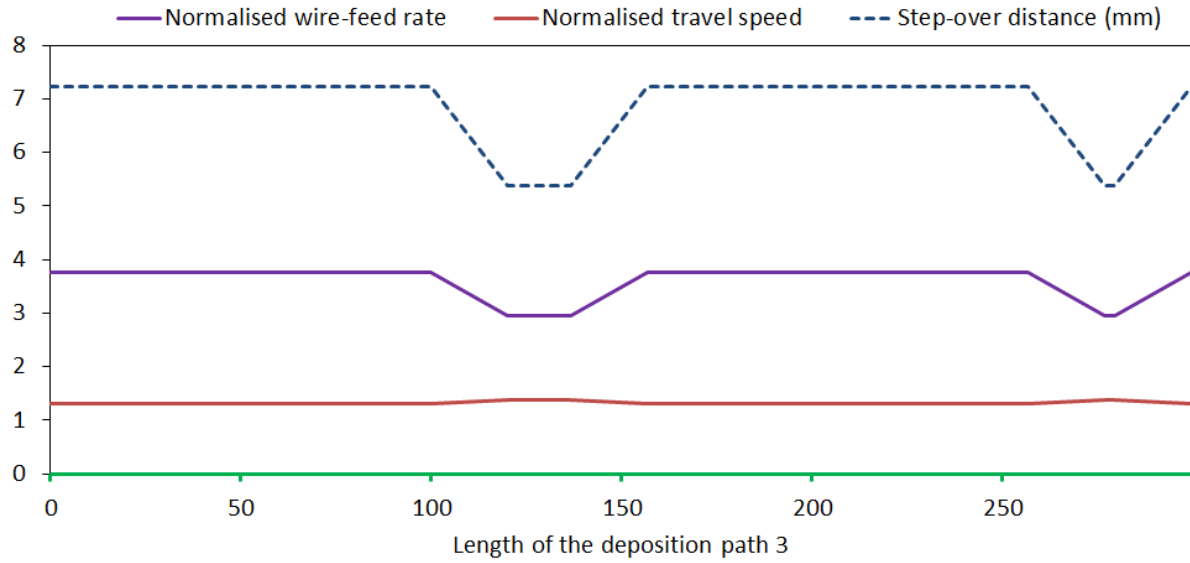


Figure 7.20 Calculated step-over distance (mm), normalised wire-feed rate, and normalised travel speed along the length of the deposition path 3 (in mm)

Although there is a large variation of geometry width from 25 mm to 50 mm, the component has been deposited through using only three closed paths with varying step-over distances. After deposition of 10-layers, the near-net shape component is shown in Figure 7.23a. The track of the deposition path can be seen from the upper surface of the shape. Figure 7.23b shows the finished part after post-process milling, free of internal voids or gaps.

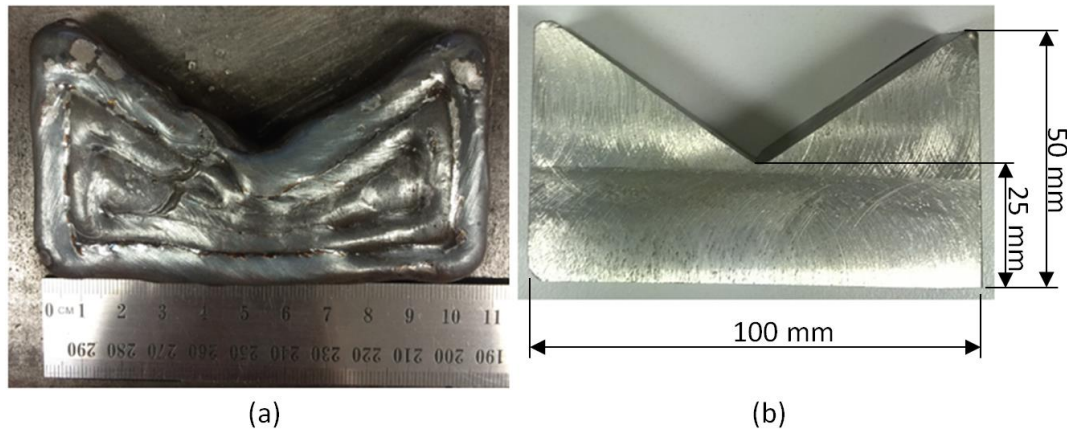


Figure 7.21 (a) Deposited near-net shape after 15 layers. (b) Finished part without voids after surface milling.

7.3.5 Discussions

The two case studies have provided examples of components having either thin-walled structures of varying thickness, or a solid structure with a large variation in across-layer

width. Both geometries provide significant challenges for the WAAM process, which has several requirements that should be met for optimum results:

1. Continuous deposits formed in closed loops to minimise start/stops that can give rise to height errors over multiple layers;
2. Continuous closed loop deposits at the component boundaries, to minimise the waste material that need to be removed by finish machining;
3. No cross-over of weld paths that create large localised variations in build height;
4. Adaptive step-over distance of the weld beads to avoid the formation of voids while producing a smooth upper surface for each layer and simultaneously conforming to the component boundaries;
5. Adaption of welding parameters to produce deposits of variable width at consistent height, to accommodate the adaptive step-over distance.

The automated path design, welding parameter selection, program code generation, and final deposition of the above two components indicates that the proposed adaptive MAT path planning algorithm is capable of generating continuous paths that can accommodate geometries with significant variations in wall thickness, while operating within the capabilities of the arc-wire welding process. The resulting deposition using the generated path produces components that are internally void-free and have good geometrical accuracy requiring minimal post-process milling. Although not exercised in these case studies, there are situations where the adaptive MAT process is not able to produce paths that conform to the component boundaries because of limitations of the welding process to deposit beads of sufficiently variable width. In such cases, the path generation algorithm defaults to using the non-adaptive MAT method. The component can still be produced automatically, but the component surface is less regular due to start/stops that must be performed at the boundary, and this would require more waste material to be removed to obtain the desired shape. This default situation is performed automatically, and hence contributes to the ultimate goal of producing a practical, computationally efficient and highly automated WAAM system for industrial application.

7.4 Summary

Various parts were fabricated to test all the aspects of the process planning in WAAM, including mild steel and aluminium alloy-fabricated components. Specifically, section 7.2

provided the whole process of additive and subtractive manufacturing of thin-walled aluminium component with finished quality. In addition, section 7.3 introduced the implementation of adaptive MAT paths in detail. The results show that the WAAM system has the capability to achieve high quality, void-free components that are geometrically accurate through properly designing the process variables. The developed automated system has been proven to be effective for WAAM.

Chapter 8

Summary and Future Work

8.1 Contributions

This study has developed a robotic Wire Arc Additive Manufacturing (WAAM) system with an integrated robotic machining process. A fully automated process planning methodology was introduced and verified through experimental tests on various metal parts. The integrated process planning methodology optimises the deposition efficiency and accuracy based on process modelling and a group of innovative algorithms. Detailed discussions of each step have been given in Chapters 2, 3, 4, 5, 6, and 7. The general contributions of this thesis are summarised as following:

Identification of process planning issues

The process planning requirements for Robotic Wire Arc Additive Manufacturing (WAAM) have been identified. There are three major challenges in producing final finished components from CAD models with minimal human intervention: accurate and practical bead geometry modelling; multi-direction 3D slicing; and deposition path planning.

The system starts from 3D CAD models in STL format, and these are sliced into a set of layers using a 3D slicing module. Then deposition paths are generated on each of layers through a 2D path planning module. Welding parameters associated with each generated paths are automatically selected using bead geometry model. Deposition paths together with the determined welding parameters are transferred into robot code proceeding to the fabrication process. Finally, the produced near-net shapes are machined through robotic post-process machining, and finished parts with the desired dimensional tolerances are obtained accordingly.

Establishment of an artificial neural network bead geometry model

The weld bead model controls two of the key slicing and path planning variables, namely layer thickness and step-over distance, respectively. In addition, it determines the optimum welding parameters corresponding to the desired bead geometry. Welding parameters are mainly wire-feed rate, travel speed, and stick-out length for the GMAW process in this study.

Special attention has been paid to develop an accurate artificial neural network bead model, in which the relationships between the welding parameters and bead profiles were established. Accordingly, a range of achievable bead height was obtained corresponding to the possible selection of layer thicknesses for slicing. In addition, the appropriate welding parameters in terms of the desired bead geometry could be determined automatically with the help of the ANN model.

Determination of the optimal step-over distance

In WAAM, the layer-by-layer building strategy incorporates the deposition of a large number of single weld beads side by side. Therefore, multi-bead overlapping plays an important role in determining the surface quality and dimensional accuracy of the fabricated products.

The tangent overlapping model (TOM) was developed and the optimal step-over distance was proposed. It has been found that the optimal step-over distance for producing a smooth upper surface is related to the bead width. A detailed experimental verification of the proposed TOM has been conducted.

Development of a multi-direction slicing algorithm

A novel multi-direction slicing algorithm was developed which extends the capability of WAAM to fabricate complex models by reducing the use of supports. Differing from the previously devised methodologies in the literature, model simplification and the concept of decomposition-regrouping are introduced in the workflow. The algorithm has been demonstrated as an efficient and flexible method for various types of CAD models in AM application. Since each step of the process maintains the integrity of STL format (triangle mesh), then intermediate results from each of the modules (such as model simplification, volume decomposition, and holes-extraction) can produce standard STL files to be used at other downstream CAD/CAM applications that are not limited to AM.

Development of MAT-based path planning methods

Medial axis transformation (MAT) –based paths were developed. MAT-based paths are particularly suitable for WAAM to fabricate void-free components through deposition of material starting from the centre and then progressing towards the boundary of the layer geometry. In addition, adaptive MAT paths were developed which varies the deposition width automatically to accommodate the changing geometry of the layer while maintaining continuous closed paths, especially at the external boundary. The adaptive MAT path enables the void-free deposition with minimum post-process machining.

8.2 Future work

Research and development of WAAM for metal components is interdisciplinary, integrating materials science, thermo-mechanical engineering, and process planning. This thesis provides a preliminary investigation on the development of an automated manufacturing system. Significant research and further understanding are required in aspects of process control and optimisation (particularly control residual stresses and distortions), and also automated process planning (3D slicing, path planning, and integrated milling). Combining the opinions proposed by other experts in the AM research field [8, 22, 110-115], the following is a summary of issues that are of particular significance for the future development of WAAM technology.

Material quality

High deposition rate is a remarkable advantage of wire-feed AM technology, but unfortunately it is accompanied by high heat input resulting in residual stresses and distortion. The control of residual stresses and distortion is a major concern especially for large-scale WAAM processes. To identify the optimum strategy for minimising residual stresses and distortion, both experiments and simulations are required. Significant investigations should focus on how stress evolution is influenced by process parameters (e.g. energy power, wire-feed rate, travel speed, wire diameter, etc.), cooling rates, preheating temperatures, and deposition patterns and sequences. Only when the residual stresses and distortions be eliminated or reduced, the components with good quality and accuracy could be achieved.

In this thesis, the mild steel and aluminium alloys have been used for deposition. Other materials, especially titanium alloys which are widely used in aerospace, are required to be

investigated using robotic WAAM. With regard to AM of titanium, more attention will need to be paid to gas shielding to avoid oxidation. It is expected that robotic post-process machining of titanium alloys will also present a unique set of challenges for producing acceptable surface finish while maintaining an economically viable cutting tool life.

Design

To date, WAAM is still only applied to simple structures. Real engineering components are more complex. A multi-direction deposition system which enhances the capability of the AM is required. However, the majority of existing 3D slicing strategies are applicable only to a subset of possible part geometries. More emphasis should be placed on multi-direction AM to develop robust algorithms capable of automatically slicing any 3D model in a manner that produce support-less and collision-free layered deposition.

Path planning for WAAM technology is made more complex when particular attention is paid to residual stress evolution and the dimensional relationship between the weld bead and the part geometry. The investigation of the evolution of residual stresses may guide the path planning methodology in terms of patterns and sequences. For components with complex geometry, the dimension related issue (especially the limited range of weld bead dimensions) is another challenge for automatic path planning.

Monitoring and Process control

The capability to achieve predictable and repeatable operations is important for WAAM. Since the deposition process has been shown to be extremely sensitive to process variations, a system for on-line monitoring and control of the deposition process is necessary. Although some preliminary studies have been reported on the control of the deposition process [35, 116, 117], more emphasis is required on this research area to increase the stability of the deposition process.

From near to net-shape

Due to limited accuracy, “stair-stepping” effect, and uneven surface finish, integrated 3D milling system is necessary for WAAM when high accuracy components are desired. For some complex components, 3D milling after the deposition of the entire component would be impossible due to the occurrence of tool collision. Periodic milling after deposition of each layer, or a number of layers, is one possible method for producing high accuracy components. However, this approach is time-consuming and potentially wasteful of materials. An effective

milling strategy will need to be developed from the geometry information of the original 3D components.

Manufacturing error analysis

In WAAM, manufacturing errors arise due to approximation of geometries during slicing and deposition path generation, as well as the finite weld bead deposit size. Predictive models that are capable to analysis the manufacturing error are required in order to improve the accuracy of the fabricated components. During the deposition process, online monitoring of the manufacturing error is also significant. When defects are detected, the deposition process needs to be suspended and corrective action taken to avoid wastage of both time and materials.

Appendix

A. Continuous path generation algorithm

This paper presents an algorithm to automatically generate continuous tool-paths for robotic wire and arc additive manufacturing (WAAM) process for a large class of geometries, especially solid geometries. The algorithm for generating deposition paths is provided as following.

The algorithm firstly decomposes 2D geometries into a set of convex polygons based on a divide-and-conquer strategy. Then, for each convex polygon, an optimal scan direction is identified and a continuous tool-path is generated using a combination of zigzag and contour pattern strategies. Finally, all individual sub-paths are connected to form a closed curve.

Decomposition of 2D geometries into convex polygons

STereoLithography (STL) is a commonly used file format for describing the 3D geometry of a component suitable for fabrication using AM. From this format, 2D slices can be readily generated. The decomposition of these 2D slices into simpler convex polygons, or monotone polygons, will make the implementation of path generation much easier. Many approaches have been developed for decomposing polygons, as described in the survey by Keil [118]. In this research, a divide-and-conquer method is used for decomposing the geometries.

The decomposition method is explained through a flowchart, as shown in Figure A.1. After slicing the input 3D CAD model, 2D geometries are obtained. Since STL is a tessellation language, the sliced 2D geometries are a set of polygons.

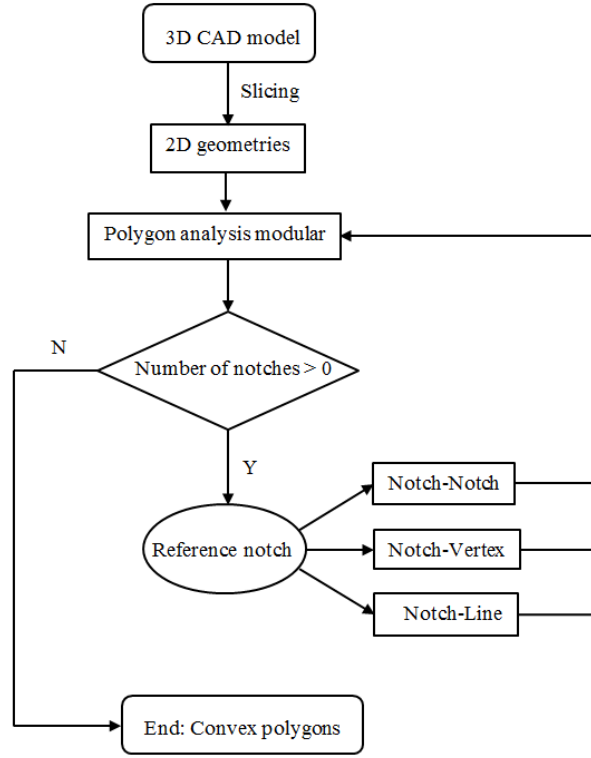


Figure A.1 The flowchart of the developed polygon decomposition method

The polygon analysis modular in Figure A.1 consist five steps.

Step 1: Identify the relationships among the polygons. The sliced 2D geometries may contain a number of polygons, either as internally nested shapes or independent entities. Using the concept of “Depth Tree” [96], the depth of a polygon refers to the number of cycles that enclose it. For example, in Figure A.2 (a), there is only one polygon and it has depth of “0”, according to the definition of “Depth Tree”, while in Figure A.2 (b) polygon 1 and polygon 2 have depths of “0” and “1”, respectively. Polygons that have even depth numbers are external cycles and those that have odd depth numbers are internal cycles. The details of this method can be found in [86].

Step 2: Order all vertices. In this study, the vertices of external cycles are ordered in clockwise direction, while those vertices of internal cycles are ordered in anti-clockwise direction. As shown in Fig. 3 (a) and (b), all vertices are ordered basing on these rules.

Step 3: Calculate the interior angles of all vertices. Assuming a polygon consists of n vertices, V_1, V_2, \dots, V_n , the interior angle φ_i at V_i can be calculated from Eq.(1) and (2)

$$\sin(\varphi_i) = \frac{\vec{e} \cdot (\overrightarrow{V_i V_{i-1}} \times \overrightarrow{V_i V_{i+1}})}{|\overrightarrow{V_i V_{i-1}}| \cdot |\overrightarrow{V_i V_{i+1}}|}, \quad (\text{A.1})$$

$$\cos(\varphi_i) = \frac{\overrightarrow{V_i V_{i-1}} \cdot \overrightarrow{V_i V_{i+1}}}{|\overrightarrow{V_i V_{i-1}}| \cdot |\overrightarrow{V_i V_{i+1}}|}. \quad (\text{A.2})$$

where, ϕ_i ranges from 0 to 2π and \vec{e} is the unit vector in the buildup direction. Both equations are needed to determine the quadrant of the angle.

Step 4: Identify notches. A notch is defined as a vertex whose interior angle is larger than π . A polygon has at least one notch is called a non-convex polygon; otherwise it is a convex polygon. The process of decomposing a non-convex polygon to convex polygons can be considered to be the process of eliminating notches. For example, the polygon in Figure A.2(a) is a non-convex polygon since the vertices V_2 , V_5 , V_6 and V_i are notches.

Step 5: Eliminate notches. The next step for polygon decomposition is to eliminate the identified notches. All the notches are sorted by their interior angle. The notch that has the greatest interior angle is set to be the reference notch, which is targeted for elimination. As shown in Figure A.3, assuming V_i is the reference notch, two radial lines are generated by extending vectors $\overrightarrow{V_{i-1}V_i}$ and $\overrightarrow{V_{i+1}V_i}$ to intersect with other part of the geometry at points A_i and B_i . There are three different cases along the geometry edges from A_i to B_i . Case 1: there are no vertices between A_i and B_i ; Case 2: there are notches between A_i and B_i ; Case 3: there are vertices between A_i and B_i but none of them are notches.

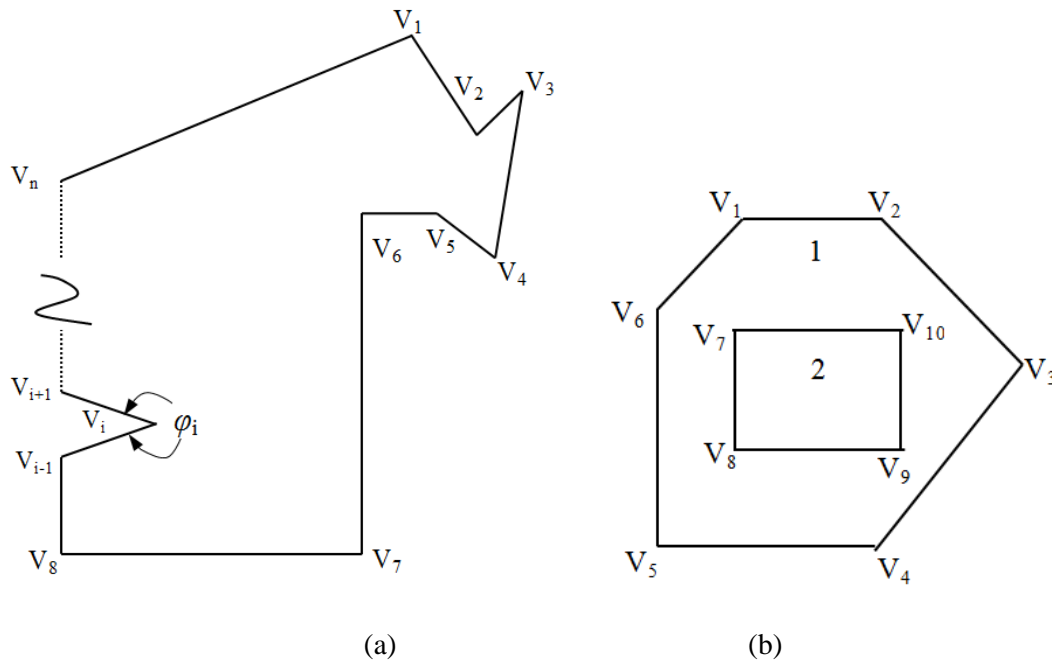


Figure A.2 Simple polygon without (a) and with inside island (b)

the simple polygon with an inside island is shown in Figure A.4. This algorithm is able to handle most 2D geometries, except for cases where there are many circular holes inside the geometry. Monotone polygon decomposition would be more suitable in such cases.

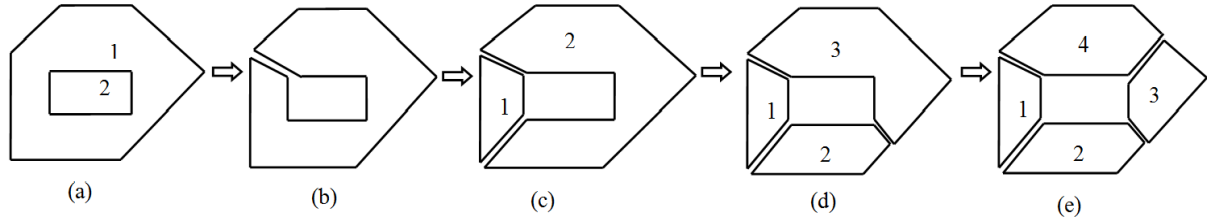


Figure A.4 Step-by-step processes of polygon decomposition

Path generation for a single convex polygon

For a convex polygon, filling the interior area using a zigzag path is an efficient strategy. To improve the geometrical accuracy, the outline of the convex polygon is fabricated using the contour method. Since a better surface finish can be obtained if there are less welding passes, the interior zigzag pattern and external contour are connected to a continuous path without starting-stopping. In order to minimize the numbers of tool-path elements, an optimal filling direction of zigzag pattern in the convex polygon should be identified. Taking the convex polygon labelled “4” in Figure A.4(e) as an example, the step-by-step algorithm for generating tool-path is described below.

Step 1: Identify the optimal zigzag direction. This problem can be restated as finding the direction where the convex polygon has the minimum height [94]. Lemma 1 explains that the optimal zigzag direction for a convex polygon must be parallel to one of its edges.

Lemma A.1. *Let P be a convex polygon, and S be an enveloping rectangle for P . For S to have the shortest height, i.e. a minimal number of weld passes is needed to fill S , there must be two vertices of P that lie on one of the long edges of S .*

Proof. As shown in Figure A.5, a convex polygon P is enclosed with a rectangle $ABCD$. Let AB and CD represent the long edges of the enveloping rectangle S . Let H stands for the distance between AB and CD . The problem of finding the optimal inclination of S can be considered to solve the minimum value of H . We assume the vertices V_n and V_m lie on AB and CD respectively. The distance between vertices V_n and V_m has the constant value of L . The angle $\theta_i > 0$, and $\alpha_i > 0$, $i = 1, 2, 3$, and 4. One can obtain the formula,

$$H = L \cdot \sin(\alpha_1 + \theta_1) = L \cdot \sin(\alpha_2 + \theta_2) = L \cdot \sin(\alpha_3 + \theta_3) = L \cdot \sin(\alpha_4 + \theta_4), \quad (\text{A.3})$$

$$\alpha_1 + \theta_1 = \alpha_3 + \theta_3, \quad (A.4)$$

$$\alpha_2 + \theta_2 = \alpha_4 + \theta_4, \quad (A.5)$$

$$\alpha_1 + \theta_1 = \pi - (\alpha_2 + \theta_2). \quad (A.6)$$

Without discrimination, assume $\alpha_1 + \theta_1 \leq \pi/2$ as shown in Figure A.5, S can be rotated anti-clockwise by $\Delta\theta$, where $0 \leq \Delta\theta \leq \min(\theta_1, \theta_3)$. After rotation, $H = L \cdot \sin(\alpha_1 + \theta_1 - \Delta\theta)$. Since the sine function is a monotonically increasing function in the range from 0 to $\pi/2$, H reaches the minimum value only when $\Delta\theta = \min(\theta_1, \theta_3)$. It demonstrated that H reaches the minimum value as long as one of θ_i is equal to zero by rotating the enveloping rectangle S . Therefore, two vertices of the polygon must lie on one of the long sides of the enveloping rectangle.

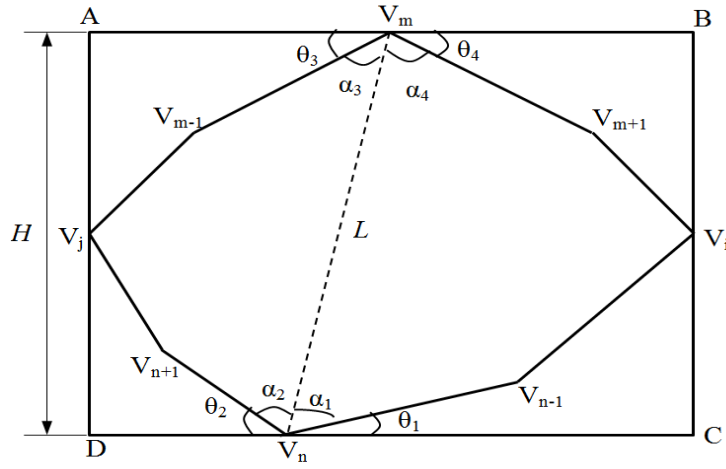


Figure A.5 A case in the proof of Lemma

Lemma 1 indicates that the optimal filling direction must be parallel to one edge of the polygon. Hence, the algorithm for identifying the optimal direction can be described as follows. For each polygon edge, calculate the distance from all the vertices to this edge. As the path should cover all of the polygon area, the maximum value of the distance should be recorded for the referred edge. When the maximum distance for all of the edges have been calculated individually, the edge that has the lowest value is selected as the direction corresponding to the optimal zigzag direction.

Step 2: Determine the left chain. The definition of left chain can be found in [91]. In Figure A.6 (a), EFA is the left chain.

Step 3: Offset the left chain (EFA) and generate a new polygon A'BCDE'F'A'.

Step 4: Generate a zigzag pattern with the calculated optimal direction in the interior area of the new polygon.

Step 5: Form a continuous path, as shown in Figure A.6 (b).

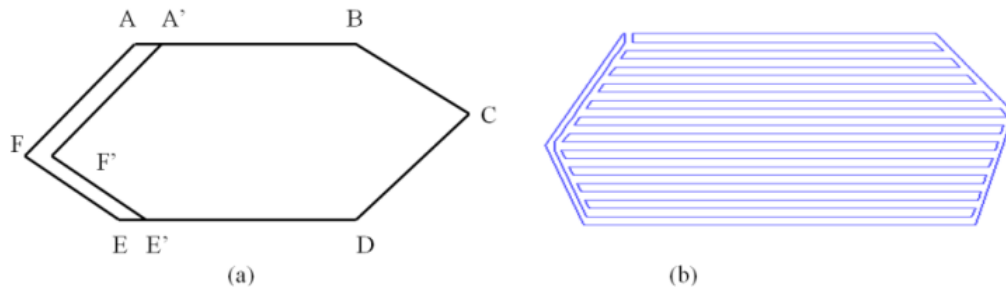


Figure A.6 An example of path generation for a convex polygon

From Step 1 to Step 5, a continuous path with the minimum number of elements can be generated for a convex polygon. Implement this approach independently to all of the convex polygons generated in Figure A.4 (e). The completed implementation is shown in Figure A.7 (a).

Path connection

The final step is to connect the sub-paths of each polygon into a closed curve. To improve the surface quality, the connecting points between two polygons are set on the outlines of the geometries.

During the decomposition of 2D geometries, the partition lines were used to regenerate the sub-polygons. The partition lines can be classified into two groups, merging lines and split lines. A merging line merges two polygons into one polygon. As shown in Figure A.4, the step from (a) to (b) is a merging process. A split line separates one polygon into two polygons. In Figure A.4, steps from (b) to (c), (c) to (d) and (d) to (e) are splitting processes. All of the split lines are stored in a new matrix for path connection. Since the split lines separate the polygons, connection lines between the separated polygons are generated that correspond to each of the split lines. As shown in Figure A.7 (b), the tool-paths in the area of the circles were reorganized. The proposed method can automatically generate a final closed-looped tool-path as shown in Figure A.7 (b). Note that this path planning strategy allows the possibility of connecting paths from consecutive layers of the model to form a continuous space curve in 3 dimensions, spanning multiple layers.

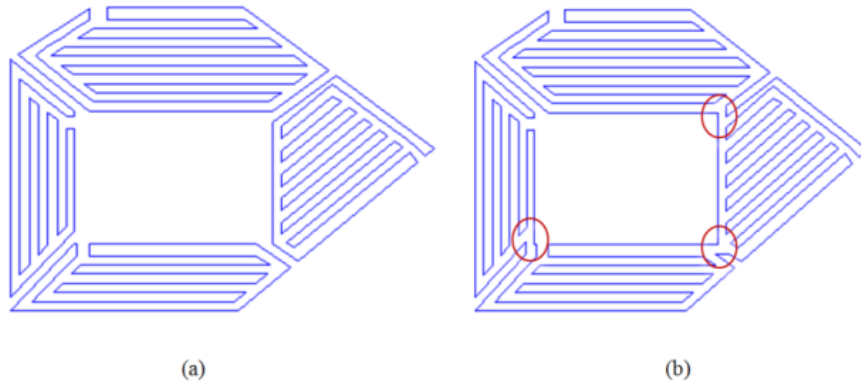


Figure A.7 Final tool-paths connection

B. Smallest enclosing crowns

First, we generate a random permutation unit vectors op_1, op_2, \dots, op_n . Points of P lie on the unit sphere with point o as the centre. Let $P_i = (p_1, p_2, \dots, p_n)$. The points are added one by one while the smallest enclosing crown C_j is maintained.

Lemma B.1 *Let $3 < i < n$, and let P_i and C_j be defined as above. Then we have*

If $P_i \in C_{j-1}$, then $C_j = C_{j-1}$, else P_i lies on the boundary of C_j .

The proof of the lemma was provided in [91].

Algorithm MiniCrown(P)

Input. A set P of n points on the sphere.

Output. The smallest enclosing sphere crown for P .

1. Compute a random permutation p_1, p_2, \dots, p_n of P .
2. Let C_3 be the smallest enclosing crown for (p_1, p_2, p_3) .
3. **For** i from 4 to n
4. **If** $P_i \in C_{j-1}$
5. **Then** $C_j = C_{j-1}$
6. **Else** $C_j = \text{MiniCrownWithPoint}((p_1, \dots, p_{i-1}), p_i)$
7. **Return** C_n

The step for determining whether the point p_i is contained in the current smallest crown C_j is given as follows.

As shown in Figure B.1, the spherical crown C_j has the bottom circular surface S_j . B_j is the current build direction. p_{ij} is the projection of p_i on the surface S_j . If C_j contains the point p_i , two conditions should be fulfilled:

$$\overrightarrow{OP_i} \cdot \overrightarrow{B_j} \geq 0;$$

$$|O_j P_{ij}| \leq R_j.$$

where, R_j is the radius of the bottom boundary circle of the spherical crown C_j .

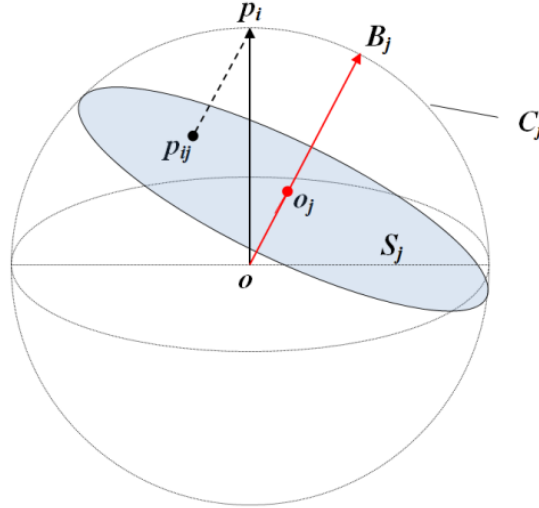


Figure B.1 Rules for determining whether the point p_i is contained in the current smallest crown C_j

The critical step occurs when p_i is not enclosed by C_{j-1} . A subroutine that finds the smallest crown enclosing P_i is required. Using the lemma B.1, p_i must lie on the boundary of the crown C_j . Let $q = p_i$. The same framework is used once more: we add the points of P_{i-1} in random order, and maintain the smallest enclosing crown of $P_{i-1} \cup \{q\}$ under the extra constraint that it should have q on its boundary. The addition of a point p_j will be facilitated by the following fact: when p_j is contained in the currently smallest enclosing crown then this crown remains the same, and otherwise it must have p_j on its boundary. So in the latter case, the crown has both q and p_j and its boundary. The following subroutine is obtained.

Algorithm MiniCrownWithPoint(P, q)

Input. A set P of n points on the surface of the sphere, and a point q such that there exists an enclosing crown for P with q on its boundary.

Output. The smallest enclosing crown for P with q on its boundary.

1. Compute a random permutation p_1, \dots, p_n of P .
2. Let C_2 be the smallest crown with q, p_1 , and p_2 on its boundary.
3. **For** j from 3 to n
4. **If** $p_j \in C_{j-1}$
5. **Then** $C_j = C_{j-1}$
6. **Else** $C_j = \text{MiniCrownWith2Point}((p_1, \dots, p_{j-1}), p_j, q)$
7. **Return** C_j

To find the smallest enclosing crown for a set under the restriction that two given points q_1 and q_2 lie on its boundary, the same approach need to be used one more time. Thus we add

the points in random order and maintain the optimal crown. When the added point p_k is inside the current crown, nothing need to do and just keep the current crown. When p_k is not inside the current crown, it must be on the boundary of the new crown. In the latter case three points on the crown boundary are obtained, namely, q_1 , q_2 , and p_k . This means there is only one crown left, the unique crown with q_1 , q_2 , and p_k on its boundary. The detailed routine is provided as following.

Algorithm MiniCrownWith2Point(P, q_1, q_2)

Input. A set P of n points on the surface of a unit sphere, and two points q_1 and q_2 such that there exists an enclosing crown for P with q_1 and q_2 on its boundary.

Output. The smallest enclosing crown for P with q_1 and q_2 on its boundry.

1. Compute a random permutation p_1, \dots, p_n of P .
2. Let C_1 be the smallest crown with q_1, q_2 , and p_1 on its boundary.
3. **For** j from 2 to n
4. **If** $P_j \in C_{j-1}$
5. **Then** $C_j = C_{j-1}$
6. **Else** $C_j =$ the Crown with q_1, q_2 , and p_j on its boundary, **Exit** for
7. **Return** C_j

This finally completes the algorithm for computing the smallest enclosing crown of a set of points on a sphere. The validation of the algorithm is similar as that for the smallest enclosing discs could be found [91].

References

- [1] E. Sachs, M. Cima, P. Williams, D. Brancazio, and J. Cornie, "Three Dimensional Printing: Rapid Tooling and Prototypes Directly from a CAD Model," *Journal of Engineering for Industry*, vol. 114, pp. 481-488, 1992.
- [2] M. Agarwala, D. Bourell, J. Beaman, H. Marcus, and J. Barlow, "Direct selective laser sintering of metals," *Rapid Prototyping Journal*, vol. 1, pp. 26-36, 1995.
- [3] J. Mireles, H.-C. Kim, I. H. Lee, D. Espalin, F. Medina, E. MacDonald, *et al.*, "Development of a fused deposition modeling system for low melting temperature metal alloys," *Journal of Electronic Packaging*, vol. 135, p. 011008, 2013.
- [4] D. L. Bourell, M. C. Leu, and D. W. Rosen, "Roadmap for additive manufacturing: identifying the future of freeform processing," *The University of Texas at Austin, Austin, TX*, 2009.
- [5] J. Ding, P. Colegrove, J. Mehnert, S. Ganguly, P. S. Almeida, F. Wang, *et al.*, "Thermo-mechanical analysis of Wire and Arc Additive Layer Manufacturing process on large multi-layer parts," *Computational Materials Science*, vol. 50, pp. 3315-3322, 2011.
- [6] J. N. Zalameda, E. R. Burke, R. A. Hafley, K. M. Taminger, C. S. Domack, A. Brewer, *et al.*, "Thermal imaging for assessment of electron-beam freeform fabrication (EBF3) additive manufacturing deposits," in *SPIE Defense, Security, and Sensing*, 2013, pp. 87050M-87050M-8.
- [7] J. Mazumder, A. Schifferer, and J. Choi, "Direct materials deposition: designed macro and microstructure," *Material Research Innovations*, vol. 3, pp. 118-131, 1999.
- [8] G. N. Levy, R. Schindel, and J.-P. Kruth, "Rapid manufacturing and rapid tooling with layer manufacturing (LM) technologies, state of the art and future perspectives," *CIRP Annals-Manufacturing Technology*, vol. 52, pp. 589-609, 2003.
- [9] D. King and T. Tansey, "Rapid tooling: selective laser sintering injection tooling," *Journal of materials processing Technology*, vol. 132, pp. 42-48, 2003.
- [10] N. Kapustka and I. D. Harris, "Exploring Arc Welding for Additive Manufacturing of Titanium Parts," *Welding journal*, vol. 93, pp. 32-35, 2014.
- [11] A. Simchi, F. Petzoldt, and H. Pohl, "On the development of direct metal laser sintering for rapid tooling," *Journal of Materials Processing Technology*, vol. 141, pp. 319-328, 2003.
- [12] P. Heintz, L. Müller, C. Körner, R. F. Singer, and F. A. Müller, "Cellular Ti-6Al-4V structures with interconnected macro porosity for bone implants fabricated by selective electron beam melting," *Acta biomaterialia*, vol. 4, pp. 1536-1544, 2008.
- [13] J.-P. Kruth, L. Froyen, J. Van Vaerenbergh, P. Mercelis, M. Rombouts, and B. Lauwers, "Selective laser melting of iron-based powder," *Journal of Materials Processing Technology*, vol. 149, pp. 616-622, 2004.
- [14] K. M. Taminger and R. A. Hafley, "Electron beam freeform fabrication: a rapid metal deposition process," in *3rd Annual Automotive Composites Conference, Troy, MI, Sept*, 2003, pp. 9-10.
- [15] C. Atwood, M. Ensz, D. Greene, M. Griffith, L. Harwell, D. Reckaway, *et al.*, "Laser engineered net shaping (LENS (TM)): A tool for direct fabrication of metal parts," Sandia National Laboratories, Albuquerque, NM, and Livermore, CA1998.
- [16] T. Furumoto, T. Ueda, N. Kobayashi, A. Yassin, A. Hosokawa, and S. Abe, "Study on laser consolidation of metal powder with Yb: fiber laser—Evaluation of line consolidation structure," *Journal of Materials Processing Technology*, vol. 209, pp. 5973-5980, 2009.

- [17] J. Milewski, G. Lewis, D. Thoma, G. Keel, R. Nemec, and R. Reinert, "Directed light fabrication of a solid metal hemisphere using 5-axis powder deposition," *Journal of Materials Processing Technology*, vol. 75, pp. 165-172, 1998.
- [18] F. Wang, S. Williams, P. Colegrove, and A. A. Antonysamy, "Microstructure and mechanical properties of wire and arc additive manufactured Ti-6Al-4V," *Metallurgical and Materials Transactions A*, vol. 44, pp. 968-977, 2013.
- [19] B. Utela, D. Storti, R. Anderson, and M. Ganter, "A review of process development steps for new material systems in three dimensional printing (3DP)," *Journal of Manufacturing Processes*, vol. 10, pp. 96-104, 2008.
- [20] B. Mueller and D. Kochan, "Laminated object manufacturing for rapid tooling and patternmaking in foundry industry," *Computers in Industry*, vol. 39, pp. 47-53, 1999.
- [21] C. Kong and R. Soar, "Fabrication of metal-matrix composites and adaptive composites using ultrasonic consolidation process," *Materials Science and Engineering: A*, vol. 412, pp. 12-18, 2005.
- [22] D. Gu, W. Meiners, K. Wissenbach, and R. Poprawe, "Laser additive manufacturing of metallic components: materials, processes and mechanisms," *International materials reviews*, vol. 57, pp. 133-164, 2012.
- [23] L. Xue and M. U. Islam, "Laser consolidation-a novel one-step manufacturing process for making net-shape functional components," DTIC Document 2006.
- [24] K. Mumtaz and N. Hopkinson, "Top surface and side roughness of Inconel 625 parts processed using selective laser melting," *Rapid Prototyping Journal*, vol. 15, pp. 96-103, 2009.
- [25] Y. Zhang, Z. Wei, L. Shi, and M. Xi, "Characterization of laser powder deposited Ti-TiC composites and functional gradient materials," *Journal of materials processing technology*, vol. 206, pp. 438-444, 2008.
- [26] H. Zhu, L. Lu, and J. Fuh, "Development and characterisation of direct laser sintering Cu-based metal powder," *Journal of Materials Processing Technology*, vol. 140, pp. 314-317, 2003.
- [27] D. Ding, Z. Pan, D. Cuiuri, and H. Li, "A multi-bead overlapping model for robotic wire and arc additive manufacturing (WAAM)," *Robotics and Computer-Integrated Manufacturing*, vol. 31, pp. 101-110, 2015.
- [28] D. Ding, Z. S. Pan, D. Cuiuri, and H. Li, "A tool-path generation strategy for wire and arc additive manufacturing," *The International Journal of Advanced Manufacturing Technology*, vol. 73, pp. 173-183, 2014.
- [29] P. Colegrove and S. Williams, "High deposition rate high quality metal additive manufacture using wire+ arc technology," ed, 2010.
- [30] K. M. Taminger and R. A. Hafley, *Electron beam freeform fabrication (EBF3) for cost effective near-net shape manufacturing*: National Aeronautics and Space Administration, Langley Research Center, 2006.
- [31] W. U. H. Syed, A. J. Pinkerton, and L. Li, "A comparative study of wire feeding and powder feeding in direct diode laser deposition for rapid prototyping," *Applied Surface Science*, vol. 247, pp. 268-276, 2005.
- [32] W. U. H. Syed, A. J. Pinkerton, and L. Li, "Combining wire and coaxial powder feeding in laser direct metal deposition for rapid prototyping," *Applied surface science*, vol. 252, pp. 4803-4808, 2006.
- [33] F. Wang, J. Mei, H. Jiang, and X. Wu, "Laser fabrication of Ti6Al4V/TiC composites using simultaneous powder and wire feed," *Materials Science and Engineering: A*, vol. 445, pp. 461-466, 2007.
- [34] K. Karunakaran, S. Suryakumar, V. Pushpa, and S. Akula, "Low cost integration of additive and subtractive processes for hybrid layered manufacturing," *Robotics and Computer-Integrated Manufacturing*, vol. 26, pp. 490-499, 2010.

- [35] A. Heralic, *Monitoring and control of robotized laser metal-wire deposition*: Chalmers University of Technology, 2012.
- [36] R. Unocic and J. DuPont, "Process efficiency measurements in the laser engineered net shaping process," *Metallurgical and materials transactions B*, vol. 35, pp. 143-152, 2004.
- [37] L.-E. Rännar, A. Glad, and C.-G. Gustafson, "Efficient cooling with tool inserts manufactured by electron beam melting," *Rapid Prototyping Journal*, vol. 13, pp. 128-135, 2007.
- [38] J. DuPont and A. Marder, "Thermal efficiency of arc welding processes," *Welding Journal-Including Welding Research Supplement*, vol. 74, p. 406s, 1995.
- [39] N. Stenbacka, I. Choquet, and K. Hurtig, "Review of arc efficiency values for gas tungsten arc welding," in *IIW Commission IV-XII-SG212, Intermediate Meeting, BAM, Berlin, Germany, 18-20 April, 2012*, 2012, pp. 1-21.
- [40] P. Dickens, M. Pridham, R. Cobb, I. Gibson, and G. Dixon, "Rapid prototyping using 3-D welding," in *Proc. Solid Freeform Fabrication Symp*, 1992, pp. 280-290.
- [41] A. F. Ribeiro and J. Norrish, "Rapid prototyping process using metal directly," 1996.
- [42] J. Spencer, P. Dickens, and C. Wykes, "Rapid prototyping of metal parts by three-dimensional welding," *Proceedings of the Institution of Mechanical Engineers, Part B: Journal of Engineering Manufacture*, vol. 212, pp. 175-182, 1998.
- [43] Y. M. Zhang, P. Li, Y. Chen, and A. T. Male, "Automated system for welding-based rapid prototyping," *Mechatronics*, vol. 12, pp. 37-53, 2002.
- [44] Y.-A. Song, S. Park, D. Choi, and H. Jee, "3D welding and milling: Part I—a direct approach for freeform fabrication of metallic prototypes," *International Journal of Machine Tools and Manufacture*, vol. 45, pp. 1057-1062, 2005.
- [45] S. Suryakumar, K. Karunakaran, A. Bernard, U. Chandrasekhar, N. Raghavender, and D. Sharma, "Weld bead modeling and process optimization in hybrid layered manufacturing," *Computer-Aided Design*, vol. 43, pp. 331-344, 2011.
- [46] J. Xiong, G. Zhang, H. Gao, and L. Wu, "Modeling of bead section profile and overlapping beads with experimental validation for robotic GMAW-based rapid manufacturing," *Robotics and Computer-Integrated Manufacturing*, vol. 29, pp. 417-423, 2013.
- [47] D. Hu and R. Kovacevic, "Sensing, modeling and control for laser-based additive manufacturing," *International Journal of Machine Tools and Manufacture*, vol. 43, pp. 51-60, 2003.
- [48] F. Bonaccorso, L. Cantelli, and G. Muscato, "An arc welding robot control for a shaped metal deposition plant: Modular software interface and sensors," *Industrial Electronics, IEEE Transactions on*, vol. 58, pp. 3126-3132, 2011.
- [49] J. Xiong, G. Zhang, Z. Qiu, and Y. Li, "Vision-sensing and bead width control of a single-bead multi-layer part: material and energy savings in GMAW-based rapid manufacturing," *Journal of Cleaner Production*, vol. 41, pp. 82-88, 2013.
- [50] R. Kovacevic and H. Beardsley, "Process Control of 3D Welding as a Droplet-Based Rapid Prototyping Technique," in *Proc. of the SFF Symposium, Univ. of Texas at Austin, Austin TX*, 1998, pp. 57-64.
- [51] R. Dwivedi and R. Kovacevic, "Automated torch path planning using polygon subdivision for solid freeform fabrication based on welding," *Journal of Manufacturing Systems*, vol. 23, pp. 278-291, 2004.
- [52] Z. Jandric, M. Labudovic, and R. Kovacevic, "Effect of heat sink on microstructure of three-dimensional parts built by welding-based deposition," *International Journal of Machine Tools and Manufacture*, vol. 44, pp. 785-796, 2004.
- [53] Y. Zhang, Y. Chen, P. Li, and A. T. Male, "Weld deposition-based rapid prototyping: a preliminary study," *Journal of Materials Processing Technology*, vol. 135, pp. 347-357, 2003.
- [54] Y.-M. Kwak and C. C. Douranidis, "Geometry regulation of material deposition in near-net shape manufacturing by thermally scanned welding," *Journal of Manufacturing Processes*, vol. 4, pp. 28-41, 2002.

- [55] R. Merz, F. Prinz, K. Ramaswami, M. Terk, and L. Weiss, *Shape deposition manufacturing: Engineering Design Research Center, Carnegie Mellon Univ.*, 1994.
- [56] W. Aiyiti, W. Zhao, B. Lu, and Y. Tang, "Investigation of the overlapping parameters of MPAW-based rapid prototyping," *Rapid Prototyping Journal*, vol. 12, pp. 165-172, 2006.
- [57] F. Martina, J. Mehnen, S. W. Williams, P. Colegrove, and F. Wang, "Investigation of the benefits of plasma deposition for the additive layer manufacture of Ti-6Al-4V," *Journal of Materials Processing Technology*, vol. 212, pp. 1377-1386, 2012.
- [58] D. Ding, Z. Pan, D. Cuiuri, and H. Li, "A practical path planning methodology for wire and arc additive manufacturing of thin-walled structures," *Robotics and Computer-Integrated Manufacturing*, vol. 34, pp. 8-19, 2015.
- [59] D. Ding, Z. Pan, D. Cuiuri, and H. Li, "Wire-feed additive manufacturing of metal components: technologies, developments and future interests," *The International Journal of Advanced Manufacturing Technology*, pp. 1-17, 2015.
- [60] Y. Ma, D. Cuiuri, N. Hoyer, H. Li, and Z. Pan, "The effect of location on the microstructure and mechanical properties of titanium aluminides produced by additive layer manufacturing using in-situ alloying and gas tungsten arc welding," *Materials Science and Engineering: A*, vol. 631, pp. 230-240, 2015.
- [61] J. Fessler, R. Merz, A. Nickel, F. Prinz, and L. Weiss, "Laser deposition of metals for shape deposition manufacturing," in *Proceedings of the Solid Freeform Fabrication Symposium*, 1996, pp. 117-124.
- [62] A. Nickel, D. Barnett, and F. Prinz, "Thermal stresses and deposition patterns in layered manufacturing," *Materials Science and Engineering: A*, vol. 317, pp. 59-64, 2001.
- [63] A. H. Nickel, "Analysis of thermal stresses in shape deposition manufacturing of metal parts," Stanford University, 1999.
- [64] E. Foroozmehr and R. Kovacevic, "Effect of path planning on the laser powder deposition process: thermal and structural evaluation," *The International Journal of Advanced Manufacturing Technology*, vol. 51, pp. 659-669, 2010.
- [65] M. Mughal, H. Fawad, and R. Mufti, "Finite element prediction of thermal stresses and deformations in layered manufacturing of metallic parts," *Acta mechanica*, vol. 183, pp. 61-79, 2006.
- [66] M. Mughal, H. Fawad, R. Mufti, and M. Siddique, "Deformation modelling in layered manufacturing of metallic parts using gas metal arc welding: effect of process parameters," *Modelling and Simulation in Materials Science and Engineering*, vol. 13, p. 1187, 2005.
- [67] R. Chin, J. Beuth, and C. Amon, "Thermomechanical modeling of molten metal droplet solidification applied to layered manufacturing," *Mechanics of Materials*, vol. 24, pp. 257-271, 1996.
- [68] P. S. Almeida and S. Williams, "Innovative process model of Ti-6Al-4V additive layer manufacturing using cold metal transfer (CMT)," in *Proceedings of the 21st Annual International Solid Freeform Fabrication Symposium*, 2010, pp. 25-36.
- [69] P. A. Colegrove, H. E. Coules, J. Fairman, F. Martina, T. Kashoob, H. Mamash, et al., "Microstructure and residual stress improvement in wire and arc additively manufactured parts through high-pressure rolling," *Journal of Materials Processing Technology*, vol. 213, pp. 1782-1791, 2013.
- [70] J. Ding, P. Colegrove, J. Mehnen, S. Williams, F. Wang, and P. S. Almeida, "A computationally efficient finite element model of wire and arc additive manufacture," *The International Journal of Advanced Manufacturing Technology*, vol. 70, pp. 227-236, 2014.
- [71] S. Sun, H. Chiang, and M. Lee, "Adaptive direct slicing of a commercial CAD model for use in rapid prototyping," *The International Journal of Advanced Manufacturing Technology*, vol. 34, pp. 689-701, 2007.

- [72] P. Singh and D. Dutta, "Multi-Direction Layered Deposition—An Overview of Process Planning Methodologies," in *Proceedings of the Solid Freeform Fabrication Symposium*, 2003, pp. 279-288.
- [73] Y. Cao, S. Zhu, X. Liang, and W. Wang, "Overlapping model of beads and curve fitting of bead section for rapid manufacturing by robotic MAG welding process," *Robotics and Computer-Integrated Manufacturing*, vol. 27, pp. 641-645, 2011.
- [74] M. I. S. Ismail, Y. Okamoto, and A. Okada, "Neural Network Modeling for Prediction of Weld Bead Geometry in Laser Microwelding," *Advances in Optical Technologies*, vol. 2013, 2013.
- [75] J. Xiong, G. Zhang, J. Hu, and L. Wu, "Bead geometry prediction for robotic GMAW-based rapid manufacturing through a neural network and a second-order regression analysis," *Journal of Intelligent Manufacturing*, vol. 25, pp. 157-163, 2014.
- [76] H. Tang, K. C. Tan, and Y. Zhang, "Neural networks: Computational models and applications," ed: Berlin, Germany: Springer, 2007.
- [77] S. Choi and K. Kwok, "A tolerant slicing algorithm for layered manufacturing," *Rapid Prototyping Journal*, vol. 8, pp. 161-179, 2002.
- [78] P. Singh and D. Dutta, "Multi-direction slicing for layered manufacturing," *Journal of Computing and Information Science in Engineering*, vol. 1, pp. 129-142, 2001.
- [79] Y. Yang, J. Fuh, H. Loh, and Y. Wong, "Multi-orientational deposition to minimize support in the layered manufacturing process," *Journal of manufacturing systems*, vol. 22, pp. 116-129, 2003.
- [80] J. Ruan, T. E. Sparks, A. Panackal, F. W. Liou, K. Eiamsa-ard, K. Slattery, *et al.*, "Automated slicing for a multiaxis metal deposition system," *Journal of manufacturing science and engineering*, vol. 129, pp. 303-310, 2007.
- [81] J. Zhang and F. Liou, "Adaptive slicing for a multi-axis laser aided manufacturing process," *Journal of Mechanical Design*, vol. 126, pp. 254-261, 2004.
- [82] P. Singh and D. Dutta, "Offset slices for multidirection layered deposition," *Journal of Manufacturing Science and Engineering*, vol. 130, p. 011011, 2008.
- [83] R. Dwivedi and R. Kovacevic, "Process planning for multi-directional laser-based direct metal deposition," *Proceedings of the Institution of Mechanical Engineers, Part C: Journal of Mechanical Engineering Science*, vol. 219, pp. 695-707, 2005.
- [84] L. Ren, T. Sparks, J. Ruan, and F. Liou, "Process planning strategies for solid freeform fabrication of metal parts," *Journal of Manufacturing Systems*, vol. 27, pp. 158-165, 2008.
- [85] A. Razdan and M. Bae, "A hybrid approach to feature segmentation of triangle meshes," *Computer-Aided Design*, vol. 35, pp. 783-789, 2003.
- [86] N. Volpato, A. Franzoni, D. C. Luvizon, and J. M. Schramm, "Identifying the directions of a set of 2D contours for additive manufacturing process planning," *The international journal of advanced manufacturing technology*, pp. 1-11, 2013.
- [87] W. Zhao, S. Gao, and H. Lin, "A robust hole-filling algorithm for triangular mesh," *The Visual Computer*, vol. 23, pp. 987-997, 2007.
- [88] X. Wang, X. Liu, L. Lu, B. Li, J. Cao, B. Yin, *et al.*, "Automatic hole-filling of CAD models with feature-preserving," *Computers & Graphics*, vol. 36, pp. 101-110, 2012.
- [89] T. C. Woo, "Visibility maps and spherical algorithms," *Computer-Aided Design*, vol. 26, pp. 6-16, 1994.
- [90] J. Zhang and F. Liou, "Adaptive slicing for a multi-axis laser aided manufacturing process," *Journal of Mechanical Design*, vol. 126, p. 254, 2004.
- [91] M. De Berg, M. Van Kreveld, M. Overmars, and O. C. Schwarzkopf, *Computational geometry*: Springer, 2000.
- [92] M. R. Dunlavey, "Efficient polygon-filling algorithms for raster displays," *ACM Transactions on Graphics (TOG)*, vol. 2, pp. 264-273, 1983.
- [93] S. C. Park and B. K. Choi, "Tool-path planning for direction-parallel area milling," *Computer-Aided Design*, vol. 32, pp. 17-25, 2000.

- [94] V. Rajan, V. Srinivasan, and K. A. Tarabanis, "The optimal zigzag direction for filling a two-dimensional region," *Rapid Prototyping Journal*, vol. 7, pp. 231-241, 2001.
- [95] R. Farouki, T. Koenig, K. Tarabanis, J. Korein, and J. Batchelder, "Path planning with offset curves for layered fabrication processes," *Journal of Manufacturing Systems*, vol. 14, pp. 355-368, 1995.
- [96] Y. Yang, H. Loh, J. Fuh, and Y. Wang, "Equidistant path generation for improving scanning efficiency in layered manufacturing," *Rapid Prototyping Journal*, vol. 8, pp. 30-37, 2002.
- [97] H. Li, Z. Dong, and G. W. Vickers, "Optimal toolpath pattern identification for single island, sculptured part rough machining using fuzzy pattern analysis," *Computer-Aided Design*, vol. 26, pp. 787-795, 1994.
- [98] H. Wang, P. Jang, and J. A. Stori, "A metric-based approach to two-dimensional (2D) tool-path optimization for high-speed machining," *Transactions-American Society of Mechanical Engineers Journal of Manufacturing Science and Engineering*, vol. 127, p. 33, 2005.
- [99] F. Ren, Y. Sun, and D. Guo, "Combined reparameterization-based spiral toolpath generation for five-axis sculptured surface machining," *The international journal of advanced manufacturing technology*, vol. 40, pp. 760-768, 2009.
- [100] G. Jin, W. Li, and L. Gao, "An adaptive process planning approach of rapid prototyping and manufacturing," *Robotics and Computer-Integrated Manufacturing*, vol. 29, pp. 23-38, 2013.
- [101] M. Bertoldi, M. Yardimci, C. Pistor, and S. Guceri, "Domain decomposition and space filling curves in toolpath planning and generation," in *Proceedings of the 1998 Solid Freeform Fabrication Symposium, The University of Texas at Austin, Austin, Texas*, 1998, pp. 267-74.
- [102] T. Wasser, A. D. Jayal, and C. Pistor, "Implementation and evaluation of novel buildstyles in fused deposition modeling (FDM)," *Strain*, vol. 5, p. 6, 1999.
- [103] J. Mehnen, J. Ding, H. Lockett, and P. Kazanas, "Design for wire and arc additive layer manufacture," in *Global Product Development*, ed: Springer, 2011, pp. 721-727.
- [104] J.-H. Kao and F. B. Prinz, "Optimal motion planning for deposition in layered manufacturing," in *Proceedings of DETC*, 1998, pp. 13-16.
- [105] H. Blum, "A Transformation for Extracting New Descriptions of Shape," *Models for the perception of speech and visual form*, W. Wathen-Dunn (editor), MIT Press, pp362-380, 1967.
- [106] D. Lee, "Medial axis transformation of a planar shape," *Pattern Analysis and Machine Intelligence, IEEE Transactions on*, pp. 363-369, 1982.
- [107] V. Srinivasan and L. R. Nackman, "Voronoi diagram for multiply-connected polygonal domains 1: algorithm," *IBM Journal of Research and Development*, vol. 31, pp. 361-372, 1987.
- [108] H. I. Choi, S. W. Choi, H. P. Moon, and N.-S. Wee, "New algorithm for medial axis transform of plane domain," *Graphical Models and Image Processing*, vol. 59, pp. 463-483, 1997.
- [109] J.-H. Kao, "Process planning for additive/subtractive solid freeform fabrication using medial axis transform," Citeseer, 1999.
- [110] F. P. Melchels, M. A. Domingos, T. J. Klein, J. Malda, P. J. Bartolo, and D. W. Huttmacher, "Additive manufacturing of tissues and organs," *Progress in Polymer Science*, vol. 37, pp. 1079-1104, 2012.
- [111] K. Karunakaran, A. Bernard, S. Suryakumar, L. Dembinski, and G. Taillandier, "Rapid manufacturing of metallic objects," *Rapid Prototyping Journal*, vol. 18, pp. 264-280, 2012.
- [112] N. Guo and M. C. Leu, "Additive manufacturing: technology, applications and research needs," *Frontiers of Mechanical Engineering*, vol. 8, pp. 215-243, 2013.
- [113] H. Lipson, "Frontiers in Additive Manufacturing," *Bridge*, vol. 42, pp. 5-12, 2012.
- [114] B. Lyons, "Additive Manufacturing in Aerospace," *Bridge*, vol. 42, pp. 13-19, 2012.
- [115] J.-P. Kruth, M. Leu, and T. Nakagawa, "Progress in additive manufacturing and rapid prototyping," *CIRP Annals-Manufacturing Technology*, vol. 47, pp. 525-540, 1998.

- [116] C. Doulamanidis and Y.-M. Kwak, "Multivariable adaptive control of the bead profile geometry in gas metal arc welding with thermal scanning," *International Journal of Pressure Vessels and Piping*, vol. 79, pp. 251-262, 2002.
- [117] J. Xiong, G. Zhang, Z. Qiu, and Y. Li, "Vision-sensing and bead width control of a single-bead multi-layer part: material and energy savings in GMAW-based rapid manufacturing," *Journal of Cleaner Production*, 2012.
- [118] J. M. Keil, "Polygon decomposition," *Handbook of Computational Geometry*, vol. 2, pp. 491-518, 2000.

Selected Publications

- [1] **D. Ding**, Z. Pan, D. Cuiuri, and H. Li, "A multi-bead overlapping model for robotic wire and arc additive manufacturing (WAAM)," *Robotics and Computer-Integrated Manufacturing*, vol. 31, pp. 101-110, 2015.
- [2] **D. Ding**, Z. Pan, D. Cuiuri, and H. Li, "A practical path planning methodology for wire and arc additive manufacturing of thin-walled structures," *Robotics and Computer-Integrated Manufacturing*, vol. 34, pp. 8-19, 2015.
- [3] **D. Ding**, Z. S. Pan, D. Cuiuri, and H. Li, "A tool-path generation strategy for wire and arc additive manufacturing," *The International Journal of Advanced Manufacturing Technology*, vol. 73, pp. 173-183, 2014.
- [4] **D. Ding**, Z. Pan, D. Cuiuri, and H. Li, "Wire-feed additive manufacturing of metal components: technologies, developments and future interests," *The International Journal of Advanced Manufacturing Technology*, pp. 1-17, 2015.
- [5] **D. Ding**, Z. Pan, D. Cuiuri, H. Li, N. Larkin, and S. van Duin, "Automatic multi-direction slicing algorithms for wire based additive manufacturing," *Robotics and Computer-Integrated Manufacturing*, vol. 37, pp. 139-150, 2016.
- [6] **D. Ding**, Z. Pan, D. Cuiuri, H. Li, N. Larkin, and S. van Duin, "Towards an automated robotic arc-welding-based additive manufacturing system from CAD to finished part," *Computer-Aided Design*, vol. 73, pp. 66-75, 2016.
- [7] **D. Ding**, Z. Pan, D. Cuiuri, H. Li, and N. Larkin, "Bead modelling and implementation of adaptive MAT path in wire and arc additive manufacturing," *Robotics and Computer-Integrated Manufacturing*, vol. 39, pp. 32-42, 2016.
- [8] **D. Ding**, Z. Pan, D. Cuiuri, and H. Li, "Process planning strategy for wire and arc additive manufacturing," *The 4th International Conference on Robotic Welding, Intelligence and Automation, RWIA*, Shanghai, China, 2014, September. (Excellent Presentation Award).
- [9] **D. Ding**, Z. Pan, D. Cuiuri, and H. Li, "Wire-feed additive manufacturing of metal components: technologies, developments and future interests," *67th IIW Annual Assembly & International Conference, Commission XII*, Seoul, Korea, 2014, July.
- [10] **D. Ding**, Z. Pan, D. Cuiuri, and H. Li, "Programming for robotic wire and arc additive manufacturing," *The 10th IEEE Conference on Industrial Electronics and Applications (ICIEA)*, Auckland, New Zealand, 2015, June.

- [11] **D. Ding**, Z. Pan, D. Cuiuri, H. Li, and S. van Duin, “Multi-direction slicing of STL models for robotic wire-feed additive manufacturing,” *The 2015 Annual International Solid Freeform Fabrication Symposium – An Additive Manufacturing Conference*, Texas, USA, 2015, August.
- [12] **D. Ding**, Z. Pan, D. Cuiuri, H. Li, and N. Larkin, “Robotic wire and arc additive manufacturing: Innovative fabrication for large metal components,” *Australasian Welding Journal*, vol. 60, pp. 8-9, First Quarter – 2015.
- [13] **D. Ding**, Z. Pan, D. Cuiuri, H. Li, and N. Larkin, “Path planning for wire-feed additive manufacturing using adaptive medial axis transformation,” *Journal of Cleaner Production*, **Major revision**.